New Jersey Institute of Technology
Digital Commons @ NJIT

Dissertations | Electronic Theses and Dissertations

Spring 5-31-2000

The impact and fate of aqueous sodium nitrate on hydrocarbon flames

Ann Marie Flynn
New Jersey Institute of Technology

Follow this and additional works at: https://digitalcommons.njit.edu/dissertations

 Part of the Chemical Engineering Commons

Recommended Citation

Flynn, Ann Marie, "The impact and fate of aqueous sodium nitrate on hydrocarbon flames" (2000). *Dissertations*. 401.
https://digitalcommons.njit.edu/dissertations/401

This Dissertation is brought to you for free and open access by the Electronic Theses and Dissertations at Digital Commons @ NJIT. It has been accepted for inclusion in Dissertations by an authorized administrator of Digital Commons @ NJIT. For more information, please contact digitalcommons@njit.edu.

Copyright Warning & Restrictions

The copyright law of the United States (Title 17, United States Code) governs the making of photocopies or other reproductions of copyrighted material.

Under certain conditions specified in the law, libraries and archives are authorized to furnish a photocopy or other reproduction. One of these specified conditions is that the photocopy or reproduction is not to be "used for any purpose other than private study, scholarship, or research." If a, user makes a request for, or later uses, a photocopy or reproduction for purposes in excess of "fair use" that user may be liable for copyright infringement,

This institution reserves the right to refuse to accept a copying order if, in its judgment, fulfillment of the order would involve violation of copyright law.

Please Note: The author retains the copyright while the New Jersey Institute of Technology reserves the right to distribute this thesis or dissertation

Printing note: If you do not wish to print this page, then select "Pages from: first page # to: last page #" on the print dialog screen

NJIT New Jersey's Science & Technology University

The Van Houten library has removed some of the personal information and all signatures from the approval page and biographical sketches of theses and dissertations in order to protect the identity of NJIT graduates and faculty.

ABSTRACT

THE IMPACT AND FATE OF AQUEOUS SODIUM NITRATE ON HYDROCARBON FLAMES

by
Ann Marie Flynn

This study examined the impact and fate of sodium (fed as an aqueous nitrate solution) in fuel-rich methane/air and methane/methyl chloride/air flames as a function of equivalence ratios that experienced diffusion of air from the surroundings. The flames were stabilized on a slotted, uncooled burner. The data set was divided into profiles of relative sodium atom concentrations, temperatures, and selected stable species concentrations. The flames were simulated using a modified version of the Sandia FORTRAN program for modeling steady laminar one-dimensional premixed flames complete with detailed mechanisms. The results showed that maximum sodium atom concentration in the flame is decreased by an increase in equivalence ratio as well as an increase in chlorine loading. In addition, the location of maximum sodium atom concentration is shifted to a higher height above burner as the equivalence ratio is increased.

THE IMPACT AND FATE OF AQUEOUS SODIUM NITRATE ON HYDROCARBON FLAMES

by
Ann Marie Flynn

A Dissertation
Submitted to the Faculty of
New Jersey Institute of Technology
In Partial Fulfillment of the Requirements for the Degree of
Doctor of Philosophy

Department of Chemical Engineering,
Chemistry, and Environmental Science

May 2000

Copyright © 2000 by Ann Marie Flynn

ALL RIGHTS RESERVED

APPROVAL PAGE

THE IMPACT AND FATE OF AQUEOUS SODIUM NITRATE ON HYDROCARBON FLAMES

Ann Marie Flynn

Dr. Robert Barat, Dissertation Advisor — Date
Associate Professor of Chemical Engineering, NJIT

Dr. Joseph Bozzelli — Date
Distinguished Professor of Chemistry, NJIT

Dr. Barbara Kebbekus — Date
Professor of Chemistry, NJIT

Dr. Lev Krasnoperov — Date
Professor of Chemistry, NJIT

Dr. Henry Shaw — Date
Professor of Chemical Engineering, NJIT

Dr. John Stevens — Date
Professor of Mathematics, Montclair State University

Dr. Arthur Poulos — Date
Optomechanical Enterprises, Inc.

BIOGRAPHICAL SKETCH

Author: Ann Marie Flynn

Degree: Doctor of Philosophy in Chemical Engineering

Date: May 2000

Education:

Doctor of Philosophy in Chemical Engineering
New Jersey Institute of Technology, NJ, 2000

Master of Engineering in Chemical Engineering
Manhattan College, Riverdale, New York, 1991

Bachelor of Engineering in Chemical Engineering
Manhattan College, Riverdale, New York, 1981

Major: Chemical Engineering

Presentations and Publications

Flynn, A.M., and R.B. Barat, "The Inhibitory Impact of Sodium on a Methane/Air Flame", Submitted to *Combustion Theory and Modeling* (999)

Flynn, A.M., D. Apostolou, and R.B. Barat, "The Modeling of Sodium in a Hydrocarbon/Air Flame", Paper Presented at AIChE National Meeting, Los Angeles, CA (1997)

Flynn, A.M., and R.B. Barat, "The Experimental Monitoring of Sodium in a Methane/Air Flame", Paper Presented at Eastern States Combustion Conference, Hartford, CT (1997)

Flynn, A.M., and R.B. Barat, "Experimental Characterization of Metals in a Partially Premixed Hydrocarbon/Air Flame", Paper Presented at Eastern States Combustion Conference, Worcester, MA (1995)

Flynn, A.M., and R.B. Barat, "Characterization of a Slotted, Partially Premixed Laminar Methane/Air Flame", Paper Presented at Eastern States Combustion Conference, Princeton, NJ (1993

This thesis is dedicated to
my husband, Kevin, and
my children, Taylor and Kevin.

ACKNOWLEDGEMENT

First of all, I would like to thank the members of my committee, Dr. Bozzelli, Dr. Kebbekus, Dr. Shaw, Dr. Krasnoperov, Dr. Stevens and Dr. Poulos, for their advice and guidance during the course of this work and the writing of this dissertation. In addition, I would like to thank the committee for their patience in allowing me to finish my work while I started my career in academia and raised my two children. I would also like to thank Benedict Barat for the many hours that he labored with me helping me to construct my experimental apparatus and for the many pleasant conversations that we shared.

I would also like to thank the many students whose paths I have crossed at NJIT, in particular Helen, Stephanie, Harry, and Costas. The hours we shared are among my most pleasant memories as a graduate student.

However, as I look back on the eight years that it took me to complete this work, I would like to make special mention of a certain few. I would like to thank Dr. Helen C. Hollein, my mentor and my friend. She has often been a light at the end of a very dark tunnel for me. I would like to thank my brother Charles for his never—ending unconditional support. We share the same heart and soul. I would like to thank my advisor, Dr. Robert Barat, for his guidance and counsel and friendship through these many years. It was invaluable as I negotiated the mountains and valleys of research work. Finally, I would like to thank my husband, Kevin, for his endless love and support. His dedication to our marriage and to our children is unequaled.

I would also like to let my children know that this was for them. I want you both to live your life like every day is your last. And remember, "*Climb every mountain, cross every stream, follow every rainbow, 'till you find your dream*"

TABLE OF CONTENTS

TABLE OF CONTENTS
(Continued)

Chapter **Page**

TABLE OF CONTENTS
(Continued)

Chapter **Page**

TABLE OF CONTENTS
(Continued)

Chapter **Page**

TABLE OF CONTENTS
(Continued)

Chapter **Page**

TABLE OF CONTENTS
(Continued)

Chapter **Page**

TABLE OF CONTENTS
(Continued)

Chapter **Page**

LIST OF TABLES

LIST OF FIGURES

LIST OF FIGURES
(Continued)

Figure **Page**

LIST OF FIGURES
(Continued)

Figure **Page**

LIST OF FIGURES
(Continued)

Figure **Page**

LIST OF FIGURES
(Continued)

Figure **Page**

LIST OF FIGURES
(Continued)

Figure **Page**

LIST OF FIGURES
(Continued)

Figure **Page**

LIST OF FIGURES
(Continued)

Figure **Page**

LIST OF FIGURES
(Continued)

Figure **Page**

LIST OF FIGURES
(Continued)

Figure **Page**

CHAPTER 1

INTRODUCTION

1.1 Motivation for Study

1.1.1 Incineration Emissions

Incineration is a highly engineered process that employs decomposition via thermal oxidation at high temperatures (usually 900°C or greater) to destroy the organic fraction of the waste and reduce volume (20). Generally, combustible wastes or wastes with significant organic content are considered the most appropriate for incineration. However, technically speaking, any waste with a hazardous organic fraction, no matter how small, is at least a candidate for incineration.

Ideally, the primary products from combustion are carbon dioxide, water vapor, and inert ash. In reality, what appears to be a straightforward, simple process is actually an extremely complex one involving hundreds of physical and chemical steps, reaction kinetics, catalysis, combustion aerodynamics, and mass and heat transfer (20). While combustion and incineration devices are designed to optimize the chances for completion of these reactions, they never completely reach the ideal. Instead, small quantities of a large variety of other products may be formed, depending on the chemical composition of the waste and the combustion conditions

encountered. These by-products, along with any unreacted components of the waste stream, become the emissions from the incinerator.

Incineration will also change the form of metal species in waste streams; for example, elemental mercury might be converted to chloromethyl mercury, a highly toxic compound. The principal environmental concern, therefore, centers on the physical or chemical form of the metals (speciation) and where they emerge from the combustion system (partitioning), i.e., bottom ash, in air pollution control device residues, or stack emissions (20).

In general, data on metal emissions and partitioning for hazardous waste incineration is limited and often incomplete. Barton, Clark and Seeker (25) have indicated that the partitioning of metals in incinerators is dependent on the temperature history, chlorine content, residence time, and cooling rates downstream. Pilot scale studies by Waterland (24) support the findings of these researchers.

Over the past three or four decades, there have been important advances in the understanding of the actions, exposure-response characteristics, and mechanisms of action of many common air pollutants. The passage of the Clean Air Act Amendment of 1990 reflects a growing public concern over human exposure to air toxics (38). Studies that have been inspired and initiated by such legislation have shown that air pollutants have been known to cause responses ranging from reversible changes in respiratory symptoms and lung function, changes in airway reactivity and

inflammation, structural remodeling of pulmonary airways, and impairment of pulmonary host defenses, to increased respiratory morbidity and mortality (39).

1.1.2 Flame Retardants

The Montreal Protocol effectively banned the use of many halogenated products such as Freons due to their deleterious effect on the ozone layer. Related halo-compounds serving as flame retardants are also being replaced. While effective as retardants, these compounds often produce toxic byproducts during use as fire-fighting agents (64). At present, considerable effort is being spent to find alternative fire retardants.

Earlier combustion literature indicates that sodium compounds were once considered for flame retardants. Iya and coworkers (48) showed that sodium inhibition, as measured by temperature rises in post flame gases of quenched CH_4/air flat flames and by OH absorption spectroscopy, was due to a homogeneous gas phase chemical mechanism in which peak OH radical concentrations are reduced. They also suggested that Na atoms catalyze radical recombination. Vanpee and Shirodkar (49) showed that organo-sodium compounds were effective flame inhibitors, as measured by increased oxygen mass fraction at extinction in an opposed jet liquid fuel burner.

1.1.3 Rationale for Study

The environmental awareness and activism, which catalyzed passage of the major hazardous waste laws of the 1980's, have in many ways switched to skepticism about the safety and effectiveness of the solutions initiated by those laws. Citizen distrust of the waste management facilities, owners, and operators remains high. One of the major barriers to increased incineration capacity is public opposition to the permitting and siting of new facilities as a result of reports of trace quantities of chlorinated dioxins, furans, heavy metals and other combustion byproducts in the stack emissions of municipal solid waste (MSW) and polychlorinated biphenyl (PCB) incinerators (20-22) such as cement kilns.

In an attempt to further understand the complexities governing incinerator emissions, this study proposes to consider the fate of metals in a flame. By employing the waste management practice of "waste minimization at the source of generation", the flame could possibly produce less volatile metal species (e.g., salts) that are easily collected by a downstream electrostatic precipitator (ESP) or a baghouse. In addition to considering the metal species as a potential incineration emission, it is also worth considering what the potential effects of the metal on the flame are. Certain metal species might have either accelerating or retarding effects on combustion.

1.2 General Overview of this Study

It has been previously stated that metal emissions are of concern to the general public, and as a result, the scientific community. In an attempt to illuminate answers that might diminish some of these concerns, this study hopes to create an experimental template to investigate:

- the fate of metals *in* a flame
- the effect of metals *on* a flame

The metal that was investigated by this study was sodium (Na) and the particular flames of interest were:

- Methane/Air (CH_4/Air)
- Methane/Air/Methyl Chloride (CH_4/Air/CH_3Cl)

Sodium was chosen as the metal to be studied in this work for the following reasons:

1. Aqueous sodium nitrate solutions were chosen as the sodium source because they are non-toxic, as well as easily handled and stored. More importantly, the combustion of this salt produced harmless vapors.
2. As will be discussed later, optical absorbance served as the primary metal diagnostic in the flame. For the light source used, sodium offers a convenient and strong visible atomic absorption wavelength at 589 nm.
3. Once an apparatus had been built that successfully generated experimental data and a model had been developed to simulate the combustion of a metal in a flame, it was hoped that it would be a

relatively smooth transition to switch from the study of sodium to the study of a more hazardous, environmentally toxic metal such as chromium or mercury.

1.2.1 Experimental Overview

In order to monitor the fate of sodium in the methane/ air flame, Atomic Absorption Spectroscopy (AAS) was employed. A beam from a broad-band (wavelength) light source (Xenon arc lamp) was passed through the flame and into a monochromator. The monochromator, a wavelength dispersion device, was set at 589 nm to correspond to the sodium atom absorption. A photomultiplier tube (PMT) connected to the exit slit of the monochromator detected the transmitted light. A chart recorder reported the PMT signals profiles, from which absorbances were determined.

Optical absorbance profiles and thermocouple temperature profiles were monitored as a function of height above burner (HAB) and fuel equivalence ratio, ϕ[1]. Stable species concentration profiles were also monitored in the same fashion using a quartz sampling microprobe and gas chromatograph (GC).

1.2.2 Overview of Flame Model

A modified version of an existing FORTRAN program for modeling steady, laminar, one-dimensional, premixed flames by Sandia National Laboratories (26) was used to simulate the experimental flames for this study. It should be noted that this one-dimensional model was used simply as a first-approximation when attempting to describe the two-dimensional flame in this study. It should not be assumed that the flame could be accurately modeled as one-dimensional. However, in the absence of an available more comprehensive flame model, this was viewed as a reasonable starting point.

The Existing Model

In its most common configuration, the existing code models a round, burner-stabilized flat flame (i.e., no radial dependencies) with a known mass flow rate. The user inputs the measured temperature profile along with a detailed chemical reaction mechanism.

Modifications to the Model

The modifications that were made to the existing code for this study were as follows:

---

[1] $\phi = \frac{(\text{Fuel} / \text{Air})_{\text{actual}}}{(\text{Fuel} / \text{Air})_{\text{stoich.}}}$ using molar or volumetric rates.

1. The existing model assumes a constant gas mass flow rate, $\dot{M}$, in the flame, as given by the continuity equation:

$$\dot{M} = \rho u A \tag{1.1}$$

where ρ is the mass density, u is the velocity of the fluid mixture and A is the cross sectional area of the stream tube encompassing the flame. However, in this study, the flame was not shielded from the surrounding air by a nitrogen shroud, as is often done with a flat flame burner. As a result, the flame entrained air from the surroundings. At any given HAB, the total mass flow was equal to the total gas flow fed to the burner *plus* the amount of air that had been entrained up to that point. This additional entrained air was a function of HAB, defined by x. For this study, the existing mass flow rate term in the model was replaced by the following expression:

$$\frac{\dot{M}}{\dot{M}_o} = 1 + Cx \tag{1.2}$$

In this expression, $\dot{M}_o$ represents the initial mass flow rate of gases fed to the burner while $\dot{M}$ represents the local, total mass flow rate of gases, including the entrained air. The constant, C, was determined from a "best

fit" simulation of selected baseline flames. A more detailed explanation of this simulation is presented in Chapter 5, Modeling. It should also be noted that, like the one-dimensional flame code, this entrainment expression was viewed simply as a reasonable first approximation when attempting to describe the increase in mass flow rate in the flame due to mass transfer of species from the surroundings. It is hoped that future work would produce a more comprehensive expression to describe the increased mass flow rate. This more comprehensive expression could then be incorporated into the flame code.

2. The governing species balance and enthalpy balance equations were originally derived for the model assuming a constant mass flow rate. These expressions were rederived to include the air entrainment term, and the source code was modified accordingly.
3. A sodium reaction subset, which accounted for the reactions of sodium in a hydrogen/ oxygen flame (20), was added to a previously published methane/ air oxidation mechanism (27). For selected cases, the sodium reaction subset and reactions that accounted for sodium interaction with chlorine were incorporated into a previously published methane/ methylchloride/ air mechanism (27).
4. An option was incorporated into the FORTRAN code to request net Rate-Of-Production (ROP) information obtained from calls to selected CHEMKIN subroutines. The net generation and destruction rates for

selected species were calculated, including breakdowns of these net rates into the rates of each contributing reaction (27), at each HAB.

Model Input and Output

The experimentally determined temperature profile, input mass flow rate, and feed mole fractions were user-supplied input to the model. The output of the model contains the mole fractions of the gases produced as a result of the combustion of the fuel, air and metal (if included), all as a function of HAB. The species of most interest would be CH_4, CO and CO_2, and sodium atom, Na. These results are then compared to the results found experimentally. Rate of production calculations provide key information to illuminate flame reaction pathways, especially for sodium.

1.3 Available Data and New Advances

1.3.1 Available References

The literature referenced in this study on sodium—containing flames is but a small fraction of the literature available on the subject. However, the cited references on sodium are all relevant to one or more of the following aspects of the experimental portion of this work:

- monitoring of sodium in a CH_4/air flame
- use of a continuous light source
- use of a slotted burner

- experiencing entrainment of air
- use of atomic absorption spectroscopy

1.3.2 New Advances Furthered by this Study

The novelty of this research is the detailed chemical reaction modeling of sodium in a CH_4/air flame which entrains air, in order to create a general template for the study of other metals in a flame. In all of the exhaustive literature searches performed, there is little or no evidence of such detailed modeling of any metal in a flame. Kindevater and O'Haver (8) modeled copper and magnesium using a slotted burner and an acetylene/air flame in a very simple fashion. Because of its empirical approach, this model is not capable of producing detailed species concentrations as a function of HAB in the flame.

CHAPTER 2

A LITERATURE SURVEY

An extensive literature survey was made on the various aspects of the work. Each topic is presented separately for the sake of clarity.

2.1 Experimental Apparatus

2.1.1 The Light Source

In general, the most common light source used in flame atomic absorption spectroscopy has been the hollow cathode lamp. It consists of a tungsten anode and a cylindrical cathode sealed in a glass tube that is filled with neon or argon to a pressure of 1-5 torr. The cathode is constructed of the particular metal whose spectrum is desired—in this case, sodium.

In an effort to build this experimental apparatus as a tool for multi-element analysis, the use of a continuous source was investigated. Although multi-element hollow cathode lamps were available, they were considered to have relatively low intensity and high background noise compared to the single element lamps, resulting in reduced sensitivity. Indeed, some studies in the literature have shown that attempts to make atomic absorption spectroscopy (AAS) a multi-element technique have centered around the use of continuum sources (1, 2). Zander, O'Haver and Keliher (1) reported using

wavelength modulation. Cochran and Hiefje (2) developed continuum source AAS using spectral line modulation. In addition, many workers (3-8) over the past three decades have shown that the interest and growth of continuum source AAS has included the high pressure xenon arc lamp as the standard light source. For this reason, the xenon arc lamp was chosen as the light source for this study.

2.1.2 The Burner

For successful performance of AAS, a sample must first be atomized. Many procedures, which operate at various temperatures, already exist. These include: flame atomization (1700-3150°C), electrothermal (1200-3000°C), inductively coupled argon plasma (6000-8000°C), direct current argon plasma (6000-10,000°C), electric arc (4000-5000°C) and electric spark (40,000°C). However, for absorption spectroscopy, electrothermal (graphite furnace) and flame atomization are the most common.

Many studies (9-10) employed the use of a graphite furnace for AAS and were fairly successful. A graphite furnace confines the atomized sample in the optical path for a residence time of several seconds compared to a residence time of only a fraction of a second in flame atomization. This results in increased absorption and higher sensitivity. Also, the graphite furnace requires as little as 1 μL for analysis compared to 1-2 mL for flame analysis (11). However, Jones, Smith and Winefordner (9), who used a

graphite furnace in their study, describe some less obvious disadvantages of a graphite furnace when compared to a flame for atomization. Besides the fact that a furnace requires more operator skill to determine the proper conditions for each type of sample, they list the following disadvantages: poor source intensity below 250 nm; the need for a high resolution monochromator; the need for multiple detectors; and the need for wavelength modulation to overcome the instability of the continuum source and broad-band background absorption. Three years after the publication of this work, Jones (3) went on to improve the detection limits of his continuum source atomic absorption spectrometry (CSAAS) apparatus. One of these improvements was the replacement of the graphite furnace by a Perkin-Elmer nebulizer burner system with a slotted head.

A 10 cm x 0.07 cm slotted burner was used for this study, based on the successful completion of other AAS studies (3, 4, 12) using a similar burner. It should be noted that in spectroscopy studies, flat flames are also used. However, these studies (12) are generally limited to emission spectroscopy. The long path length provided by the slotted burner favors the absorption measurements required for this work.

2.1.3 Optical Alignment

It has previously been discussed that a 300 W xenon arc lamp was used for this study because of its versatility. However, the actual manipulation of the

light produced by this lamp presented a problem. The light beam exiting the arc lamp is approximately 50 mm in diameter. The width of the flame that the light passes through is approximately 1mm. For good spatial resolution within the flame, the diameter of the light beam should ideally be less than the width of the flame and fairly collimated.

Two studies were investigated in which a xenon arc lamp was used with a slotted burner for AAS. The first study was conducted by Fernando, Calloway and Jones (3). A schematic of the optical alignment used in their continuum source atomic absorption spectrometer (CSAAS) appears below.

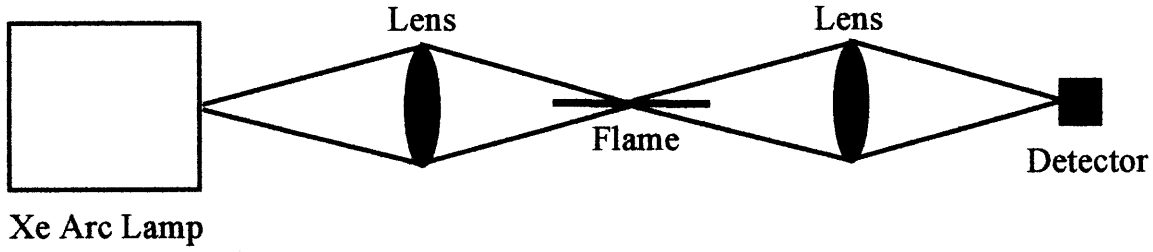

Figure 2.1 Optical Alignment of CSAAS from Fernando, Calloway and Jones (3)

This optical arrangement was reproduced in this work, but it was found that the beam was not sufficiently collimated over the length of the burner. In fact, because the beam was not collimated at all, this configuration was subsequently rejected.

A second study using a xenon arc lamp and slotted burner was conducted by Rann and Hambley (12). Their optical arrangement used for the

measurement of the distribution of atoms in a flame is presented below.

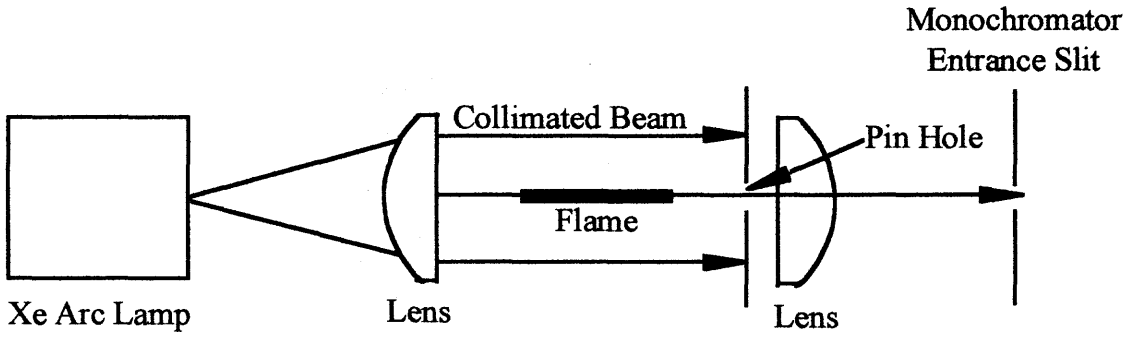

Figure 2.2 Optical Arrangement from study of Rann and Hambley (12)

This optical system was also tested in the current work. It was found that this particular arrangement produced a very poor signal to noise (S/N) ratio. This S/N ratio was discussed by Rann and Hambley in their study. As a result, this configuration was also rejected.

A third possible solution was to use a lower wattage arc lamp, since it is suggested that lower-wattage arc lamps come close to being point sources and are ideal for use in projection systems and for obtaining well-collimated beams (13). However, the *unattenuated* beam from a lower wattage lamp would not have produced sufficient light throughput for good S/N ratios.

The optical alignment of the beam from the arc lamp used for this work was a modified version of that seen in the work of Rann and Hambley (12). A schematic of the alignment appears in the following figure.

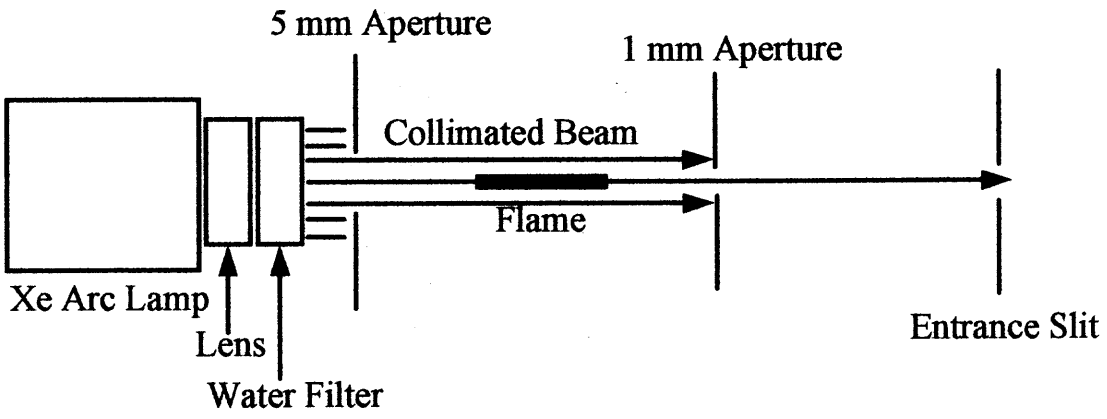

Figure 2.3 Optical Alignment Used to Monitor Sodium in this Study

This arrangement produced an acceptable S/N ratio as well as sufficient light throughput to the monochromator.

2.1.4 Salt Solution Feed

The aqueous sodium salt solution that was introduced to the burner was in the form of a fine droplet, liquid spray. None of the literature reviewed suggested a particular sodium salt for use in an AAS study. Sodium nitrate ($NaNO_3$) was chosen for this study because it is inexpensive, readily available, and easily soluble in water. The initial salt concentration used was 0.01 mol/L $NaNO_3$ (approximately 8.5 g/L). The salt concentration suggested by the literature survey ranged from 1g/L (3) to 0.01 g/L (4). Since the type of salt varied so widely, the concentration of salt suggested by the literature search proved inconclusive. The actual $NaNO_3$ concentration used for this work was 0.02 mol/L (1.7 g/L). It was found to be the maximum salt

concentration that did not saturate the absorbance signal.

2.1.5 Choice of Flame

It is widely accepted that the desired flame for the study of sodium in flame AAS is acetylene/ air (3,4,12,14,15). When the sodium salt solution is sprayed into the flame, the high temperature of the acetylene/air flame (2100-2400°C) insures rapid formation of sodium atoms. However, this study has attempted to model (in a broad sense) a commercial incinerator. In order to do this, the flame chosen was methane/air (1700-1900°C) (24) to emulate natural gas/air. Skoog (16) addresses the problem of whether or not these temperatures are sufficient enough to atomize the sodium ions entrained in the liquid droplets. The temperatures provided by the burning of natural or manufactured gas in air are low enough that only the alkali and alkaline-earth metals, with relatively low excitation energies, produce useful spectra. Therefore, the methane/air flame fulfills the two-prong objective of simulating a commercial incinerator while also providing sufficiently high temperatures to produce sodium atoms from aqueous sodium ions for useful AAS work.

2.2 Modeling

2.2.1 Sodium Mechanism

The literature contains studies of the chemistry of alkali metals in flames as far back as 1950 (17). However, a literature search provided only one

complete mechanism for flames containing sodium – that of Hynes, Steinberg and Schofield (18) in their 1983 study. The mechanism lists the likely reactions of Na, NaO, NaO_2, and NaOH in H_2/O_2 flames. However, the flame used in this study is CH_4/air, not H_2/O_2. This problem was addressed by Schofield (19) in a later paper. He discussed that the one aspect of alkali and alkaline earth flame chemistry that appears to be well established is its independence of fuel type. Except for the cyanides, no metal/carbon chemistry plays any role in the gas phase. As a result, the same reactions occur in hydrogen or fossil fueled flames and noted differences stem simply from the differing flame radical concentrations, temperatures, or time scales. Therefore, using a sodium mechanism developed for a hydrogen/oxygen flame with the methane/air flame was a reasonable approach.

2.2.2 Development of Air Entrainment Expression

There were little literature data available regarding entrainment. According to Spalding (30), the mass flow rate, M, in a laminar jet increased with increasing height above burner (HAB), denoted by x. He developed the following expression to describe the mass flow rate, which was independent of the velocity of the injected fluid:

$$M = 8\pi\mu x \qquad (2.1)$$

where μ is the jet fluid viscosity. The entrainment rate, i.e., the rate of increase of M with x, was a constant.

$$\frac{dM}{dx} = 8\pi\mu = \text{Constant} \tag{2.2}$$

The above expressions were used as a starting point in the development of an expression to describe air entrainment for the slotted flame examined by this study.

2.3 Data Analysis

2.3.1 Flame Absorbance Profiles

Figure 2.4 shows typical flame absorbance profiles for magnesium, silver and chromium as discussed in detail by Skoog (16). The profiles are interpreted according to the ability of the elements to form an oxide. The elements are rated (16) in the following fashion:

(not readily oxidized) Ag < Mg < Cr (forms very stable oxides)

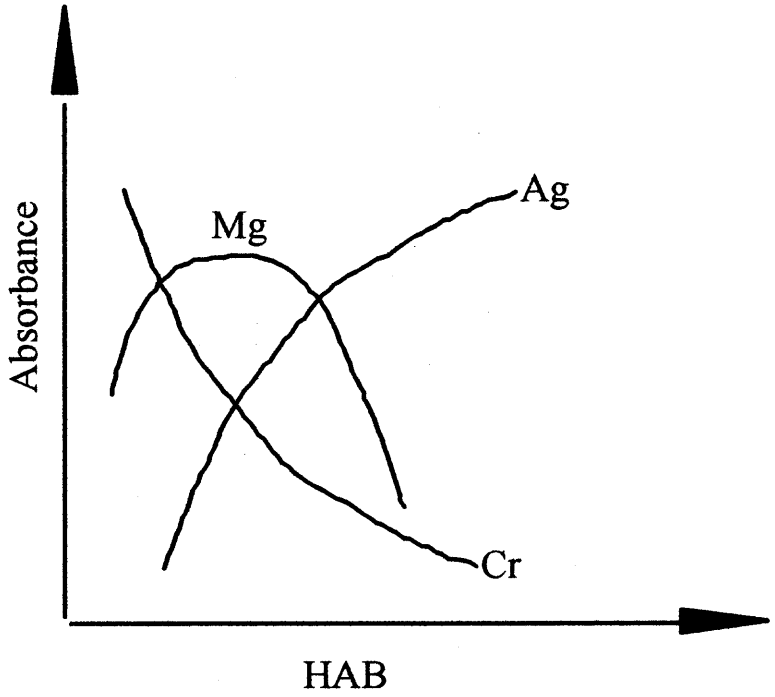

Figure 2.4 Flame Absorbance Profiles for Magnesium, Silver and Chromium (16)

With respect to magnesium, it seems to exhibit a maximum in absorbance at about the middle of the flame because of two opposing effects. The initial increase in absorbance with HAB results from an increased number of magnesium atoms produced by the longer exposure to the heat of the flame. As the outer zone is approached, however, appreciable oxidation of the magnesium begins. This process leads to an eventual decrease in absorbance because the oxide particles formed do not absorb at the wavelength used (16).

The behavior of silver, which is not readily oxidized, is quite different. A continuous increase in the number of atoms and as a result, the

absorbance, is observed from the burner to the upper edge of the flame. In contrast, chromium, which forms very stable oxides, shows a continuous decrease in absorbance. This observation suggests that oxide formation exists from the start.

It had been expected during the course of this work that sodium will behave in a manner similar to that of magnesium. Both Schofield (19) and Goodings (17) have discussed the flame chemistry of alkali (Na) and alkaline earth metals (Mg) interchangeably. It was expected that the absorption profile of sodium would quickly climb to a maximum and then drop off, similar to that of Mg.

2.3.2 Non-Metallic Stable Species Profiles

The primary non-metallic stable species concentration profiles examined in this study are methane (CH_4), carbon monoxide (CO) and carbon dioxide (CO_2). It has been detailed in many other studies (flames without air entrainment) (37, 45, 51) that the primary reactant, CH_4, monotonically declines. Figure 2. 5 details that for a fuel-lean flame, the CO rises to a maximum and then falls as CO is converted to CO_2:

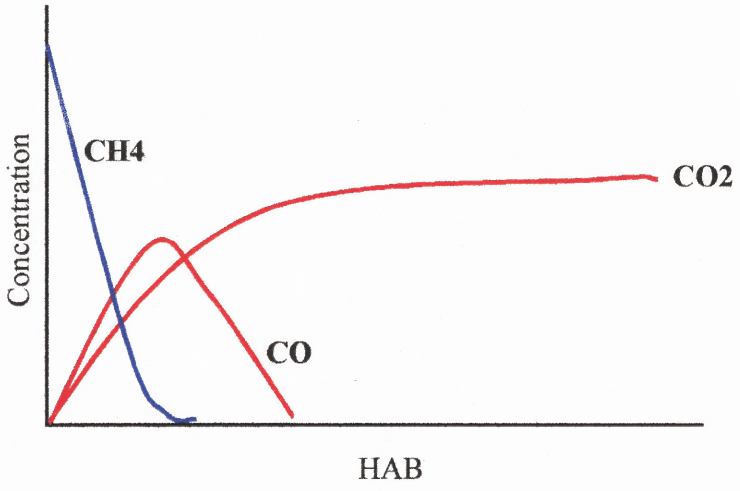

Figure 2.5 Stable Species Profiles for Fuel—Lean Flame Without Air Entrainment

Figure 2.6 shows that for fuel-rich flames, the CO rises and then remains constant as oxygen is depleted:

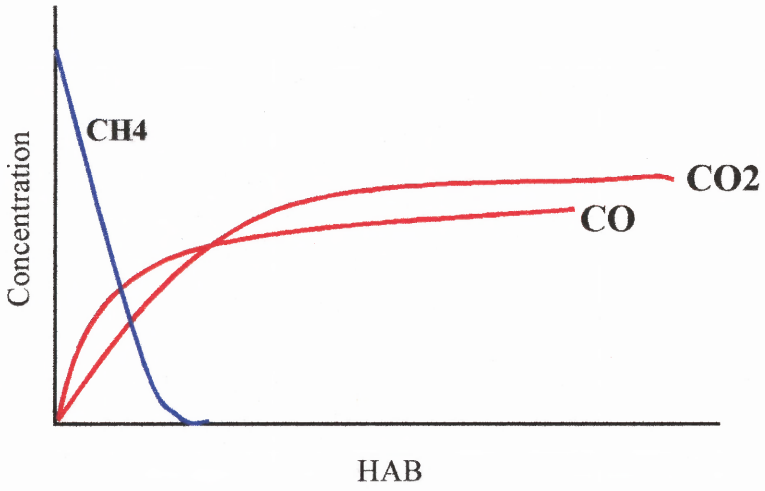

Figure 2.6 Stable Species Concentration Profile for Fuel—Rich Flame Without Air Entrainment

For the fuel-rich slotted flames in this study, it was anticipated that the CO and CO_2 profiles would likely be affected by the air entrainment.

CHAPTER 3

OBJECTIVES

The primary objectives of this research are as follows:

1. To investigate the chemical fate of sodium in a methane/air flame (as a simple metal in an incinerator) and how this fate is altered in the presence of chlorinated species.
2. To investigate the impact of sodium on CH_4/air and CH_4/CH_3Cl/air flames with respect to temperature profiles and non-metallic stable species profiles.

These objectives were investigated in the following sequence:

- Study methane/air baseline flame
- Dope with sodium
- Study baseline flame doped with chlorinated species
- Dope with sodium

These previously outlined objectives were met through the collection of a large quantity of experimental data, the development of a detailed chemical reaction/ flame model, and the simulation of these flames with the model.

CHAPTER 4

MATERIALS AND EXPERIMENTAL METHODS

4.1 Experimental Apparatus

4.1.1 Burner

The burner used in this study is a stainless steel slotted type that is typically found in an atomic absorption spectroscopy (AAS) apparatus, seen below in Fig. 4.1. This burner, which has a slot 0.07 cm wide and 10 cm long, was chosen because it provided a long path length for light to pass through the flame for stronger absorption measurements. The burner was then mounted on a vertical-lateral translation stage to provide two-dimensional spatial resolution of the flame relative to the stationary light source. The movement of the burner with respect to the light beam is crucial for data collection since all of the data taken is with respect to height above burner (HAB).

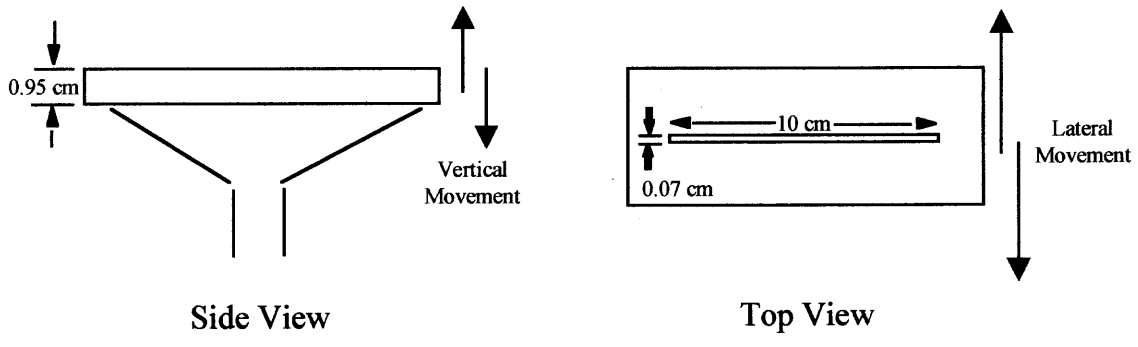

Figure 4.1 Burner Side and Top Views

4.1.2 Mixing Chamber

The mixing chamber originally used for this experimental setup was taken from a conventional AAS assembly. However, the original solution atomization device proved unreliable as well as inflexible since solution introduction rates could not be varied. The present experimental configuration (Figure 4.2A) utilizes a customized mixing chamber constructed of polyvinyl chloride (PVC) plastic. Its dimensions are 15 cm x 4 cm x 4 cm. In its development, the mixing chamber was optimized in the following manner:

1. The mixing chamber was fitted with two ports to accommodate the safe introduction of the primary and an auxiliary fuel or oxidant. The ports are offset from each other, on either side of the mixing chamber, as seen in Figure 4.2B. This offset allows the components to combine in a swirling fashion to encourage more complete mixing.
2. The oxidant is introduced into the chamber tunnel, via an air atomizing nozzle, perpendicular to the fuel port. The sample provided reliable atomization as well as variable solution notes.
3. The actual section of the mixing chamber where most of the mixing between the fuel and oxidant takes place was made longer than that which is found in typical AAS setups. This again was done to encourage better mixing.

It should be noted that all flows entering the mixing chamber are individually metered.

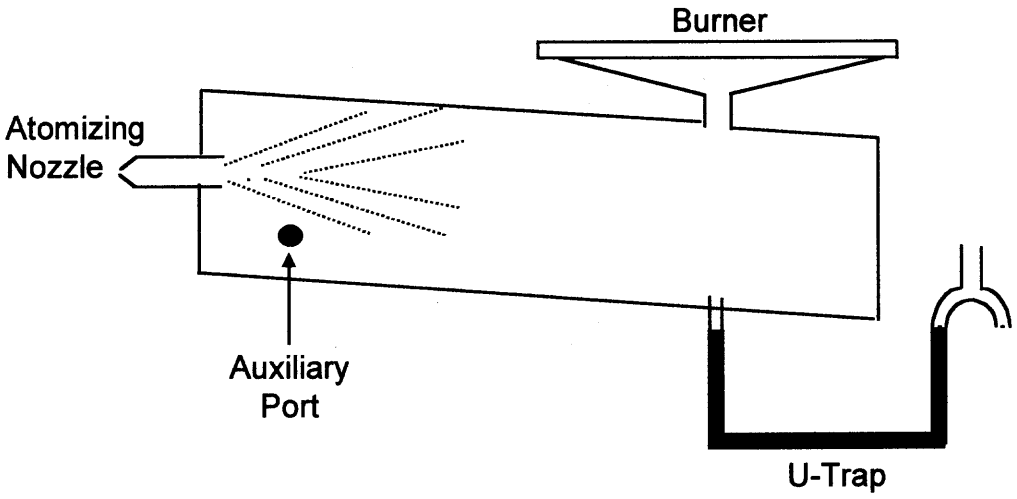

Figure 4.2(a) Side View of Mixing Chamber

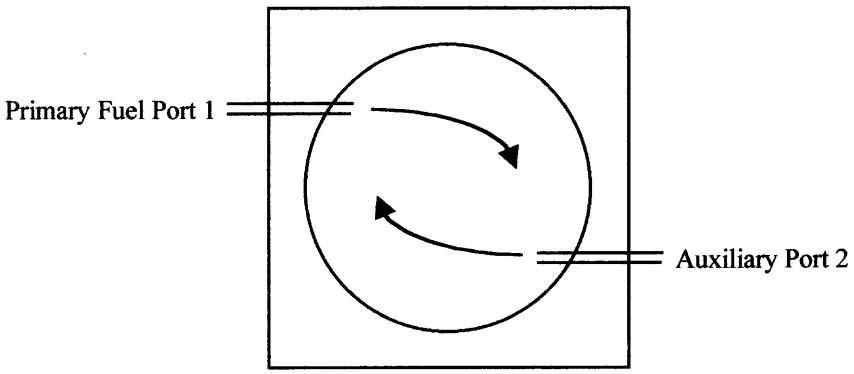

Figure 4.2(b) Cross-Sectional View of Mixing Chamber

The stainless steel slotted burner described in 4.1.1 was fitted into a metal collar and sealed using a rubber o-ring. The collar was press fitted into the PVC chamber. The mixing chamber was then mounted to an X-Y translation stage at a slight incline (approximately 8°). The atomized spray incline was necessary because only a small portion of the atomized spray supplied to the mixing chamber actually gets entrained up into the burner. Unentrained liquid

that falls out of the gas stream is drained from the mixing chamber via an exit port found on the underside of the chamber. A simple water tube trap seals the chamber from the ambient air.

4.1.3 Fuel and Oxidant

When analyzing sodium via atomic absorption or atomic emission experiments, the recommended choice of fuel and oxidant is acetylene and air, respectively (5). Certain metals require a minimum flame temperature in order to generate sufficient atoms, and the choice of fuel and oxidant determines that temperature. For example, sodium requires a flame temperature of approximately 1700°C to allow the formation of atoms, whereas a metal like chromium requires a temperature of at least 2100°C. Table 1 below shows how the temperature of a flame is directly related to the choice of fuel and oxidant (4). The highlighted fuel and oxidant combination characterizes a flame similar to that used for this study.

The primary fuel used for these experiments was methane. For certain cases, methylchloride was introduced as a secondary source of fuel and to simulate the existence of chlorinated waste often present in incinerator feeds together with metals. Even though a second port was available, the two fuels were combined *before* they reached the primary fuel port in order to utilize a flame arrestor for safety. The fuels were then introduced simultaneously as a premixed fuel to the mixing chamber.

Table 4.1 Flame Temperatures (4)

Fuel	Oxidant	Temperature (°C)
Natural Gas	**Air**	**1700-1900**
Natural Gas	Oxygen	2700-2800
Hydrogen	Air	2000-2100
Hydrogen	Oxygen	2550-2700
Acetylene	Air	2100-2400
Acetylene	Oxygen	3050-3150
Acetylene	Nitrous Oxide	2600-2800

Figure 4.3 presents an overall schematic of the gas delivery system to the burner. Other gases (oxygenated acetylene) were available, though not used.

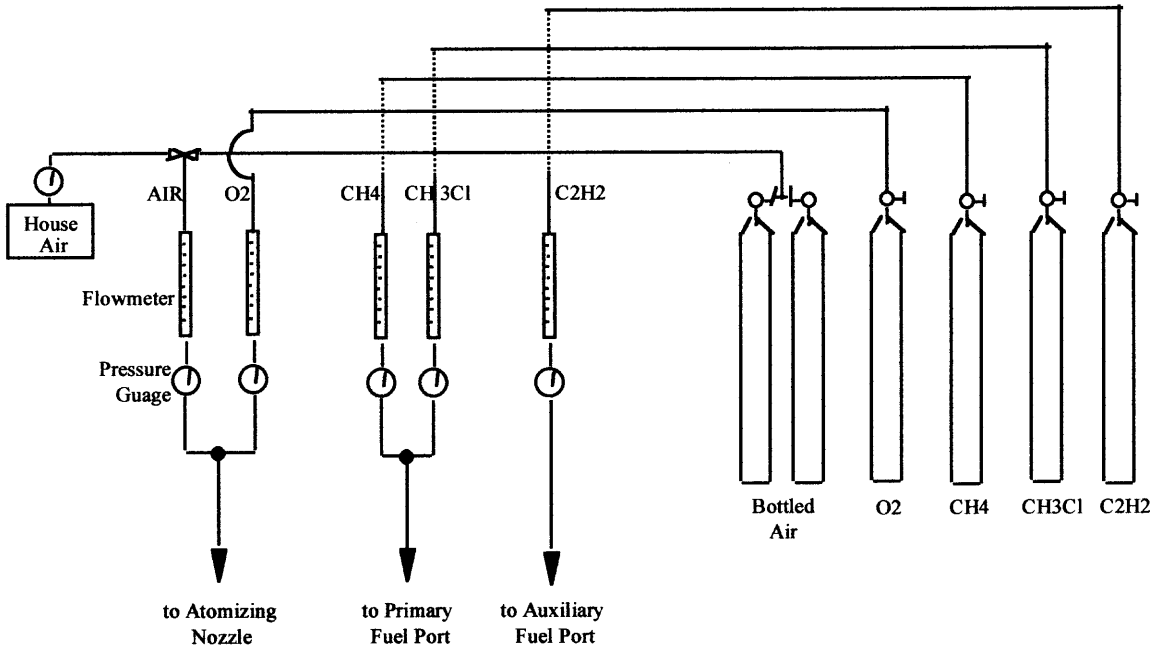

Figure 4.3 Gas Delivery System

As can be seen from the figure, all of the fuels (methane, methyl chloride and acetylene) as well as the oxidants (bottled/house air and oxygen) were individually metered.

4.1.4 Sodium Solution and Feed Reservoir

Feed Preparation

The sodium was supplied to the flame as a 0.02 mol/L sodium nitrate ($NaNO_3$) solution. The solution was prepared from stock $NaNO_3$ crystals (Fisher Scientific Company) and deionized water. Deionized water was chosen over distilled or house water in order to minimize the amount of interference from foreign trace ions.

Feed Reservoir System

Depending on the particular case being studied, either $NaNO_3$ solution or pure deionized water was fed to the burner, as seen in Figure 4.4. Each feed was kept in its own separatory funnel that supplied individual 250-milliliter burettes. The burettes were used to accurately monitor the amount of solution fed to the system over any given period of time. Each type of feed, $NaNO_3$ solutions or deionized water, then flowed from the burettes by gravity to its own positive displacement pump. A separate pump was used for each feed because of the contamination expected when changing from salt solution to pure water when using only one pump. The discharge from both pumps combined at a two-way

metering valve. Depending on the position of the valve handle, either $NaNO_3$ *or* deionized water was fed to the burner at a rate determined by the calibrated setting of the metering valve.

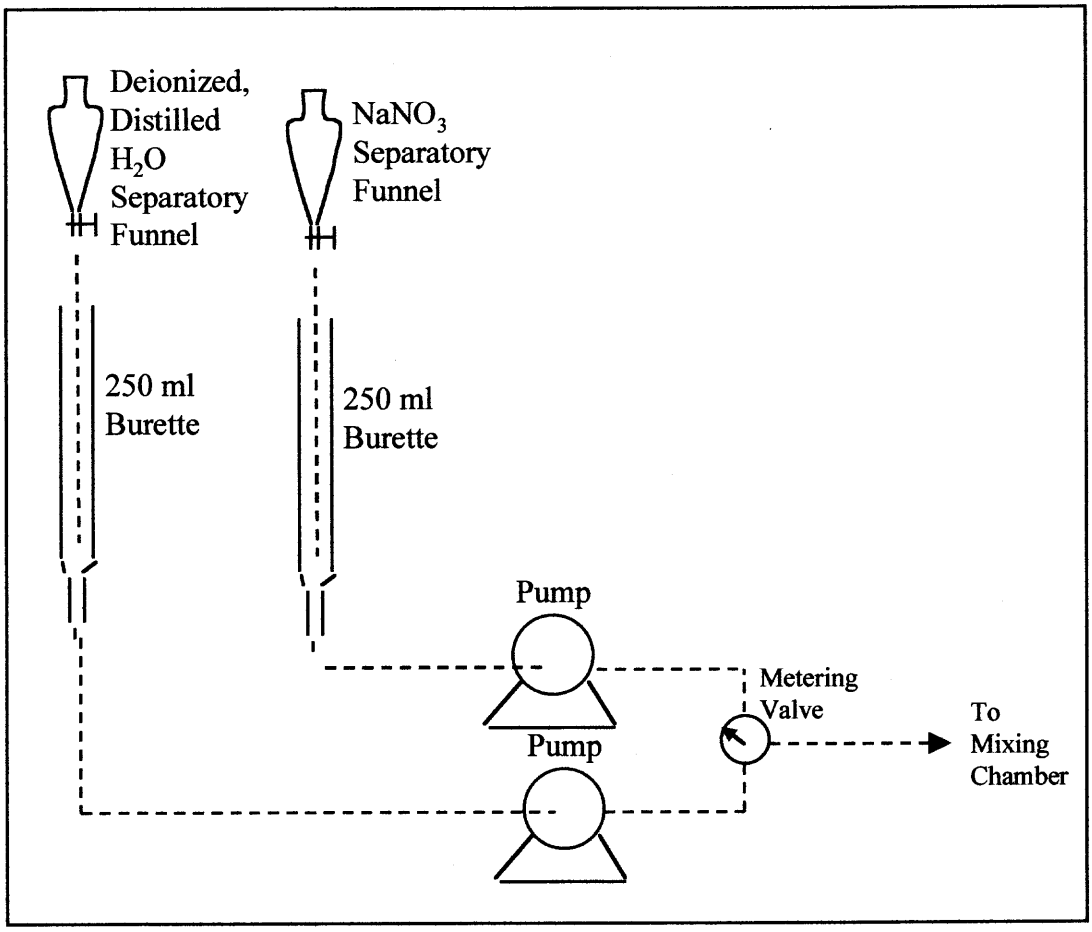

Figure 4.4 Feed Reservoir System

Atomization of Feed

As previously stated, the mixing chamber was customized to suit the needs of this particular work. Therefore, the nebulizer usually found in a typical AAS mixing chamber was replaced by a commercial air atomizing nozzle (Hago

Company). It was found that, in this particular setup, a nebulizer restricted both air flow and solution flow to the mixing chamber. The air atomizing nozzle removed this restriction. The Hago nozzle was made of stainless steel to minimize corrosion. It was attached to the mixing chamber at the end opposite the burner location. The liquid was introduced to the side of the nozzle while the pressurized combustion air was introduced at the back end of the nozzle. The air (60 psig) atomized the liquid and also served as transport for the atomized spray through the mixing chamber. Fine droplets were sprayed perpendicularly into the swirling gases of fuel at an angle of 45°. A small portion of these atomized droplets were then carried to the burner with the fuel and air. However, a rather large portion of these atomized droplets simply deposited on the floor of the mixing chamber and were collected via the exit port. The actual percent of liquid getting to the flame will be discussed later in this chapter (Calibration of Metering Valve and Liquid Flowrate to Burner)

4.1.5 Arc Lamp

The light source chosen for use in this work was a spectrally broad continuum light source—a 300 W xenon arc lamp from Oriel (Model 6259). In conventional atomic absorption spectroscopy (AAS), spectrally narrow atomic line sources such as hollow cathode lamps are used. However, one of the major disadvantages associated with conventional line source AAS is that only one element can be determined at a time. This was an important consideration, since

future plans for this apparatus had included the detection of atomic species other than sodium as well as the possibility of some diatomics. The replacement and realignment of single element lamps can be time consuming and expensive. And even though some multi-element hollow cathode lamps are available, they are not widely used due to their relatively low intensity, reduced sensitivity, and high background noise compared to the single element lamps (1,2).

Using a continuum source such as an arc lamp, studies have shown that as many as 11 elements can be detected in a single spectrum. More importantly, as many as 6 elements have been determined simultaneously at maximum sensitivity (i.e. sensitivity of atomic absorption with conventional line source) (1).

Therefore, a single continuum light source has the potential to detect a wide variety of species such as NaO. It is unlikely that there is a dedicated single light source available to detect such unique diatomics. A notable exception to this is the OH radical. In this case, the emission from a copper hollow cathode lamp can be strongly absorbed by OH at 306 nm. However, exceptions such as these are few. Therefore, the xenon arc lamp was chosen simply for its versatility.

4.1.6 Aperture, Lens and Mirror Alignment

Aperturing the light from the arc lamp (see Figure 2.3), while completed innovatively and successfully, reduced the very intense beam to at least 1/20 of its original power. The goal was to make a large diameter light source (50 mm at

the lamp exit) *resemble* a collimated laser beam (1mm). As outlined in Chapter 2, an optical arrangement for work similar to this has been published (3). This particular reference suggested not to aperture the light until after the light had passed through the flame. This would result in a relatively large diameter beam of light passing through a narrow slotted flame. When this system was reproduced, it was found that it did not work to any degree of satisfaction. A configuration such as this allowed a lot of movement (steering) of the beam, which resulted in a very noisy signal. Modifications of this configuration produced significantly better results.

Initially, the beam exiting the arc lamp was 50 mm in diameter. A step-down adapter (aperture) converted this beam to 37 mm. A black water walled filter was attached to this adapter to reduce the infrared output of the high power lamp. Located immediately at the end of the water filter is a 5 mm aperture. Having the 5 mm aperture directly attached to the water filter allows it to act as a "lens cap" for the lamp. In this way, it eliminates any stray lamplight entering the room, which over a sustained period, would be a health risk due to the ultraviolet component. Located immediately after the 5 mm aperture was a shutter. Rather than turning the lamp on and off every time an experiment required light/no light, the light from the lamp was shuttered instead, before it even reached the flame.

The slightly diverging light exited the 5 mm aperture and passed through the slotted flame. Once the light had passed through the flame it then passed

through a 1 mm aperture. The 1 mm hole was lined up exactly with the burner slot and was used to view particular areas of the flame. Note should be taken that even though the aperture always viewed the same section of light from the lamp, the area of the flame that the light passes through changed, as the HAB changed. This ability to view portions of the flame with a small diameter aperture allowed for good spatial resolution.

As the light from the 1 mm aperture traveled towards the monochromator, it was necessary to incorporate a mirror pair and a prism pair for vertical and horizontal beam steering (see Figure 4.6). These optics were required because a lab bench long enough to mount the entire apparatus was not available. Steering the light beam an extra six feet allowed the 1 mm beam to diverge to a diameter of approximately 25 mm. Therefore, a 25 mm diameter, short focal length collection lens was used to focus the diverged beam onto the monochromator entrance slit.

Experiments have shown that placement of this lens was critical to the resolving power of the monochromator. In order to create an optimum image for throughput to the monochromator, the lens was located approximately one focal length away from the monochromator. At this distance, the light was focused down to a point having a diameter slightly *smaller* than the width of the entrance slit. This procedure allowed all of the collected, focused light to pass through the entrance slit to the monochromator, even when any flickering motion of the flame caused the beam to move and bend,. In this manner, the

light throughput to the monochromator was maximized. On the contrary, had the light been focused to a diameter larger than the entrance slit, the slit would then act as an aperture, reducing light input.

4.1.7 Monochromator and Photomultiplier Tube

The monochromator used in this experimental setup was the first half of a Spex 1400-11 Double Spectrometer. As can be seen in the figure below, light enters the entrance slit S1. This slit was held constant at 20 μm for all experiments. The light expands to fill concave mirror M1, and is then reflected to grating G1, which had a ruling of 1800 grooves/mm. The light is then reflected from the grating to a second concave mirror M2. A swingaway mirror M3 can divert the "monochromatic" beam through S3, into the second-half of the instrument for even greater spectral resolution. For the current flame experiments, mirror M3 was moved out of position and the instrument was operated as a single spectrometer. The slit S2 was used as an exit slit for all cases studied and the width was held constant at 100 μm. The monochromator has a focal length of 750 mm (i.e., a 3/4 meter monochromator), and a variable scanning speed in the forward and reverse direction of 1-20 nm/min (1-200 $\text{Å}/\text{min}$). Due to the unavailability of a scanning motor controller, a generic power supply was adapted for this purpose.

Attached to the exit slit of the monochromator was a side-on EMI/Thorn Photomultiplier Tube (PMT). The PMT had once been replaced by a photodiode

because it was thought that the light from the arc lamp would saturate the PMT. However, a simple linearity experiment using neutral density filters proved that this was not the case. Therefore, the present configuration utilizes a PMT for the following two reasons:

1. the extensive aperturing of the light, resulting in such a decrease in power, suggested that saturation of the PMT was no longer an issue.
2. the photodiode did not have the sensitivity of the PMT.

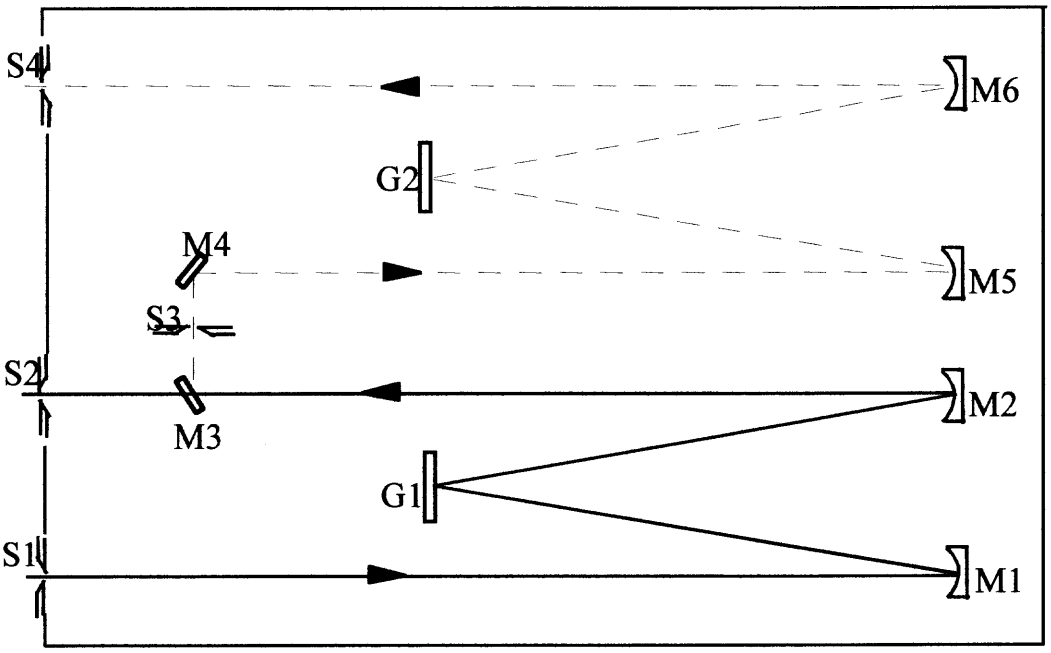

Figure 4.5 Top View of Monochromator

4.1.8 Thermocouple

Flame temperatures were measured with an uncoated Type R (Pt, Pt/13% Rd) thermocouple, having a bead diameter of approximately 0.5mm. The useful temperature range of the thermocouple was consistent with the methane/ air

flame temperatures produced i.e., T< 1900°C. The thermocouple was connected to an Omega High Performance Temperature Indicator (Model DP41-TC). This instrument converted the voltage signal produced by the thermocouple to an actual measurement of bead temperature in degrees Fahrenheit or Celsius. In addition to a digital read out of temperature, the unit also provided a proportional analog output signal.

4.1.9 Plexiglass Housing

The entire burner and mixing chamber assembly, quartz probe for gas sampling and thermocouple are housed in a vented five sided, transparent Plexiglass structure. The approximate dimensions are 18"x18"x24". One side of the structure is hinged to allow easy access to the equipment. The top of the enclosure is partly open for exhaust venting to a mildly induced draft hood. Enclosure of the flame in this manner greatly reduced disturbances of the flame by room air currents and, as a result, helped minimize noise in the signal from the PMT.

4.1.10 Chart Recorder

A Linear chart recorder was used to track the signal from the PMT which was later interpreted as absorbance measurements. In a similar fashion, it was also used to chart the voltage signal from the Omega Temperature Indicator to determine temperature profiles.

The complete optical configuration with all of the previously described components is outlined in figure 4.6.

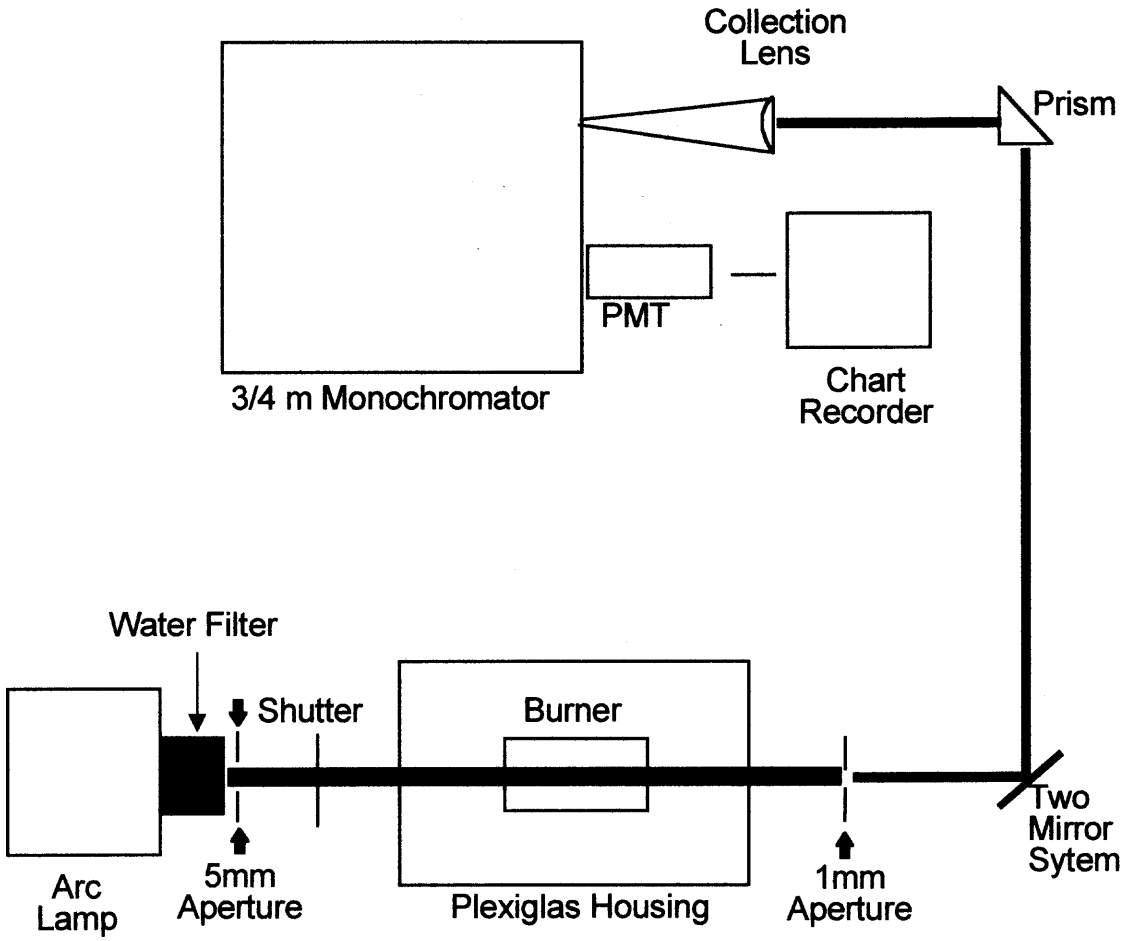

Figure 4.6 Optical Arrangement (Top View)

4.1.11 Stable Species Sampling and Analysis System

A first step in understanding the impact of the sodium nitrate and methyl chloride additives was to measure their effect on the important stable species CH_4, CO and CO_2. The stable species experimental data in the absence of sodium and chlorine were used to calibrate the flame model. As will be discussed later, the stable species profiles for this particular flame are unique due to

entrained air. Following, is a description of the individual units that make up the gas sampling and analysis system for stable species.

Gas Sampling Probe

The hot gases were drawn from the flame with a water-cooled, quartz microprobe connected to a vacuum. The probe orifice is approximately 50 μm. Heat transfer in the probe cools the hot gases, effectively stopping any reaction. The cooled sample gases are fed to a Gas Chromatograph via heated transfer lines. The following figure depicts the microprobe.

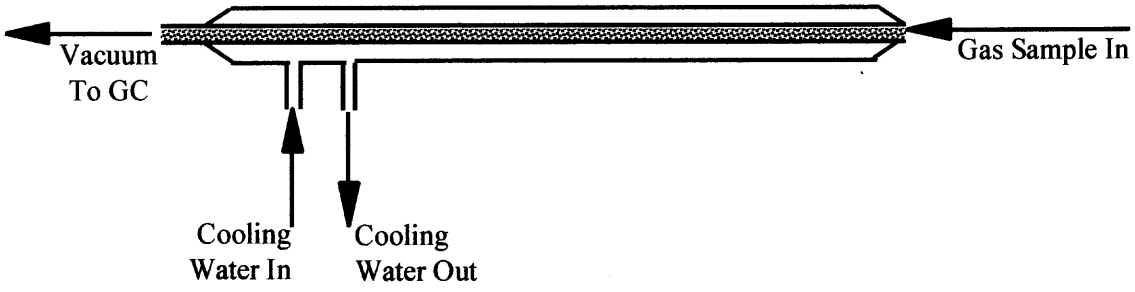

Figure 4.7 Quartz Microprobe (Simplified)

Gas Chromatograph

The analytical system is highlighted in Figure 4.8. The gas flowed through the heated transfer line into sample loop-equipped, six-port Valco gas sampling valves. The samples were injected into packed columns in a Perkin-Elmer 3920 gas chromatograph (GC). With temperature programmed heating, a six foot Carbosphere 80/100 column was used to separate CO, CO_2, and light

hydrocarbons. After separation, the CO and CO_2 were catalytically reduced with H_2 to CH_4 over a heated (300°C) ruthenium catalyst packed bed reacts. This sample was then directed into a flame ionization detector (FID). (An auxiliary six foot 1% AT-1000 on Graphpac 60/80 column, not used for this current study, was available to separate hydrocarbons and any chlorinated hydrocarbons in the sample. After separation, the sample was directed into a second FID). A Hewlett-Packard 3396 Series II Integrator was used to process the FID signal and record the results. The entire system was calibrated by filling the sample loops with standard gas (*Scotty IV*) to the same pressure (at the same temperature) as was maintained during flame sampling.

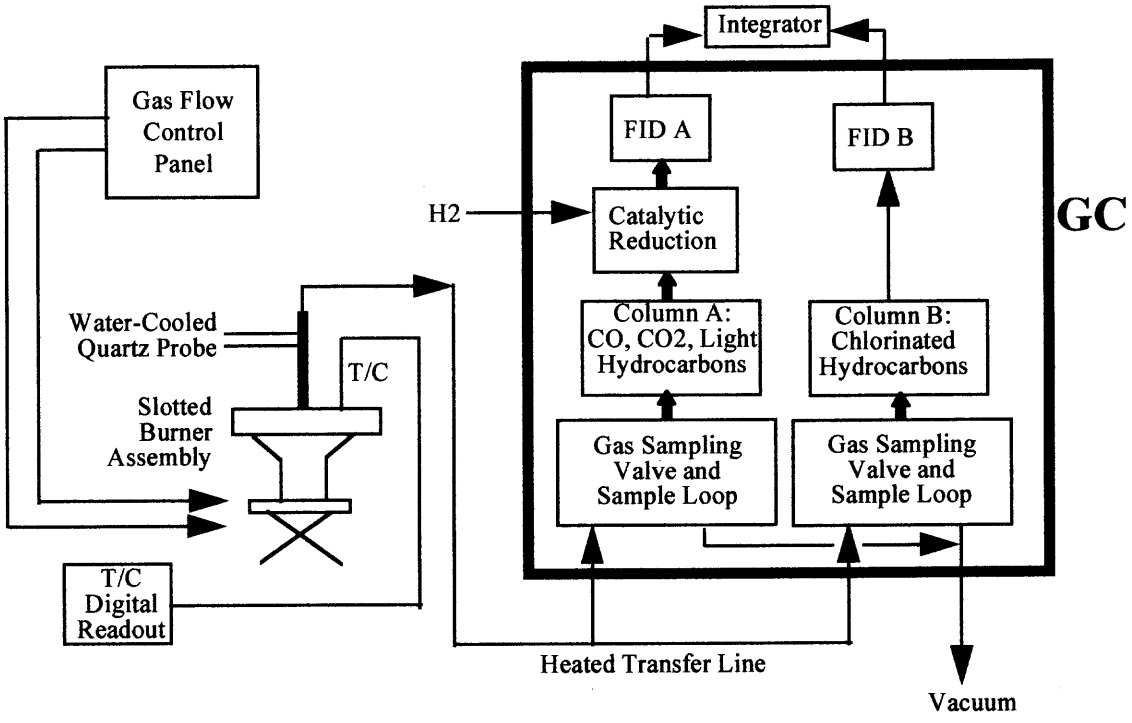

Figure 4.8 Gas Sampling and Analysis System

4.2 Equipment Calibration and Data Acquisition

4.2.1 Calibration of Apparatus

The following section describes the calibration of each instrument in the experimental set-up.

4.2.1.1 Calibration of 3/4 Meter Monochromator with Sodium Lamp

A sodium lamp was placed immediately in front of the 50 mm collection lens (see figure 4.6), the room lights were turned off, and the light from the lamp was focused directly onto the monochromator entrance slit. The monochromator was scanned in both the forward and reverse direction in an attempt to resolve the sodium doublet found at 589 and 589.5 nm. The light from the exit slit on the monochromator was directed onto the PMT, with the signal monitored on the strip-chart recorder. Figure 4.9 below shows that the sodium doublet was indeed resolved by the 3/4 m monochromator, as evidenced by the spikes in the chart recorder output. At first, the doublet appeared at different wavelengths in the forward and reverse directions. It was determined that this was due to backlash in the scanning mechanism. The instrument manual suggests to "reverse scan about 100 A between trials, to remove backlash...". Subsequent scans were sufficiently long to compensate for backlash.

It should be noted that the monochromator had to be calibrated with a sodium lamp in order to find the actual location of the sodium doublet. In other words, the monochromator dial did not corresponded to the actual numerical

wavelength, as can be seen in the following two figures which were taken directly from the lab notebook.

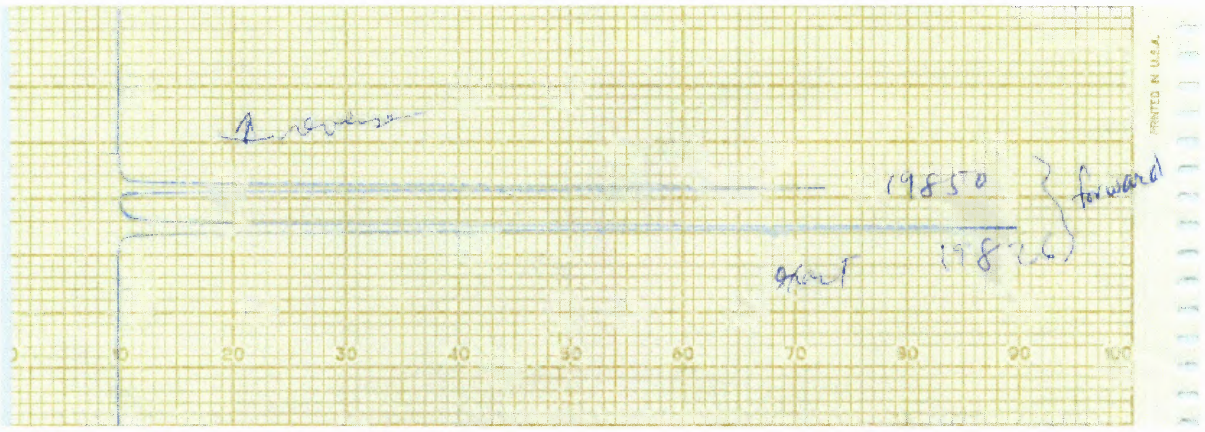

Figure 4.9 Sample Experimental Data to Show Existence of Sodium Doublet Using Sodium Lamp

4.2.1.2 Detection of Entrained Sodium in Flame

Once it was determined that the monochromator was capable of resolving the sodium doublet, it was necessary to determine if the monochromator and attached PMT could detect attenuation of the light due the existence of sodium in the flame. An arbitrary amount of sodium nitrate solution was aspirated into a methane/air flame of arbitrary equivalence ratio, ϕ and the arc lamp was focused on the flame. As can be seen in the following figure 4.10, a reduction in the signal from the PMT due to attenuation of the light by sodium atoms in the flame was observed in both the forward and reverse directions. Furthermore, the sodium doublet was also observed.

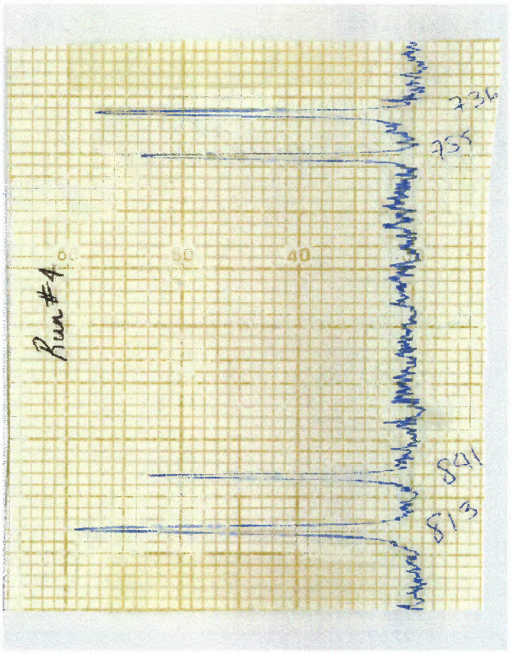

Figure 4.10 Sample Data to Show Attenuation of Light Due to Sodium Atoms in Flame

4.2.1.3 Calibration of Metering Valve and Liquid Flowrate to Burner

Calibration of Flow Metering Valve

In order to regulate the amount of liquid supplied to the spray mixing chamber, a fine metering valve was installed in-line between the pump from the feed reservoir and the mixing chamber. Not all of the liquid supplied to the mixing chamber actually goes into the flame. A large portion of the liquid collects on the floor of the mixing chamber and is then drained from the system. Therefore, it was necessary to calibrate the metering valve to determine the total liquid flowrate to the mixing chamber. Then, the fraction of total liquid actually reaching the flame burner (determined by difference) could later be expressed as a function of metering valve setting. Figure 4.11 shows the calibration curve for

the metering valve at an operating pressure of 60 psig, the pressure at which all of the experiments were performed.

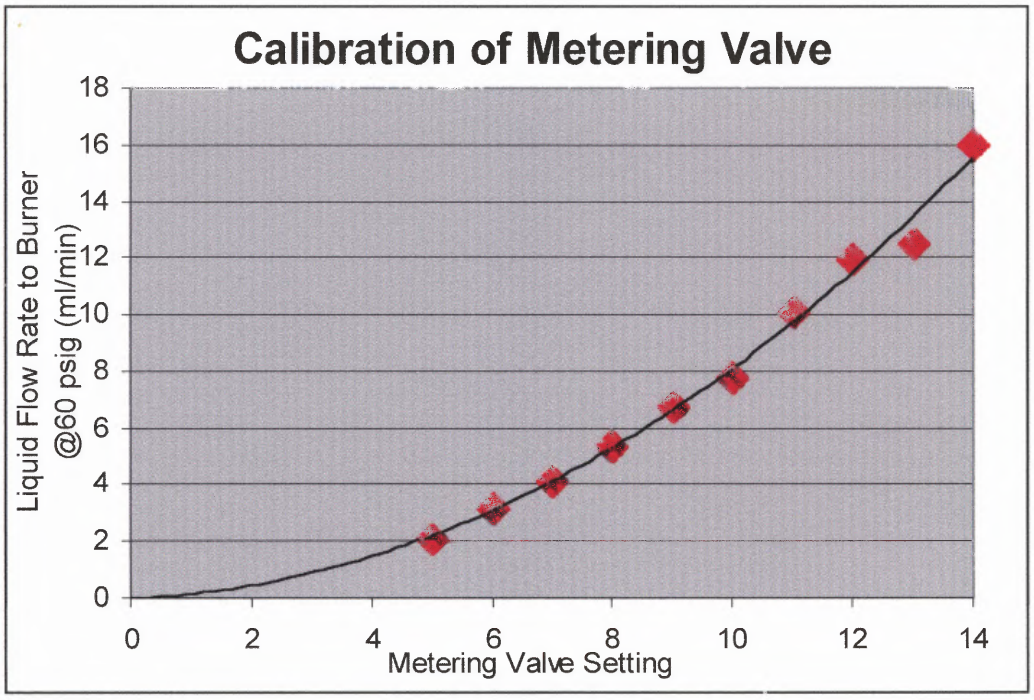

Figure 4.11 Calibration Curve of Solution Fine Metering Valve

Calculation of Fraction of Liquid to Flame Burner

A simple liquid mass balance was performed on the mixing chamber. The overall mass balance on the liquid around the mixing chamber was calculated as follows:

$$\text{Liquid Input} = \text{Output to Drain} + \text{Liquid to Flame} \qquad (4.1)$$

The liquid input to the mixing chamber was known (via metering valve) and the amount of liquid sent to the drain was measured. The percent liquid going to the flame was calculated in the following manner:

$$\%\text{Liquid to Flame} = \left[1 - \frac{\text{output}}{\text{input}}\right] * 100 \tag{4.2}$$

Figure 4.12 schematically describes the liquid mass balance around the mixing chamber. Forty-eight runs were performed for varying metering valve settings and air pressures using the air atomizing nozzle. The average amount of liquid sent to the flame based on total liquid input to the mixing chamber was 8.1%.

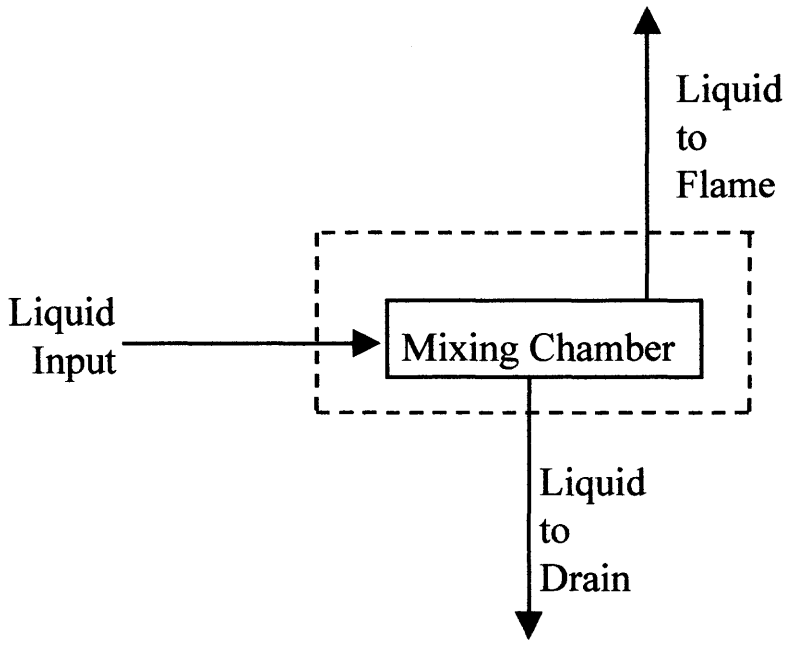

Figure 4.12 Schematic of Liquid Mass Balance Around Mixing Chamber

Saturation of Absorbance Signal

In order to eliminate the possibility of saturating the flame with sodium solution, an experiment was also performed to determine an optimum metering valve setting. Figure 4.13 shows that for a 0.02 mol/L $NaNO_3$ solution (the concentration at which the experiments were performed) the absorbance approaches a constant at a flow rate of approximately 5.5 ml/min. This corresponded to a metering valve setting of 7. It is assumed that at this point that the flame is saturated with sodium. For this reason, all of the experiments were performed at a metering valve setting of 5. This is equivalent to a liquid flowrate to the burner of 2.1 ml/min.

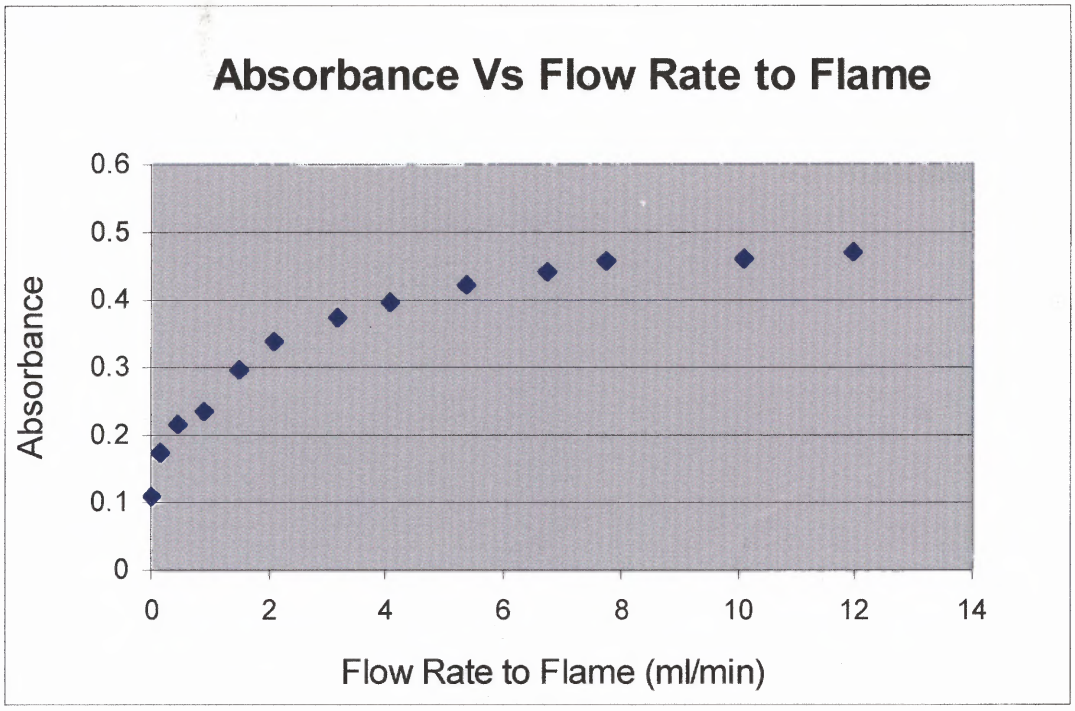

Figure 4.13 Absorbance Versus Flow Rate to Flame

4.2.2 Temperature Profiles

As mentioned earlier, a Type R thermocouple was used to take all temperature measurements. In general, whenever a temperature profile is discussed in this thesis, it is implied that it is a temperature profile of the flame taken in the vertical direction. However, in order to better characterize the flame itself without entrained sodium or water, it was necessary to perform horizontal as well as vertical temperature profiles.

4.2.2.1 Horizontal Temperature Profile

In order to collect horizontal temperature profile data, the thermocouple was set at a certain height above the burner. The center of the 0.07cm slot in the burner was aligned with the bead of the thermocouple. The burner was translated in the horizontal direction *away* from the thermocouple approximately 0.3 cm. Temperature readings were taken as the burner was translated in the horizontal direction *towards* the thermocouple in increments of 0.05 cm. Readings continued to be taken as the thermocouple passed over the center of the burner slot and ended when the thermocouple reached 0.3 cm on the other side of the burner. A typical horizontal temperature profile for a fuel lean methane/air flame is presented in Figure 4.14.

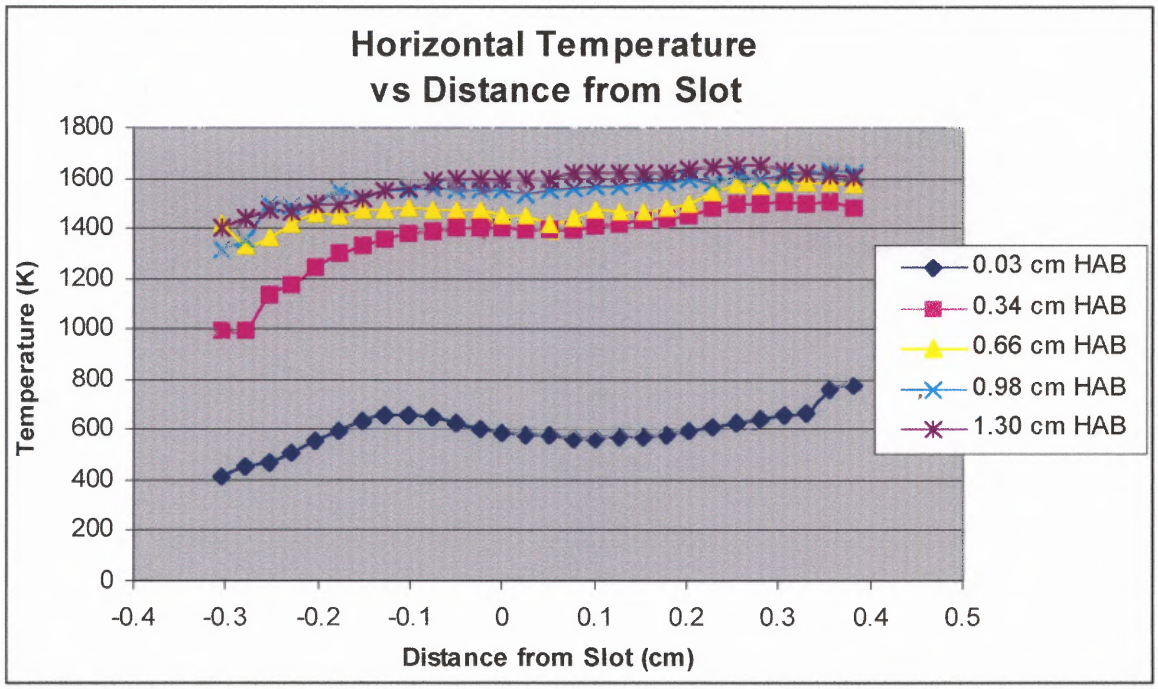

Figure 4.14 Sample Horizontal Temperature Profile

Note should be taken that the asymmetric nature of the profiles is an anomaly of the measurement. As the flame is traversed, more of the thermocouple is immersed in the flame. This causes less conductive losses from the thermocouple bead, resulting in an artificially higher reading. Test measurements taken by traversing the flame in the opposite direction produce mirror image profiles, thus confirming the argument.

4.2.2.2 Vertical Temperature Profile

When gathering data for a vertical temperature profile, the initial requirement is that the burner be set at a height equivalent to 0.0 cm HAB. In other words, the burner is translated in the vertical direction until the light from the arc

lamp (which is stationary) appears to be "resting" directly on the burner, centered over the burner slot. The thermocouple is placed such that the bead from the thermocouple sits in the center of the burner slot. When the light from the arc lamp and the thermocouple bead are correctly aligned over the burner slot, the lamp illuminates the thermocouple bead. Temperatures are recorded after the lamp is powered down.

A ruler then marks the vertical height of the top of the burner as that which is equivalent to 0.0 cm HAB. The flame with entrained sodium solution or water is ignited, and a temperature measurement is taken at 0.0 cm HAB. The Linear Chart Recorder, which has been calibrated over the temperature range of the flame, then records the temperature. To record the next temperature, the burner is lowered 0.25 cm. The thermocouple is now recording the temperature at 0.25 cm HAB. This procedure is repeated for 6-12 data points depending on the equivalence ratio of the flame. An example of how the chart recorder monitored the temperature of the flame is shown in Figure 4.15.

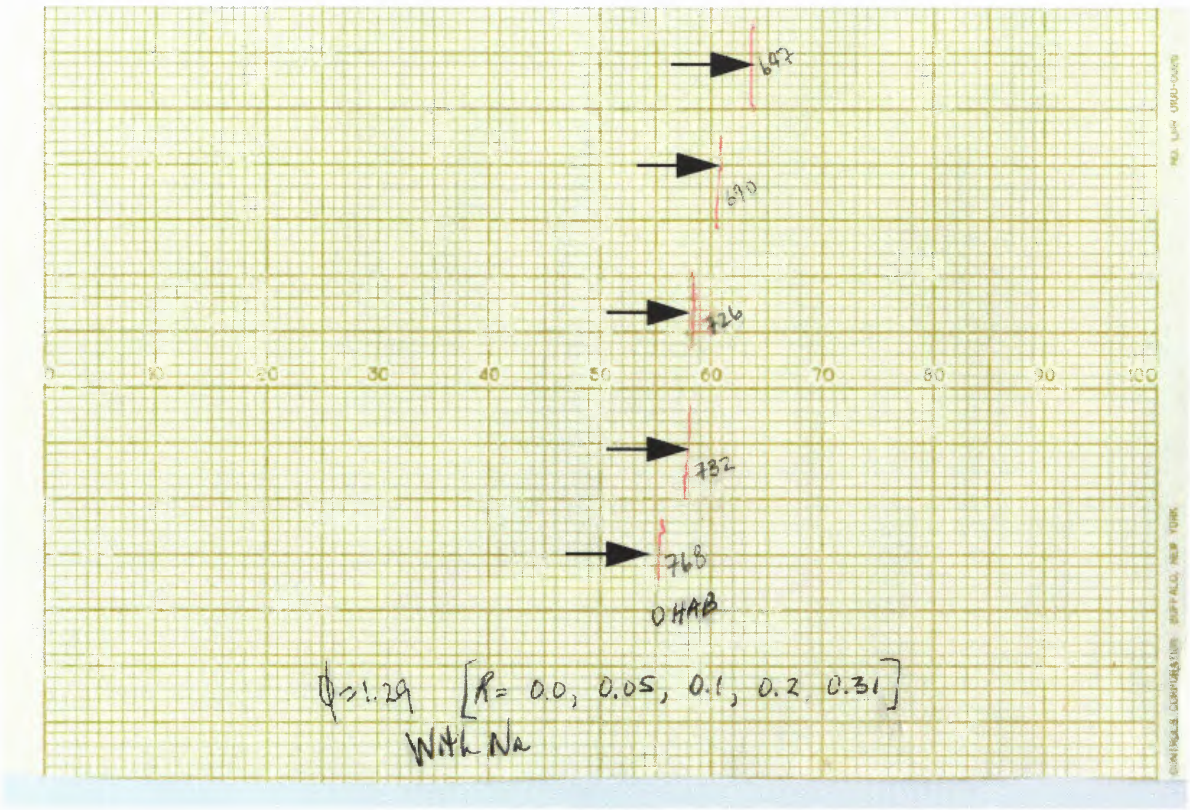

Figure 4.15 Sample Data for Vertical Temperature Profile

It should be noted that the temperature profiles were difficult to acquire at times due to occasional flame fluctuations. Therefore, for each equivalence ratio ϕ at a given HAB, temperatures were recorded for all of the flames with sodium. Likewise, all of the flames without sodium were done together. At a certain HAB, the airflow was held constant and the feed CH_3Cl/ CH_4 ratio, R, was adjusted for different conditions. The HAB was then changed and this procedure was repeated. An example of a typical vertical temperature profile for a methane/air flame with sodium and chlorine is shown in Figure 4.13 below.

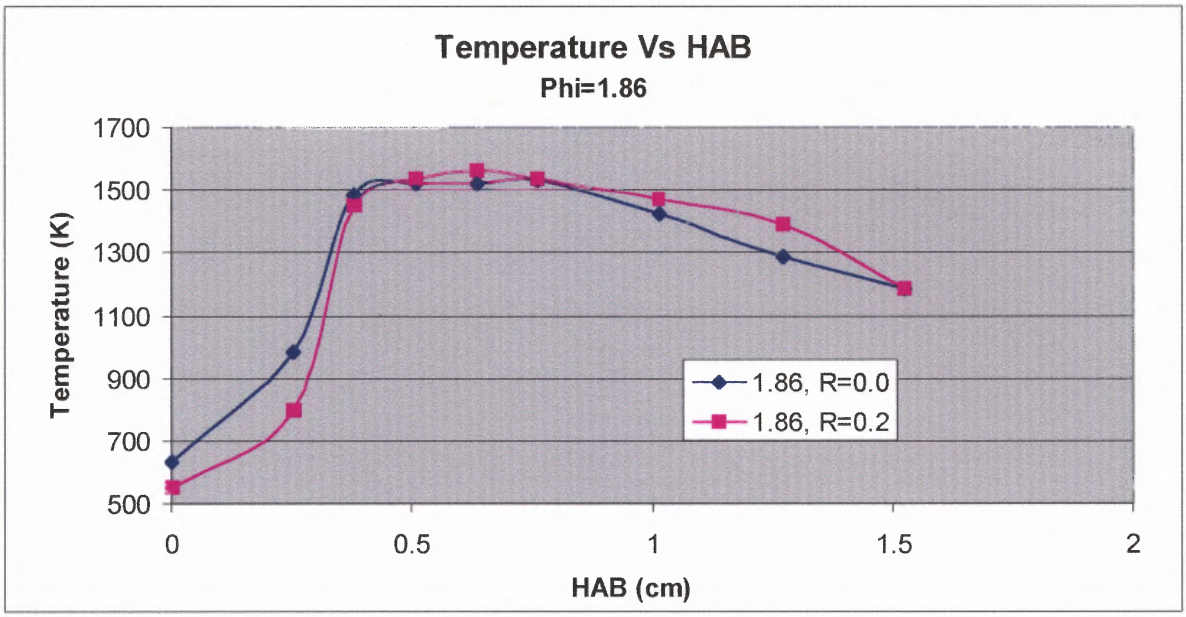

Figure 4.16 Vertical Temperature Profile

4.2.3 Absorption Profiles

The following step-wise procedure illustrates how absorption of light was quantified for this work:

1. The flame was turned on and the monochromator was set at a wavelength located immediately before 589 nm. A dark spectrum, D, was collected with the shutter in front of the lamp closed, the room lights turned off, and the sodium sample aspirated into the flame, i.e., this is equivalent to an emission signal.
2. The shutter was opened allowing the light beam to pass through the flame and the signal due to the incident source radiation, V_o, was obtained.
3. The monochromator was scanned slowly passed the wavelength of interest and the signal due to attenuation of light by the sample, V, was obtained.

Fernando, Calloway and Jones (3) describe the manipulation of similar data to determine the absorbance spectrum. When the following replacements are made, $V_o = I_o$ and V=I, Fernando, Calloway and Jones propose the following for calculation of absorbance:

$$A = \ln \frac{(I_o - D)}{(I - D)} \tag{4.3}$$

It should be noted that the room lights were turned off in order to *include* any signal due to emission in the dark signal. Then, when the dark signal, D, is subtracted from either signal, I_o or I, any interference due to emission is eliminated from the absorbance calculation.

The procedure for collecting reliable intensity data to determine absorbances was based on the following experimental observations:

1. In order to compare the intensity of light having passed through the flame with entrained water to that of a flame with entrained aqueous sodium nitrate solution, it was originally decided to compare a 3-5 nm scan across 589 nm of the two flames at a certain HAB. It was thought that the scan with sodium would be identical to the scan of the flame with water, except that the sodium scan would contain a drop in optical transmission (DIP) due to absorbance by the sodium atoms at 589 and 589.5 nm. This was not the case. The time it took to free the system of sodium salt solution was approximately 10-12 minutes after the solution flow was stopped in favor of pure water. In

this time, some drift in the intensity of the arc lamp was possible; hence, while the two scans were very *similar*, they were not exact.

2. An alternative to scanning over a certain wavelength range was to simply sit on a particular wavelength such as 589 or 589.5 nm. The attenuation of the light due to sodium would be compared to the attenuation of light due to aspirated water in the flame. This also, was not *completely* successful. Once again, in the amount of time that it took to switch between the two solutions, the intensity of the lamp could drift. This was proven experimentally by sitting at a wavelength away from 589 or 589.5 nm.
3. Finally, it was observed that a scan with water in the region of the signal DIP appeared to be a straight line, just as the scan with sodium would appear *without* the DIP. It was then assumed that in the region immediately before and immediately after the DIP, the scan with water and the scan with sodium were identical. Therefore, it was concluded that the magnitude of the sodium DIP would be determined from a sodium scan alone, as the difference between the intensity observed immediately *before* 589 nm and the intensity *at* 589 nm.

A typical sodium scan is presented in Figure 4.17, as well as an example of how absorbance (A) is calculated from these results.

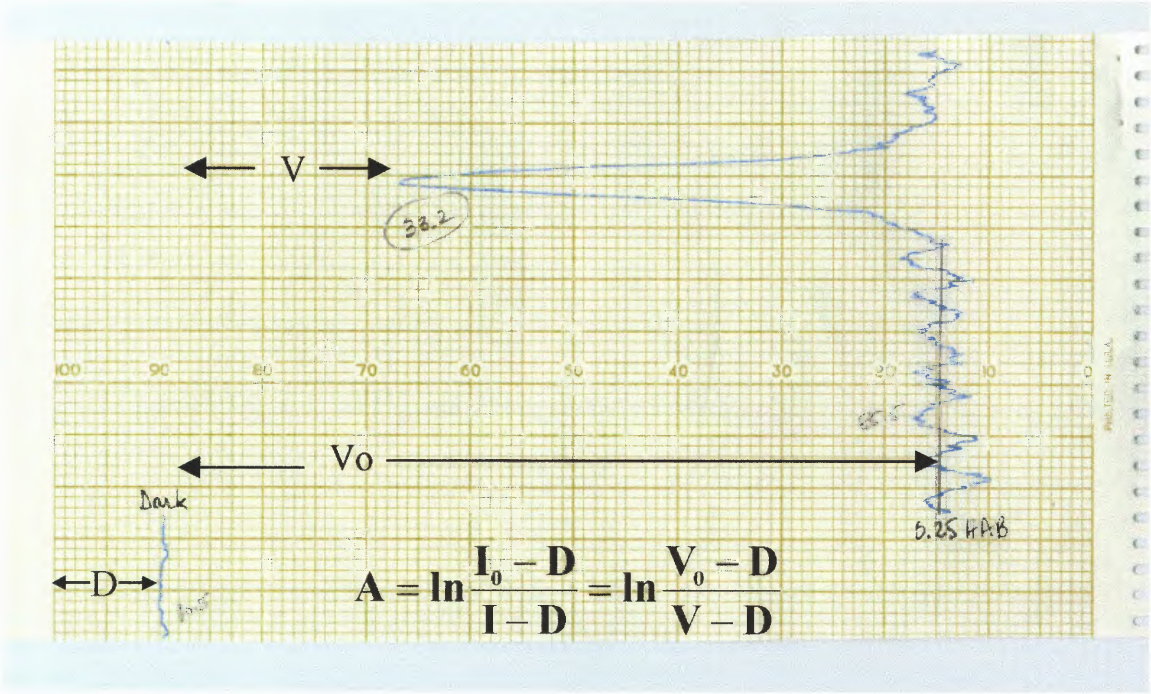

Figure 4.17 Sample Scan of Absorption Data

With the benefit of these experimental observations, the following procedure was formulated. At a given HAB, the shutter to the lamp was closed, the flame with entrained sodium was ignited, and the room lights were turned off. The PMT dark signal that was then recorded, accounting for any signal due to flame emission. The shutter was then opened and a quick scan was performed in the forward direction. This was done for two reasons. The first was to verify that the two DIPs were indeed there- one at 589 nm and the other at 589.5 nm. The second reason was that the DIP at 589 nm was larger than the DIP at 589.5 nm. The larger DIP was used for analysis. In the reverse direction, the smaller DIP appeared first. When the smaller DIP appeared, this was then used as an indicator to significantly slow down the speed of the scanning device (drive

motor) to the monochromator. When the second DIP had been observed, the scanning device was turned off and the procedure was repeated for a different HAB.

4.2.4 Stable Species Profiles

A water-cooled quartz microprobe was used in conjunction with a Perkin-Elmer 3920 gas chromatograph (GC) to determine how the concentration of major species such as CO, CO_2 and CH_4 were affected by the introduction of sodium (as $NaNO_3$(aq)) and/or chlorine (as CH_3Cl)into the flame. However, unlike the absorption profiles, the only equivalence ratio used for the study of stable species was ϕ=1.86. This equivalence ratio was chosen because it was the "best" flame to work with, i.e., the flame was tall enough to allow good spatial resolution and was also well stabilized.

Once the GC was given sufficient time to warm up, the entire system was calibrated by filling the evacuated sample loop with a standard gas (Scotty IV Analyzed Gases) to the same temperature and pressure as was maintained during flame sampling. This was then followed by the analysis of the stable species in the flame at various heights above burner. The Quartz probe was positioned in the flame in the exact same fashion as the positioning of the thermocouple in the flame described earlier. Gas samples were drawn from the flame with the probe, which has also been described earlier. The fuel type and equivalence ratio were varied and the stable species profiles were recorded.

These results will be presented in Chapters 6 and 7. Sample results from experiments with a standard gas and flame gases are presented below.

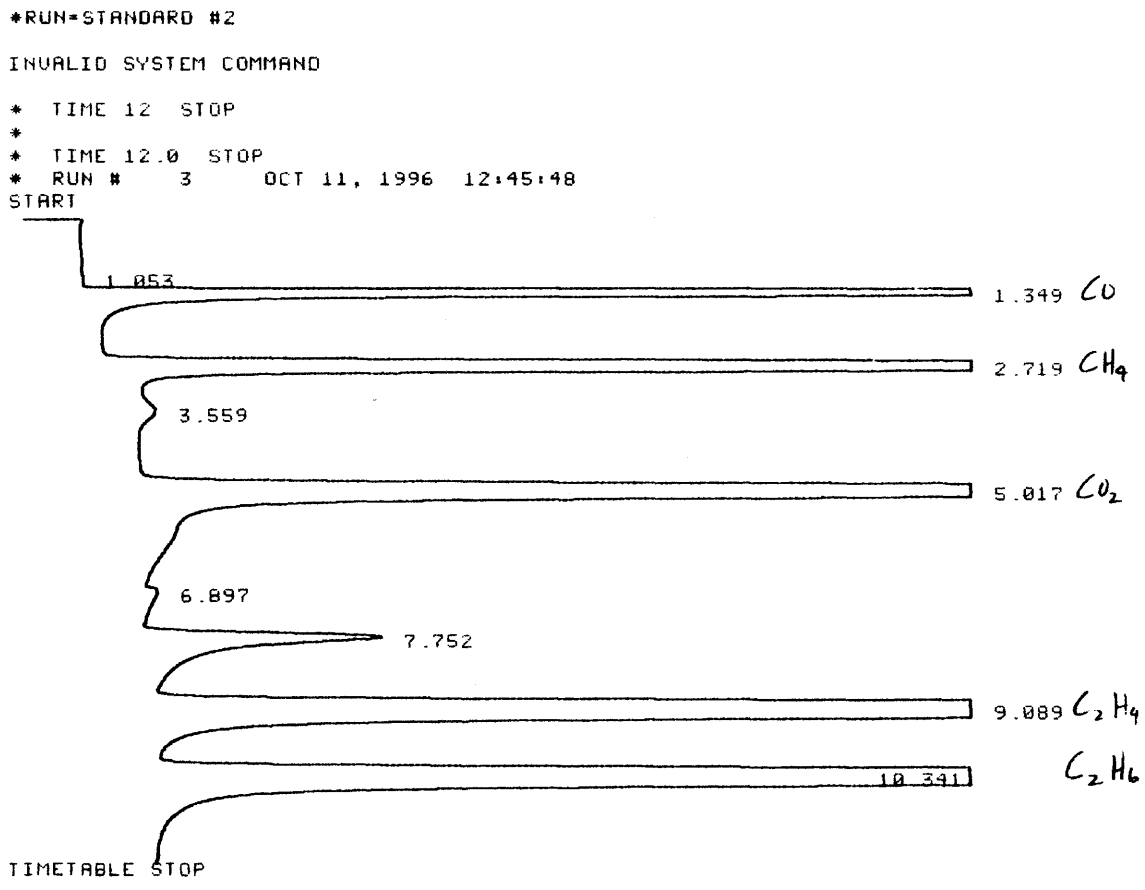

Figure 4.18(a) Standard Sample GC Analysis

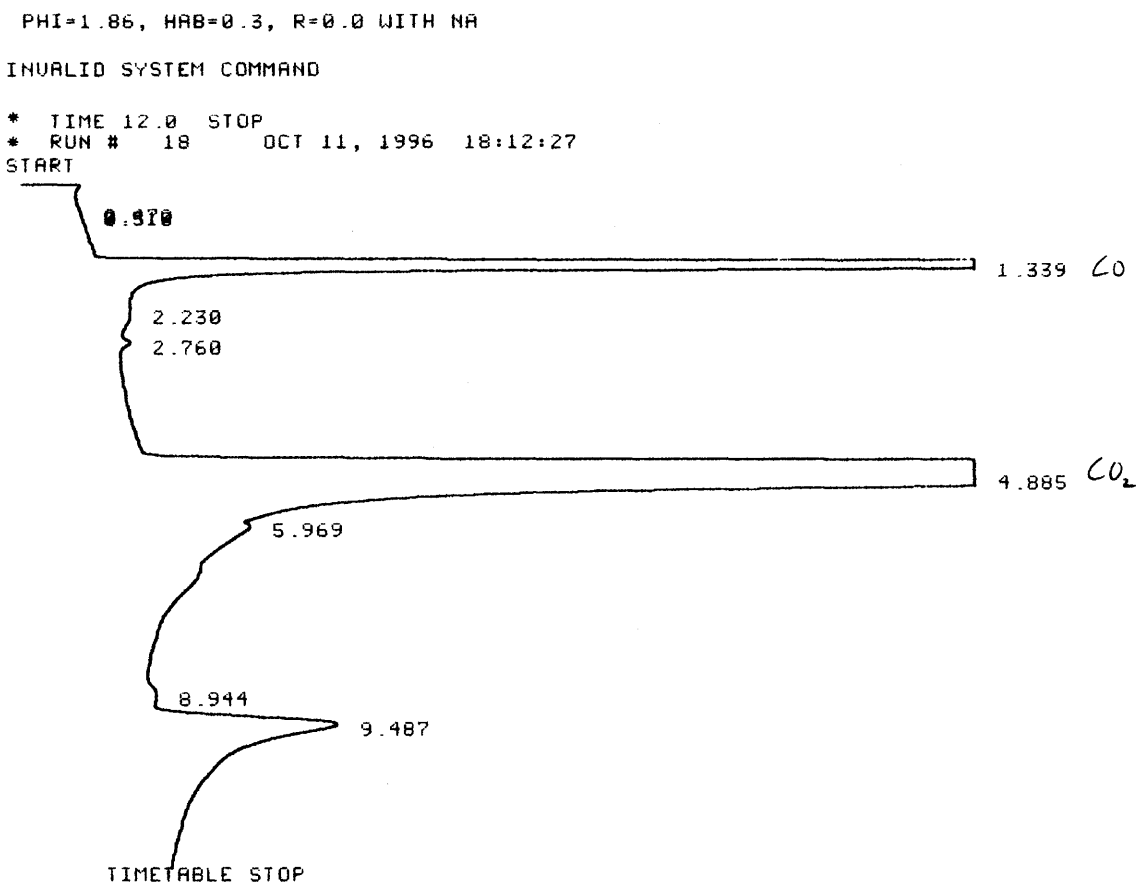

Figure 4.18(b) Flame Sample GC Analysis

CHAPTER 5

MODELING METHODS

The first part of this chapter discusses the Sandia Fortran program for modeling steady, laminar, one-dimensional, premixed, flat flames as it was written by Kee, Grcar, Smooke and Miller (26). The second part of this chapter addresses the modifications that were made to this existing code in order to model the experimental data collected in this study. It should be noted however, that during the course of this study, these flames were modeled as one-dimensional flames. This was considered a reasonable first approximation and starting point. However, further examination of the results suggested that the flames would have been better modeled as two-dimensional. This theory and a comparison of the flames as one dimensional versus two-dimensional is discussed in great detail in chapter 8.

5.1 The Sandia FORTRAN Program

The premixed flame model developed by Kee et al. (26), PREMIX, predicts temperature and species profiles in two laminar, flat flame configurations. The first configuration is a freely propagating, adiabatic flame. The second configuration - and the configuration of interest in this study - is the burner-stabilized flame. For the latter configuration, two cases exist: one where the temperature profile is known and input, and one where the temperature profile is determined by the energy conservation equation. However, due to

the difficulties in accurately accounting for the significant heat losses to the external environment, predicted temperatures are less desirable than measured ones (26). Therefore, if a temperature profile can be measured accurately, it is better to use this measurement rather than the calculated temperature profile obtained by solving an energy conservation equation.

5.1.1 The Governing Equations

The equations that govern steady, isobaric, adiabatic, quasi-one-dimensional flames (freely propagating or burner stabilized), as described by Kee et al. (26) may be written as follows:

Continuity Mass Balance

$$\dot{M} = \rho u A \tag{5.1}$$

The Species Balance

$$\underset{\textit{Convection}}{\dot{M}\frac{dY_k}{dx}} + \underset{\textit{Diffusion}}{\frac{d}{dx}\left(\rho A Y_k V_k\right)} - \underset{\textit{Reaction}}{A\dot{\omega}_k W_k} = 0 \tag{5.2}$$

where (k=1,.....K)

The Enthalpy Balance

$$\dot{M}c_p\frac{dT}{dx} - \frac{d}{dx}\left(\lambda A\frac{dT}{dx}\right) + A\sum_{k=1}^{K}\rho Y_k V_k c_{p_k}\frac{dT}{dx} + A\sum_{k=1}^{K}\dot{\omega}_k h_k W_k = 0 \qquad (5.3)$$

Convection *Conduction* *Diffusion* *Reaction*

Equation of State

$$\rho=\frac{P\overline{W}}{RT} \qquad (5.4)$$

In all of the above equations, x denotes the spatial coordinate; $\dot{M}$ is the mass flow rate (which is independent of x, as presented by Kee et al. (26)); T is the absolute temperature; Y_k is the mass fraction of the kth species (there are K species); P is the absolute pressure; u is the linear velocity of the fluid mixture; ρ is the mass density; W_k is the molecular weight of the kth species; $\overline{W}$ is the mean molecular weight of the mixture; R is the universal gas constant; λ is the thermal conductivity of the mixture; c_p is the heat capacity of the mixture; c_{pk} is the heat capacity of the kth species; $\dot{\omega}_k$ is the molar rate of production by chemical reaction of the kth species per unit volume; h_k is the specific enthalpy of the kth species; V_k is the diffusion velocity of the kth species; and A is the cross sectional area of the stream tube encompassing the flame.

The final equation of interest is found in the formulation of the species diffusion. This formulation assumes that the diffusion velocity, V_k, is composed of three parts.

$$V_k = V_k + W_k + V_c \tag{5.5}$$

V_k is the ordinary diffusion velocity and is given in the Curtiss-Hirschfelder (32) approximation by

$$V_k = -D_k \frac{1}{X_k} \frac{dX_k}{dx} \tag{5.6}$$

where X_k is the mole fraction. The mixture-averaged diffusion coefficient D_k is given explicitly in terms of the binary diffusion coefficients D_{jk} by

$$D_k = \frac{1 - Y_k}{\sum_{j \neq k}^{K} X_j / D_{kj}} \tag{5.7}$$

W_k is a non-zero thermal diffusion velocity and is included only for the low molecular weight species H, H_2, and He. The trace, light-component limit is employed in determining W_k as follows:

$$W_k = \frac{D_k k_{T_k}}{X_k} \frac{1}{T} \frac{dT}{dx} \tag{5.8}$$

V_c is a correction velocity which is included to insure that the mass fractions sum to unity, i.e.,

$$\sum_{k=1}^{K} Y_k V_k = 0 \tag{5.9}$$

as recommended by Coffee and Heimerl (33,26).

The conservation equations governing the two types of flames considered by the program, the burner stabilized and the freely propagating flame, are exactly the same. However, the boundary conditions are not. For the traditional burner stabilized flame, $\dot{M}$ is a known constant, the temperature and mass flux fractions ($\varepsilon_k = Y_k + \rho Y_k V_k A / \dot{M}$) are specified at the cold boundary, and vanishing gradients are imposed at the hot boundary.

5.1.2 The Reaction Mechanism

The net chemical production rates of species k, ω_k, are determined by CHEMKIN subroutines with the aid of the user input reaction mechanism and measured temperature (26). CHEMKIN is a FORTRAN chemical kinetics code (28) and transport package (29). The rate of each reaction involving species k is calculated according to the law of mass action and the

required, user-supplied forward rate coefficient, k_f. The coefficients are expressed by:

$$k_f = AT^n \exp\left(\frac{-E_A}{RT}\right) \tag{5.10}$$

where A, n and E_A in this particular situation are fitted parameters. If n=0, A is the usual Arrhenius pre-exponential factor and E_A is the activation energy. The reverse rate constant, k_r, is related to the forward rate constant, k_f, through the reaction equilibrium constant K as:

$$k_r = \frac{k_f}{K} \tag{5.11}$$

The equilibrium constant K is calculated by CHEMKIN based upon the temperature and species thermodynamic properties. The user-supplied thermodynamic database consists of species standard enthalpy of formation H^0_f (298K), species standard entropy S^0 (298K) and species heat capacities C_p as functions of temperature (27).

The user-supplied reaction mechanisms are primarily drawn from the literature. Specific modifications to the literature mechanisms will be discussed in the following appropriate chapters.

5.1.3 The Numerical Solution

The numerical solution (26) begins by making finite difference approximations to reduce the boundary value problem to a system of algebraic equations. The initial approximations are usually on a very coarse mesh that may have as few as five or six points. After obtaining a solution on the course mesh, new mesh points are added in regions where the solution or its gradients change rapidly. An initial guess for the solution on the finer mesh is obtained by interpolating the course mesh solution. This procedure continues until no new mesh points are needed to resolve the solution to the degree specified by the user.

The damped modified Newton algorithm solves the system of algebraic equations (26). However, if the Newton algorithm fails to converge, the solution estimate is conditioned by a time integration. This provides a new starting point for the Newton algorithm that is closer to the solution, and thus more likely to be in the domain of convergence for Newton's method.

5.1.4 Program Structure

The premixed flame code is written in two major modules. One contains software to solve boundary value problems i.e., the numerical method. It is completely independent and could easily be used for problems not related to flames. The other module contains the flame- specific coding. It reads input from the user, defines the governing equations, makes calls to the boundary value solver, and prints solutions for the flame problem. In addition to input

directly from the user, the flame program depends on data and subroutines from CHEMKIN.

The CHEMKIN Interpreter, Chem.exe, reads user supplied information from the following files:

- Chem.inp – contains kinetic information about the species and chemical reactions for a particular reaction mechanism.
- Therm.dat – a data base that contains the thermodynamic properties of all reactant, intermediate and product species in the flame.

Execution of Chem.exe creates a binary file, Chem.bin.

Tran.exe represents TRANFIT, the transport property-fitting program in the above figure. The following files are required to execute this program:

- Chem.bin – produced by execution of Chem.exe
- Tran.dat – a data base that contains the transport properties of all the species in the flame

A second binary file, Tran.bin, is created as a result of the execution of this program.

The flame code, Premix.exe, requires the following files as input:

- Chem.bin – output from Chem.exe
- Tran.bin – output from Tran.exe
- Premix.inp – contains user-supplied information that defines a particular flame and the parameters needed to solve it, in a Keyword format e.g.,

mass flux to the burner, reactant mole fractions, and flame temperature profile.

Successful execution of the flame code results in the following output:

- Premix.out – contains all of the information previously supplied by Premix.inp as well as all calculated species mole fractions as a function of HAB.
- Save.bin - this binary file can be renamed as Rest.bin and used to either restart the same problem and continue iterating, or it can be read as a starting estimate for a new and different flame.

Figure 5.1 provides a schematic description of the relationship between the various components of the code as well as a broad outline of the inputs required and the outputs generated by the model. Samples of these files are placed in Appendix A.

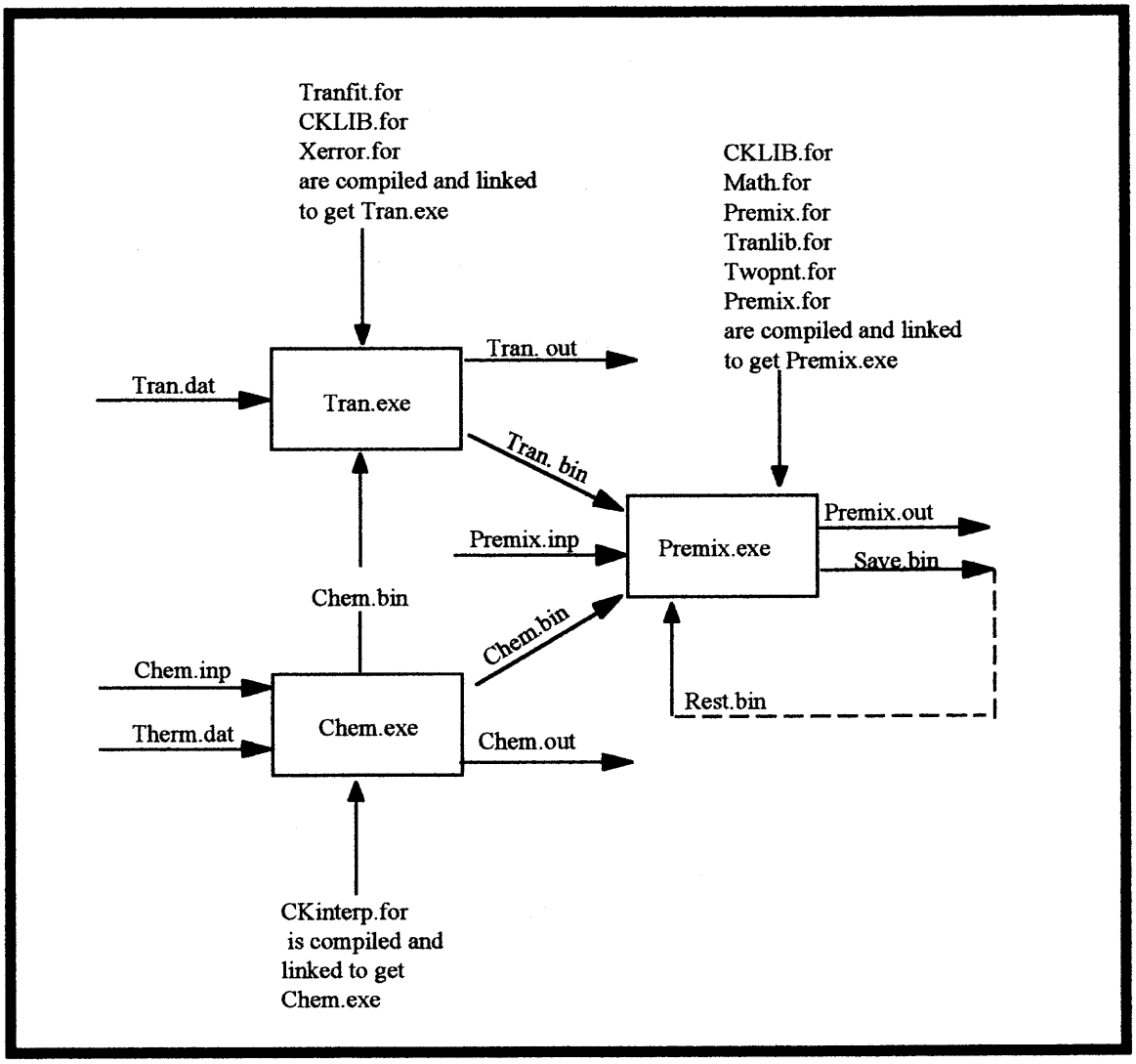

Figure 5.1 Flowchart of Inputs and Outputs to CHEMKIN Premixed Flat Flame Code

5.2 Flame Model Development and Calibration

5.2.1 Background

It was recognized early on that the slotted burner used in this work is clearly different (see Figure 5.2) from the usual flat flame burner for which the Sandia code just described was developed.

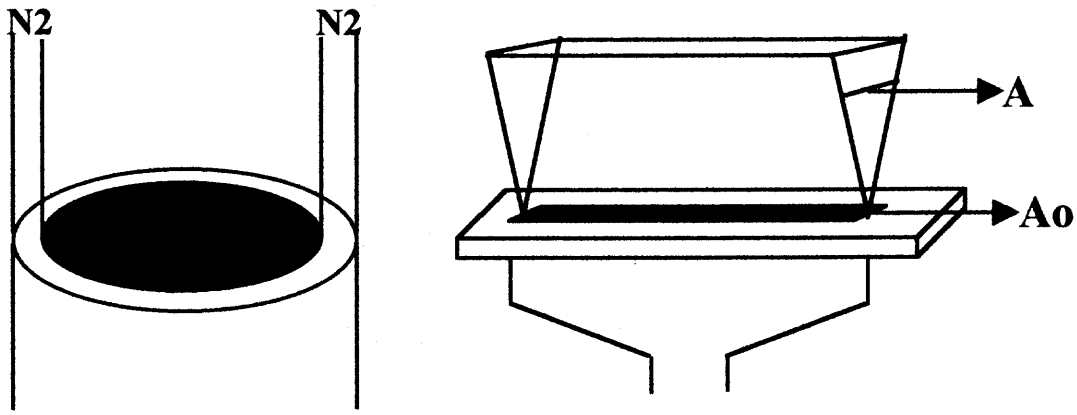

Flat Flame Burner Slotted Flame Burner

Figure 5.2 Schematic of Flat Flame Burner and Slotted Burner

Aside from the shape, the principal difference is entrainment (transport) of outside air (see section 2.2.2). The laminar flat flames are typically operated with a nitrogen shroud isolating the flame from ambient air while the slotted flame can be considered a laminar jet subject to air entrainment (30). In addition to the differences, the slotted burner is uncooled.

There are, however, similarities in the flames. Both flames are laminar. The flat flame is characterized by no radial gradient. Horizontal temperature profiles taken in the slotted flame suggest a fairly thin and spatially uniform (horizontal) flow at a given height above burner. Hence, the slotted flame might be treated as a one-dimensional (i.e. vertical) problem, as is the flat flame as a first approximation.

The similarities are sufficient between the two flames that development of a CHEMKIN-based model for the slotted flame can begin

with the flat flame code. It is desirable, therefore, to modify the flat flame code in a way that allows reasonable simulations of observed data within the existing FORTRAN code structure and numerical solution technique.

The modifications made to the existing flame code can be divided into two categories:

1. There were those changes that were intrinsic to the flame, i.e., independent of burner type or environment. An example of such a modification would be the inclusion of sodium kinetics to the methane/ air mechanism. These changes will be presented in later chapters (6 and 7).
2. The second type of modifications made were those changes that were extrinsic to the flame, such as the shape and size of the burner and the fact that the burner (and flame) was exposed to the environment. This exposure allowed the transport of air from the surroundings into free flowing gases in the flame.

This chapter will deal with those modifications that are independent of flame chemistry. Once completed, the slotted flame model must be tested. Since the primary objective of this study is the investigation of the role of sodium, testing (or calibration) of the new flame model had to be done in a flame where the chemistry was relatively well known, i.e., methane/air. Experimental data were collected for the following methane/air flames:

Table 5.1 Methane/Air Flames Examined by this Study

Equivalence Ratio ϕ	Temperature Profile	Stable Species Profiles (CH_4, CO, CO_2)
1.29	√	
1.86	√	√
2.48	√	
3.15	√	

The experimental data from the methane/ air flame, $\phi = 1.86$, were used to calibrate and confirm all non-mechanism adjustments made to the CHEMKIN flat flame code. This calibrated program was then used to model methane/ air flames that contained additional species such as sodium (introduced to the flame as sodium nitrate aqueous solution) and chlorine (introduced as methyl chloride). These results are discussed in chapters 6 and 7, respectively.

5.2.2 The Species and Enthalpy Balances

The governing premixed, flat flame equations (26) were originally derived using the assumption of a *constant* mass flow rate. It has also been discussed that the flames in the current study encountered entrainment of air and, consequently, had a *variable* local mass flow rate. As a result, both the species and enthalpy balances were rederived from first principles in order to account for a variable mass flow rate (see Figure 5.3).

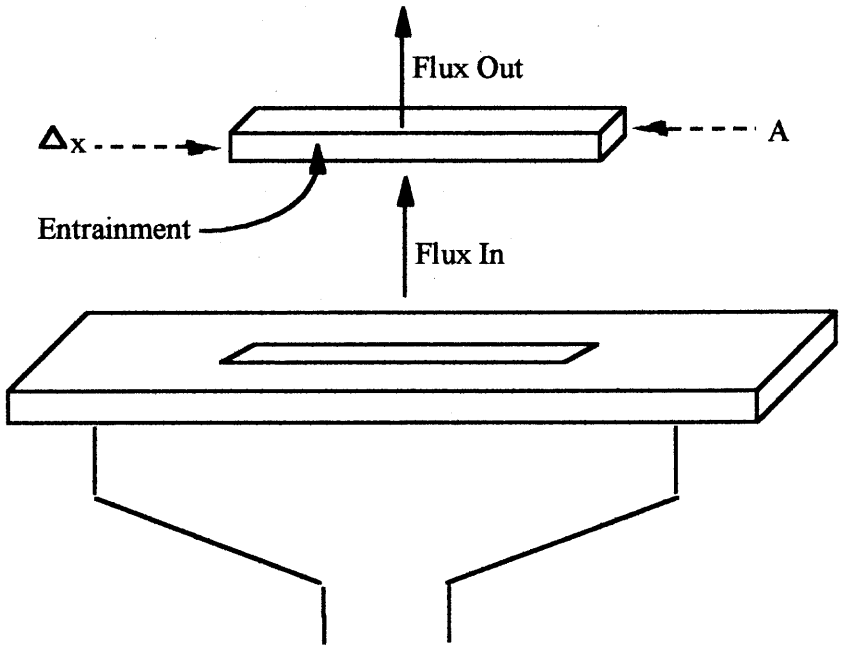

Figure 5.3 Schematic Representation of Control Volume for a Slotted Burner

The following equations show that the rederived expressions are identical to the original expressions--with the exception of one additional term in each balance due to entrainment of air. These new expressions were incorporated into the FORTRAN source code and were used in the modeling of all cases presented by this study.

The Species Balance

$$\underset{\textit{Convection}}{M\frac{dY_k}{dx}} + \underset{\textit{Diffusion}}{\frac{d}{dx}(\rho A Y_k V_k)} - \underset{\textit{Reaction}}{A\omega_k W_k} + \underset{\textit{Entrainment}}{(Y_k - Y_{sk})\frac{dM}{dx}} = 0 \qquad (5.12)$$

The Enthalpy Balance

$$\underbrace{\dot{M}c_p\frac{dT}{dx}}_{\textit{Convection}} - \underbrace{\frac{d}{dx}\left(\lambda A\frac{dT}{dx}\right)}_{\textit{Conduction}} + \underbrace{A\sum_{k=1}^{K}\rho Y_k V_k c_{p_k}\frac{dT}{dx}}_{\textit{Diffusion}} + \underbrace{A\sum_{k=1}^{K}\omega_k h_k W_k}_{\textit{Reaction}} + \underbrace{Y_{s_k}\left(\sum h_k - \sum h_{s_k}\right)\frac{dM}{dx}}_{\textit{Entrainment}} = 0 \qquad (5.13)$$

In the above expressions, Y_{sk} and h_{sk} refer to the mass fraction and specific enthalpy of the kth species in the surroundings, respectively. In practice, $Y_{sk} = 0$ for all species except oxygen and nitrogen.

5.2.3 Streamtube Area

The cross sectional area of the streamtube (i.e. flame cross section) encompassing the flame, A, can be generally described by the following expression:

$$A = A_o f(x) \qquad (5.14)$$

where A_o is the cross sectional area of the burner opening and f(x) is an n^{th} order polynomial which describes the variation of A with HAB (x). The original CHEMKIN program assumed that, in the absence of information about the streamtube area, the value of A is constant and equal to unity,

while the mass flux (g/cm^2-s) through the burner (assumed constant) is a user-defined input value.

In this study, however, the streamtube area increases due to thermal expansion and entrainment. The horizontal temperature profiles of the flame (figure 4.14) provided an approximate mapping of the area expression. Using these data, an AREA subroutine was generated to specify the streamtube area as a function of the spatial coordinate, x. The following simple, linear expression approximately relates the dependence of the area with the HAB:

$$A = A_o(1 + 2x) \tag{5.15}$$

This relationship was incorporated into the model and was used for all cases presented in this study.

5.2.4 Temperature Profile Correction

A type R thermocouple (T/C) was used to measure the temperature at any point in the flame. However, the temperature that is reported by the digital indicator does not account for the heat lost by radiation from the T/C bead to the surroundings. The following diagram and heat balance around the T/C bead illustrates how this omission is corrected.

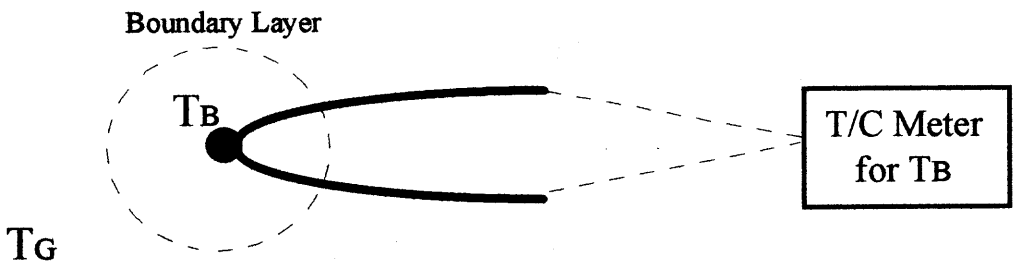

Figure 5.4 Thermocouple Bead Schematic Used for Heat Balance

A total heat balance around the bead produces the following relationship:

$$ha(T_G - T_B) = \sigma\varepsilon a\left(T_B^4 - T_S^4\right) - 2k_w a_c\left(\frac{dT}{dx}\right)_{x=0} \quad (5.16)$$

Convective Heat Transfer from Gas to Bead	Radiation of Heat from Bead to Surroundings	Conduction of Heat Along Wires from Bead

For the previous equation, the following constants are defined: h is the heat transfer coefficient; a is the bead surface area; σ is the Stefan-Boltzmann constant; ε is the bead emissivity; k is the thermal conductivity of the wire; a_c is the cross sectional area of the wire; x is the coordinate along the wire; T_W is the temperature of the wire; T_S is the temperature of the surroundings (assumed 300K for an open flame); T_B is the temperature of the bead; and T_G is the temperature of the flame gases (assume $T_G > T_B$). All temperatures are in Kelvin (K).

Note should be taken that for this study, the second term which accounts for heat loss due to conduction along the thermocouple wire was considered insignificant and it was assumed to be essentially zero. The

validity of this assumption is reconsidered in Chapter 8 and results of the sensitivity of this term i.e., the significance of the contribution of this term, is discussed.

When the conductivity along the thermocouple wire is neglected, manipulation of the above heat balance results in the following equation (manipulation of this same heat balance when the conductivity term is not neglected is presented in chapter 8 for comparison).

$$T_G = T_B + \frac{\sigma\varepsilon}{h}\left(T_B^4 - T_S^4\right) \tag{5.17}$$

This expression was used to correct the experimental flame temperature data for radiation. Similar expressions have been used in the literature (34, 43, 44). The heat transfer coefficient was calculated using the following Nusselt number relationship for laminar flow around a cylinder (31):

$$Nu = 0.42\,Pr^{0.2} + 0.57\,Re^{0.5}\,Pr^{1/3} \tag{5.18}$$

where,

$$Nu = \frac{hd}{k} \tag{5.19}$$

$$Re = \frac{dG}{\mu} \tag{5.20}$$

$$Pr = \frac{C_p \mu}{k} \tag{5.21}$$

For the above relationships, the following additional constants are defined: d is the bead diameter; k is the thermal conductivity of the gas; G is the gas mass velocity (ρu); μ is the gas viscosity; and C_p is the specific heat capacity of the gas.

The properties of the gases in the boundary layer (properties of nitrogen were assumed) (34), and the key dimensionless groups were initially calculated at the bead temperature. They were subsequently calculated at the film temperature, T_f,

$$T_f = \frac{T_G + T_B}{2} \tag{5.22}$$

The emissivity of the bead (31) was calculated at the bead temperature. The gas temperature and a new film temperature were calculated. The above procedure was repeated and this iterative process continued until the gas temperature calculation converged.

The following flow chart gives a general description of the FORTRAN program used to correct the measured flame temperature for radiation.

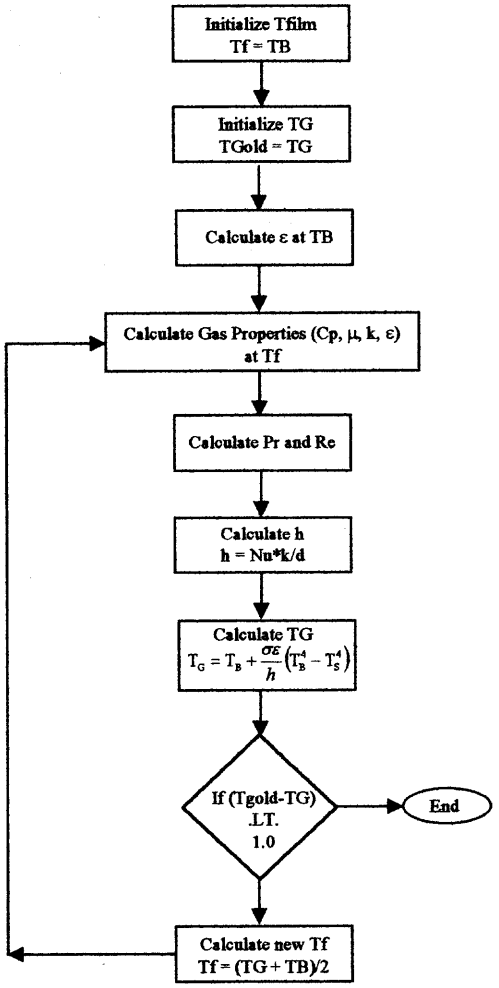

Figure 5.5 Flowchart for Temperature Profile Correction for Radiation

Figure 5.6 illustrates measured and corrected temperature profiles (corrected for radiation only) for a representative $\phi = 1.86$ methane/air flame. The maximum temperature correction is approximately 230K. An uncertainty analysis of the radiation correction procedure was performed and it suggested that the uncertainty in the corrected temperature could be as much as 100K.

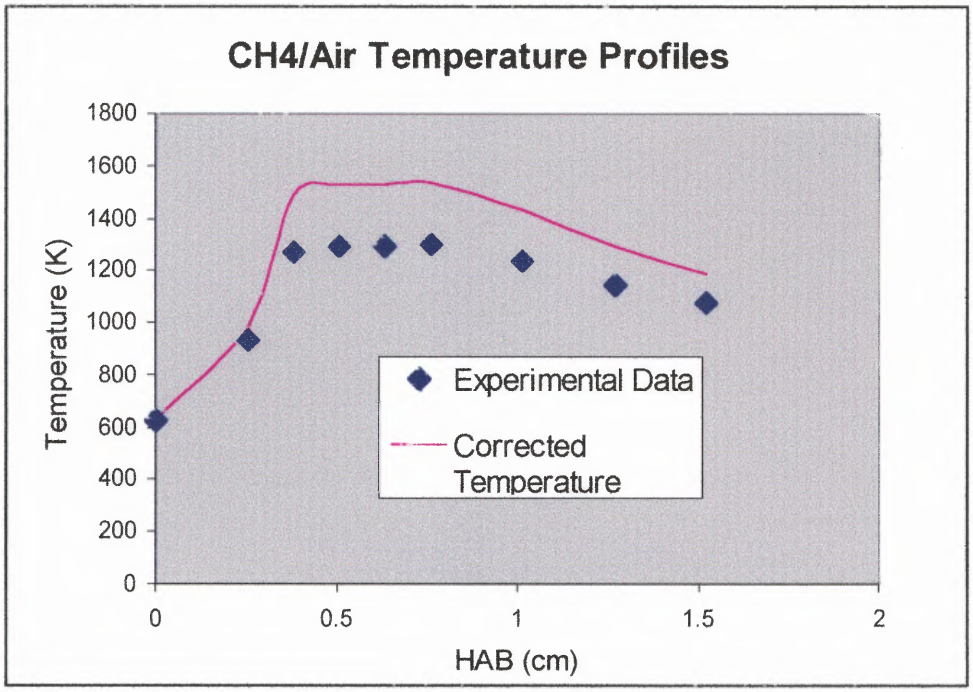

Figure 5.6 Corrected and Uncorrected Experimental Temperature Profiles for CH_4/Air Flame, ϕ=1.86

In an effort to determine an upper limit to the correction, the methane/ air model was run as an adiabatic case wherein the temperature profile is calculated in the absence of any heat losses. The lower limit was assumed to be the raw, experimental temperature data. The maximum difference between the two limits, ΔT_{Limit}, was approximately 600 K. Therefore, the radiation-corrected temperatures are less than the adiabatic profiles, which is consistent with the fact that the flame experiences heat loss to the surroundings – especially the burner.

5.2.5 Air Entrainment Modification and Analysis

In the original Sandia development of the premixed flame equations, the total mass flow rate of gases in the flame, $\dot{M}$, is assumed to be a constant. However, the flame used in this work was exposed to the environment and experiences transport of air from the surroundings. The total mass flow rate of gases in the flame is no longer a constant, but is a function of height above burner (30). It should be noted that for this study, the entrainment rate was expressed as a linear function of height, x and that diffusion of species into the flame from the surroundings begins at x = 0.0 HAB. This was considered a reasonable starting point in the development of the entrainment expression and a good first approximation. However, the possibility that the flame in this study could be more accurately described as a two-zone flame (an inner premixed flame surrounded by an outer diffusion flame) is discussed further in chapter 8. In this particular scenario, the premixed region does not experience diffusion of species from the surroundings, but rather diffusion begins at the interface between the premixed zone and the diffusion zone.

Development of Air Entrainment Expression for a Slotted Flame

The entrainment of air by the slotted flame was depicted in figure 5.3. In this study, the following relationship exists between the metered feed rate and the total mass flow rate:

$$\dot{M}_o + \text{Entrainment} = \dot{M} \tag{5.23}$$

where $\dot{M}_o$, is the metered feed rate and the entrained air is a function of HAB (x). As a result, the total mass flow rate, $\dot{M}$, is also a variable and a function of HAB.

Spalding (30) showed that the mass flow rate, $\dot{M}$, in a laminar jet was not a constant, but rather increased with x. He also showed that $\dot{M}$ was actually independent of the velocity of the injected fluid and the size of the nozzle outlet:

$$\dot{M} = 8\pi\mu x \tag{5.24}$$

where μ is the fluid viscosity.

Further development of this expression for a laminar jet (30) showed that the entrainment rate, i.e. the rate of increase of $\dot{M}$ with x, was a constant:

$$\frac{d\dot{M}}{dx} = 8\pi\mu = \text{Constant} \tag{5.25}$$

The above results were used as a starting point for the development of an expression for the variable mass flow rate found in this study. Once a trial expression was formulated, it was inserted into the source code and the model was executed. The model output was compared to the measured stable species profiles for CO, CO_2 and CH_4 for a methane/ air flame, $\phi = 1.86$. The working assumption here was that the reaction mechanism for methane/air combustion (27) is accurate. In fact, this mechanism has been used successfully in several studies by Mao (27).

Some initial, sample expressions for air entrainment for a slotted flame took the following form:

$$\dot{M} = M_o + C\sqrt{x} \tag{5.26}$$

$$\dot{M} = M_o + Cx \tag{5.27}$$

$$\dot{M} = M_o + Cx^2 \tag{5.28}$$

$$\dot{M} = M_o + \frac{C}{\sqrt{x}} \tag{5.29}$$

$$\dot{M} = M_o + \frac{C}{x} \tag{5.30}$$

The above expressions were individually incorporated into the flame model for various integer values of C. The following figures detail some of the better results.

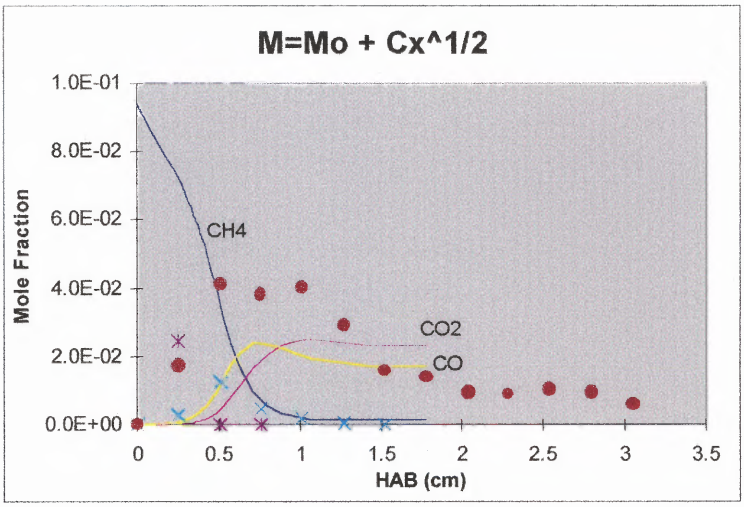

Figure 5.7 Experimental and Modeling Stable Species Profiles for CH_4/Air Flame, ϕ=1.86, using $M = M_o + Cx^{0.5}$ as Air Entrainment Expression

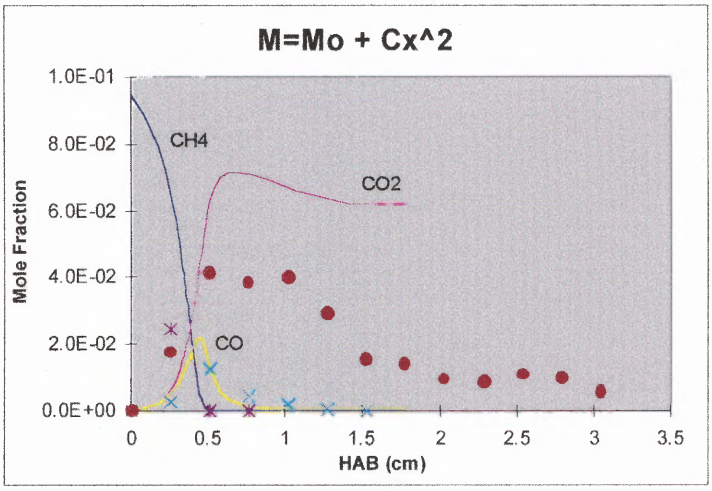

Figure 5.8 Experimental and Modeling Stable Species Profiles for CH_4/Air Flame, ϕ=1.86, using $M = M_o + Cx^2$ as Air Entrainment Expression

All of the above expressions were rejected because a poor fit to the experimental data was produced.

In the development of the entrainment expression, it was an important consideration and limitation that the expression for $\dot{M}$ should have some reasonable, physical interpretation. It was concluded that the family of expressions for variable mass flow rate that produced the most acceptable results took the following form:

$$\dot{M} = \dot{M}_o + C' x^n \tag{5.31}$$

or, more simply,

$$\frac{\dot{M}}{\dot{M}_o} = 1 + C x^n \tag{5.32}$$

where n is a positive, real number. Incremental values of n in the range of $0 < n \leq 3$ were tested and evaluated. The following is a sample of the most acceptable results that were produced.

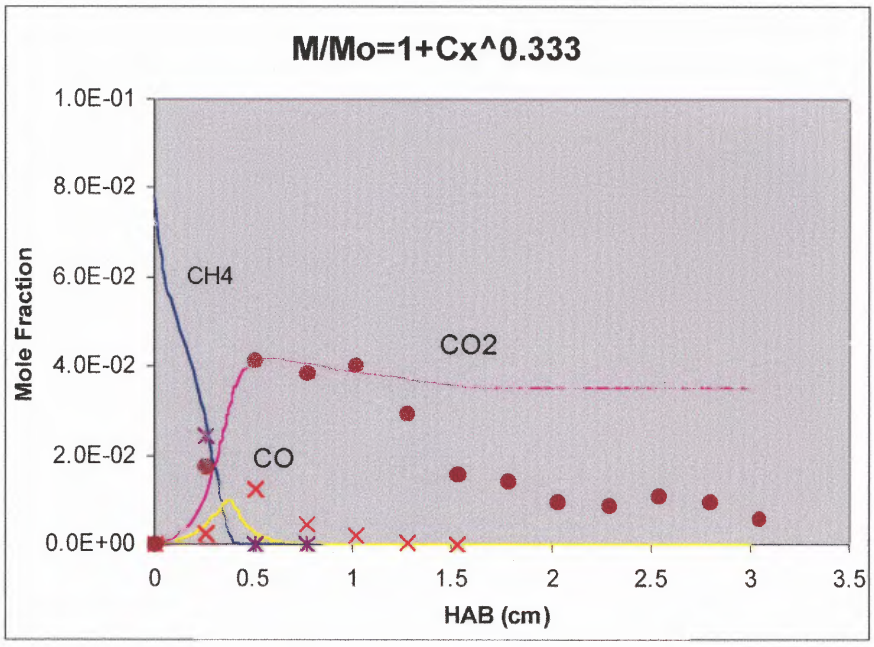

Figure 5.9 Experimental and Modeling Stable Species Profiles for CH_4/Air Flame, ϕ=1.86, using $M/M_0=1+Cx^{0.33}$ as Air Entrainment Expression

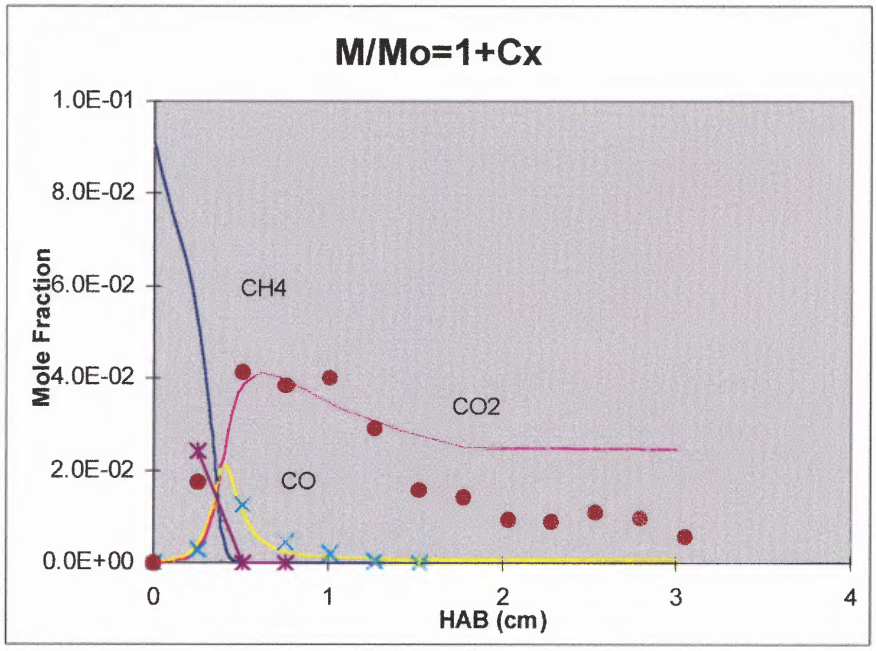

Figure 5.10 Experimental and Modeling Stable Species Profiles for CH_4/Air Flame, ϕ=1.86, using $M/M_0=1+Cx$ as Air Entrainment Expression

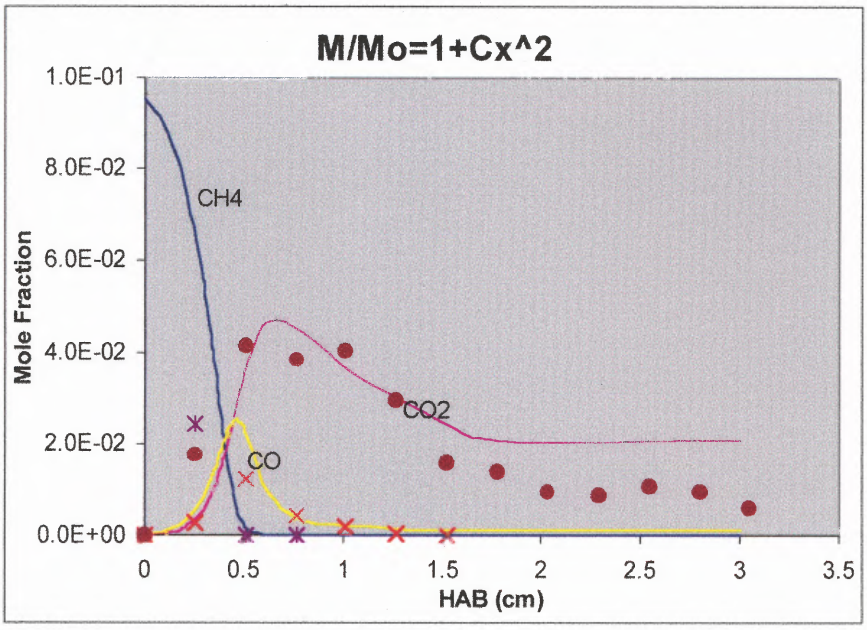

Figure 5.11 Experimental and Modeling Stable Species Profiles for CH_4/Air Flame, ϕ=1.86, using $M/M_0=1+Cx^2$ as Air Entrainment Expression

It can be seen from the above figures, that the expressions represented by :

$$\frac{\dot{M}}{\dot{M}_o} = 1 + Cx \tag{5.33}$$

and

$$\frac{\dot{M}}{\dot{M}_o} = 1 + Cx^2 \tag{5.34}$$

produced the most reasonable results. However, the expression represented by equation 5.33 was chosen for use in this study based on its close resemblance to the laminar jet expression (30) and its simple, reasonable, physical interpretation. That is: at any given height in the flame, the mass flow rate is equal to the initial mass flow rate, plus an incremental amount of entrainment, that is directly proportional to the HAB. It should also be noted that the derivative of this expression, i.e. the entrainment rate, resulted in a constant:

$$\frac{d\dot{M}}{dx} = C \cdot \dot{M}_o \equiv \text{Constant} \tag{5.35}$$

This is a reasonable hypothesis, based on the development and results of the entrainment rate in a laminar jet, as discussed by Spalding (30).

Development of Air Entrainment Constant, C

At first, an arbitrary, positive, real number was chosen for the air entrainment constant C. The model was then run and the results were compared to the experimental data. Figure 5.12 illustrates how the CO_2 profiles in a methane/air flame (ϕ =1.86) vary with air entrainment constant.

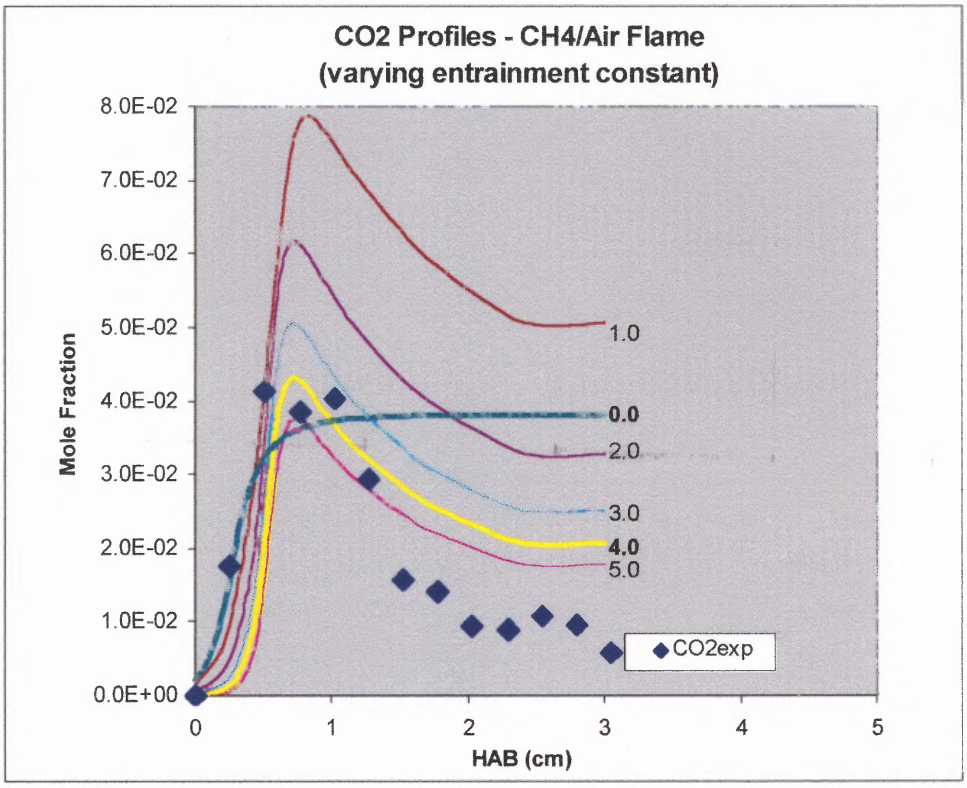

Figure 5.12 Experimental and Modeling Results of CO_2 Concentration Profiles for CH_4/Air Flame, ϕ=1.86, for Varying Air Entrainment Constant

The first significant result is that when the entrainment constant is set equal to zero (i.e., no entrainment), the CO_2 profile is flat. This result indicates that there is no dilution of species due to entrained air, and is typical of results reported in the literature (37) for flat flames with nitrogen shrouds (i.e. no air entrainment). The second result of significance is that as the entrainment constant decreases, the amount of air available for dilution only, decreases. As a result, the CO_2 mole fraction begins to increase. This result is reasonable and was expected.

Analysis of the above results led to the conclusion that when the air entrainment expression for a slotted burner is of the form expressed by equation 5.33, the most suitable constant for a methane/ air flame was C=4.0 cm^{-1}. It should be noted that while the above entrainment expression was used for all slotted flames in this study, a unique constant was developed for each flame class (i.e. CH4/air, CH4/air/Na etc.). These other results will be presented in chapters 6 and 7.

Figure 5.13 shows similar results for CO profiles in a methane/air flame (ϕ =1.86), as the entrainment constant was varied, for which comparable conclusions were reached.

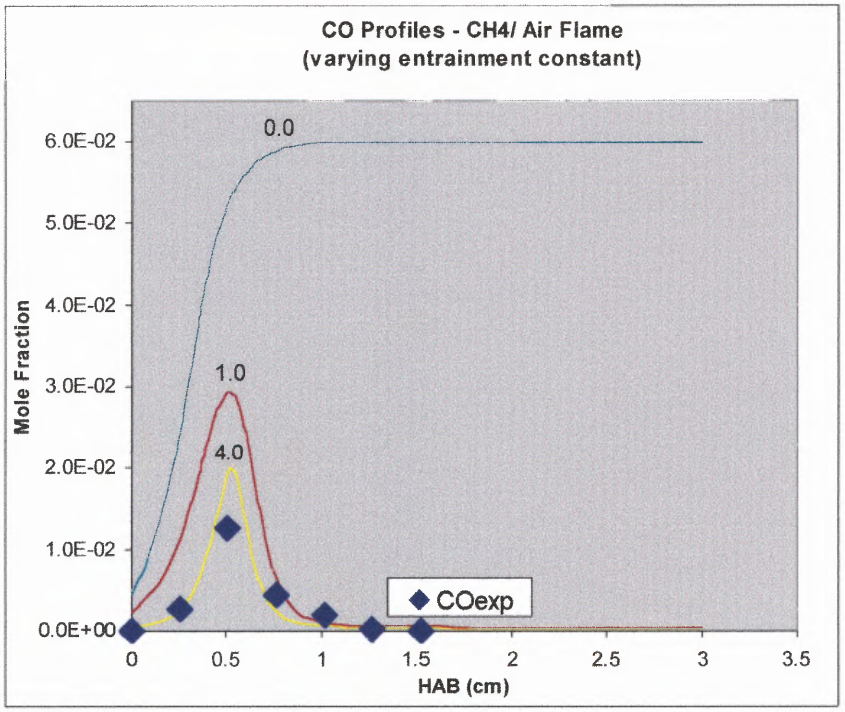

Figure 5.13 Experimental and Modeling Results of CO Concentration Profiles for CH_4/Air Flame, ϕ=1.86, for Varying Air Entrainment Constant

In fuel-lean flat flames without air entrainment, the CO profile rises to a maximum and then falls as CO is converted to CO_2, as seen in figure 5.14.

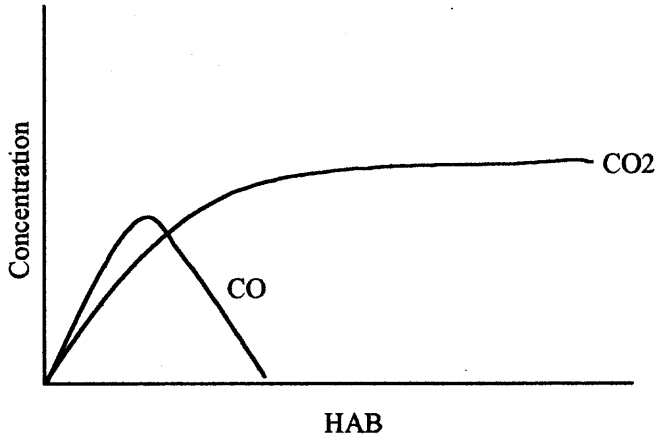

Figure 5.14 Schematic of CO and CO_2 Concentration Profiles for a Fuel—Lean Flame Without Air Entrainment

For fuel-rich flames, the CO rises and then remains constant as O_2 is depleted (45), as seen in figure 5.15.

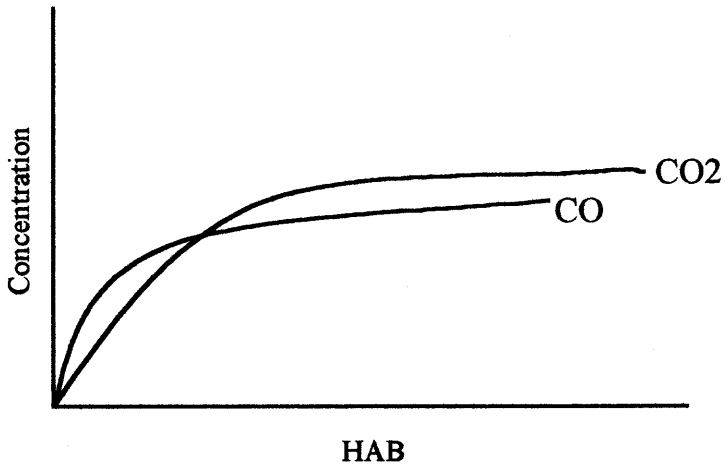

Figure 5.15 Schematic of CO and CO_2 Concentration Profiles for a Fuel—Rich Flame Without Air Entrainment

For the fuel-rich slotted flame in this study, both the CO and CO_2 rise and fall due to air entrainment. This is seen in Figure 5.16

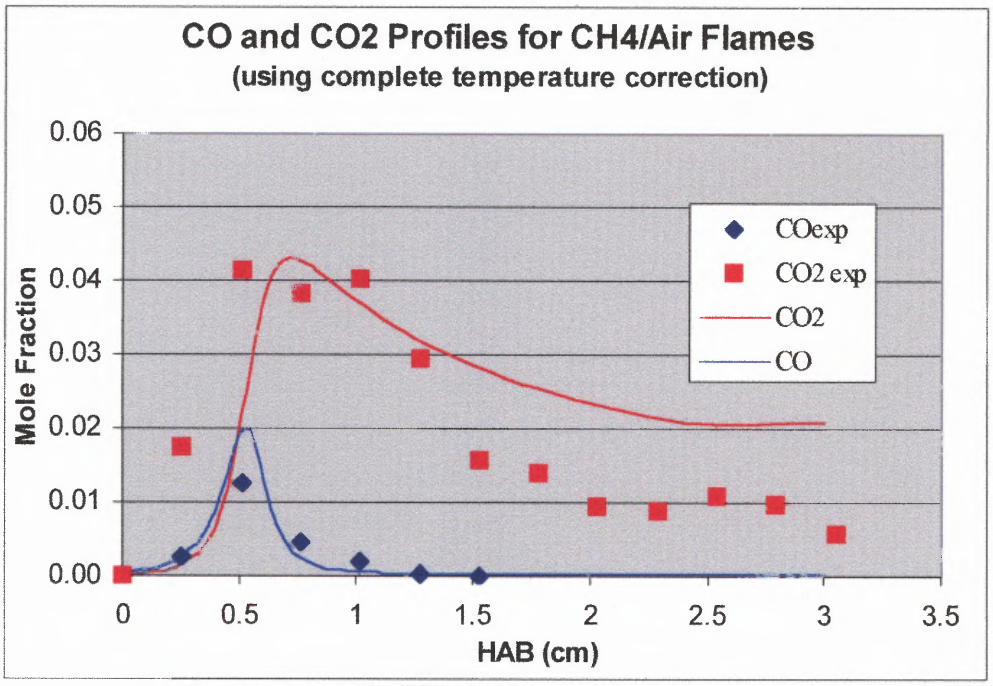

Figure 5.16 Experimental and Modeling Results for CO and CO_2 Concentration Profiles for a CH_4/Air Flame, ϕ=1.86, Including Air Entrainment

5.2.6 Summary of Calibration Results

The following list summarizes the tasks and results related to development and calibration of a FORTRAN program for modeling the slotted flames in this study. It should be noted that further discussion of the assumptions used as a basis to arrive at these results is presented in chapter 8. In particular, the method of temperature correction as well as the phenomenon describing mass transfer of species from the surroundings is further examined.

However, for the purposes of this study, experimental data from a methane/air flame, $\phi = 1.86$, were used as a calibration database.

1. The species and enthalpy balances were rederived. This resulted in an extra term in each balance to account for entrainment of air, by the flame, from the surroundings.
2. The cross sectional area of the flame, A, was estimated as a function of distance from the burner (HAB). The result was the following expression:

$$A = A_0(1 + 2x) \tag{5.15}$$

3. The experimental temperature profiles were corrected to account for heat loss due to radiation. The result was a temperature correction, ΔT, in the following range:

$$10K \leq \Delta T \leq 230K$$

4. The following expression was developed to account for entrainment of air, for all flame types, when using a slotted burner:

$$\frac{\dot{M}}{\dot{M}_0} = 1 + Cx \tag{5.33}$$

5. The constant, C, in the entrainment expression was determined for a CH_4/air flame. This constant is independent of equivalence ratio, ϕ, and was found to have the following value of C = 4.0 cm^{-1}.

5.3 Procedure for Executing the Model

The procedure for executing the model on a personal computer (PC) can be found in Appendix B.

CHAPTER 6

DISCUSSION OF EXPERIMENTAL DATA AND MODELING RESULTS FOR METHANE/AIR AND METHANE/AIR/SODIUM FLAMES

6.1 Introduction

The four flame types studied in this project can be categorized in the following manner:

1. Methane/air flames without sodium
2. Methane/air flames with sodium (fed as aqueous $NaNO_3$ solution)
3. Methane/air/chlorine (fed as CH_3Cl) flames without sodium
4. Methane/air/chlorine flames with sodium

This chapter will examine the experimental data and the modeling results for the first two categories, a comparison of methane/air flames without sodium to methane/air flames which have been doped with sodium.

Preliminary experimental and modeling results have been presented in chapter 5 for methane/air flames in an effort to highlight the calibration and modifications that were made to the packaged CHEMKIN flat flame code. The first part of this chapter will describe the additional modifications that needed to be made to the previously calibrated code in order to model methane/air flames with sodium. The second part of this chapter will

compare the modeling with the experimental results obtained. This chapter will also discuss the trends that were expected (as indicated by the literature), observations and hypotheses.

The following table outlines the experimental data and modeling results, which will be reviewed in this chapter:

Table 6.1 Outline of Experimental and Modeling Analysis of CH_4/Air and CH_4/Air/Na Flames by this Study

		Methane/Air Flames				Methane/Air/Sodium Flames			
ϕ		1.29	1.86	2.48	3.15	1.29	1.86	2.48	3.15
Experimental Data	Temp. Profile		√	√	√	√	√	√	√
	Absorb. Profile					√	√	√	√
	Stable Species Profile		√				√		
Modeling			√			√	√	√	√

6.2 Physical Appearance of the Flame

6.2.1 Relationship Between Equivalence Ratio, Flame Speed and Flame Height

For the methane/air flames, with and without sodium, the flame speed appeared to decrease as the fuel equivalence ratio increased. This was evidenced by an increase in the overall size of the flame (i.e., height and width) as well as the inner core. The casual observer might note that the

lower equivalence ratio (e.g., ϕ=1.29) produced a "smaller, tighter, neater, sharper" flame while the higher equivalence ratio (e.g., ϕ=3.15) resulted in a "larger, floppier, looser" flame. This is consistent with published dependence of flame speed on ϕ for CH_4/air Bunsen flames (66).

Strehlow (53) has discussed many techniques for measuring flame speed. One of them, the burner method, relates the flame speed to the flame height for a premixed flame on a round burner. The speed of a flame on a circular port of radius r is given by the following equation:

$$S_u = \frac{2V}{\pi r\sqrt{h^2 + r^2}} \tag{6.1}$$

where h is the flame height of the inner, premixed cone (core) and V the volumetric flow rate of the combustible gas mixture. Assuming that the volumetric flow rate and the burner opening are held constant, the flame speed is related to the flame height in the following manner:

$$S_u \propto \frac{1}{h} \tag{6.2}$$

It should be noted that this relationship was developed for a conical shaped flame on a round burner. The flame used in this study was an

"elongated" conical flame i.e., a tent shaped flame. However, in both cases, the flame volume is defined as follows:

$$\text{Flame Volume} = \text{Burner Opening} \times h \tag{6.3}$$

In each case, the constant burner opening was replaced by the proportionality relationship. In effect, as the flame height increases with increase in equivalence ratio, the flame speed decreases.

Figures 6.1 and 6.2 are photographs taken of the burner used for this work. The camera used was set at a shutter speed of 1 second. The camera remained stationary on a tripod at a fixed distance from the burner (approximately 48 inches) as the fuel and oxidant flow rates were altered to obtain the four equivalence ratios of importance for this study; 1.29, 1.86, 2.48, and 3.15.

The changes in the physical appearance of the flame resulted in the following observations.

1. For both types of flames, increased ϕ resulted in increased flame dimensions, especially the overall height and the premixed inner core.

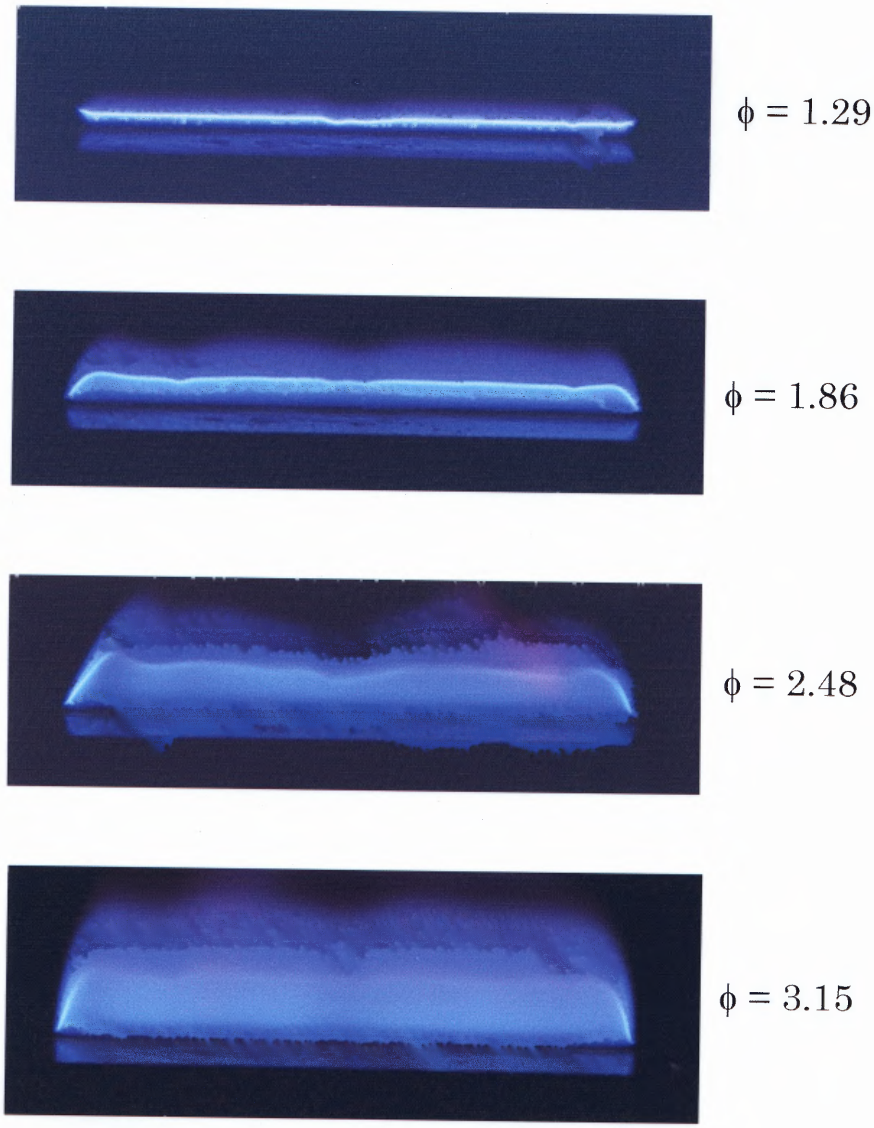

Figure 6.1 CH_4/Air Flames

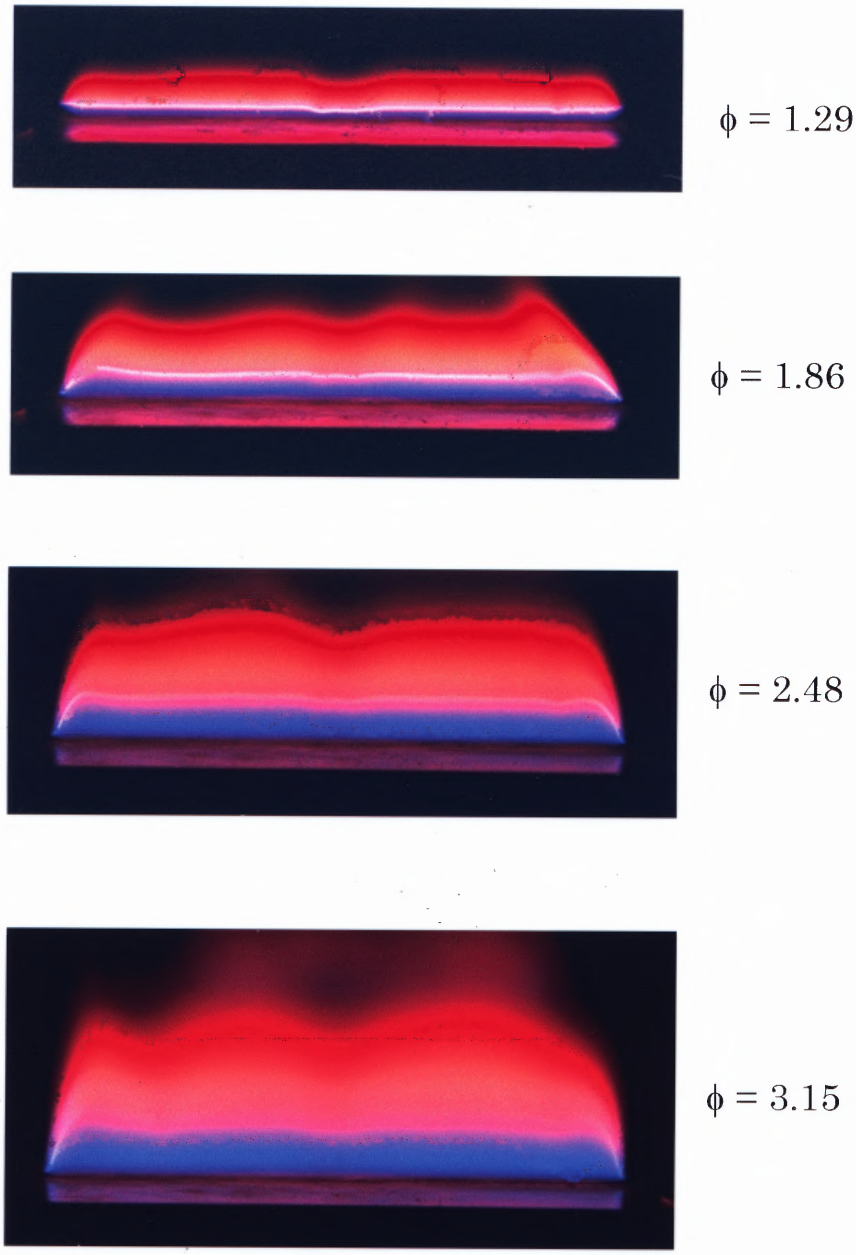

Figure 6.2 CH_4/Air/Na Flames

2. As seen in figure 6.1 and 6.2 for $\phi = 1.29$, the flame was lifting slightly off the burner. A wire mess screen was needed to stabilize these particular flames. However, note should be taken that the sodium-free flame was smaller and much more unstable than the flame that contained sodium, i.e., the flame with sodium did not appear to require a wire screen as much as the sodium-free flame in order to be stabilized.
3. ϕ=1.86 was the preferred equivalence ratio for stable species data collection. As ϕ increased from 1.86, the flame became "sloppy" and resulted in an increase in noise in the data. As ϕ decreased from 1.86, the flame size also decreased which resulted in a decrease in spatial resolution.

6.2.2 Changes Resulting from Addition of Sodium

A 0.02 mol/liter sodium nitrate ($NaNO_3$) solution was aspirated into the methane/air flame at a rate of 2.1 ml/min. When the flame was not doped with sodium, deionized water replaced the metal solution. The most obvious effect of sodium addition is the bright orange color due to sodium atom emission (589 nm.) It can be seen from figure 6.3 that for each ϕ, the physical size of the outer mantle increased with the addition of sodium.

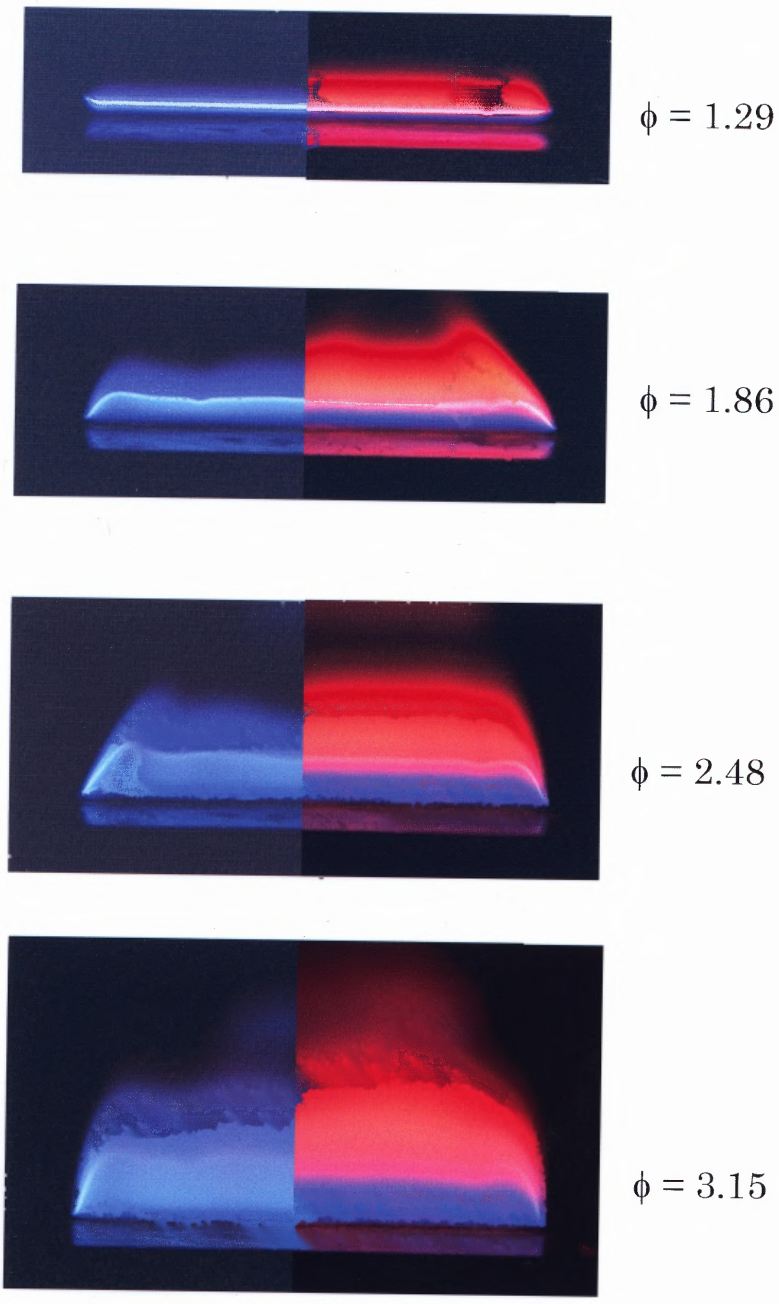

Figure 6.3 CH_4/Air and CH_4/Air/Na Flames

It should also be noted that the changes produced from the addition of sodium were comparable to the changes in the flame resulting from an increase in ϕ, e.g., flame became "sloppy". Possible explanations that will be investigated further later in this chapter are as follows:

1. The flame that was doped with sodium did not *actually* grow in size, but rather only *appeared* to grow in size. It is possible that more of the flame was visible due to the bright orange color resulting from addition of the sodium.

or

2. When the sodium atoms produced in the flame begin to react, the flame becomes inhibited. As the combustion slows, the flame remains more fuel rich locally. This is analogous to increasing the equivalence ratio. As previously discussed, an increase in equivalence ratio causes the size of the flame to increase.

6.3 Temperature Profiles

6.3.1 Background

All temperature profiles were obtained using a type R thermocouple. The thermocouple, which remained stationary as the burner was translated vertically, was connected to a chart recorder which had been calibrated. These temperatures were then corrected for heat loss due to radiation and plotted as a function of height above burner (HAB). The following sections

will discuss and analyze those trends. It should be noted that all runs with sodium were performed *separately* from those runs without sodium, i.e., on different days. This was done so as to eliminate any residual effects of sodium salt left on the probe or sodium solution in the lines. In addition, these temperature profiles have been corrected for radiation heat loss only. As stated earlier, a discussion of the correction of the raw temperature data for radiation as well as conduction is presented in chapter 8.

6.3.2 Temperature Profiles for Methane/Air Flames Without Sodium

Figure 6.4 shows the radiation-corrected temperature profiles for methane/air flames for ϕ = 1.86, 2.48 and 3.15. Temperature profiles for ϕ=1.29 were unattainable for methane/ air flames without sodium.

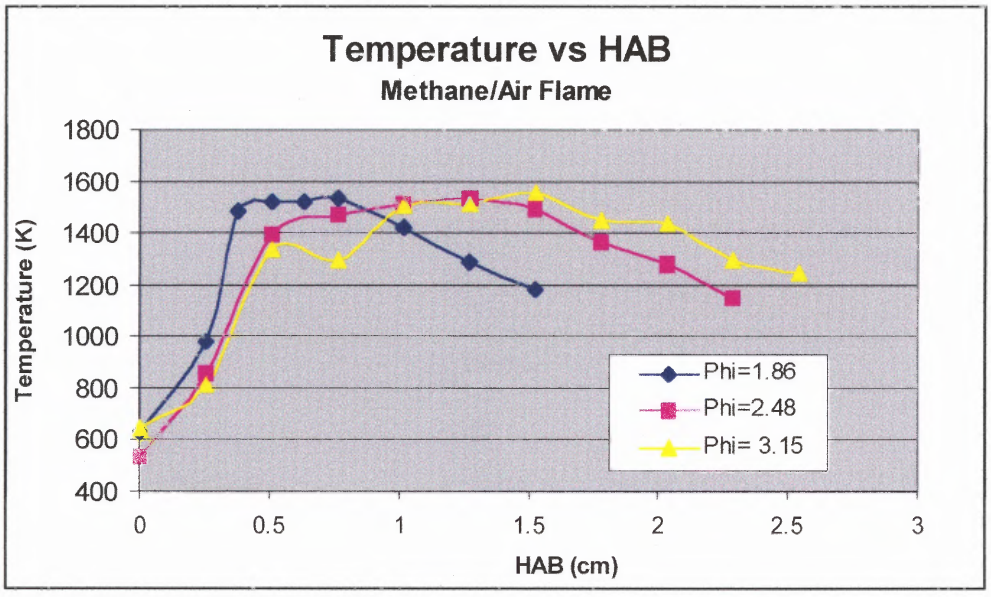

Figure 6.4 Experimental Temperature Profiles for CH_4/Air Flames, ϕ=1.86, 2.48, and 3.15

As previously mentioned, it appears that the addition of sodium to the flame causes the flame to grow in size. Without sodium in the flame, the flame for ϕ=1.29 was simply too small to obtain any measurements and data were not available for the above graph.

Table 6.2 outlines the approximate location of maximum temperatures for each of the above flames.

Table 6.2 Comparison of HAB of Maximum Temperatures for CH_4/Air Flames

Methane/Air Flames		
ϕ	**Max. Temp (K)**	**HAB (cm)**
1.86	1531	0.76
2.48	1536	1.3
3.15	1554	1.52

Observations

1. It can be seen from figure 6.4 as well as table 6.2 that as ϕ increases, the location of maximum temperature shifts to higher HAB.
2. The maximum temperature varied by only 23K (1531-1554 K) even though the equivalence ratio nearly doubled going from 1.86 to 3.15 (a factor of 1.7).

6.3.3 Temperature Profiles for Methane/Air/Sodium Flames

Figure 6.5 and table 6.3 outline the temperature profiles for methane/air flames doped with sodium that have been corrected for radiation losses as well as the location of maximum temperatures. In contrast to the methane/air flames without sodium, data *were* available for ϕ=1.29. When sodium was added to this flame, the flame grew sufficiently large so that when the thermocouple was inserted, the flame remained stable. This was not the case for ϕ=1.29, without sodium.

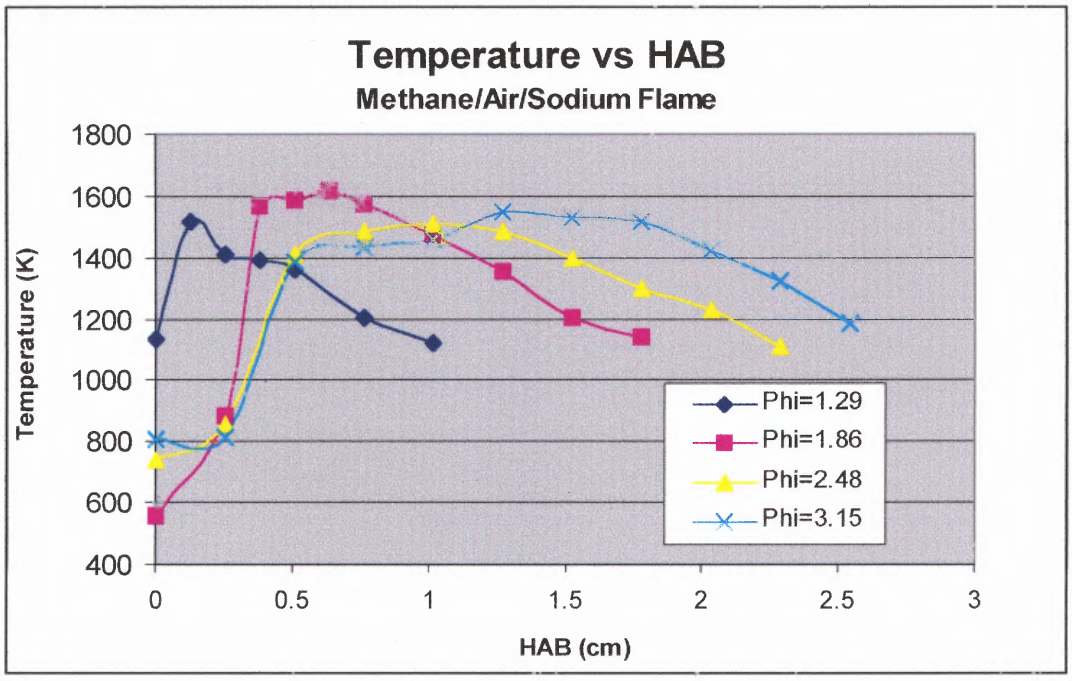

Figure 6.5 Experimental Temperature Profiles for CH_4/Air/Na Flames, ϕ=1.29, 1.86, 2.48, and 3.15

Table 6.3 Comparison of HAB of Maximum Temperatures for CH_4/Air/Na Flames

Methane/Air/Sodium Flames		
ϕ	**Max. Temp (K)**	**HAB (cm)**
1.29	1516	0.13
1.86	1615	0.64
2.48	1511	1.0
3.15	1548	1.3

Observations

1. As with the temperature profiles for methane/air without sodium, the location of maximum temperature is found at a larger HAB as ϕ increases.
2. The maximum temperature for ϕ=1.86 seems to be slightly higher than the maximum temperature for all the other cases. In general, however, as ϕ more than doubles as it increases from 1.29 to 3.15, the maximum temperature increases by only 32 K.

6.3.4 Comparison of Temperature Profiles for Methane/Air Flames, With and Without Sodium

Figures 6.6-6.8 shows how the experimental temperature profiles (corrected for radiation only) for methane/air flames without sodium (indicated by the blue lines) compare to the profiles for flames with sodium (indicated by the orange lines), for ϕ=1.86, 2.48 and 3.15 respectively.

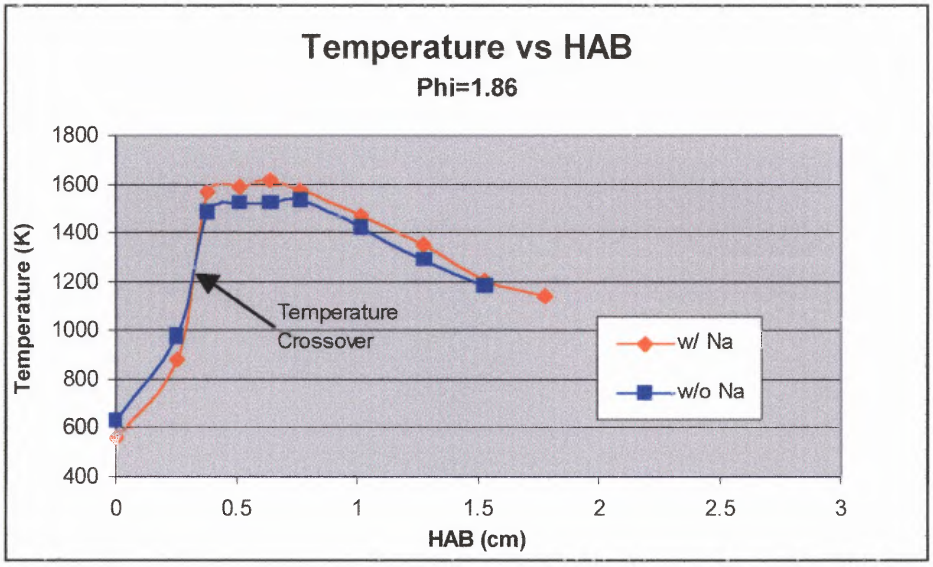

Figure 6.6 Comparison of Experimental Temperature Profiles for CH_4/Air and CH_4/Air /Na Flames, ϕ=1.86

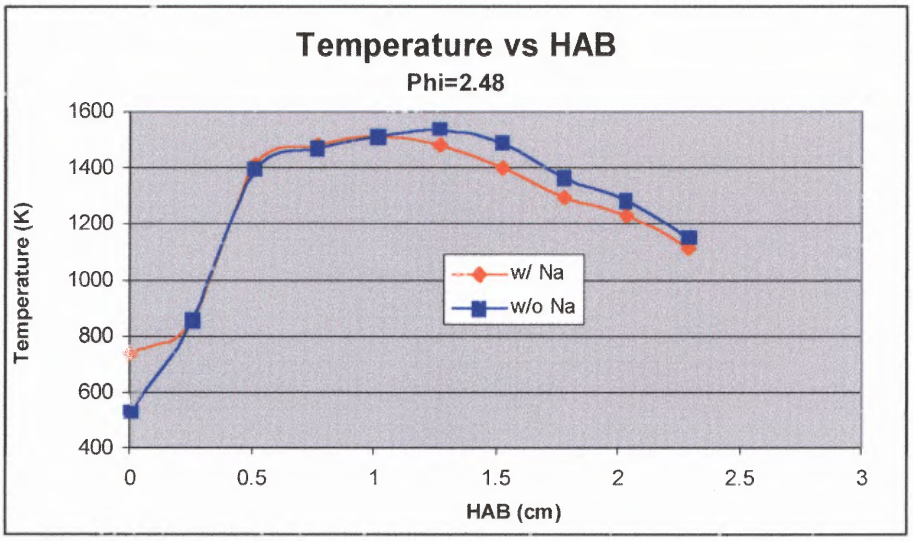

Figure 6.7 Comparison of Experimental Temperature Profiles for CH_4/Air and CH_4/Air /Na Flames, ϕ=2.48

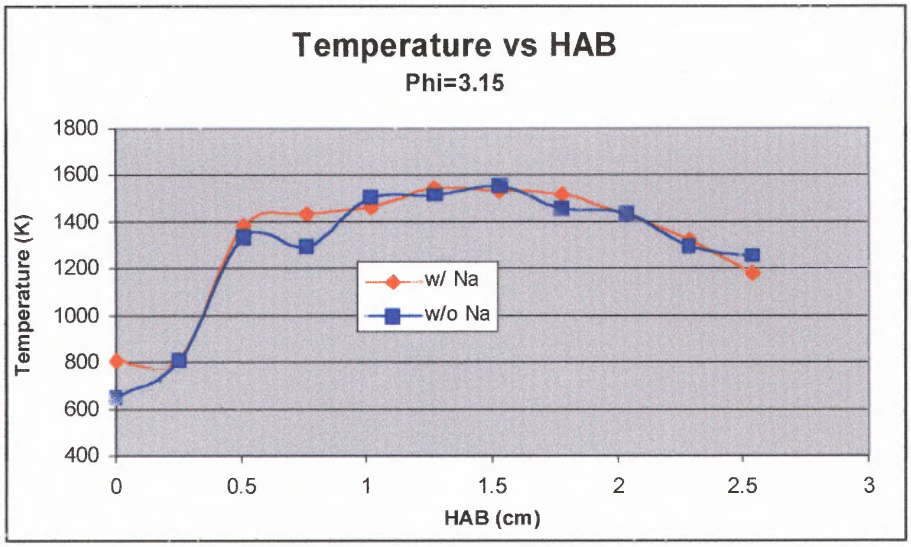

Figure 6.8 Comparison of Experimental Temperature Profiles for CH_4/Air and CH_4/Air/Na Flames, ϕ=3.15

Observations

1. It appears that for ϕ=1.86, there is a temperature profile *crossover* i.e., the flame experiences an increase in flame temperature later on in the flame. This crossover of temperature profiles is not evident for ϕ=2.48 and 3.15.
2. Table 6.4 shows that the maximum temperature is located *lower* in the flame when sodium is present for each ϕ.

Table 6.4 Comparison of HAB of Maximum Temperatures for CH_4/Air and CH_4/Air/Na Flames

Maximum Temperature & Location (HAB)				
ϕ	Max Temp (K)		HAB (cm)	
	w/o Na	w/ Na	w/o Na	w/ Na
1.29	N/A	1516	N/A	0.13
1.86	1531	1615	0.76	0.64
2.48	1536	1511	1.3	1.0
3.15	1554	1548	1.52	1.3

3. The maximum temperature in the flame does not change significantly with the addition of sodium.
4. The data for ϕ=3.15 appears to contain the most noise, as evidenced by the absence of a smooth line. This was expected. The high equivalence ratio coupled with the addition of sodium created a very "floppy, loose, wandering" flame.

Hypotheses

1. From figure 6.6 and figure 6.7, it is seen that as ϕ increases, the location of maximum temperature increases in HAB. This was not a surprise. As the equivalence ratio increased, so too did the overall physical size of the flame. From this, one would expect that the size of the primary combustion zone, or the inner core, would also increase (Figure 6.9 highlights the important regions of flame).

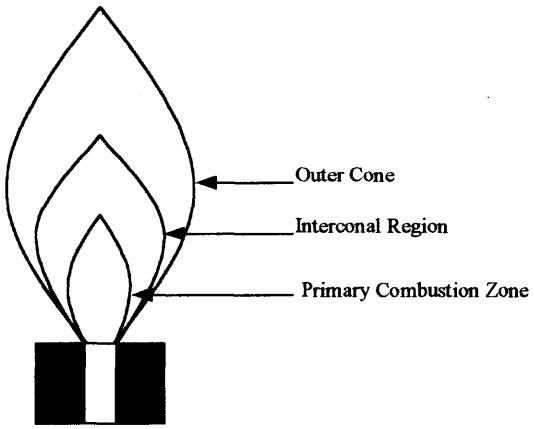

Figure 6.9 Schematic Diagram of Flame Regions

Since the maximum temperature is generally located somewhat above the primary combustion zone, as the upper boundary of the primary combustion zone increased so too would the location of maximum temperature (16).

2. The maximum temperature for methane/air and methane/air/sodium flames seemed to be independent of equivalence ratio. With the exception of ϕ=1.86 with doped sodium, the maximum temperatures asymptotically approached 1525 ± 20K. One possible explanation for this is that the equivalence ratio that was calculated based on the metered fuel and oxidant flows is not the same as the local equivalence ratio in the flame. This calculation does not take into account the additional oxygen that is entrained by the flame. A calculation was performed for ϕ=1.86 where it is shown that, at 1.8 mm HAB, the local equivalence ratio has been reduced from 1.86 to 1.0. As a result, it is quite possible that the local equivalence

ratios may be *more similar than different*, due to the fact that the flames are diluted with entrained air.

3. For each ϕ, the temperature profile for the flame with sodium and the flame without sodium can be considered effectively the same within experimental error.

6.4 CHEMKIN Flame Code Modifications

6.4.1 Reaction Mechanism

The CH_4/air and CH_4/CH_3Cl/air reaction mechanisms used by the computer flame model in this study are from a previously published source (27). However, a complete reaction mechanism was not available in the literature for the combustion of either a CH_4/air or CH_4/CH_3Cl/air flame doped with sodium. What was indeed available was a subset of the reaction mechanism for sodium in a hydrogen/oxygen flame (18). This subset included only those reactions that contained sodium species. However, as discussed earlier, sodium chemistry is assumed to be effectively independent of fuel type because the metal/carbon chemistry is not likely to be significant in the gas phase (19). As a starting point, this subset of sodium species reactions was simply *added* to the existing CH_4/air mechanism.

The reaction scheme which includes all the possible reactions of Na, NaO, NaO2, and NaOH is illustrated schematically in figure 6.10 and the

actual reactions are listed in table 6.5 (18). All additional relevant information regarding the sodium reaction subset is listed in Appendix C

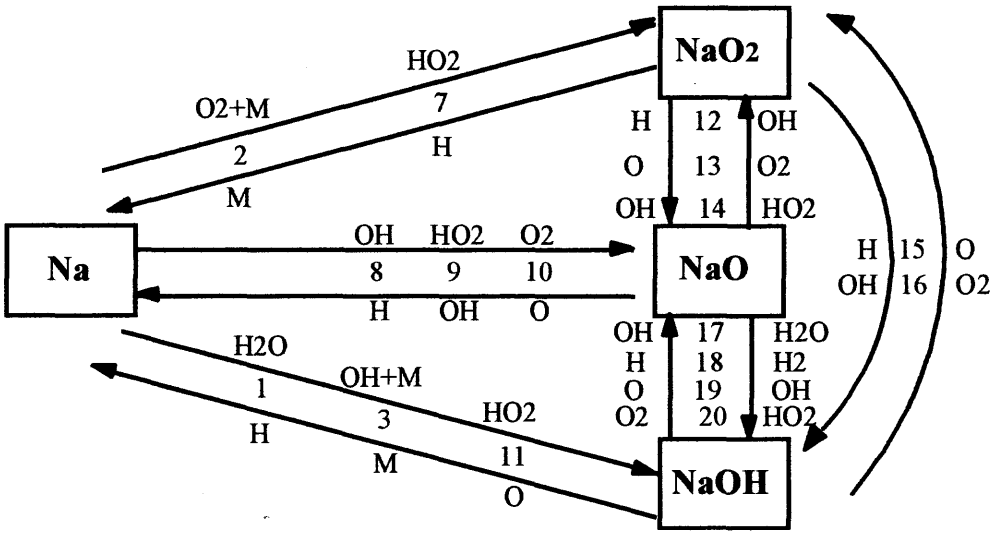

Figure 6.10 Sodium Reaction Scheme

Table 6.5 Sodium Combustion Reactions (18)

Reaction No. (+) forward, (-) reverse	**Reaction**
(1), (-1)	$Na + H_2O = NaOH + H$
(2), (-2)	$Na + O_2 + M = NaO_2 + M$
(3), (-3)	$Na + OH + M = NaOH + M$
(7), (-7)	$Na + HO_2 = NaO_2 + H$
(8), (-8)	$Na + OH = NaO + H$
(9), (-9)	$Na + HO_2 = NaO + OH$
(10), (-10)	$Na + O_2 = NaO + O$
(11), (-11)	$Na + HO_2 = NaOH + O$
(12), (-12)	$NaO_2 + H = NaO + OH$
(13), (-13)	$NaO_2 + O = NaO + O_2$
(14), (-14)	$NaO_2 + OH = NaO + H O_2$
(15), (-15)	$NaO_2 + H = NaOH + O$
(16), (-16)	$NaO_2 + OH = NaOH + O_2$
(17), (-17)	$NaOH + OH = NaO + H_2O$
(18), (-18)	$NaOH + H = NaO + H_2$
(19), (-19)	$NaOH + O = NaO + OH$
(20), (-20)	$NaOH + O_2 = NaO + HO_2$

According to Schofield et al. (18), an examination of the possible reactions of NaH (sodium hydride) indicates that this species need not be considered. Also, due to very low sodium concentrations, molecules containing more than one atom of sodium are unlikely.

In addition, for the purposes of this study only, a reaction set was included to account for sodium atom production from sodium ion, since the sodium was introduced to the flame as aqueous $Na^+NO_3^-$ solution. Further

examination of this theory suggests that the Na^+ is more likely converted directly to atomic sodium. This theory is discussed in chapter 8. However, the model that was run to simulate the flames in this study during the course of this work included a reaction subset that accounted for sodium ion to atom conversion. These reactions are outlined in the following table.

Table 6.6 Sodium Ion Reactions

Additional Reactions for Sodium Atom Production	
Reaction No. (+) forward, (-) reverse	**Reaction**
(21), (-21)	$CH + O = HCO^+ + E$
(22), (-22)	$HCO^+ + E = H + CO$
(23), (-23)	$Na + M = Na^+ + E + M$

Reaction (21) is the major source of electrons in the flame mechanism (37). The kinetics for this reaction were drawn from the neutral analogue, CH+O = CH+H (37). Reaction (-23) illustrates how sodium atom is produced from sodium ion, in the presence of bath gas, M. Reaction (22) is a sink for electrons, E.

The second subset of reactions that was added to the existing mechanism was the likely reactions between Cl radical and Na species. These additional reactions, which were added to the sodium subset, will be outlined in chapter 7.

6.4.2 Development of Air Entrainment Constant for Methane/Air Flames Containing Sodium

The general development of the air entrainment constant for the flame code and the specific development of the constant used to model methane/air flames was discussed in section 5.2.4. This section will discuss the development of the constant used in the air entrainment expression that effectively models methane/air flames that contain sodium.

Figure 6.11 illustrates experimental and modeling CO_2 profiles as function of HAB for methane/air flames doped with sodium for ϕ=1.86. The values of entrainment constant, C, vary from $1.0 \leq C \leq 3.0$ cm^{-1}. As expected, CO_2 concentrations reached a maximum and then decreased due to dilution with entrained air. A starting point was to use the entrainment constant for methane/air flames, i.e., C=4.0 cm^{-1}. However, figure 6.11 shows that as $C \rightarrow$ 4.0 cm^{-1}, the fit between the results and the experimental data worsens. Analysis of the results shows that the compatibility of the experimental data with the model is optimized at an entrainment constant equal to 2.0 cm^{-1}.

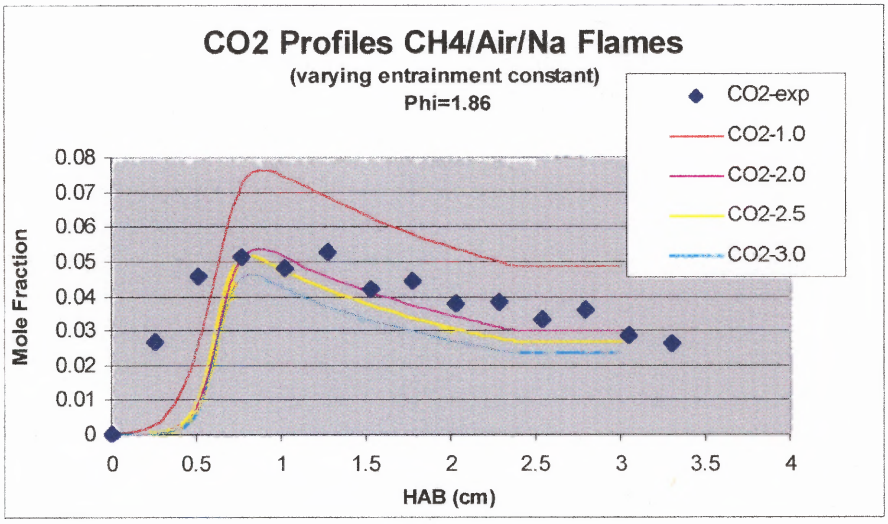

Figure 6.11 Experimental and Modeling CO_2 Concentration Profiles for CH_4/Air/Na Flames for Varying Entrainment Constants

Similarly, figure 6.12 shows how a change in entrainment constant affects the CO profiles for the same methane/air/sodium flame. Once again, these results strengthen the conclusion that a best fit is obtained between experimental data and the model when C=2.0 cm^{-1} is used as the entrainment constant.

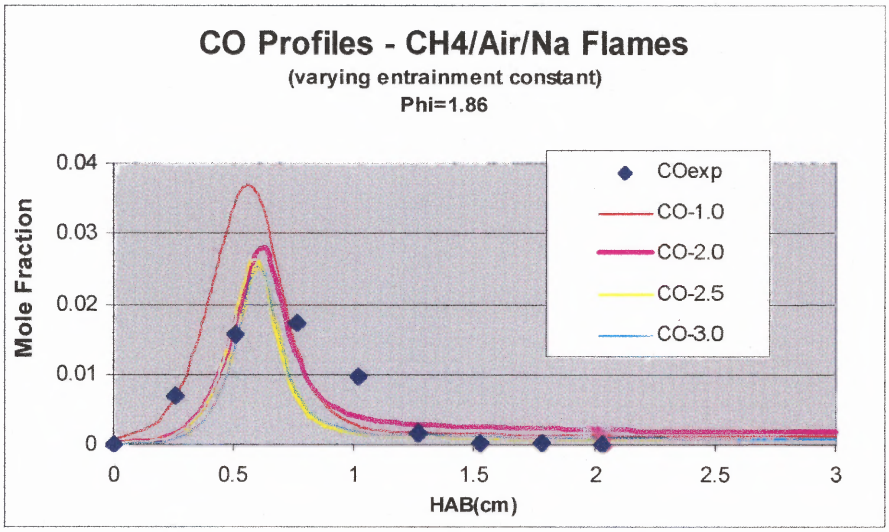

Figure 6.12 Experimental and Modeling CO Concentration Profiles for CH_4/Air/Na Flames for Varying Entrainment Constants

Therefore, for all flames containing methane + air + sodium only, an entrainment constant of c=2.0 cm^{-1} was used. This entrainment constant is independent of equivalence ratio.

6.5 Stable Species Profiles

Experimental stable species profiles were collected for all flame types for ϕ = 1.86 only. This section will discuss the comparisons between experimental data and modeling for the following flame types:

1. Methane/air
2. Methane/air/sodium

Methane/air flames will be discussed separately first, followed by methane/air/sodium flames. Modeling results only (i.e., no experimental data) will be presented for ϕ =1.29, 2.48, 3.15 in an effort to illuminate any trends in stable species profiles as a function of changing equivalence ratio.

6.5.1 Methane/Air Flames

The experimental data for stable species profiles were collected via the gas sampling system, outlined in section 4.1.11. Figure 6. 13 shows how the experimental data compare to the modeling results for CH_4, CO_2 and CO for ϕ = 1.86.

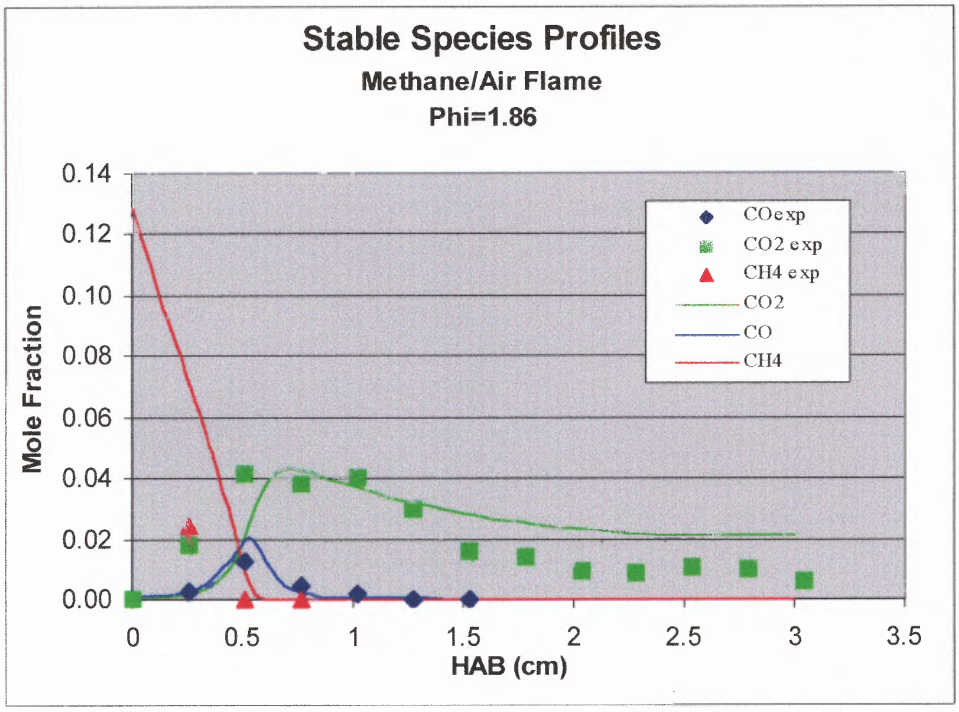

Figure 6.13 Experimental and Modeling Results of Stable Species Profiles for CH_4/Air Flame, C=4.0, ϕ=1.86

The experimental data, as well as the modeling results, follow the expected trends that were discussed in section 5.2.4. The mole fraction of the primary reactant, CH_4, declines monotonically. The mole fraction of the intermediate, CO, reaches a maximum at approximately the same HAB as the CH_4 mole fraction effectively disappears, at 0.5 cm HAB. The CO mole fraction then falls as it is converted to CO_2. The CO_2 mole fractions reach a maximum later at approximately 0.7 cm HAB. After reaching a maximum, CO_2 mole fractions decrease due to air entrainment. In general, the fit between the experimental data and the model is reasonable.

Comparison of the stable species profiles and the temperature profile for this flame shows that the temperature peaks at approximately 0.75 cm HAB, as seen in figure 6.14. This is where the CO has effectively disappeared and CO_2 has peaked. Methane is long gone. Therefore, combustion is over. Air entrainment is acting to drop the temperature as well as CO_2 concentration after their peaks.

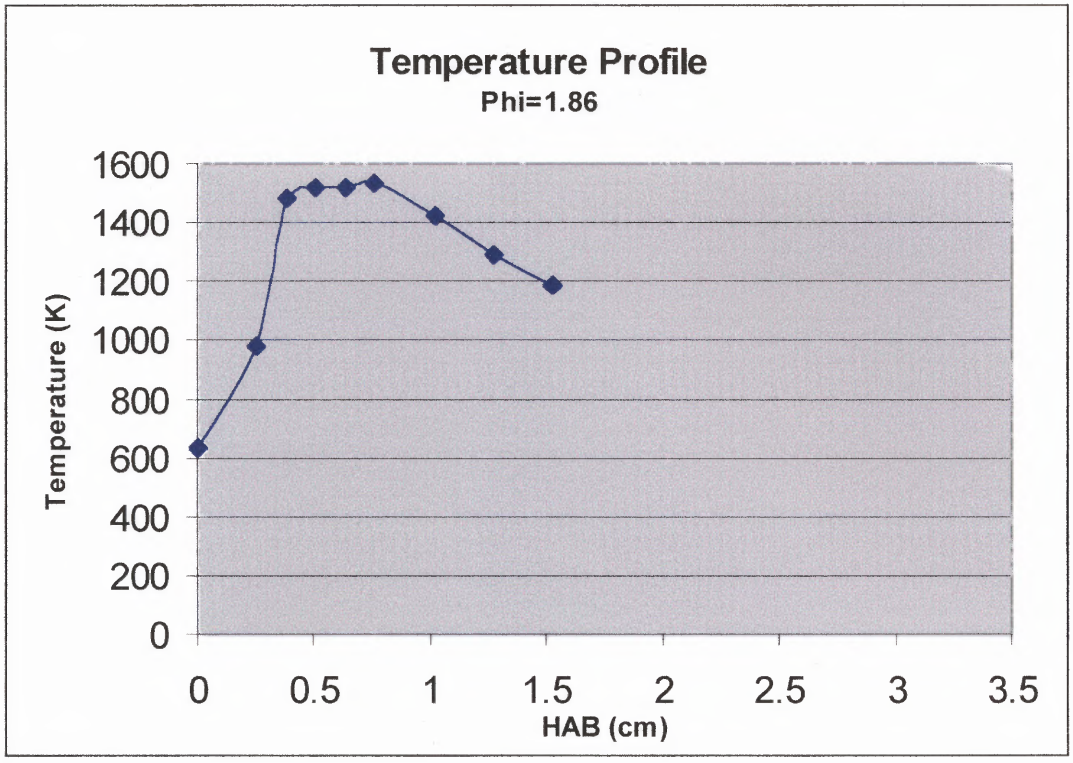

Figure 6.14 Experimental Temperature Profile for CH_4/Air Flame, C=4.0, ϕ=1.86

6.5.2 Methane/Air/Sodium Flames

Figure 6.15 shows the stable species profiles for methane/air flames doped with sodium. As expected, the CH_4 concentrations decline monotonically. The CO mole fraction rises to a maximum at approximately 0.5 HAB, after which it falls as it is converted to CO_2. The CO_2 peaks at 0.7 HAB, but eventually drops off due to dilution with entrained air. As with the methane/air flame, the fit between the experimental data and the model for the methane/air/sodium flame is also reasonable.

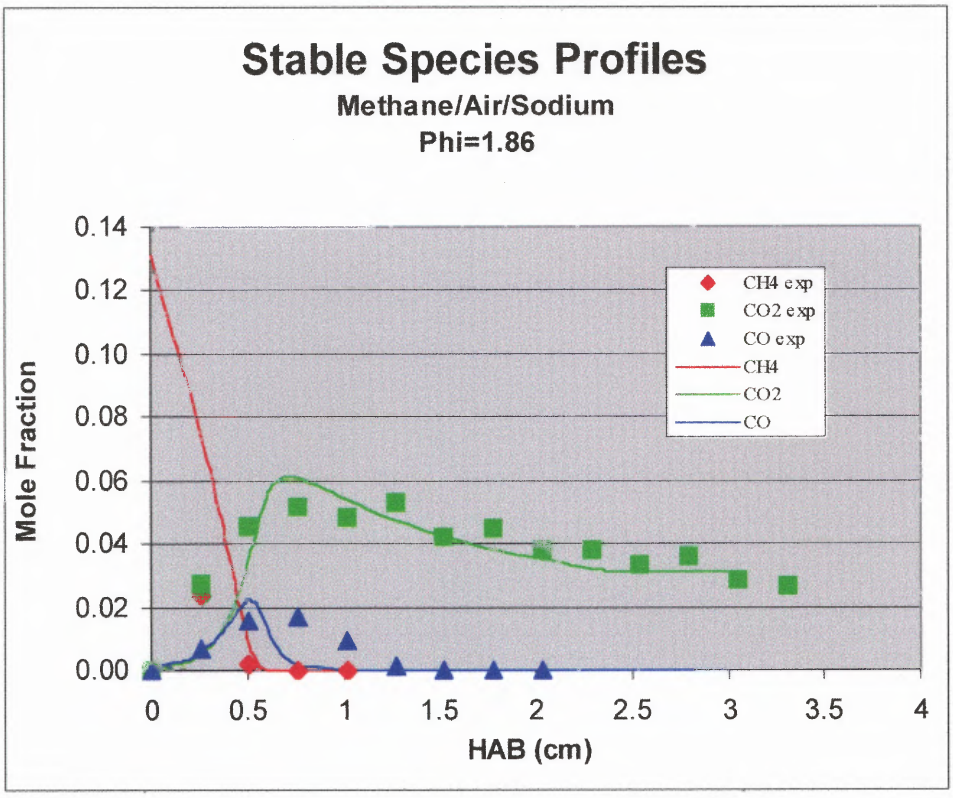

Figure 6.15 Experimental and Modeling Results of Stable Species Profiles for CH_4/Air/Na Flame, C=2.0, ϕ=1.86

Comparison of the stable species profiles with the temperature profile for the same flame (figure 6.16), shows that a maximum temperature is effectively reached at the point where the CO has disappeared and the CO_2 has peaked and is starting to fall.

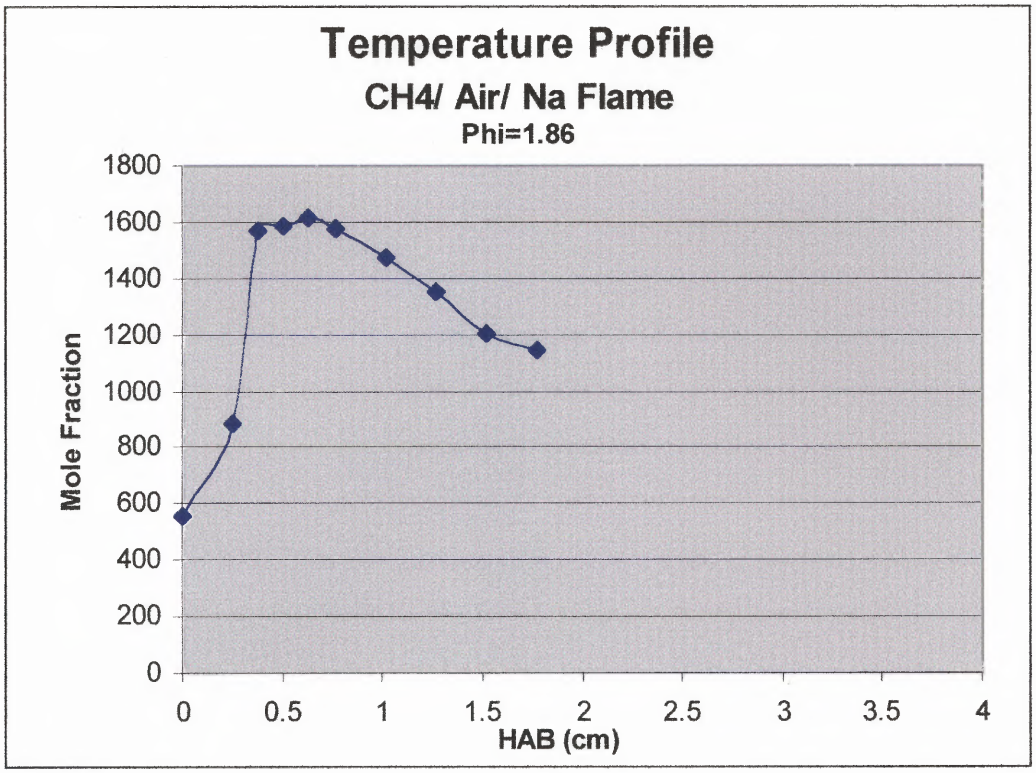

Figure 6.16 Experimental Temperature Profile for CH_4/Air/Na Flame, C=2.0, ϕ=1.86

6.5.3 Comparison of Stable Species Profiles for Methane/Air Flames, With and Without Sodium

The experimental profiles, as well as the modeling results for methane/air and methane/air/sodium flames, were as expected. It is not until the individual species profiles are compared directly that the actual affects of sodium on the methane/ air flame are observed.

It is clear from figure 6.17, that the CH_4 profiles for methane/air flames for ϕ=1.86 is effectively unaffected by the addition of sodium.

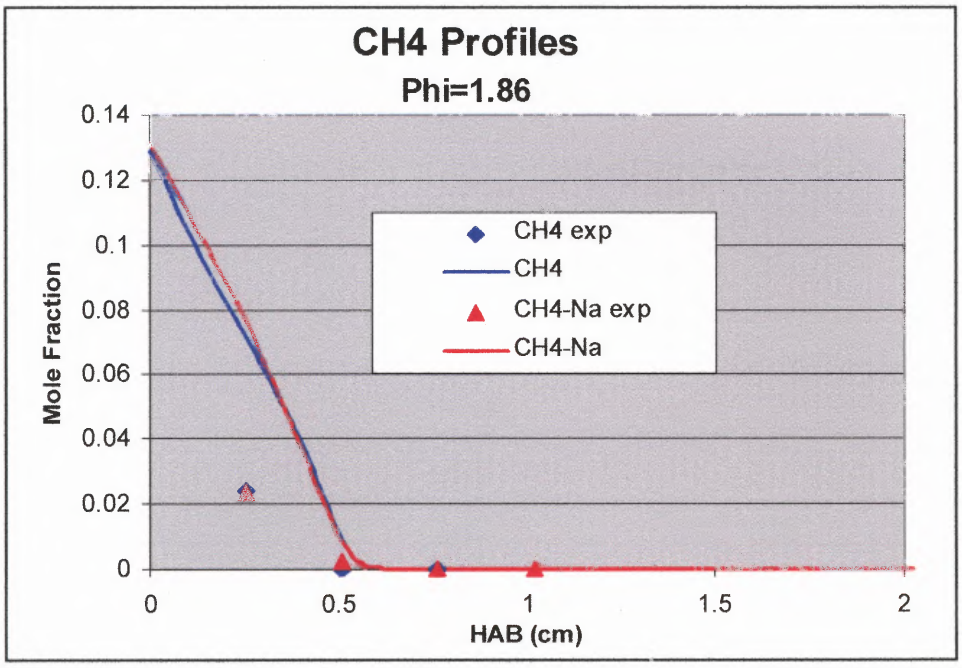

Figure 6.17 Comparison of Experimental and Modeling Results of CH_4 Profiles for CH_4/Air and CH_4/Air/Na Flames, ϕ=1.86

The following figure 6.18 depicts the CO profiles.

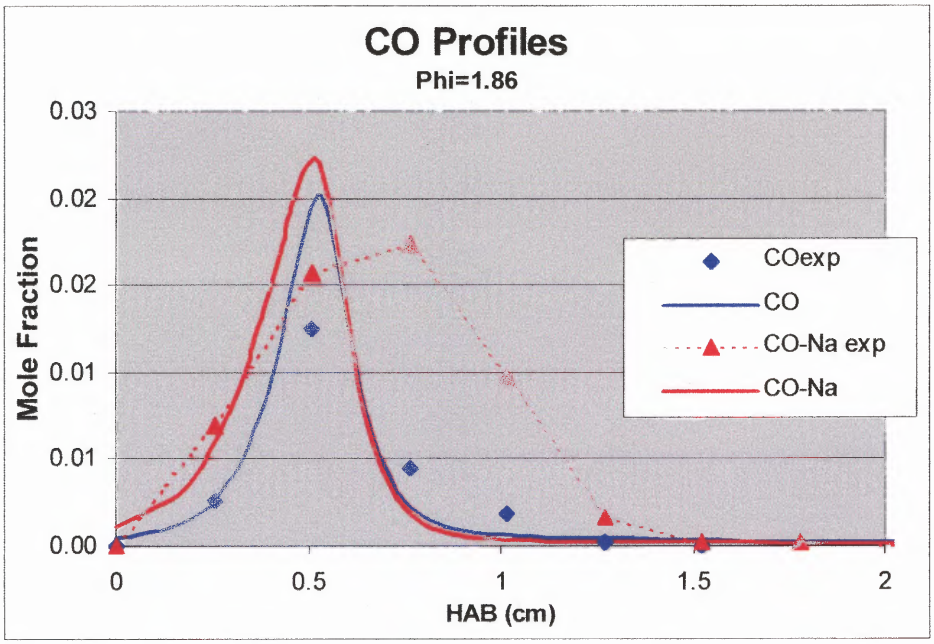

Figure 6.18 Comparison of Experimental and Modeling Results of CO Profiles for CH_4/Air and CH_4/Air/Na Flames, ϕ=1.86

It appears that the addition of sodium allows for the production of more CO, earlier on in the flame. However, though the modeling results do not show this, the experimental data indicates that the CO falls more rapidly in the absence of Na after the peaks.

It is not until the CO_2 profiles are compared, that the significance of the addition of sodium to the methane/air flame is observed. Figure 6.19 illustrates the CO_2 profiles using experimental data as well as modeling results for methane/air and methane/air/sodium flames.

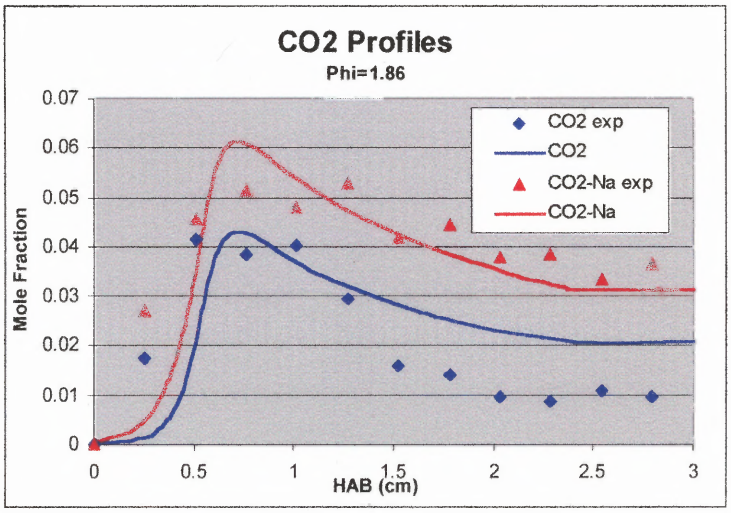

Figure 6.19 Comparison of Experimental and Modeling Results of CO_2 Profiles for CH_4/Air and CH_4/Air/Na Flames, ϕ=1.86

It is clear that there is a significant increase in the concentration of CO_2 produced when sodium is present in the flame.

Figure 6.20 represents the modeling results for the CO/CO_2 ratio for ϕ=1.86. However, no conclusions can be drawn from this profile since the model does not accurately represent the experimental CO profile.

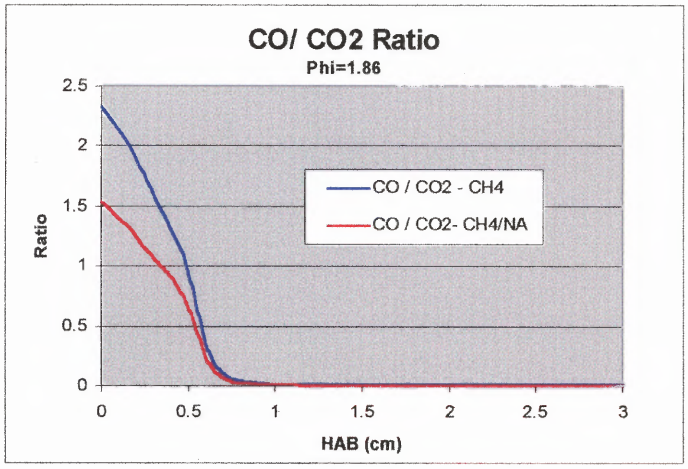

Figure 6.20 Comparison of Modeling Results of CO/CO_2 Ratios for CH_4/Air and CH_4/Air/Na Flames, ϕ=1.86

Figure 6.21 represents the CO/CO_2 ratio for ϕ=1.86 using *experimental data.*

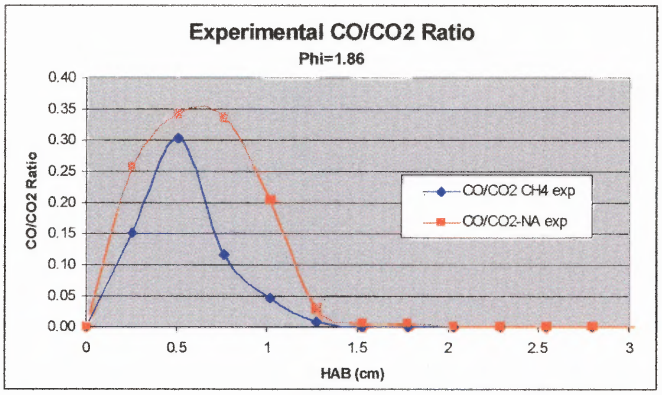

Figure 6.21 Comparison of Experimental CO/CO_2 Ratios for CH_4/Air and CH_4/Air/Na Flames, ϕ=1.86

6.6 Sodium Profiles in Methane/Air/Sodium Flames

6.6.1 Background

During the course of this study, the relative mole fraction of sodium in the flame was extracted from the experimental absorption data and this approach is discussed and derived in the following sections. The trends of these relative mole fraction profiles were then compared directly to absolute mole fraction profiles of sodium atom obtained from the model. At the time of this work, it was assumed that absolute sodium atom concentrations in the flame were not necessary. It was viewed that what was more important than absolute concentrations was the trends in the profiles and how they were affected by changes in the flame; namely changes in equivalence ratio and chlorine loading. However, in hindsight, a more thorough analysis of the results showed that while the changes in trends observed in sodium mole fraction profiles may have been in the right "direction", the assumptions made in achieving those results were flawed. Indeed, the raw absorption data would have been better utilized and the conclusions drawn would have been more emphatic had the data been directly converted to absolute sodium atom concentrations.

The comparison of relative mole fraction of sodium atom from the experimental data with absolute mole fractions from the model will be presented in the following sections as a coarse, initial attempt at examining

the how the fate of sodium (as depicted by the trends observed) is affected by changes in equivalence ratio and chlorine loading.

A discussion of the flawed assumptions made during the course of this study regarding Beer's law as well as a comprehensive discussion of how absolute sodium atom concentrations in the flame can be extracted from experimental absorbance data is presented in chapter 8. Additional plots of absorbance versus HAB will also be presented since experimental data and modeling results that are presented on the same graph (with different axes) may serve to confuse rather than enlighten.

During the course of this work, relative sodium concentration profiles were obtained experimentally via manipulation of the atomic absorption profiles. The data collection method was discussed in section 4.2.3. The experimentally determined absorbance, A, was related to the concentration of the absorbing species (i.e. sodium atom) through Beer's Law in the following manner (50):

$$A = abc \tag{6.4}$$

where a is the proportionality constant called the absorptivity; b is the path length through the flame; and c is the concentration of sodium atom in the flame. For the purposes of this study, the absorptivity and the path length were considered constant. Therefore,

$$A \propto c \tag{6.5}$$

According to the ideal gas law,

$$c = \left(\frac{P}{RT}\right) \cdot y \tag{6.6}$$

where y is defined as the species mole fraction; R is the ideal gas constant; P is the total system pressure; T is the temperature. Since the total system pressure, P and R are constant, the concentration may be rewritten in the following manner:

$$c \propto \frac{y}{T} \tag{6.7}$$

Therefore, the mole fraction, y, of sodium species can be found by the following relationship:

$$y \propto A \cdot T \tag{6.8}$$

For the purposes of this study, the relative mole fraction of sodium in the flame is determined from the product of absorbance measurements and the

corresponding radiation-corrected temperature. The shape and maxima of the experimentally determined *relative* sodium mole fractions are then compared to the *absolute* sodium mole fractions found from execution of the model.

6.6.2 Trends Observed From Experimental Data

Figure 6.26 shows how the experimental sodium absorption profiles (relative mole fraction) vary with equivalence ratio.

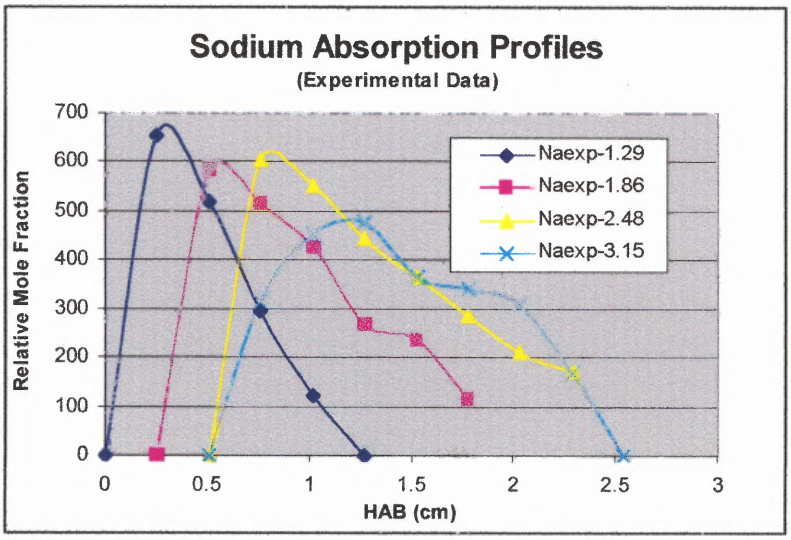

Figure 6.22 Comparison of Experimental Sodium Absorption Profiles for CH_4/Air/Na Flames, ϕ=1.29, 1.86, 2.48, and 3.15

It should be noted that for all ϕ except ϕ=1.29, the sodium profiles start at HAB>0. Quite simply, sodium was undetectable at lower HAB for all other equivalence ratios (i.e., the signal dip due to absorption by sodium atoms was *smaller* than the signal noise). These HAB>0 are consistent with the

approximate HAB of the small, blue, innermost cores still apparent in the sodium flames pictured in Figure 6.2

Observations

1. From the above graph (figure 6.26), it is clear that maximum absorbance, and hence maximum production of sodium atoms, increases with decreasing ϕ. From an experimental viewpoint, when collecting data at lower equivalence ratios (e.g., ϕ=1.29), the drop in optical transmission due to absorbance by sodium atoms was sharp. This was in spite of the fact that the flame was very small and data was difficult to collect in general. In contrast, the drop in transmission produced by sodium absorption for higher equivalence ratios (e.g., ϕ=3.15) appeared less sharp.
2. The location of maximum absorbance for each equivalence ratio increased with increasing ϕ. (i.e., shifted to higher HAB).
3. The shape of the absorption profiles followed the overall shape of the flame, for a given equivalence ratio. For example, at ϕ=1.29, the flame as well the absorption profile was narrow and sharp. However, for ϕ=3.15, the shape of the absorption profile and flame was broad and flatter.

6.6.3 Comparison of Modeling Results with Experimental Data for Sodium Absorption Profiles

Figures 6.27–6.30 depict how the modeling results compare with the experimental data for ϕ=1.29, 1.86, 2.48 and 3.15, respectively. Note that the left and right y axes, respectively, on all four graphs are on the same scale.

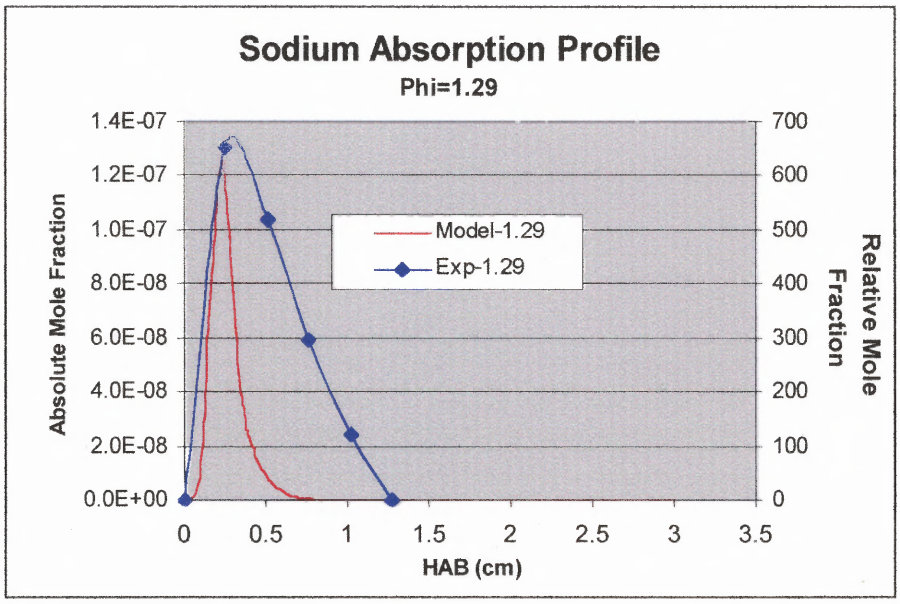

Figure 6.23 Comparison of Experimental and Modeling Results of Sodium Absorption Profiles for a CH_4/Air/Na Flame for ϕ=1.29

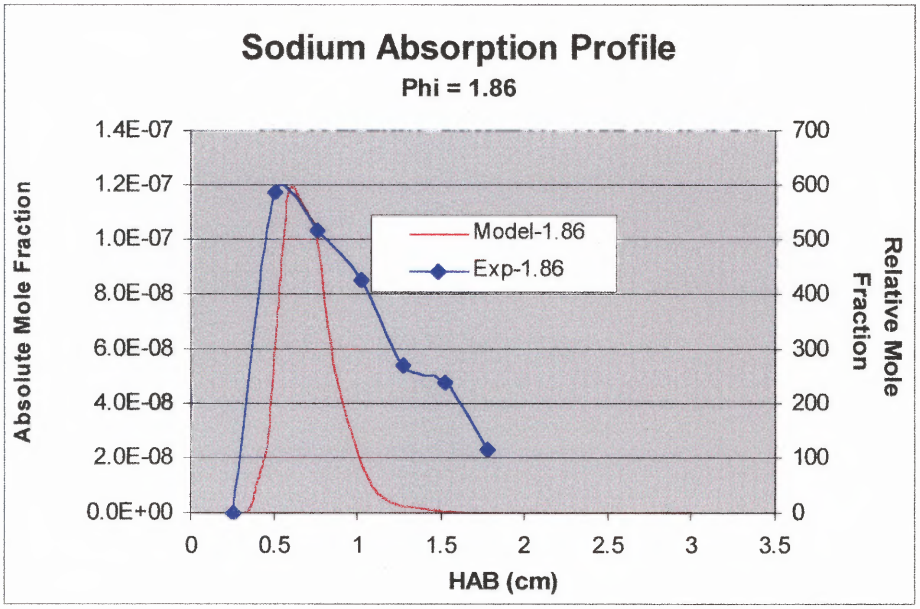

Figure 6.24 Comparison of Experimental and Modeling Results of Sodium Absorption Profiles for a CH_4/Air/Na Flame for ϕ=1.86

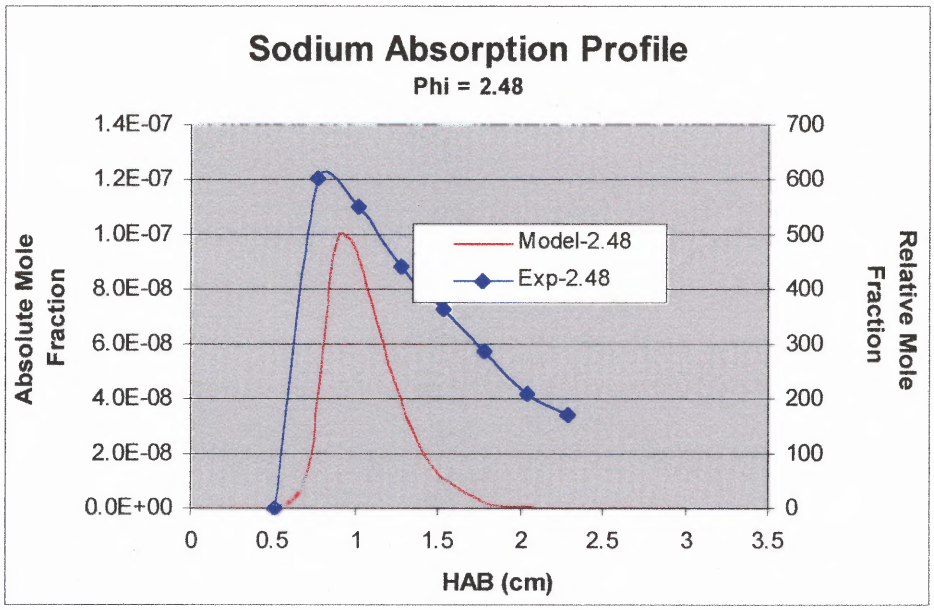

Figure 6.25 Comparison of Experimental and Modeling Results of Sodium Absorption Profiles for a CH_4/Air/Na Flame for ϕ=2.48

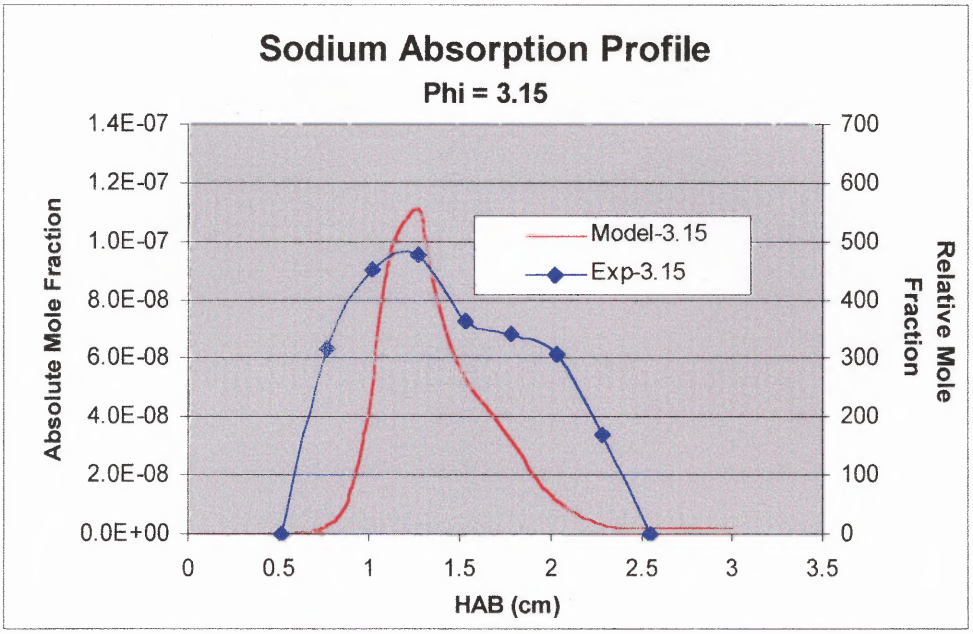

Figure 6.26 Comparison of Experimental and Modeling Results of Sodium Absorption Profiles for a CH_4/Air/Na Flame for ϕ=3.15

In general, the agreement is good, especially the HAB location of maxima, between the experimental data and the modeling. The following modeling results mirrored the experimental trends:

Observations

1. As with the experimental data, the modeling results also generally show that maximum sodium mole fraction increases with decreasing equivalence ratio.
2. The location of maximum sodium mole fraction increases in HAB as equivalence ratio increases.
3. The shape of the mole fraction profiles got broader with increasing ϕ.

CHAPTER 7

EFFECTS OF CHLORINE ADDITION TO METHANE/AIR AND METHANE/AIR/SODIUM FLAMES

7.1 Introduction

Chapter 6 discussed the experimental and modeling results of methane/air flames when compared to methane/air flames doped with sodium. This chapter will take the investigation of these flames once step further by examining the effects of chlorine addition.

Most of the discussion in this chapter regarding the effects of chlorine addition to methane/air and methane/air/sodium flames will be based primarily on experimental data. Modeling results will be presented for the methane/air/chlorine flames. However, it was found that our modified CHEMKIN flame code was not robust enough numerically to generate a converged solution to the methane/air/sodium/chlorine flames. There will be a discussion of the modifications made to the code in addition to the partial results obtained for this particular flame, as well as possible improvements that could be made in an effort to reach a solution.

Chlorine was introduced to the methane/air and methane/air/sodium flames in the form of methyl chloride (CH_3Cl). The actual amount of methyl chloride introduced to each flame was measured as a feed molar ratio (R) of methyl chloride to methane. For any given equivalence ratio, the air flow rate

was kept constant. The methane flow rate was then decreased as the methyl chloride flow rate was increased. The flow rates were chosen so as to keep the total unburned gas flow rate nearly constant. The ratio, R, varied from 0.0 to 0.31.

The following table gives a brief overview of the type of data as well as the type of flames that will be discussed in this chapter:

Table 7.1 Outline of Experimental and Modeling Analysis of CH_4/Air/CH_3Cl and CH_4/Air/CH_3Cl/Na Flames by this Study

ϕ	R	CH_4/CH_3Cl/Air Flames				CH_4/CH_3Cl/Air/Sodium Flames			
		Experimental			Model	Experimental			Model
		Temp	Abs.	G.C.		Temp	Abs.	G.C.	
1.29	0					√	√		
	0.05					√	√		
	0.1					√	√		
	0.2					√	√		
	0.31					√	√		
1.86	0.0	√		√	√	√	√	√	
	0.07	√		√		√	√	√	
	0.11	√		√	√	√	√	√	
	0.16	√		√		√	√	√	
	0.2	√		√	√	√	√	√	
2.48	0.0	√				√	√		
	0.06	√				√	√		
	0.1	√				√	√		
3.15	0.0	√				√	√		
	0.05	√				√	√		

7.2 Physical Appearance of the Flame

As discussed in Chapter 6, the physical size of the flame including the inner core, increased with an increase in equivalence ratio. This was true for all flame types. It is hypothesized that this increase in flame size is due to a decrease in flame speed according to Equation 6.1. This chapter will explore the change in flame characteristics due to addition of chlorine, for both methane/air and methane/air/sodium flames.

7.2.1 Methane/Air Flames

Figures 7.1—7.4 depicts how the appearance of the flame varies for a given ϕ, as the CH_3Cl/CH_4 ratio in the flame is altered. As previously stated in chapter 6, all photographs were taken with a camera placed at a fixed distance away from the burner while the fuel and/or air flow rates were manipulated.

Observations:

1. As the ratio (R) of CH_3Cl to CH_4 is increased, the color of the inner core is intensified. This is most evident for ϕ=1.29 and 1.86 where the color of the inner core becomes more opaque and changes from blue to a lighter blue-green.
2. The physical dimensions of this slotted methane/air flame do not exhibit any radical change due to the addition of chlorine. For ϕ=1.29 (R= 0, 0.1

and 0.31) and 1.86 (R= 0, 0.1 and 0.2) the size of the flame increases slightly. However this is not evident for ϕ=2.48 and 3.15. This is most likely due to the low chlorine content (e.g., R=0.05) used in these flames.

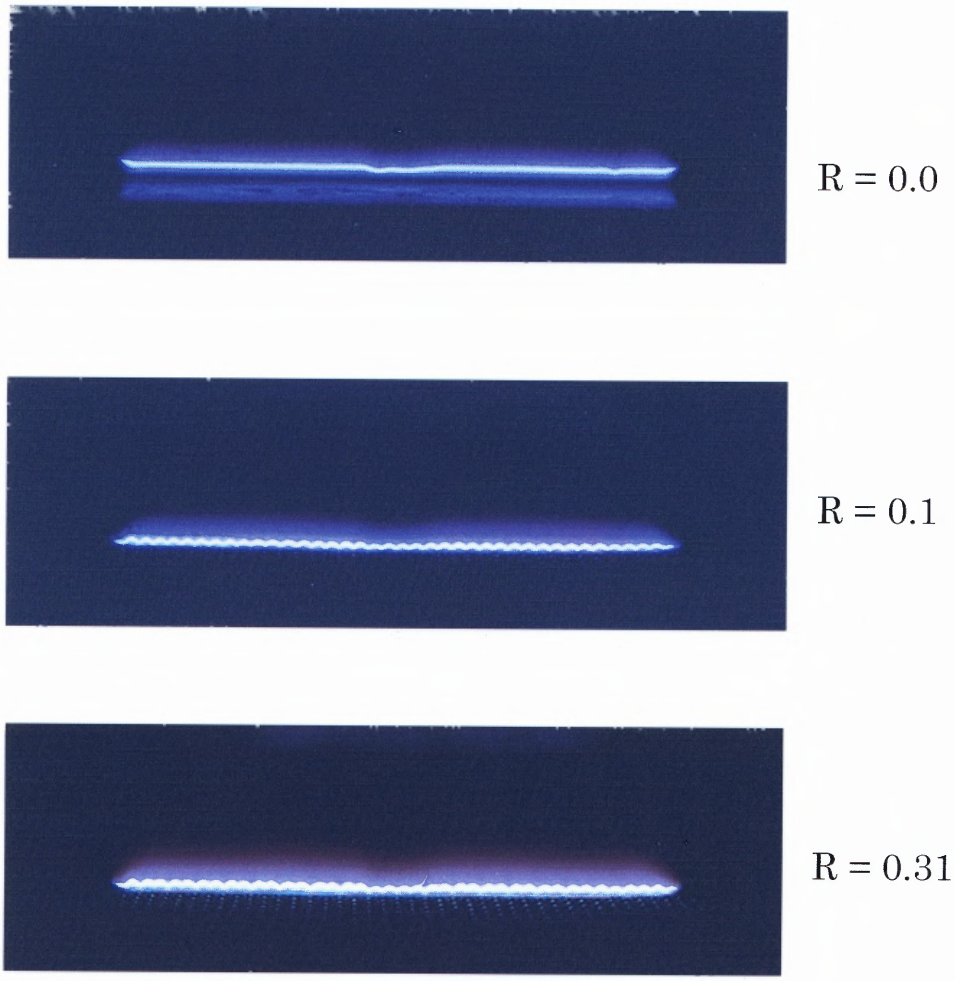

Figure 7.1 CH_4/Air/CH_3Cl Flames, ϕ=1.29

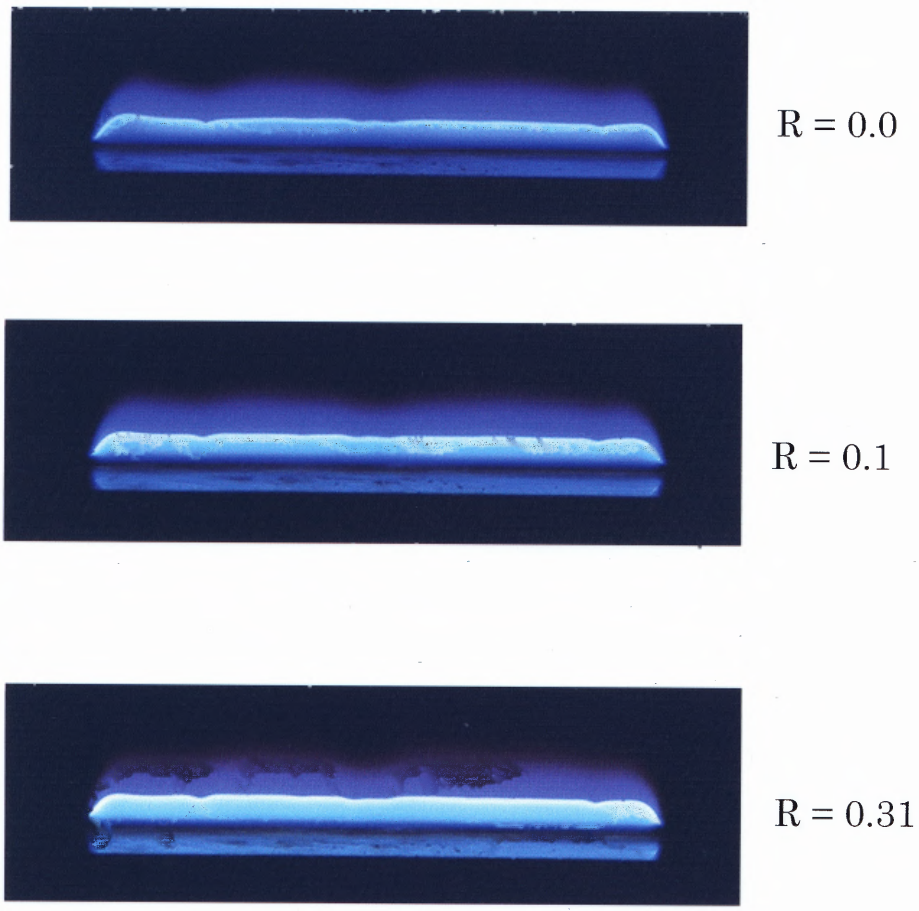

Figure 7.2 CH_4/Air/CH_3Cl Flames, ϕ=1.86

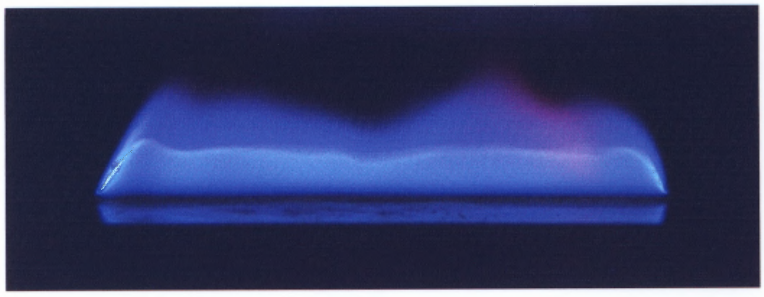

R = 0.0

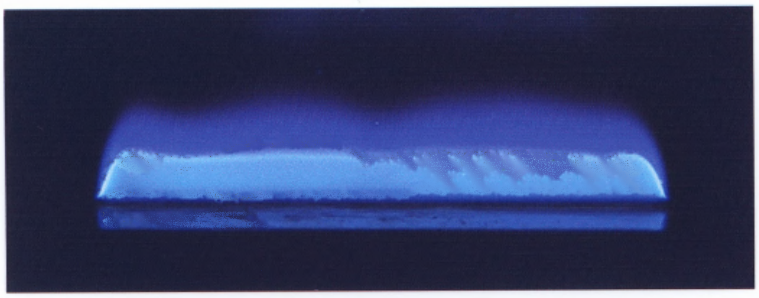

R = 0.1

Figure 7.3 CH_4/Air/CH_3Cl Flames, ϕ=2.48

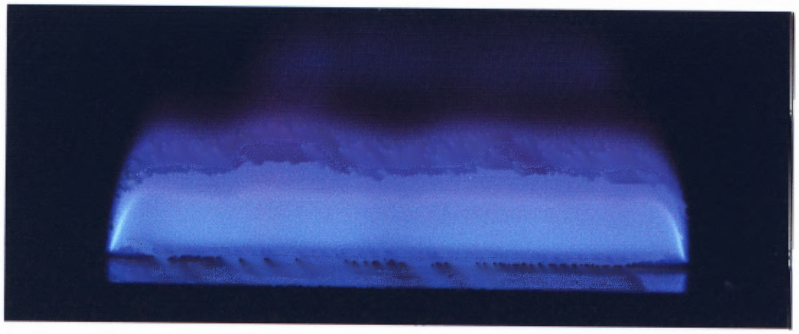

R = 0.0

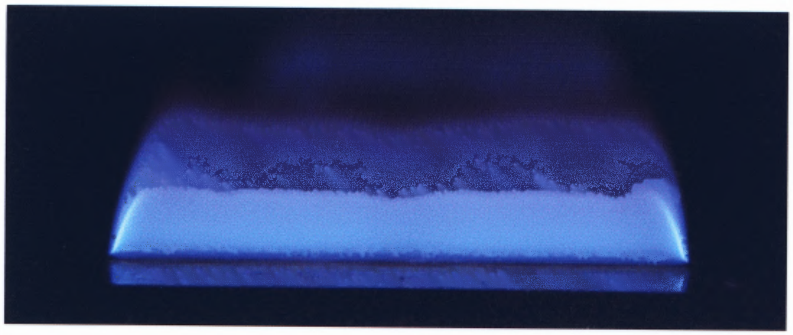

R = 0.05

Figure 7.4 CH_4/Air/CH_3Cl Flames, ϕ=3.15

Hypotheses:

1. As the equivalence ratio is increased from 1.29 to 3.15, the size of the inner core also increases. This increase in flame height, h, corresponds to a decrease in flame speed, S_u. It should be noted however, that a change in flame height is not observed within a given ϕ due to a change in chlorine content.
2. The greenish shift of the blue methane/air flames as R increases could be due to the presence of C_2 (carbon radical dimer) radical (60, 66). It emits a series of molecular bands called the Swan Spectroscopic System. The enhancement of C_2 and other di-carbon and higher species is a likely consequence of the H abstraction capability of the Cl atom (45) and the subsequent formation of carbon-carbon bonds.

7.2.2 Methane/Air/Sodium Flames

Figures 7.5—7.8 illustrates the changes in color as well as size for methane/air/sodium flames that contain varying amounts of chlorine.

Observations:

1. As with the methane/air flame, the color of the inner core changes with the addition of chlorine. As R is increased, the intensity of the blue-green color observed in the inner core also increases. This is more obvious in the sodium flame compared to the non-sodium flame because the appearance

of the blue-green inner core coincides with the disappearance of the pink inner core (due to the presence of sodium).

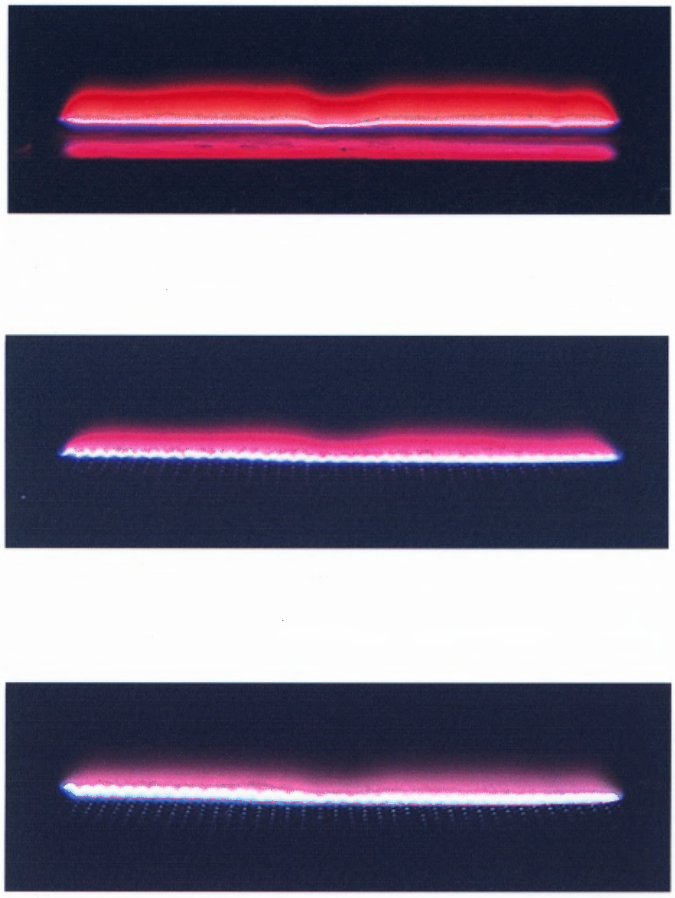

Figure 7.5 CH_4/Air/CH_3Cl/Na Flames, ϕ=1.29

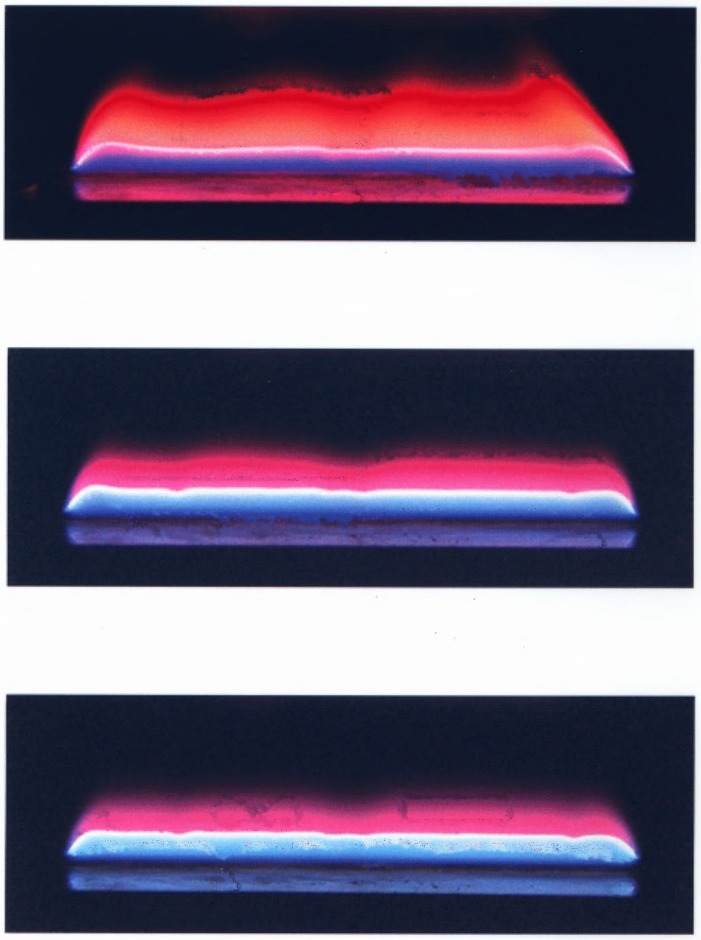

Figure 7.6 CH_4/Air/CH_3Cl/Na Flames, ϕ=1.86

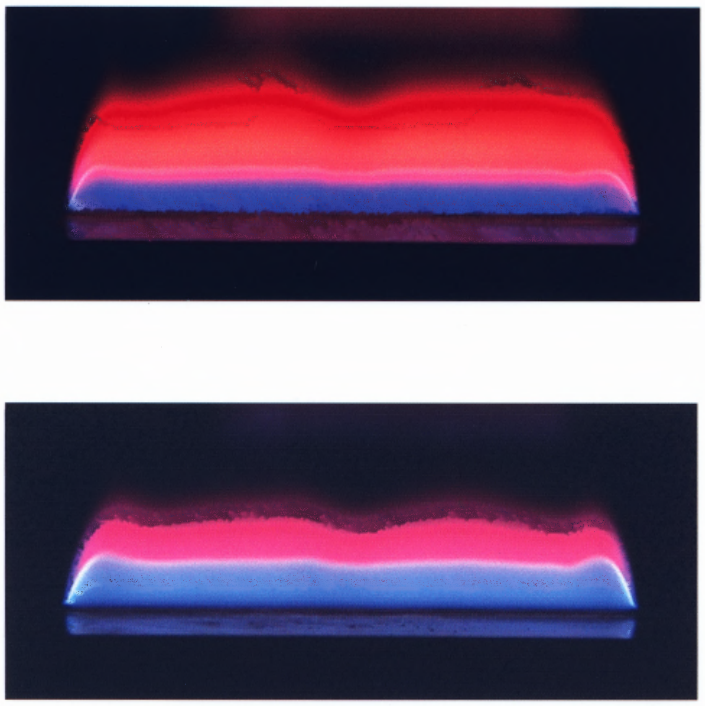

Figure 7.7 CH_4/Air/CH_3Cl/Na Flames, ϕ=2.48

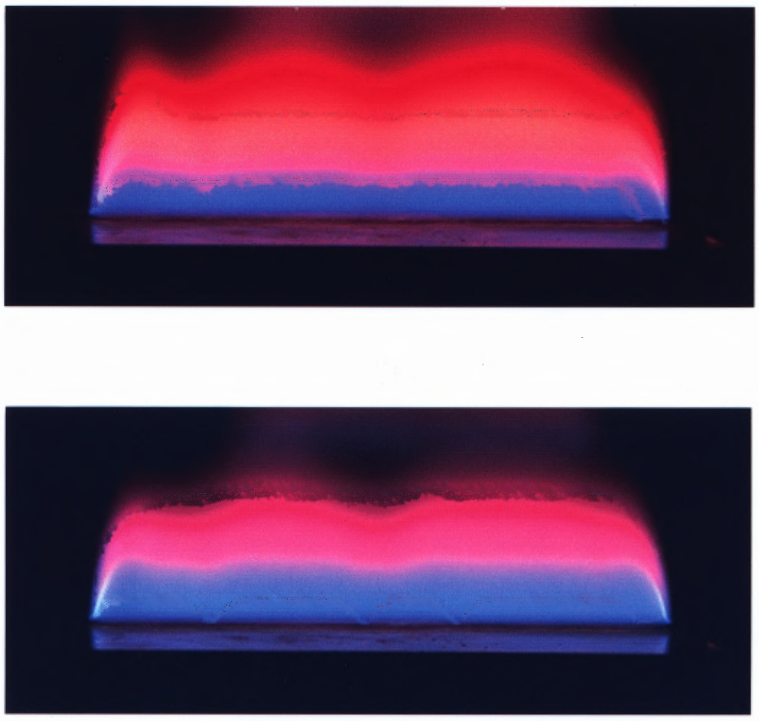

Figure 7.8 CH_4/Air/CH_3Cl/Na Flames, ϕ=3.15

2. Conversely, as the chlorine content in the flame increased (i.e., R increases), the orange color in the outer mantle (a by-product of the combustion of sodium) *decreased* in intensity.
3. For any given ϕ, the size of the outer mantle *decreased* as R increased. As the CH_3Cl/ CH_4 ratio was increased, the flame became "tighter" and "neater". This change in flame size is quite evident for all ϕ.

Hypotheses:

1. The increase in intensity of the blue-green inner core as R is increased is possibly due to the increased production of C_2 radical (60,66).
2. The decrease in the orange color of the outer mantle may be due to a reduction in *net* sodium atom production (i.e., a reduction in intensity of orange flame color) as a result of sodium/chlorine combination reactions (discussed later in this chapter).
3. As observed with all of the flames (i.e. CH_4/Air, CH_4/Air/Na, CH_4/Air/CH_3Cl, CH_4/Air/CH_3Cl/Na), as the equivalence ratio is increased, the size of the inner core also increases. This leads to the hypothesis that the flame speed decreases as ϕ increases, even when sodium and chlorine are added to a CH_4/Air flame.

7.3 Temperature Profiles

7.3.1 Methane/Methyl Chloride/Air Temperature Profiles

Figures 7.9, 7.10 and 7.11 depict the temperature profiles for methane/methyl chloride/air flames of varying R values for ϕ = 1.86, 2.48 and 3.15, respectively (temperature profiles for flames without sodium were not available for ϕ=1.29).

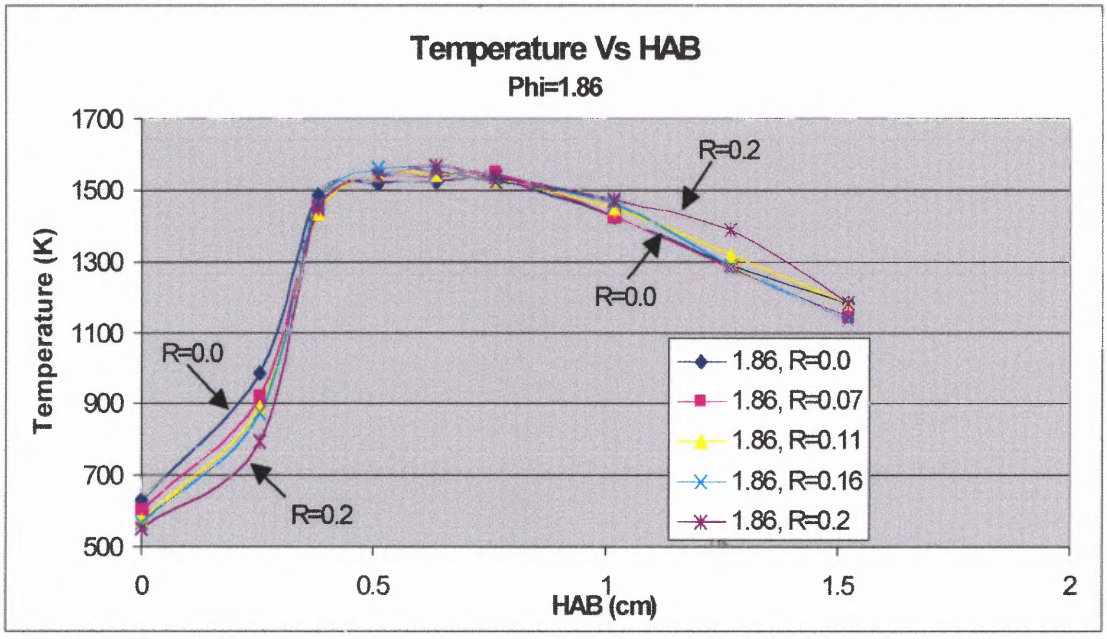

Figure 7.9 Experimental Temperature Profile of CH_4/Air/CH_3Cl Flames, ϕ=1.86

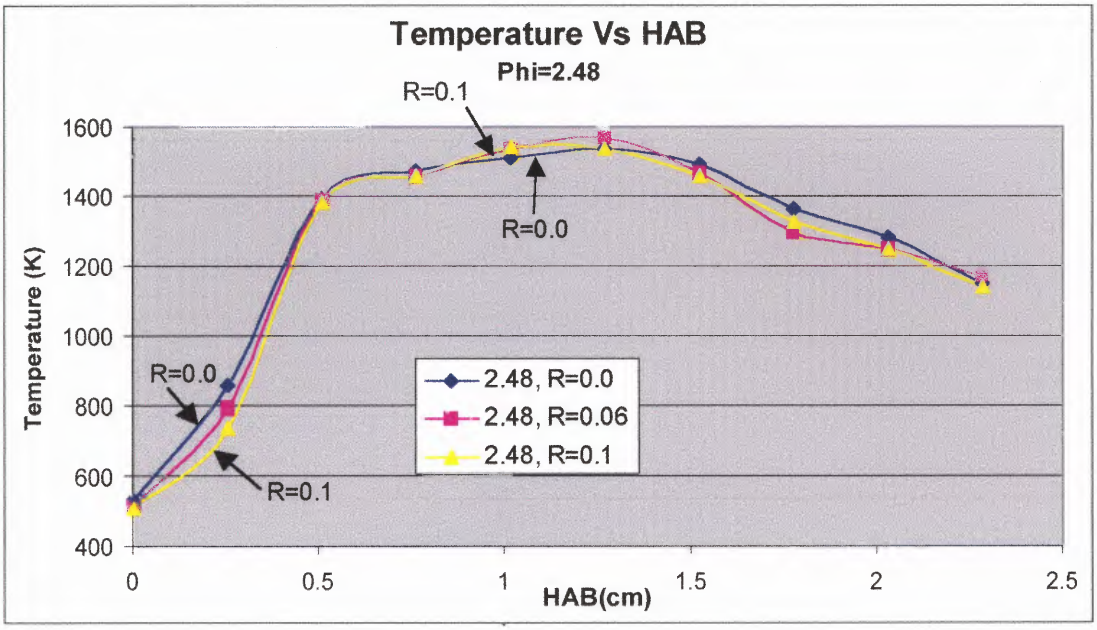

Figure 7.10 Experimental Temperature Profile of CH_4/Air/CH_3Cl Flames, ϕ=2.48

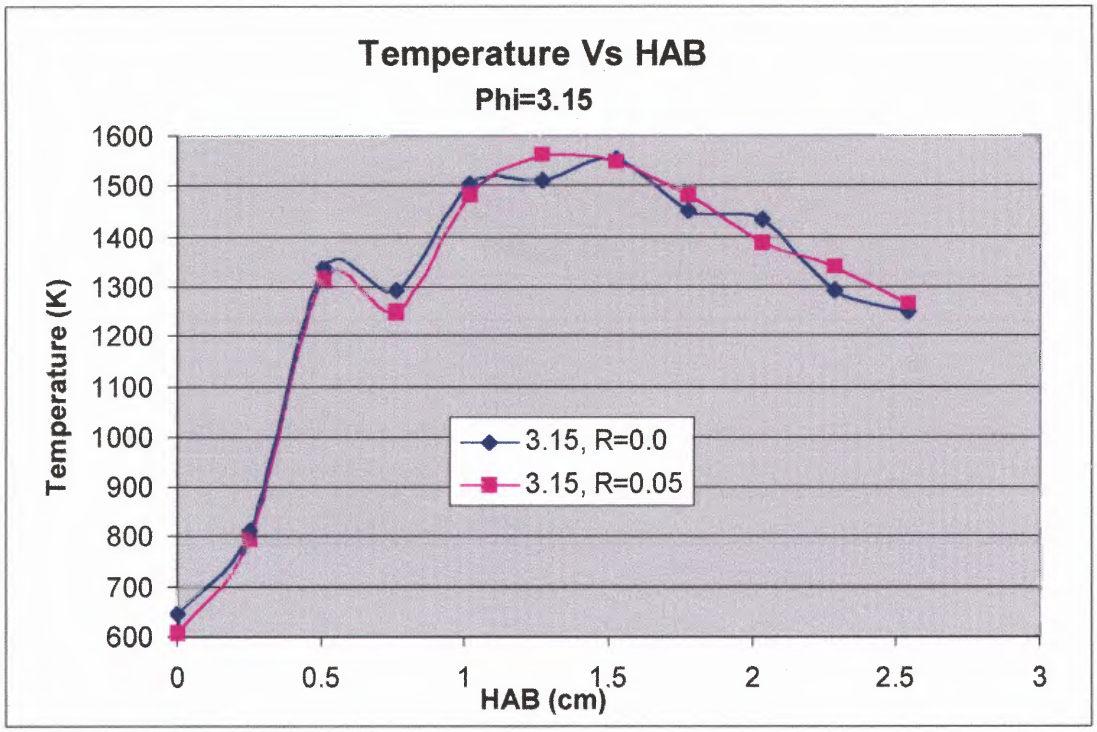

Figure 7.11 Experimental Temperature Profile of CH_4/Air/CH_3Cl Flames, ϕ=3.15

Observations:

1. As discussed in chapter 6, as ϕ increased, the physical dimensions of the flame increased. As a result, the HAB location of the maximum temperature also increased. For methane/air flames that had been doped with chlorine, as R increased from 0.0 to 0.2, the size of the flame also slightly increased. However, the slight change in physical dimension resulting from the chlorine addition did not result in any change in the location of maximum temperature.
2. A dip in the ϕ=3.15 temperature profile at approximately 0.8 cm HAB was observed. At this time, it is unclear whether or not this dip is real. There will be further comment on this dip in section 7.3.2.

Hypotheses:

The observation that the location of maximum temperature does not change as the chlorine content changes may be due to the fact that the relative amounts of chlorine added were not significant enough. However, another explanation involves the assumed relationship of laminar flame speed and air entrainment for this flame. The slight increase in flame height as the chlorine content rises suggests a slightly lower flame speed (eq. 6.1). It is possible that a slightly slower flame experiences less transport of air (O_2) from the surroundings. The literature flames (47,51) were flat flames shrouded from any air entrainment. As less air enters, less dilution occurs

from the air nitrogen. The hotter gases lose heat at a greater rate by heat transfer to the burner.

7.3.2 Methane/Methyl Chloride/Sodium/Air Temperature Profiles

This section will discuss the effects of chlorine addition on the temperature profiles of a methane/air flame that has been doped with sodium. Figures 7.12-7.15 illustrate the temperature profiles for ϕ= 1.29, 1.84, 2.48, and 3.15, respectively.

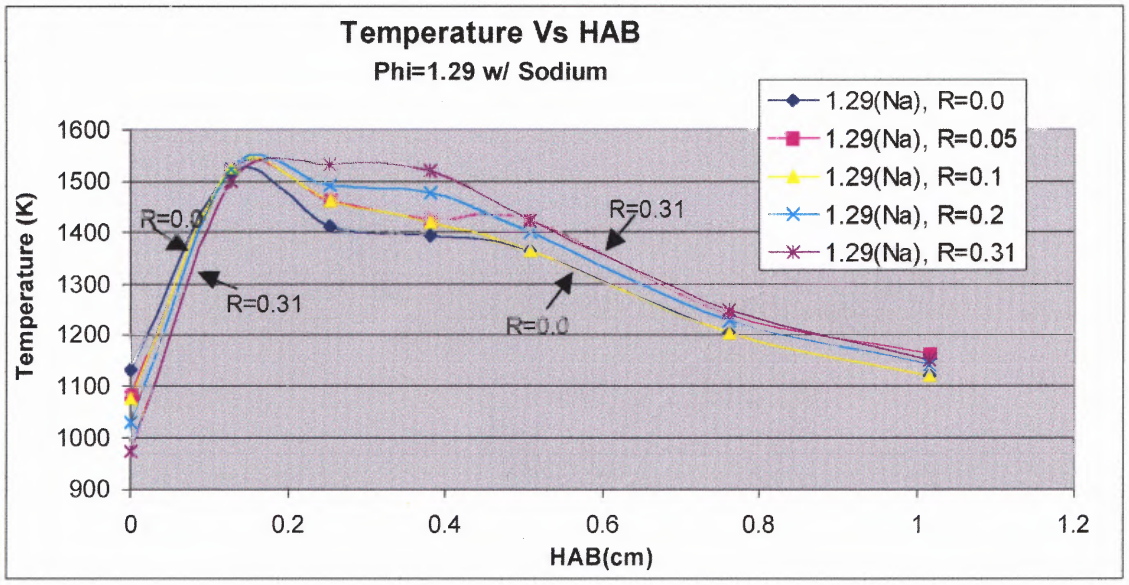

Figure 7.12 Experimental Temperature Profiles of CH_4/Air/CH_3Cl/Na Flames, ϕ=1.29

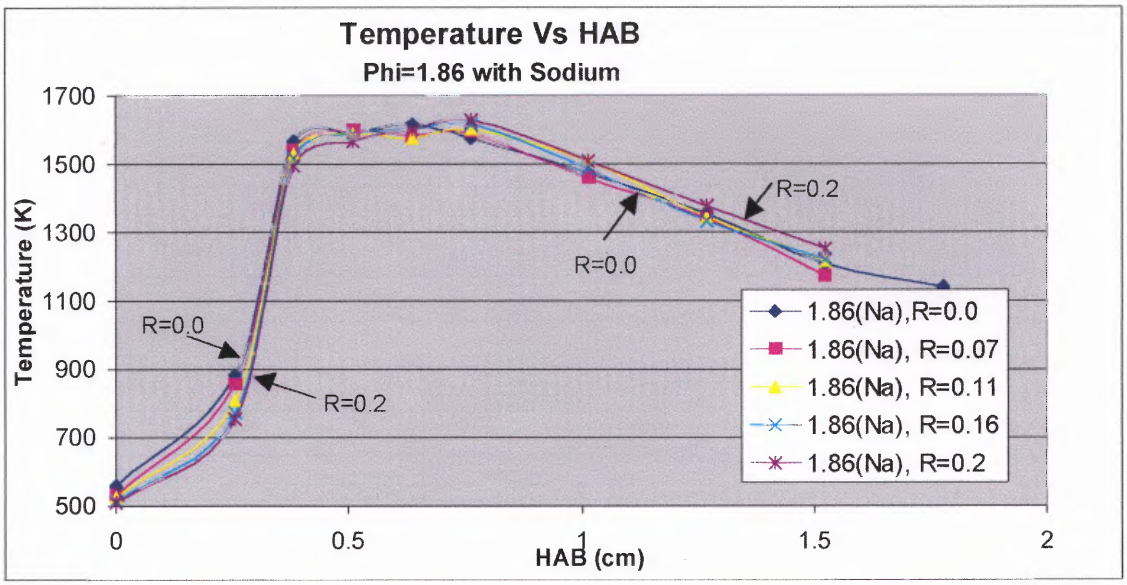

Figure 7.13 Experimental Temperature Profiles of CH_4/Air/CH_3Cl/Na Flames, ϕ=1.86

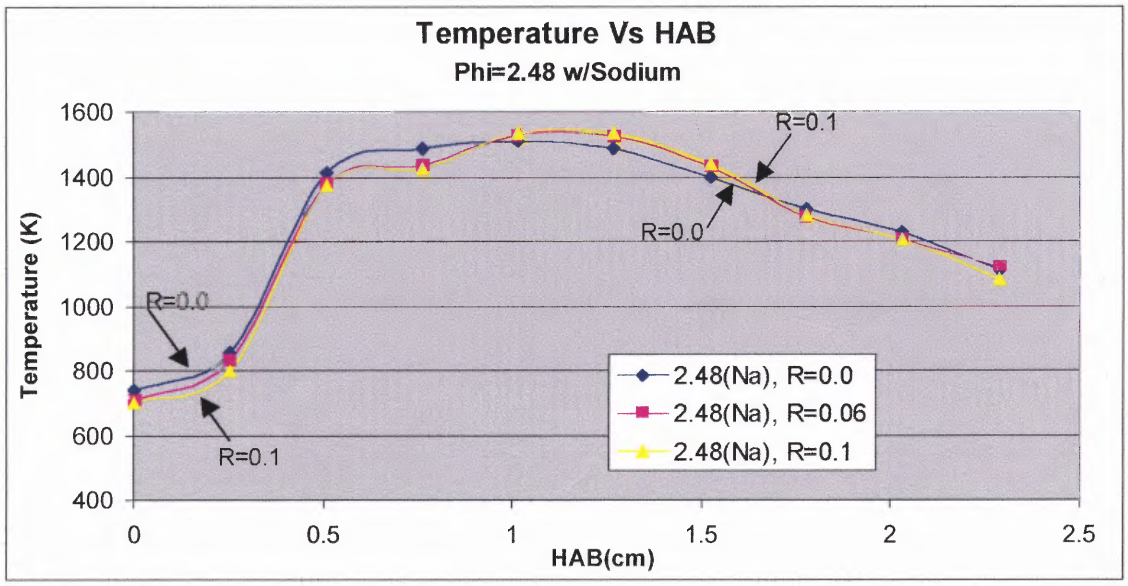

Figure 7.14 Experimental Temperature Profiles of CH_4/Air/CH_3Cl/Na Flames, ϕ=2.48

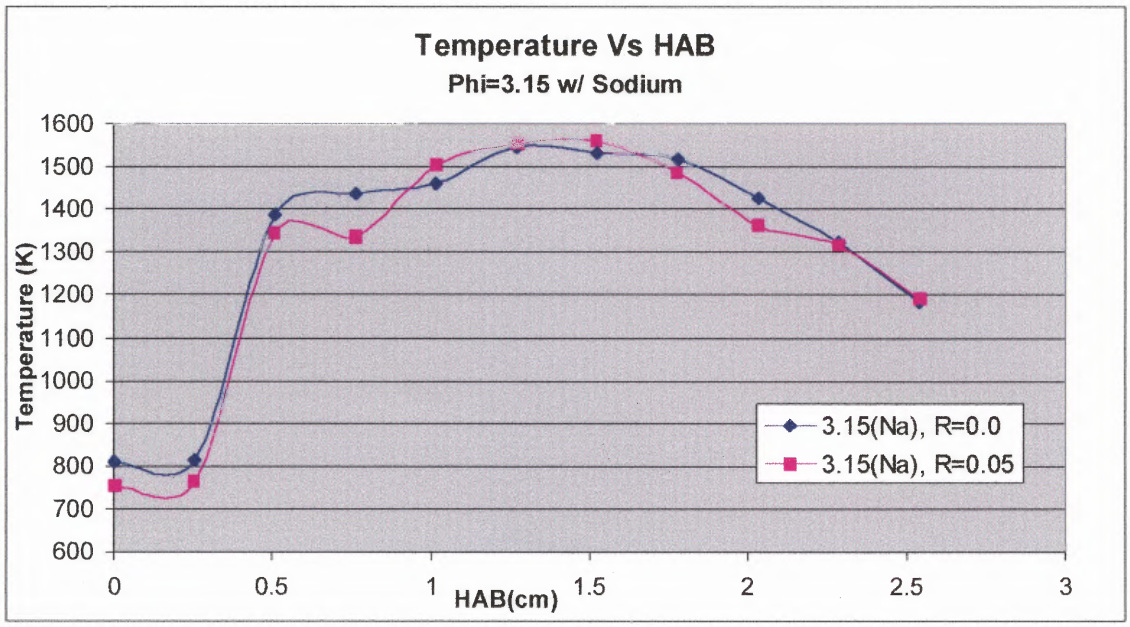

Figure 7.15 Experimental Temperature Profiles of CH_4/Air/CH_3Cl/Na Flames, ϕ=3.15

Observations:

When chlorine was introduced to a methane/air flame of a particular equivalence ratio doped with sodium, there was an obvious reduction in the physical size of the outer cone of the flame (Figure 7.5-7.8). It was illustrated in Chapter 6 that when the physical dimensions of the flame changed due to a change in equivalence ratio, the location of the maximum temperature in the flame shifted e.g., when the flame size *decreased*, the maximum temperature for that flame was found at a *lower* HAB. However, these figures show that a change in physical dimension of the flame *does not* cause a shift in the location of maximum temperature.

Hypotheses:

1. A dip in the temperature profile for ϕ=3.15 was once again observed. However, examination of the raw data does not determine whether this is real or anomalous. Therefore, in the absence of corroborating proof that this is indeed real, it will be assumed that the dip in the ϕ=3.15 temperature profile is an anomaly.
2. Even though the size of the outer mantle decreased with increase in chlorine content, the size of the inner core (i.e., the location of the primary reaction zone) remained relatively unchanged. As a result, since the location of the primary reaction zone remained relatively unchanged with a change in chlorine content, then so too did the HAB location of maximum temperature.

7.4 Sodium Absorption Profiles

Preliminary sodium absorption profiles for methane/air flames (without chlorine) have already been presented in chapter 6. It was observed that the maximum sodium absorbance shifted to higher HAB as ϕ increased. Also, the maximum sodium absorbance appeared to *decrease* with *increasing* ϕ. This section will discuss how those profiles were affected by the addition of chlorine. The fuel-rich equivalence ratios of interest are 1.29, 1.86, 2.48 and 3.15.

It should be noted once again (as discussed in chapter 6) that the trends observed in this study regarding the fate of sodium in these flames may be critically viewed as a coarse, initial investigation. A more developed and comprehensive examination of absorbance measurements and sodium concentration profiles will be presented in chapter 8. Caution should be taken in noting that it is the derivation of the relative mole fraction parameter that is based on incorrect assumptions. The absorbance versus HAB profiles are valid.

7.4.1 Background

It was shown in Figure 6.3 that the methane/air flame increased in size and changed color from blue to orange when sodium was added to the flame. It was also shown that when chlorine was added to this methane/air flame doped with sodium, that the orange color disappeared and the flame began to decrease in size. This information is critical background material when attempting to explain how the amounts of chlorine added to the sodium-doped flames were chosen for different equivalence ratios.

An experiment was performed on a methane/air flame doped with sodium (ϕ=2.48) in order to determine what was the maximum amount of chlorine (i.e., the upper limit) and the minimum amount of chlorine (i.e., the lower limit) that could be added to the sodium-doped methane/air flames. These upper and lower limits would become the minimum and maximum R

values used in this portion of the study. In general, the minimum R value usually corresponded to the lowest flow rate that could be measured on the CH_3Cl rotameter. The maximum R value usually corresponded to the greatest amount of CH_3Cl that could be added to the flame and still observe an absorbance due to the sodium atoms.

A "first guess" value of R=0.2 was chosen and the following observations were made:

1. As soon as the chlorine was introduced to the flame, the bright orange color, due to the presence of sodium, disappeared almost completely.
2. A blue-green color was observed in the flame, possibly due to increased levels of C_2 radical (60).
3. The flame got physically smaller (resembling a less fuel-rich flame).
4. The attenuation of transmitted light at 589 nm by the sodium atoms that had been previously observed in the sodium doped methane/air flame was completely gone (i.e. no absorbance).

The R value was then lowered until a reliable non-zero absorbance (i.e., where the signal attenuation was at least double the signal/noise) was observed. For ϕ=2.48, the upper limit CH_3Cl/CH_4 ratio was determined to be R=0.11. However, even at this small R value the absorbance decreased by 71%.

Similar experiments were performed on the other equivalence ratios of interest (i.e., what was the most chlorine that could be added to that

particular flame and still see attenuation due to the presence of sodium atoms). Then, incremental R values were chosen between R=0.0 and R= upper limit. In some cases, the actual incremental value of R was limited by the rotameter setting. Table 7.2 summarizes these results.

Table 7.2 Summary of CH_3Cl/CH_4 Ratios

Phi	CH_3Cl/CH_4 Ratios (R)
1.29	0.0, 0.05, 0.1, 0.2, 0.31
1.86	0.0, 0.07, 0.1, 0.16, 0.2
2.48	0.0, 0.06, 0.1,
3.15	0.0, 0.05

For ϕ=1.29, the flame appeared to be very "robust" in that the size of the signal attenuation could withstand the introduction of (relatively) large amounts of chlorine (i.e., larger R values). This suggests that, at ϕ=1.29, many sodium atoms were being produced. However, for ϕ=3.15, the slightest amount of chlorine (i.e., very small R) introduced into the flame caused a significant decrease in the absorbance. This then leads to the contrasting hypothesis that for ϕ=3.15, the flame was producing few net sodium atoms. It should be noted in all experiments, the sodium nitrate solution feed rate to the flame was constant.

7.4.2 Absorbance Profiles

Figures 7.16-7.19 depict how sodium absorbance profiles change when chlorine is added to a methane/air flame that has been doped with sodium. Note that all four plots were placed on the same scale in order to facilitate comparisons between the different equivalence ratios.

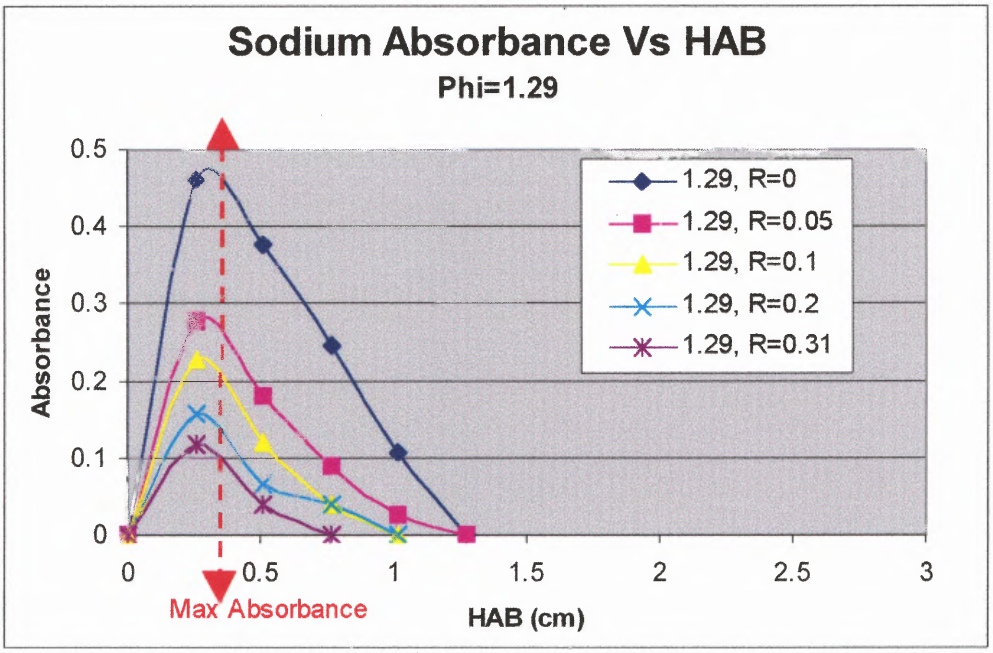

Figure 7.16 Experimental Sodium Absorbance Profiles for CH_4/Air/CH_3Cl/Na Flames, ϕ=1.29

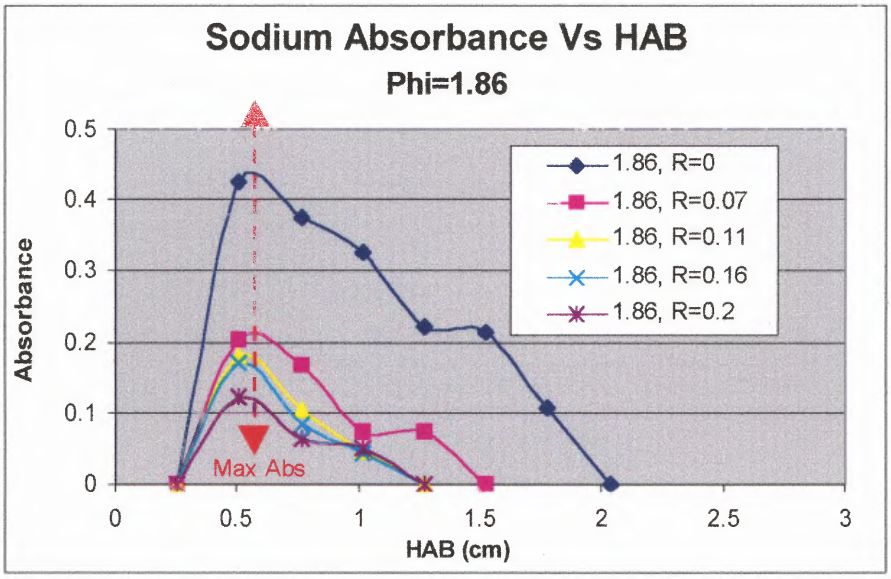

Figure 7.17 Experimental Sodium Absorbance Profiles for CH_4/Air/CH_3Cl/Na Flames, ϕ=1.86

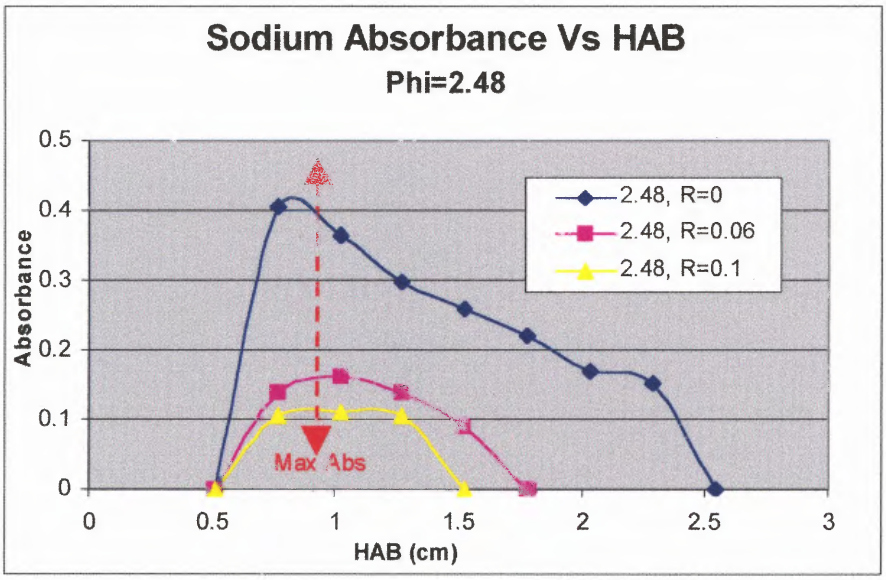

Figure 7.18 Experimental Sodium Absorbance Profiles for CH_4/Air/CH_3Cl/Na Flames, ϕ=2.48

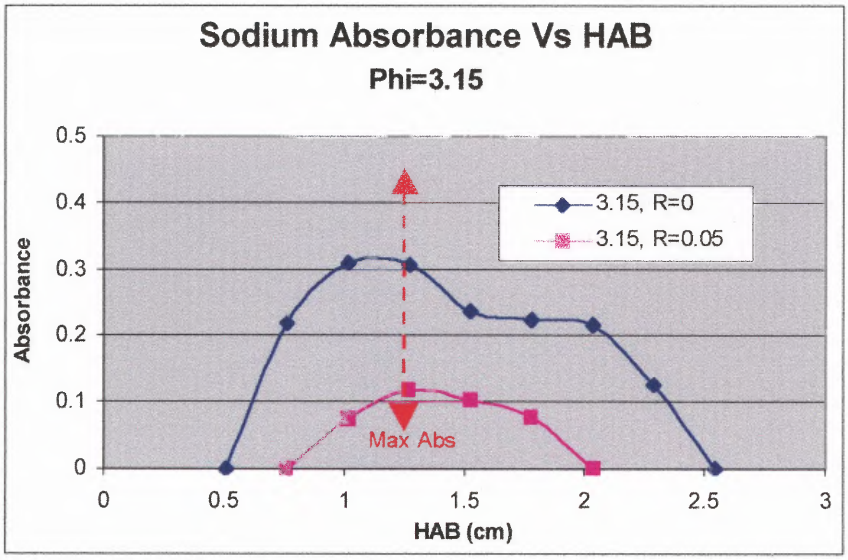

Figure 7.19 Experimental Sodium Absorbance Profiles for CH_4/Air/CH_3Cl/Na Flames, ϕ=3.15

The negative impact of chlorine on the maximum concentration of sodium atoms for any given R value can be seen in Figure 7.20.

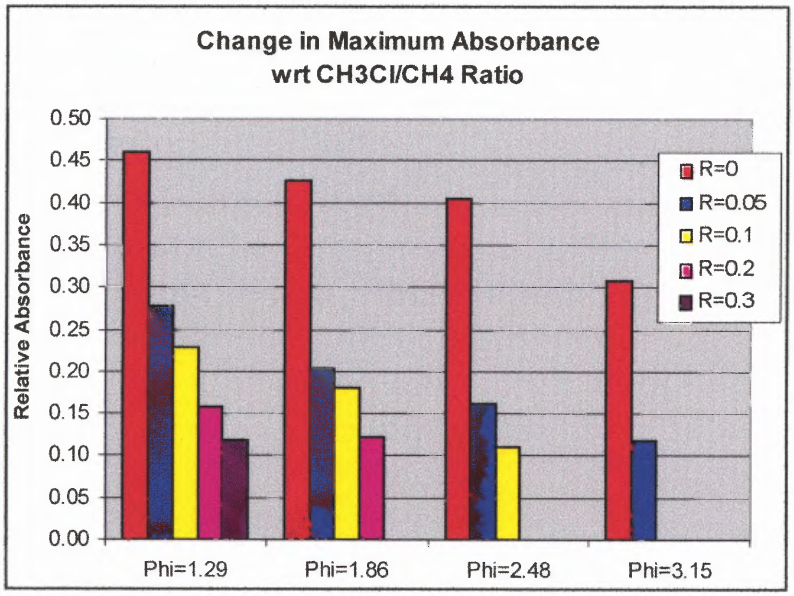

Figure 7.20 Change in Maximum Absorbance With Respect to CH_3Cl/CH_4 Ratio, ϕ=1.29, 1.86, 2.48, and 3.15

Observations:

1. The overall concentration of sodium atoms decreased as the equivalence ratio increased. This is evidenced by a decrease in sodium absorption signal with increasing ϕ.
2. The addition of chlorine had a much more profound effect on the absorbance signals as the equivalence ratios were increased. The maximum absorbance peaks drop as the chlorine content increases. Also, as ϕ increases, the relative drop in absorbance with respect to R is accelerated.
3. The location of maximum absorbance shifts to higher HAB as equivalence ratio was increased.
4. The absorbance signal profiles "broadened" with increase in equivalence ratio. This was expected since the overall size of the flame increased with increase in equivalence ratio.
5. The general location of the locust of points that constitute maximum absorbance has been highlighted. It appears that for any given equivalence ratio, the HAB location of maximum absorbance *did not change* with a change in chlorine content.

Hypothesis:

1. Figure 7.21 depicts how the maximum absorbance signal is affected by chlorine loading, for a given ϕ.

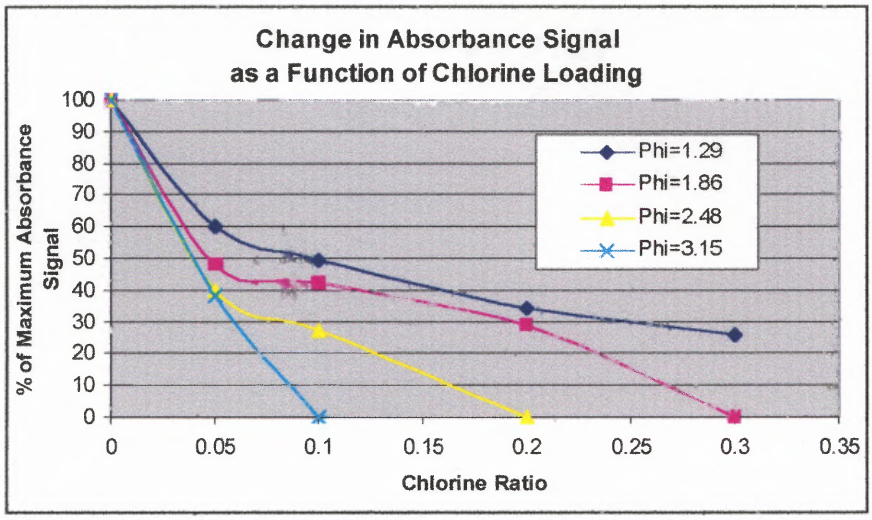

Figure 7.21 Change in Maximum Absorbance Signal as a Function of Chlorine Loading, ϕ=1.29, 1.86, 2.48, and 3.15

It is clear that a chlorine loading of R=0.1 has a much greater impact on a flame where ϕ=3.15 compared to ϕ=1.29. It is hypothesized that any given chlorine loading has an *overall* greater impact on sodium in the flame as the equivalence ratio is increased possibly because the amount of sodium atoms produced is not as great, as the equivalence ratio is increased. A complimentary explanation is that, at higher ϕ, the chlorine is more effective in sodium removal – possibly due to higher concentrations of those chlorine species which remove sodium atom.

2. The amount of chlorine added to a methane/air flame that has been doped with sodium *directly* affects the concentration of sodium atoms in the flame. It appears that, as the chlorine loading is increased, sodium atom levels are decreased (as evidenced by a decrease in sodium absorption

signal). This is possibly due to the combination reactions between sodium and chlorine. These reactions will be discussed in section 7.5.1, Reaction Mechanism Modifications.

3. As outlined in sections 6.3 and 7.3, the location of maximum temperature shifted to higher HAB as the equivalence ratio increased. It was also shown in section 7.4.2 that the location of maximum sodium absorbance shifted to higher HAB as equivalence ratio increased. Figures 7.22 – 7.24, representing a methane/air flame that has been doped with sodium and chlorine (R=0.1), show how the absorbance profiles and temperature profiles are related. Note that data for R=0.1 were not available for ϕ=3.15.

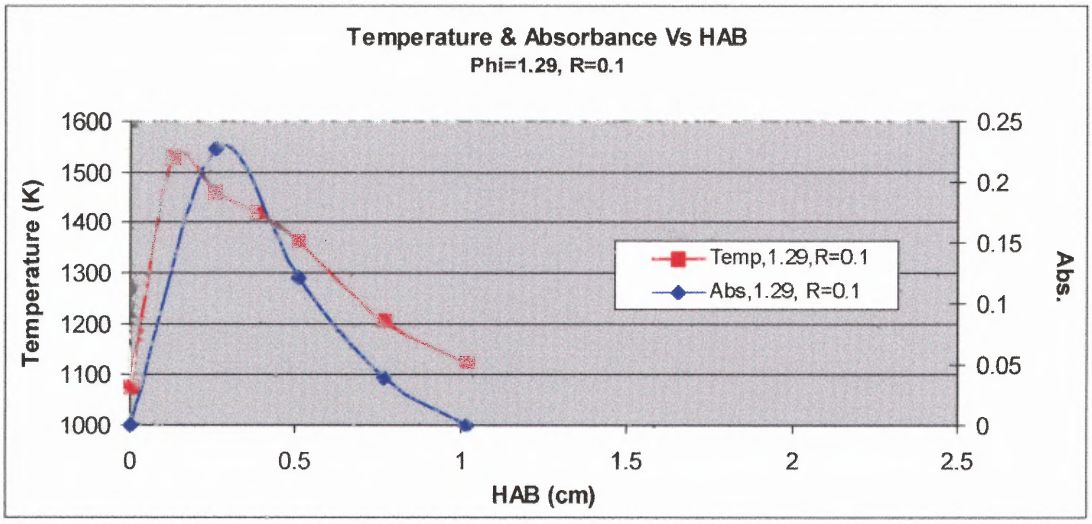

Figure 7.22 Comparison of Experimental Temperature Profiles and Relative Absorbance Profiles for CH_4/Air/CH_3Cl and CH_4/Air/CH_3Cl/Na Flames, ϕ=1.29

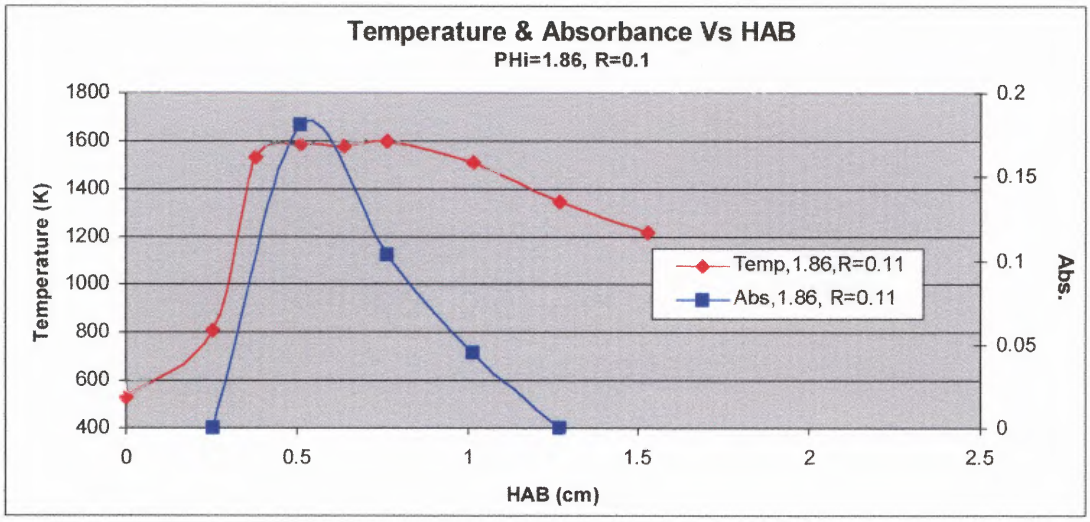

Figure 7.23 Comparison of Experimental Temperature Profiles and Relative Absorbance Profiles for CH_4/Air/CH_3Cl and CH_4/Air/CH_3Cl/Na Flames, ϕ=1.86

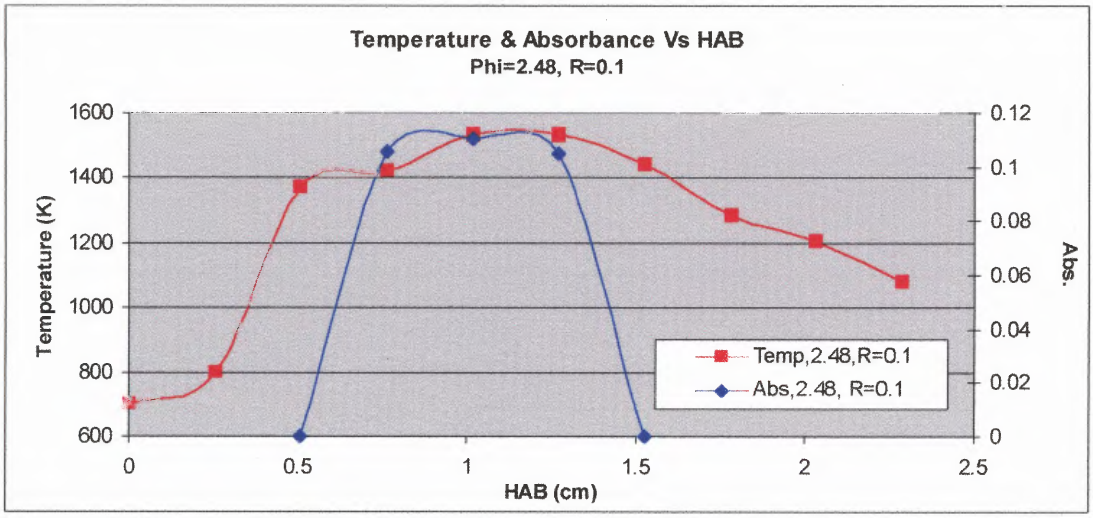

Figure 7.24 Comparison of Experimental Temperature Profiles and Relative Absorbance Profiles for CH_4/Air/CH_3Cl and CH_4/Air/CH_3Cl/Na Flames, ϕ=2.48

It appears that, as ϕ increases, the maximum absorbance shift to higher HAB is synchronous with the maximum temperature shift. This suggests that a change in sodium atom production might be a consequence of a

change in temperature i.e., as opposed to a delayed response due to a chain reaction. As a result, the absorption profiles (and maxima) appear to "follow" the temperature profiles. This is what led to the observation that the absorbance profiles seemed to broaden with increase in equivalence ratio—the temperature profiles had also broadened with increase in equivalence ratio.

4. Because the general HAB location of maximum temperature in the flame does not change with increased chlorine content, the HAB location of maximum absorbance signal *also* does not change with increased chlorine content. It is hypothesized that the HAB location of maximum concentration of sodium atoms in the flame is dependent upon the temperature profile, while the magnitude of maximum production of sodium atoms is dependent on the chlorine loading. This hypothesis is characterized by the following figure, figure 7.25.

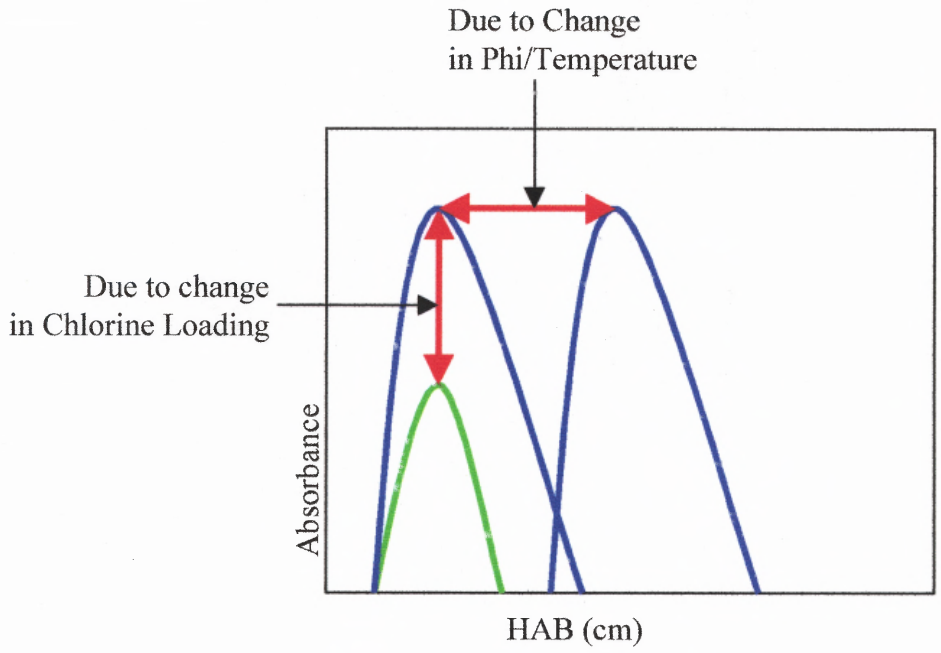

Figure 7.25 Schematic Diagram of Shift in Absorbance Profile With Respect to Change in Chlorine Loading and/or Phi/Temperature

7.5 Stable Species Profiles

This section will examine how the stable species profiles (CO, CO_2, and CH_4) were affected by the addition of chlorine to methane/air and methane/air/sodium flames. Experimental data for this part of the study were collected for ϕ=1.86 only. Of the four flames studied, this flame had the best combination of flame height and "steadiness" for probe sampling. These characteristics optimized spatial resolution and reproducibility of the data.

7.5.1 CO Profiles

Figures 7.26-7.27 depict CO profiles for methane/air and methane/air/sodium flames that have been doped with chlorine, respectively.

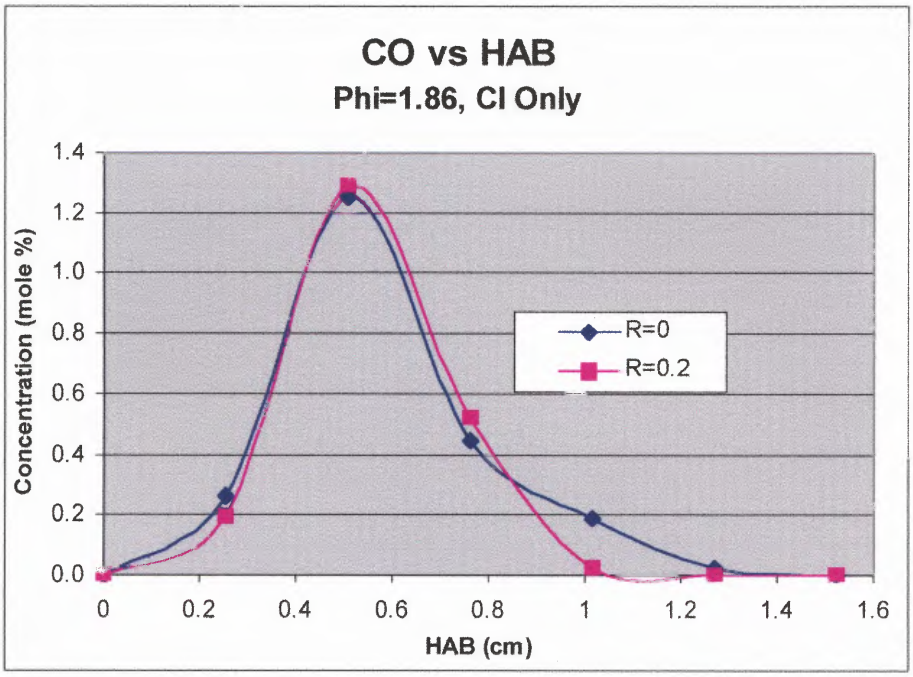

Figure 7.26 Experimental CO Concentration Profiles for CH_4/Air/CH_3Cl Flames, ϕ=1.86

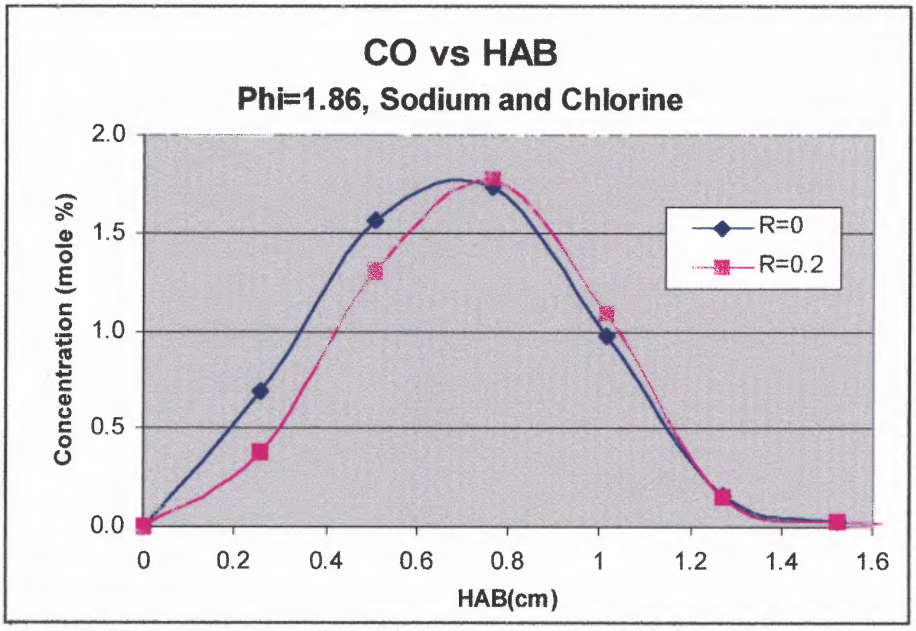

Figure 7.27 Experimental CO Concentration Profiles for CH_4/Air/CH_3Cl/Na Flames, ϕ=1.86

Observations:

1. For the methane/air flame, it appears that the CO profiles are relatively unaffected by the addition of chlorine.
2. For the methane/air/sodium flame, it appears that the addition of chlorine slightly decreases the production of CO for HAB less than 0.8 cm. At HAB=0.8cm, the CO profiles appear to crossover, similar to the phenomenon exhibited by the temperature profiles (section 7.3).

7.5.2 CO_2 Profiles

Figures 7.28-7.29 depict CO_2 profiles for methane/air and methane/air/sodium flames that have been doped with chlorine, respectively.

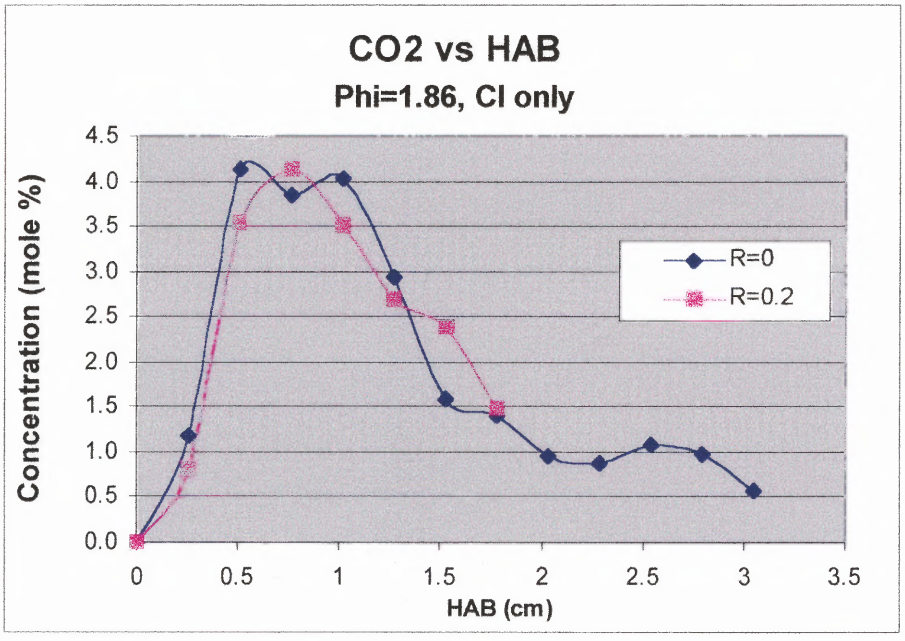

Figure 7.28 Experimental CO_2 Concentration Profiles for CH_4/Air/CH_3Cl Flames, ϕ=1.86

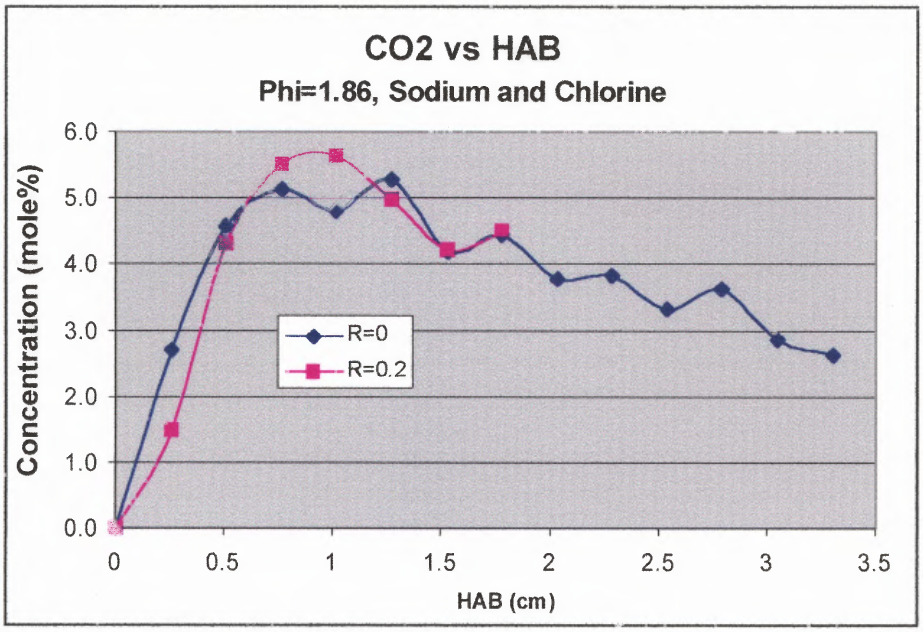

Figure 7.29 Experimental CO_2 Concentration Profiles for CH_4/Air/CH_3Cl/Na Flames, ϕ=1.86

When evaluating the CO and CO_2 profiles, the noise in the experimental data limits the number of conclusive observations that can be drawn regarding chlorine inhibition after approximately 1 cm HAB. However, comparison of Figures 7.28 and 7.29 leads to the following observations. Note should be taken that these observations serve to reinforce previously stated conclusions.

Observations:

1. It appears that within the noise of the experimental data, the CO_2 profiles for the methane/air and the methane/air/sodium flames are relatively unaffected by the addition of chlorine.

2. The effect of air entrainment is evident in both profiles as a decrease in CO_2 mole fraction (i.e., dilution due to air entrainment).
3. The decrease in the CO_2 concentration after 1cm HAB for the methane/air flame is more rapid than that of the methane/air/sodium flame.

Hypothesis:

1. The decrease in CO_2 concentration profiles for methane/air and methane/air/sodium flames validate the effects of air entrainment.
2. The accelerated decrease of CO_2 concentration in the methane/air/chlorine flame leads to the hypothesis that this flame is more strongly affected by dilution (i.e., entrains more air) than the methane/air/chlorine flame with sodium.

7.5.3 CH_4 Profiles

Experimental profiles of parent CH_4 were obtained, as shown in Figures 7.30 and 7.31. Note should be taken that experimental data was not available for 0.0 HAB. As a result, the plots were extended back to the CH_4 mole fractions as determined by the unburned gas flow rates (represented by ----------).

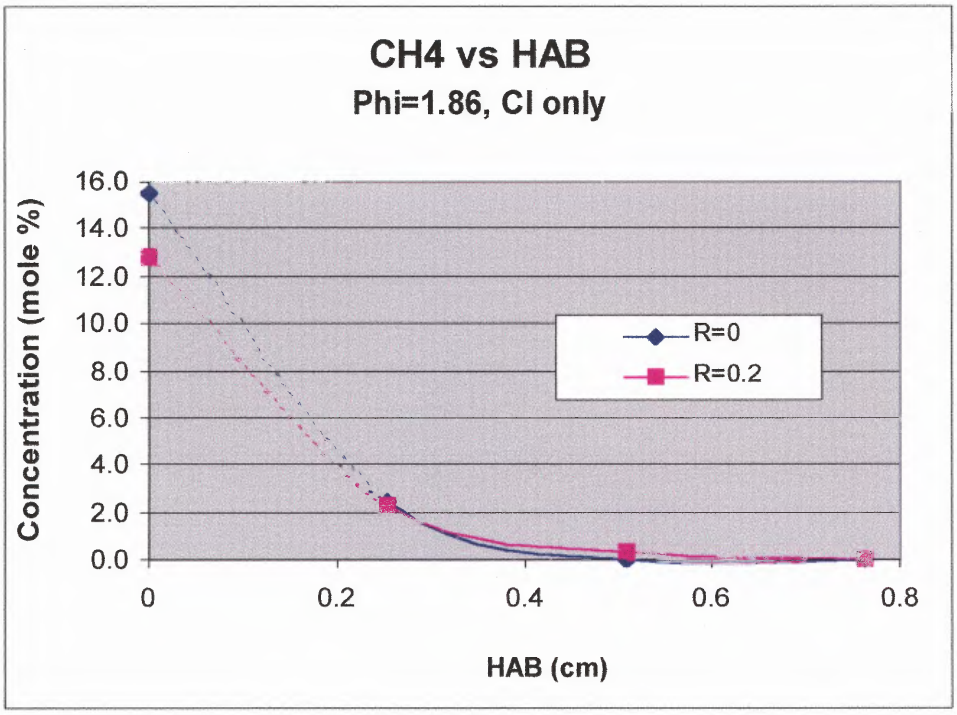

Figure 7.30 Experimental CH_4 Concentration Profiles in a CH_4/Air/CH_3Cl Flame, ϕ=1.86

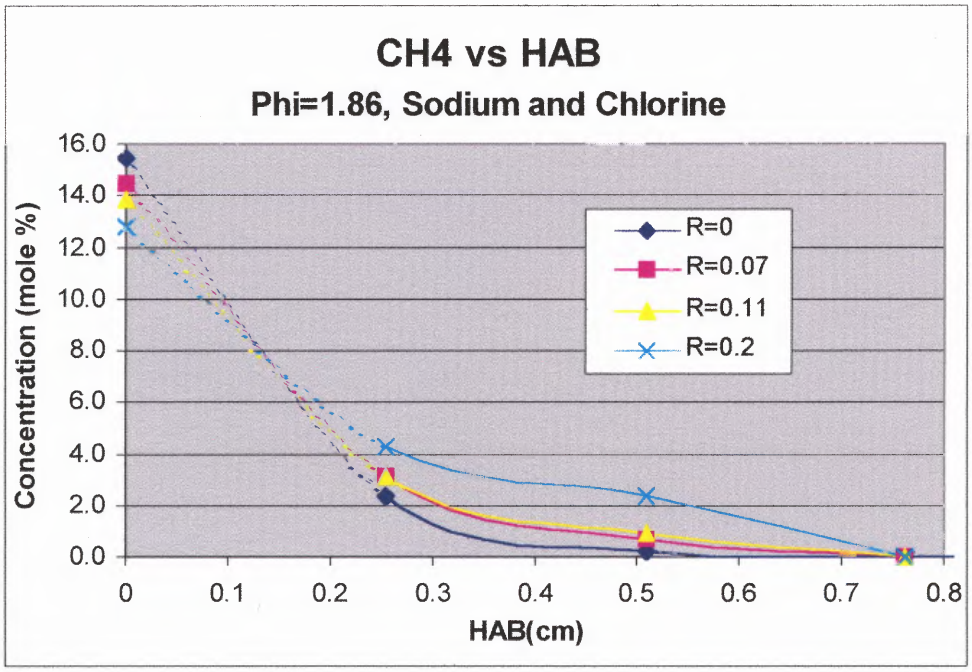

Figure 7.31 Experimental CH_4 Concentration Profiles in a CH_4/Air/CH_3Cl/Na Flame, ϕ=1.86

Figures 7.32 and 7.33 depict an enlarged portion of the CH_4 profiles which concentrate on HAB greater than 0.2 cm. The CH_4 profile for the methane/air flame doped with sodium-only is added to Figure 7.31 to assist in later discussion.

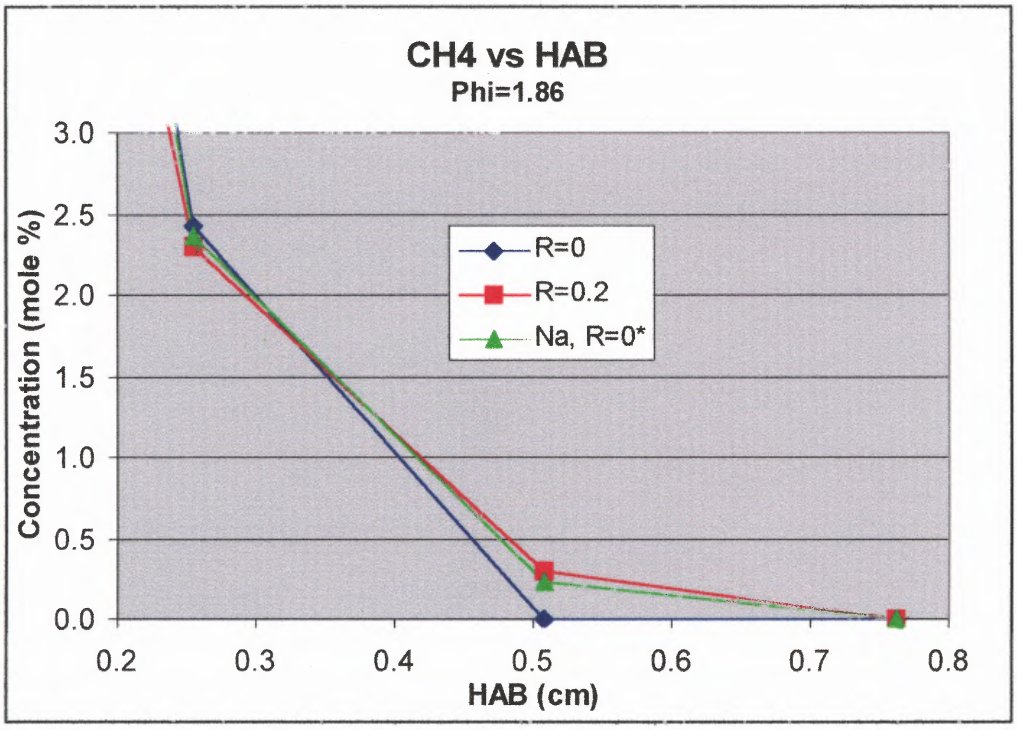

Figure 7.32 Enlargement of Experimental CH_4 Concentration Profiles in CH_4/Air/CH_3Cl and CH_4/Air/CH_3Cl/Na Flames, ϕ=1.86

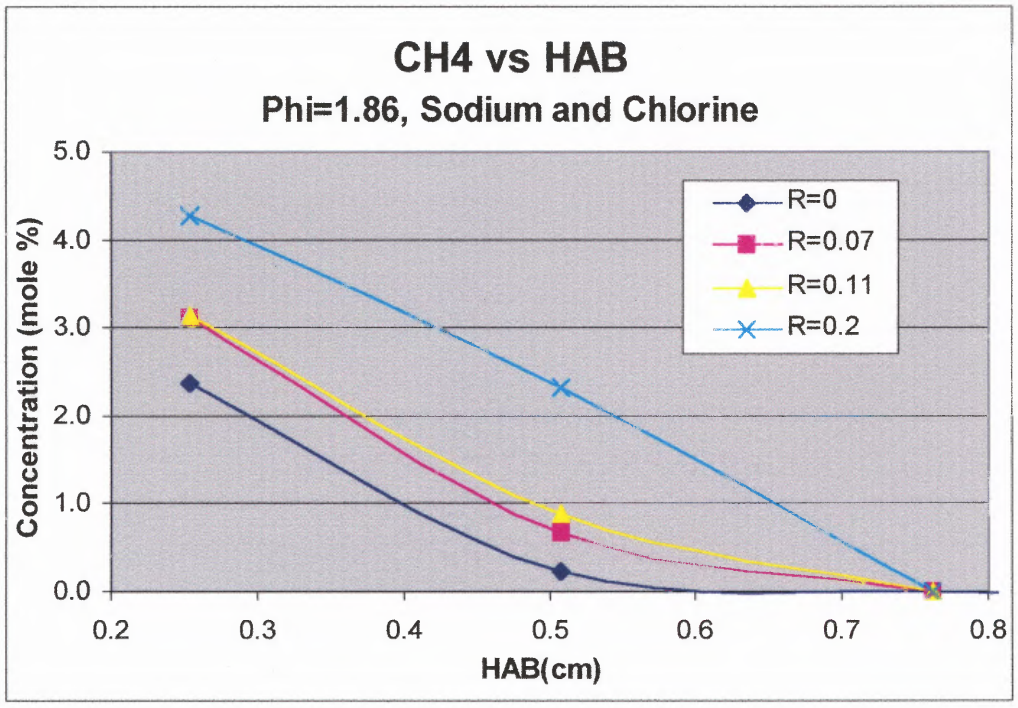

Figure 7.33 Enlargement of Experimental CH_4 Concentration Profiles in a CH_4/Air/CH_3Cl/Na Flame, ϕ=1.86

Observations:

1. Figure 7.30 shows that the addition of chlorine appears to inhibit the decay of parent CH_4. This decrease in CH_4 consumption due to chlorine is similar to the decrease in CH_4 consumption due to sodium alone.
2. Figure 7.31 shows that in the presence of sodium, increasing chlorine content appears to increase the CH_4 concentrations for all HAB.

Hypotheses:

1. It has already been shown that CO conversion from CO_2 is reduced by the addition of chlorine and/or sodium.

7.6 CHEMKIN Flame Code Modifications and Results

Section 6.4 discussed the results of the modifications made to the CHEMKIN flame code in order to model a methane/air flame *with* and *without* sodium. It also discussed the development of the air entrainment constant used in the model. The results were presented and compared to the experimental data. This section takes that previous discussion one step further. It reviews the modifications made to the CHEMKIN flame code when attempting to model methane/air and methane/air/sodium flames that have been doped with chlorine (CH_3Cl). Because of the severe convergence difficulties encountered, the methodology of trying to reach a converged solution to the model will also be outlined in the form of a flowchart. The three-pronged approach to the simulation for any particular flame with the code will also be discussed.

7.6.1 Reaction Mechanism Modifications

Methyl Chloride/Methane/Air Reactions Subset

The reaction mechanism used to describe the methane/air flames in Chapter 6 was actually a methyl chloride/methane/air mechanism that had been stripped of the chlorinated species reactions (27). This resulted in a total of 184 reactions being used to describe methane/air flames. In order to model the methyl chloride/ methane/air flames, the 71 chlorine reactions that were previously removed were simply *reinserted* into the methane/air mechanism for a total of 255 reactions (27).

Sodium-Chlorine Reactions Subset

Table 7.3 outlines the supplementary reactions that were added to the existing sodium—hydrocarbon mechanism to account for the likely interactions between sodium and chlorine when sodium is placed in a chlorinated hydrocarbon environment. The pre-exponential factors (A), activation energies (E_a) and resulting rate constants (k) presented in table 7.3 were those that were used in the flame model during the course of this study. Any modeling results presented in this chapter are a product of these input parameters. However, further analysis of these modeling results led to a re-examination of some of these parameters. While the actual reactions did not change, the value of some of the kinetics parameters associated with these reactions were improved. The results of these modifications are discussed in chapter 8 and additional information is found in appendix D.

The procedure for development of this reaction subset was as follows:

- The NIST data base was searched for all sodium species and sodium ion reactions.
- The search provided 150 possible reactions and their kinetic rate parameters.
- Of these reactions, 8 reactions were chosen and evaluated for feasibility.
- Three of these 8 reactions were found to be unfeasible and were deleted.
- Two additional reactions were added. Their rate constants were estimated with the QRRK method.

- This resulted in a total number of 7 new reactions to account for the interactions between sodium and chlorine.

The reactions used in the flame code to describe sodium-chlorine interactions are found in table 7.3. Additional information regarding these reactions can be found in appendix D.

Table 7.3 Sodium and Chlorine Reaction Mechanism

Reaction	Reference
$NaCl + H = Na + HCl$	ΔHrxn = -30.8 kcal/mol E = 3500 cal/mol A = 1.1E13 cm^3/mol-s (NIST)
$NaO + HCl = NaCl + OH$	ΔHrxn = -31.98 kcal/mol E = 2000 cal/mol A = 1.69E14 cm^3/mol-s (NIST)
$NaOH + Cl = NaO + HCl$	ΔHrxn = 16.1 kcal/mol E = 16100 cal/mol A = 1.E14 cm^3/mol-s (from $Cl+C_3H_8$)
$NaO_2 + HCl = NaCl + HO_2$	ΔHrxn = -5.79 kcal/mol E = 2000 cal/mol A = 1.39E14 cm^3/mol-s (NIST)
$Na + Cl_2 = NaCl + Cl$	ΔHrxn = -40.85 kcal/mol E = 2000 cal/mol A = 4.4E14 cm^3/mol-s (NIST)
$Na + CH_3CL = NaCl + CH_3$	ΔHrxn = 12.1 kcal/mol E = 12100 cal/mol A = 5E14 cm^3/mol-s (NIST)
$NaCl = Na + Cl$	E = 100870 cal/mol (QRRK) A = 1.261E15 cm^3/mol-s (NIST) (QRRK) n = -2.02 (QRRK)

The CHEMKIN flame code used the above findings to calculate the forward (as written) rate constant, k, in the following manner:

$$k = A \cdot T^n \exp\left(\frac{-E}{R \cdot T}\right) \tag{7.1}$$

where A ≡ pre-exponential factor or frequency factor

E ≡ activation energy, cal/mol

R ≡ gas constant = 1.987 cal/mol-K

T ≡ absolute temperature, K

n ≡ temperature exponent

ΔH_{rxn} (calculated from H_f^0 at 25°C).

Note should be taken that the existing thermodynamic data base contained data on all of the new species found in these additional reactions. However, the transport database did not contain data for sodium chloride (NaCl). The NaCl transport data parameters were taken to be the same as ClO transport data.

7.6.2 The CHEMKIN Flame Code for $CH_4/CH_3Cl/Air$ and $CH_4/CH_3Cl/Air/Na$ Flames

In order to arrive at a converged solution for *any given flame*, it was generally necessary to first find a converged solution to a flame at conditions far removed from the particular flame of interest (i.e., with respect to entrainment constant, temperature, and ϕ). One would then approach a solution to the flame of interest in a method that could be described as

parametric continuation. It was necessary to use this procedure of parametric continuation on three different parameters in order to reach a solution. The three parameters that were changed in an incremental fashion in order to reach a suitable converged solution (and the order in which they were manipulated) were as follows:

1. Entrainment constant, c
2. Equivalence ratio, Phi (ϕ)
3. Temperature profile, T

For the methane/air flames with/without sodium, all three of these parameters were changed successfully to reach a converged solution for all cases. Once a converged solution was reached, that solution could be then incrementally modified to optimize the solution. This procedure is outlined schematically in figure 7.34-7.36.

With regard to methane/air flames that contained chlorine (CH_3Cl), the flame code could not reach a converged solution at the specified (measured) temperature profiles. For the CH_4/CH_3Cl/Air flames, a solution could not be reached with input temperatures any closer than 50K above the actual temperature profile. *An incremental change as small as 10K at only one HAB would cause the convergence to fail.* For the CH_4/CH_3Cl/Air/Na flame, the code would only give a solution at temperatures approximately 200K above the actual temperature profile.

Figures 7.34-7.36 depict a flowchart that outlines how all of the options offered by the CHEMKIN flame code were completely exhausted in an effort to reach a solution to CH_4/CH_3Cl/Air flames, with/without sodium. Note should be taken that a parametric continuation was performed on only one parameter at a time. As a result, an attempt to reach a converged solution for any given flame was divided into three stages – one stage for each parameter. They were as follows:

- Stage 1 - Entrainment Constant
- Stage 2 – Equivalence Ratio (i.e., Flowrates)
- Stage 3 – Temperature Profiles

None of the chlorine cases were able to satisfy the Stage 3 requirement.

All runs were performed on an IBM personal computer (PC). A Pentium 90 MHz with 64 MB RAM (Random Access Memory) was used initially. A case with a good restart file (i.e., a previously converged solution as a first guess) could take as little as 30 minutes to converge and a case without a restart file could take up to 12 hours. The PC was upgraded to a Pentium II, 266 MHz with 128 MB RAM and the run times were decreased to 1-5 minutes for a case with a good restart file and 60-90 minutes for a case without a restart file. The large amount of RAM was needed to run the chlorine cases.

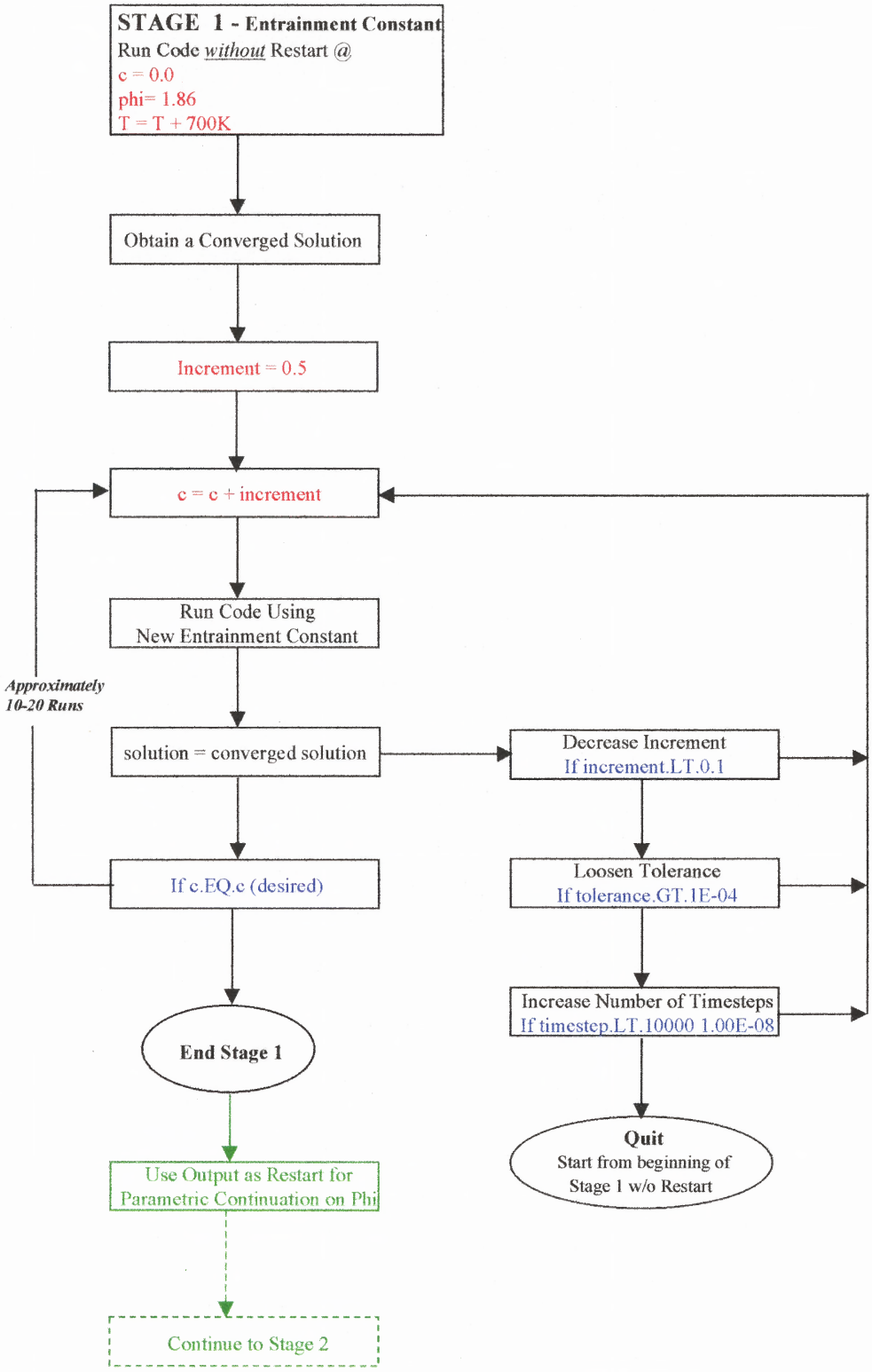

Figure 7.34 Flowchart for Execution of CHEMKIN Premixed Flame Code—Stage 1 (Entrainment Constant)

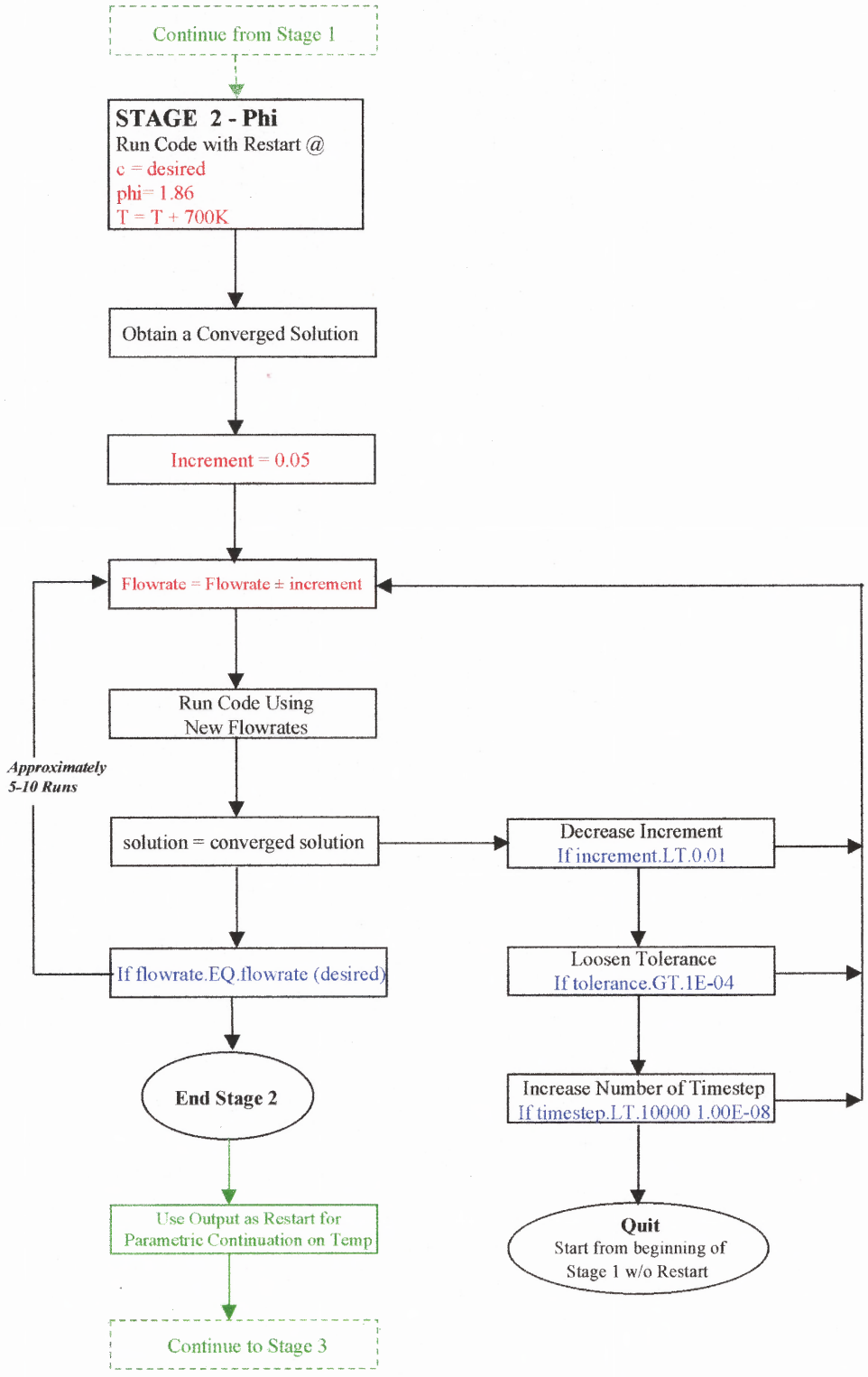

Figure 7.35 Flowchart for Execution of CHEMKIN Premixed Flame Code—Stage 2 (Equivalence Ratio)

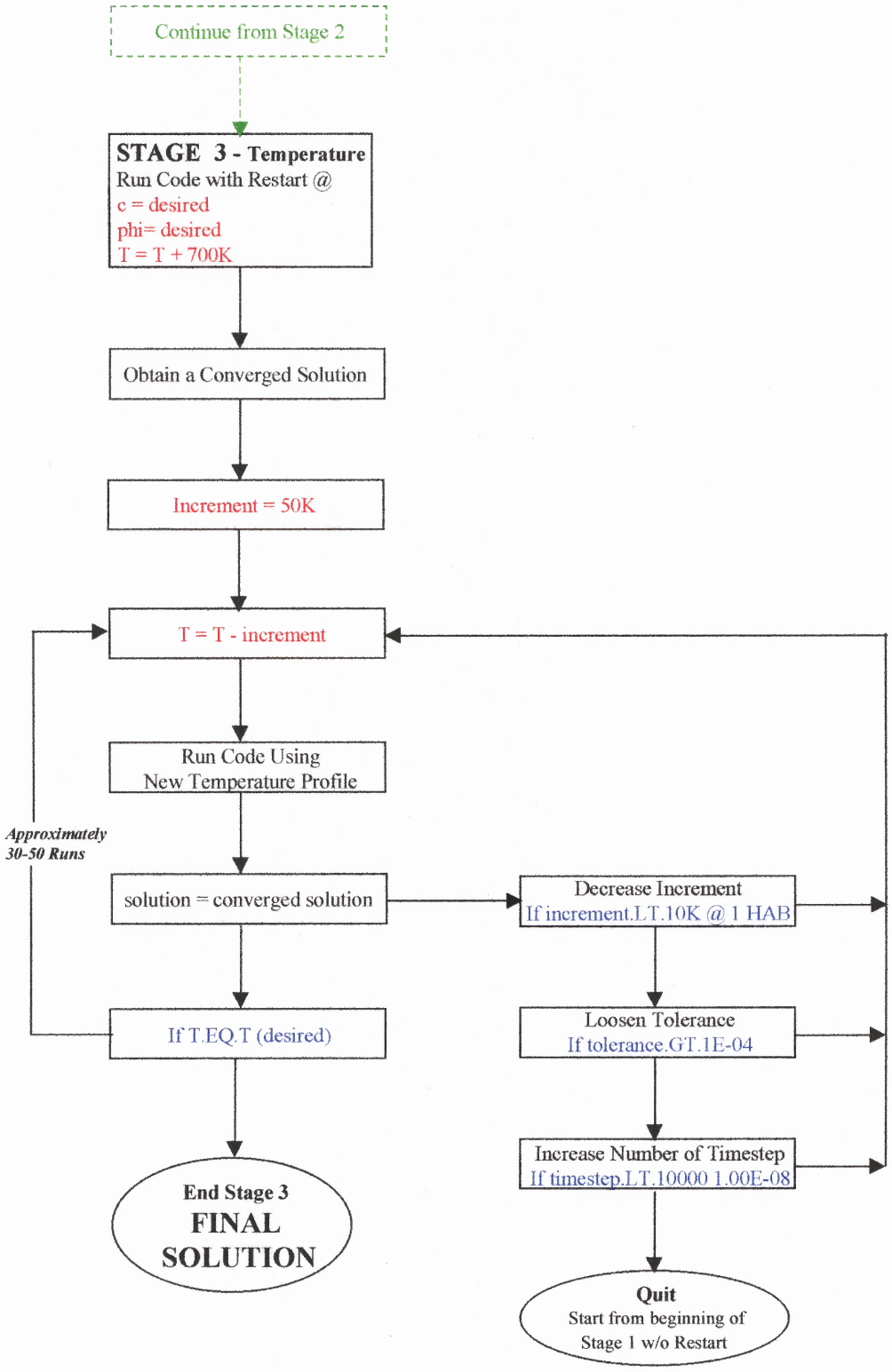

Figure 7.36 Flowchart for Execution of CHEMKIN Premixed Flame Code—Stage 3 (Temperature Profile)

It should be noted that if difficulty was not encountered in the running of the flame code (e.g., having to loosen tolerances or increase number of timesteps), it would take a minimum of 40/45 runs and up to 80 runs to reach a converged solution for a particular flame. These flames included CH_4/air, CH_4/air/Na, CH_4/air/CH_3Cl, and CH_4/air/Na/CH_3Cl for ϕ = 1.29, 1.86, 2.48, and 3.15

Once the limits of the CHEMKIN flame code were exhausted and a converged solution was not reached, additional alterations to the input files that were used in the execution of the code were examined.

Transport Data/ Thermodynamic Data

An alternate transport and thermodynamic data base (62) was used (Na species added) as an input to the code in the Tran.dat and Therm.dat files. These changes did not get any closer to a converged solution of the particular flames in question than the original data base.

A Reduced Kinetic Mechanism for CH_4/Air/CH_3Cl Flames

A reduced kinetic mechanism (58) that contained only 63 reactions replaced the 255 reactions that previously described the chlorinated hydrocarbon flame in the input file. However, the reduced mechanism resulted in less success than the larger mechanism (i.e., didn't get as far along in the parametric continuation). The reduced mechanism was then rejected in favor

of the larger CH_4/Air/CH_3Cl kinetic mechanism. It was important to the continuity of the study that the mechanism used for the chlorinated flame would be consistent with the mechanism that had been used for the non-chlorinated flame. The modeling of the non-chlorinated flame was already complete and it was previously stated that the non-chlorinated mechanism was simply a sub-set of the large CH_4/Air/CH_3Cl mechanism.

Nustart.exe

Nustart.for (Nustart) is a FORTRAN program developed by Sandia National Labs that is used to create Nustart.exe. With Nustart, the solution to a flame with one mechanism could be used to create a restart file to a flame with a *slightly* different mechanism. This was not possible before (i.e., if the mechanism was changed, the code had to executed without a restart file). However, it was not entirely clear how many reactions could be added or deleted to the old mechanism when using Nustart. A reasonable assumption was that the fewest changes to the mechanism would increase the chances of success.

During the course of the study, a converged solution was found for a CH_4/Air/CH_3Cl/Na flame at the correct temperature profile. However, the kinetic mechanism used for this solution did not include the sodium ion reactions (see Section 6.4.1) that account for the initial production of sodium atoms. Nustart was used to make the transition (using restart files) from the

"converged solution running at the proper temperatures but minus the ion reactions" to a "converged solution running at the proper temperatures with the ion reactions included". Unfortunately, the code could not reach a converged solution, even when the three ion reactions were added one at a time.

7.6.3 Development of Entrainment Constant

The general development of the air entrainment constant was discussed in chapter 5 and the development for the specific air entrainment constant for CH_4/Air flames that contain sodium was discussed in chapter 6. These developments required many executions of the CHEMKIN flame code in order to optimize a converged solution at the correct temperature profile and flow rates. Unfortunately, the CHEMKIN flame code did not converge at the proper temperatures for CH_4/Air/CH_3Cl or CH_4/Air/CH_3Cl/Na flames. Hence, manipulation of the output in order to optimize the air entrainment constant was not possible. An educated guess of the optimum air entrainment constants for chlorinated flames was based on the following observations:

1. The entrainment constant for CH_4/Air flames was c=4.0 cm^{-1}.
2. When sodium was added to a CH_4/Air flame, the flame speed appeared to decrease. The slower, floppier CH_4/Air/Na flame also appeared to entrain less air as evidenced by the decreased dilution effect in the CO_2 profiles (Figure 6.19). This dilution effect is particularly noticeable in the

experimental data. As a result, the entrainment constant used for CH_4/Air/Na flames (c=2.0 cm^{-1}) was half as large as the entrainment constant for the CH_4/Air flames (c=4.0 cm^{-1}).

3. Figure 7.37 shows analogous results regarding CO_2 concentrations when sodium was added to a CH_4/Air/CH_3Cl flame.

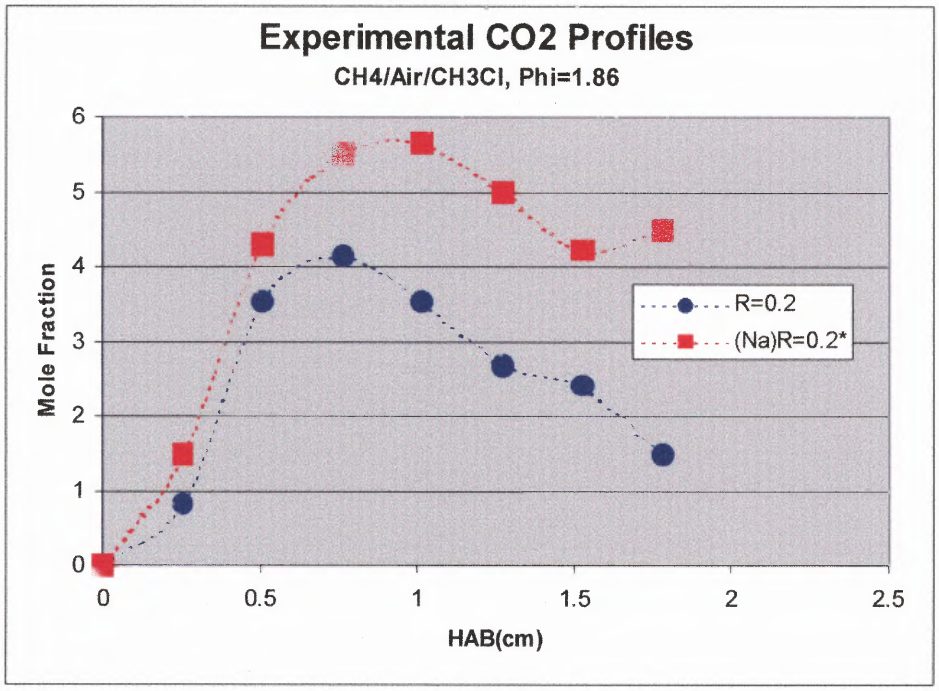

Figure 7.37 Experimental CO_2 Concentration Profiles for CH_4/Air and CH_4/Air/Na Flames, ϕ=1.86

Based on these observations and the obvious effect that sodium had on the entrainment of air, the following table summarizes the constants that were used to execute the CHEMKIN flame code for chlorinated as well as non-chlorinated flames. Note should be taken that the entrainment constants used for the non-chlorinated flames were a result of optimization of the

model. The entrainment constants used for the chlorinated flames were an educated guess based on the available data.

Table 7.4 Summary of Entrainment Constants

Flame	Entrainment Constant [cm^{-1}]
CH_4/Air	c = 4.0
CH_4/Air/Na	c = 2.0
CH_4/Air/CH_3Cl	c = 4.0
CH_4/Air/CH_3Cl/Na	c = 2.0

7.6.4 Modeling Results

The following figures represent a comparison of the obtainable modeling results with the experimental data for a CH_4/Air/CH_3Cl and a CH_4/Air/CH_3Cl/Na flame (R=0.2 and ϕ=1.86). However, since the models could not be executed at the correct temperatures, the modeling results will not be discussed and/or analyzed relative to the experimental data.

Note should be taken that the code was run during the course of this study with temperature measurements that were corrected for radiation only. Since additional examination of the temperature correction showed that conductivity through the thermocouple wires should not have been neglected (resulting in higher corrected temperatures) the results presented here may actually be closer to the experimental data than they appear.

The results outlined here are presented simply to show that the modeling results were indeed *approaching* a reasonable fit to the experimental data. Of particular interest is the shape of the sodium profile. The model predicted a reasonable fit to the experimental data, with respect to the location of the maximum mole fraction and the overall shape of the sodium profile.

Methane/Air/Methyl Chloride Flame

Figure 7.38 depicts how the stable species experimental data (CH_4, CO, and CO_2) for a CH_4/Air/CH_3Cl flame (R=0.2) compares to the modeling results of the same flame, given that the model was executed using a temperature profile 50K above the actual corrected temperature profile. The equivalence ratio of the metered feed to the flame was ϕ=1.86 and the entrainment constant used to run the model was c=4.0 cm^{-1}.

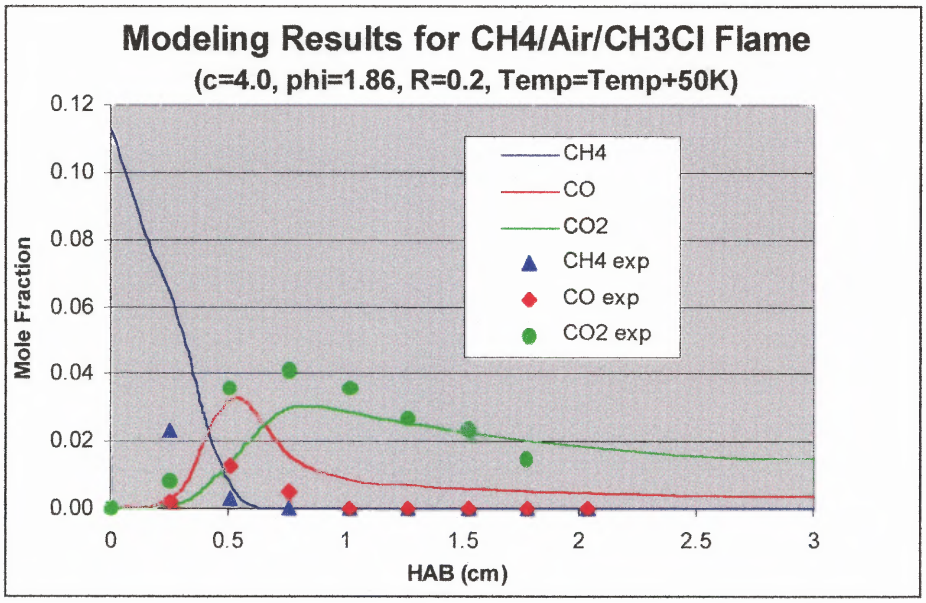

Figure 7.38 Experimental and Modeling Results of Stable Species Concentration Profiles in a CH_4/Air/CH_3Cl Flame, ϕ=1.86, R=0.2, Temperature = Corrected Temperature + 50K

Methane/Air/Methyl Chloride/Sodium Flame

Figures 7.39 and 7.40 show how the stable species and sodium experimental data compare to the modeling results for a methane/air/methyl chloride flame that has been doped with sodium. Once again, it should be pointed out that the flame code was executed using a temperature profile 200K above the actual corrected temperature profile. The equivalence ratio was ϕ=1.86 and the entrainment constant used was c=2.0 cm^{-1}.

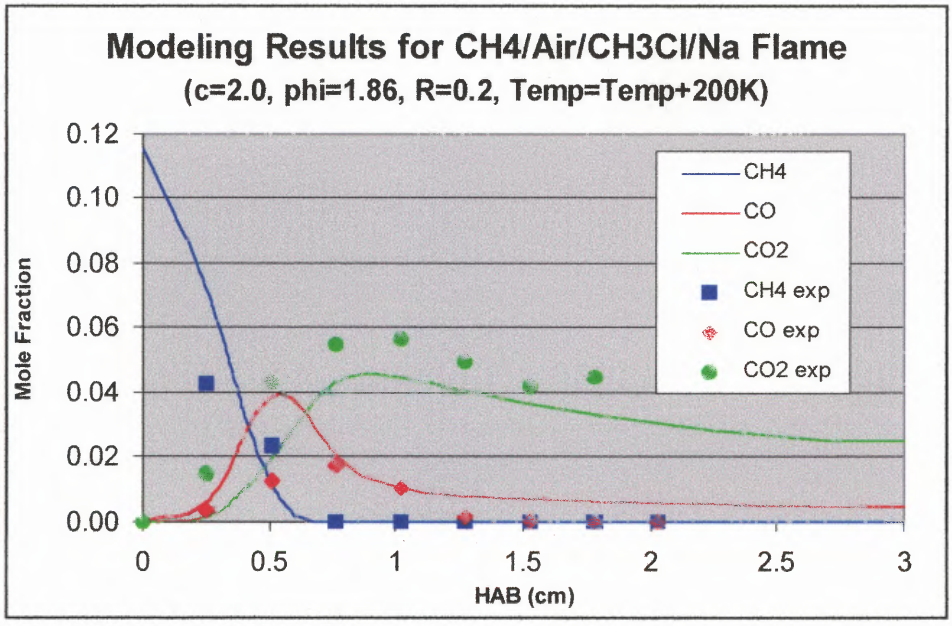

Figure 7.39 Experimental and Modeling Results of Stable Species Concentration Profiles in a CH_4/Air/CH_3Cl/Na Flame, ϕ=1.86, R=0.2, Temperature = Corrected Temperature + 200K

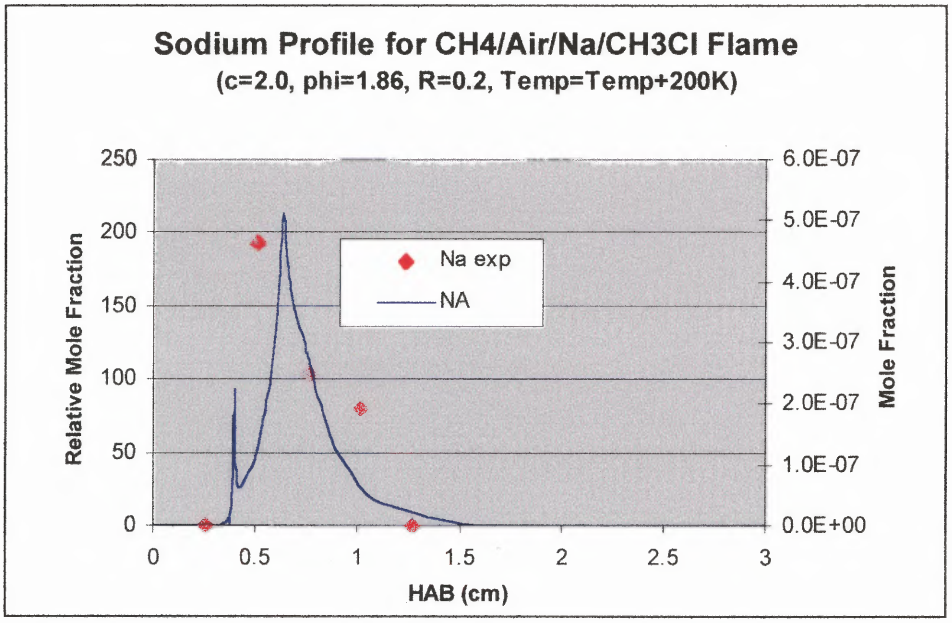

Figure 7.40 Experimental and Modeling Results of Sodium Concentration Profiles in a CH_4/Air/CH_3Cl/Na Flame, ϕ=1.86, R=0.2, Temperature = Corrected Temperature + 200K

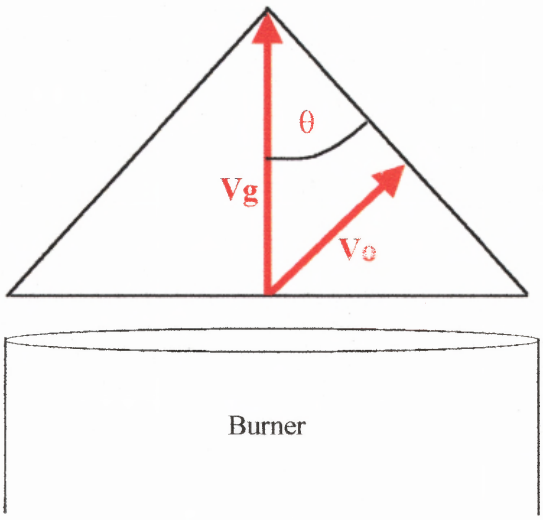

Figure 8.1 Schematic of Relationship Between V_0, V_g and θ for a Bunsen Flame

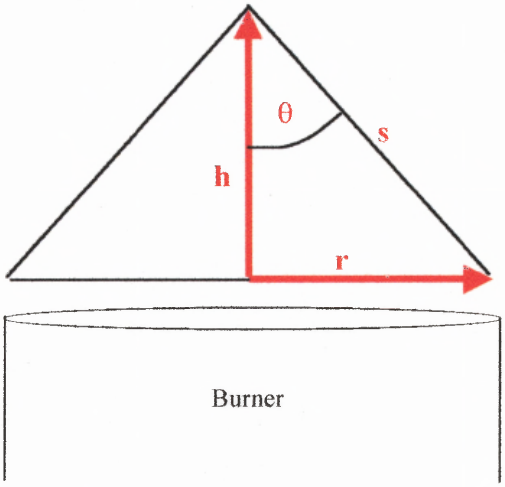

Figure 8.2 Schematic of Relationship Between Flame Inner Core Height, h, Burner Radius, r and Cone Edge, s

The burner radius, r, inner cone height, h and the cone angle, θ, are related in the following fashion:

Note should be taken that the spike in the Na model profile in figure 7.40 at an early HAB is probably an anomaly. It might very well disappear once (and if) convergence is achieved at the correct temperatures.

CHAPTER 8

CONCLUSIONS AND RECOMMENDATIONS

8.1 Conclusions

Through experimental data analysis and computer modeling, this study examined the following:

- The fate of sodium in CH_4/Air and CH_4/Air/CH_3Cl flames
- The effect of sodium on a CH_4/Air and CH_4/Air/CH_3Cl flames

Analysis of the results suggested the following conclusions:

8.1.1 The Fate of Sodium in CH_4/Air and CH_4/Air/CH_3Cl Flames

(1) Sodium was introduced into both the CH_4/Air and the CH_4/Air/CH_3Cl flames in the form of aqueous sodium ion (Na^+). This was done by aspirating a 0.02 mol/liter solution of $NaNO_3$. Therefore, even though sodium was introduced to the flame as sodium ion, the following observations provide evidence that sodium atoms were also present in the flame:

- Bright orange luminescence (Fig 6.2) characteristic of atomic sodium emission
- The absorbance of light at 589 and 589.5 nm. (Fig 4.14)

Therefore, it is concluded that the temperatures provided by the combustion of CH_4 and air ($T_{max} \cong 1600K$) as well as the combustion of CH_4/CH_3Cl and

air ($T_{max} \cong 1550K$) in an environment where there is additional entrainment (transport) of air from the surroundings are sufficient to provide Na atom concentrations capable of significant absorbance of radiation at wavelengths characteristic of electronic transitions from the *3s* state to the *3p* and the *4p* levels.

(2) The sodium absorbance profiles outlined in figures 6.22 and 7.16-7.19 for CH_4/Air/Na and CH_4/Air/CH_3Cl/Na flames, respectively, show that maximum *net* sodium atom production shifted to higher HAB as ϕ increased. That shift can be explained in the following manner:

It has already been established that as the equivalence ratio increases for values greater than about 1.0, the flame speed/burning velocity decreases (37). A schematic representation of the relationship between burning velocity, V_0 and cold gas flow rate, V_g as a function of cone angle, θ is shown in figure 8.1 for a Bunsen flame, which is similar to the slotted flame used in this study, i.e., an elongated Bunsen cone. In this relationship,

$$V_0 = V_g \sin\theta \qquad (8.1)$$

Since V_0 decreases as ϕ increases from 1.29 to 3.15, then θ must also decrease with increasing ϕ (for constant V_g). The relationship between the cone angle θ and the flame dimensions and is outlined schematically in figure 8.2:

$$\tan\theta = \frac{r}{h} \tag{8.2}$$

Since θ decreases for an increase in equivalence ratio, the height of the inner cone, h, must also increase for constant burner radius, r. Quite simply, the height of the inner cone must increase with equivalence ratio (for constant cold gas flow rate). As a result, the primary reaction zone (located at the edge of the inner cone) is shifted outward and further away from the burner. Consequently, the production of sodium atoms is also shifted outward and further away from the burner, i.e., to higher HAB.

However, an alternate description of how the burning velocity varies with flame geometry can be derived from the following relationship:

$$V = \frac{Q}{A} \tag{8.3}$$

where Q is the cold gas volumetric flow and A is the area of premixed reaction surface. As seen in figure 8.3, the height of the inner cone increases as ϕ increases for a constant burner opening. As a result, the surface area of the inner cone must also increase with an increase in ϕ. This is true for the inner cone of a Bunsen flame as well as a slotted flame. Therefore, the position of maximum heat release shifts to higher HAB i.e., from HAB_1 to HAB_2.

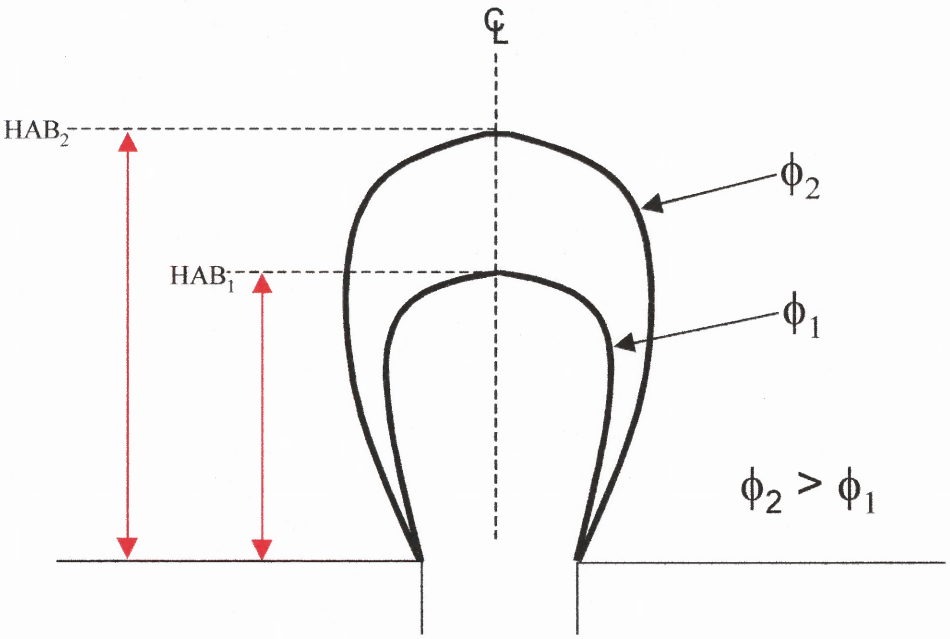

Figure 8.3 Illustration of Change in Inner Core Height with Change in ϕ

Therefore, a shift in the flame front to higher HAB that results from an increase in inner cone surface area must coincide with a decrease in burning velocity (for constant volumetric flow rate), according to equation 8.3.

(3) Figures 7.16-7.18 show that for a CH_4/Air/CH_3Cl/Na flame, the maximum net atomic sodium present in the flame decreases as the chlorine content increases for any given ϕ. In a chlorinated hydrocarbon environment, there is an increased occurrence of sodium diatomics such as sodium chloride (NaCl), due to the presence of highly electronegative chlorine atoms (described by Table 7.3, sodium and chlorine reactions). Therefore, the sodium absorbance profiles decrease as the chlorine content in the flame increases simply because there is less atomic sodium available in the flame.

It should be noted that it has *not* been concluded that overall sodium production has decreased, but rather the net atomic sodium present in the flame has been decreased due to the availability of a very stable NaCl product outlet in a chlorinated environment.

(4) Examination of the HAB location of maxima for CH_4/Air/CH_3Cl flames, figures 7.16-7.19 and 7.12-7.15, shows that the sodium absorbance profiles parallel the temperature profiles. While the *magnitude* of the maximum sodium absorbance varied with a change in chlorine content for any given ϕ, the HAB *location* of maximum sodium absorbance did not. However, because the production of sodium atoms is dependant upon flame temperature, it is concluded that the HAB location of maximum sodium absorption is not affected by a change in chlorine content in a CH_4/Air/CH_3Cl flame for any given ϕ, simply because the HAB location of maximum temperature is not affected by a change in chlorine content (within experimental error).

8.1.2 Additional Conclusions Resulting from Analysis of Experimental Data and Modeling

8.1.2.1 Atomic Absorption Spectroscopy

Atomic Line Width and Line Shape of Sodium

Atomic absorption lines are very sharp, with an inherent width of only 10^{-4} - 10^{-5} nm (11, 15, 16). This finite width reflects the natural energy spread

between the ground state and the excited state in the atom of interest, namely sodium. However, two mechanisms contribute significantly to broadening the natural line width of sodium (and indeed any atom). The first is the Doppler effect. The atoms traveling toward the radiation source absorb radiation of slightly lower frequency light than that absorbed by the atoms moving away. It is common for absorption lines to be increased to about 0.001 nm by this effect (15). The second mechanism that causes an increase in the atomic line width is pressure broadening. Collision between atoms causes a broadening of the energy levels in the ground state and the excited state and hence, a broadening of the peaks. This pressure broadening can be caused by collisions between like atoms (Holtzmark broadening) or different atoms (Lorentz broadening). It is common for pressure broadening to increase the line width to 0.002 nm (15). In addition, minor broadening can be caused by local electric fields (Stark effect) and local magnetic fields (Zeeman effect). The spectral width of the sodium absorption line at 589.5 nm that has been broadened by temperature and pressure varies with temperature in the following manner (15):

Na spectral line width (1000K) = 0.0028 nm

Na spectral line width (3000K) = 0.0048 nm

Line Shape and Line Width of the Monitoring Light

A continuous light source was used as the monitoring light in this study, namely a 300 W Xenon arc lamp. Unlike the peaked shape of the sodium absorption line, the shape of the arc lamp would be more accurately described as a band with a width that was much greater than the spectral line width of sodium. The difficulty encountered using a radiation source such as this for atomic absorption can be described by the following illustrative example (15):

> Using a typical commercial instrument, assume that a spectral wave band of about 0.1 nm would fall on a detector from a continuous source. Sodium atoms absorb over a range of approximately 0.003 nm. If all of the light in this 0.003 nm absorption band were absorbed from an emission wave band of 0.1 nm, then the detector would only record a loss of 3% of the signal falling on it. Since 100% absorption of the 0.003 nm absorption band results in only a reduction of 3% in the signal, then absorption of 1% of the 0.003 nm absorption band (the required sensitivity of most atomic absorption methods) would be extremely difficult to measure with any reasonable degree of precision. Therefore, the measurement of such small changes in the emission signal produces a non-linear relationship between the absorbance signal and sodium atom concentration.

In order for Beer's law to be obeyed in a linear fashion, desired relative line widths of the emission source, the atomic line width and the monochromator bandwidth are illustrated in the following figure (11). Note that the monochromator bandwidth is approximately one hundred times greater than the atomic line width. This is not necessarily a *desired* bandwidth, but rather what is typically commercially *available.*

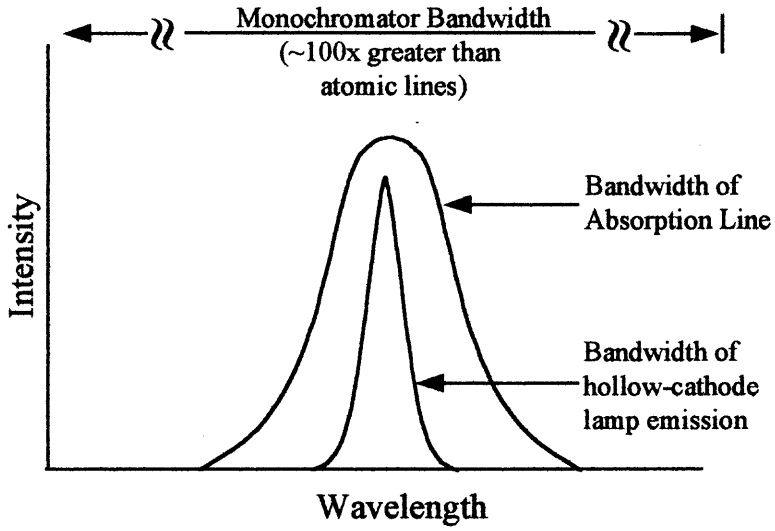

Figure 8.4 Relative Line Widths of Hollow-Cathode Emission, Atomic Absorption, and a Monochromator (11)

This was the difficulty that was encountered in this study; namely the non-linear behavior of Beer's law due to the use of a continuous source.

This difficulty would have been overcome, however, if a hollow cathode tube had been used as the radiation source. The hollow cathode emits relatively narrow spectral lines because the gas temperature in the lamp is lower than

a flame temperature (so there is less Doppler broadening) and the pressure in the lamp is lower than the pressure in a flame (so that there is less pressure broadening). In effect, the line width of the hollow cathode radiation is decidedly narrower than the atomic sodium absorption line width and, therefore, completely available for absorption.

A second difficulty that was highlighted when examining the non-linear behavior of Beer's law in this study was the effective bandwidth of the monochromator. In general, even good quality monochromators have effective bandwidths that are significantly greater than the width of the atomic absorption lines. This was indeed the situation encountered in this work. The monochromator used for this study was a Spex 1400 –11 double spectrometer. The bandwidth of the monochromator ($\Delta\lambda$), which is defined as the span of monochromator settings (in units of wavelength) needed to move the image of the entrance slit across the exit slit, can be approximated from the following expression:

$$D^{-1} = \frac{\Delta\lambda}{w} \tag{8.4}$$

where D^{-1} is the reciprocal linear dispersion [A/mm] and w is the exit slit width [mm]. The quoted linear dispersion for this monochromator (when operated as a double monochromator) was approximately 5.38 A/mm. However, this was for a 1200 groove/mm grating. This particular

monochromator was used in this study as a single monochromator i.e., the resolution is half that of a double monochromator, and the grating was 1800 grooves/mm. The conversion of the quoted linear dispersion to account for single monochromator resolution as well as the change in grating is therefore:

$$\left(5.35\frac{\text{Å}}{\text{mm}}\right)\left(\frac{\text{double}}{0.5\,\text{sin gle}}\right)\left(\frac{1200\,\text{grooves}/\text{mm}}{1800\,\text{grooves}/\text{mm}}\right)=7.2\frac{\text{Å}}{\text{mm}} \qquad (8.5)$$

Since the exit slit was held constant at 100 μm, the effective bandwidth of the monochromator ($\Delta\lambda$) used in this study was calculated as follows:

$$\Delta\lambda = wD^{-1} = (0.1\text{mm})\left(7.2\frac{\text{Å}}{\text{mm}}\right)=0.72\text{Å} \qquad (8.6)$$

Even though this resolution was sufficient to resolve the sodium doublet (separated by 6 Å) it was also responsible for contributing to the non-linear relationship between the absorbance signal and the sodium atom concentration.

Sodium Atom Resonance Absorption Cross Section

As outlined in chapter 6, Beer's law states that the absorbance of light by sodium atoms, A, is directly proportional to the concentration of sodium atoms available:

$$A = \sigma cL \tag{8.7}$$

where σ is the sodium absorbance cross section, c is the atom concentration and L is the path length. For this work, it was assumed that both σ and L were constant. Since concentration, c, was proportional to reciprocal temperature, it was also assumed that the concentration was proportional to the product of absorbance and temperature. These assumptions produced plots of relative absorbance (the product of absorbance x temperature) versus HAB. However, the assumption of constant absorption cross section was incorrect—implying that the plots of relative absorbance versus HAB are also incorrect.

The sodium absorption cross section, σ, varies with wavelength, λ. When σ is plotted as a function of λ, it may be represented by the following expression:

$$\sigma(\lambda) = \frac{\sigma_o}{1 + \left(\frac{\lambda - \lambda_o}{\Delta\lambda}\right)^2} \tag{8.8}$$

where σ_o is the peak absorption cross section at λ_o, and $\Delta\lambda$ is half the width of the absorbance cross section measured at the half the height of the peak (HWHM). The peak absorbance cross sections of sodium (σ_o) decrease slightly with temperature as the Doppler width increases in the following manner (74):

$$\sigma_o\ (5890\ A) = (10^{-12}\ cm^2)(8.037 - 1.31E\text{-}02\ T + 2.3E\text{-}5\ T^2) \tag{8.9}$$

$$\sigma_o\ (5896\ A) = (10^{-12}\ cm^2)(3.968 - 6.4E\text{-}02\ T + 1.11E\text{-}5\ T^2) \tag{8.10}$$

where temperature in the above expression is in degree centigrade and covers a range of -28°C to 144°C. It should also be noted that the literature reports that the sodium absorption coefficient is further reduced in the far wings (i.e., tails) of the sodium-D doublet broadened by molecules such as O_2, N_2, CO_2 and H_2O (75).

Expected Dependence of Absorption Vs Concentration

This study assumed that there were no deviations from the direct proportionality between the measured absorbance and sodium atom

concentration in the flame i.e., Beer's law was obeyed. This assumption was incorrect for the following reasons:

1. Beer's Law is successful in describing the absorption behavior of dilute solutions only (16). At high concentrations (usually > 0.01 M) the average distance between the species responsible for absorption is diminished to the point where each affects the charge distribution of its neighbors and this phenomenon alters their ability to absorb a given wavelength of radiation. The concentration of the solution aspirated into the flame for this work was 0.02M – twice the concentration of the prescribed upper limit.
2. The sodium absorbance cross section was incorrectly assumed to be constant rather than a function of wavelength as outlined above.
3. In order for Beer's law to be obeyed, the line width of the radiation source must be narrower than the sodium spectral line width (11). Since a continuous light source was used for this study, not only was the bandwidth of the source not narrower than the atomic line width, but rather it was orders of magnitude wider than the atomic line width. The resultant signal is described by the following figure:

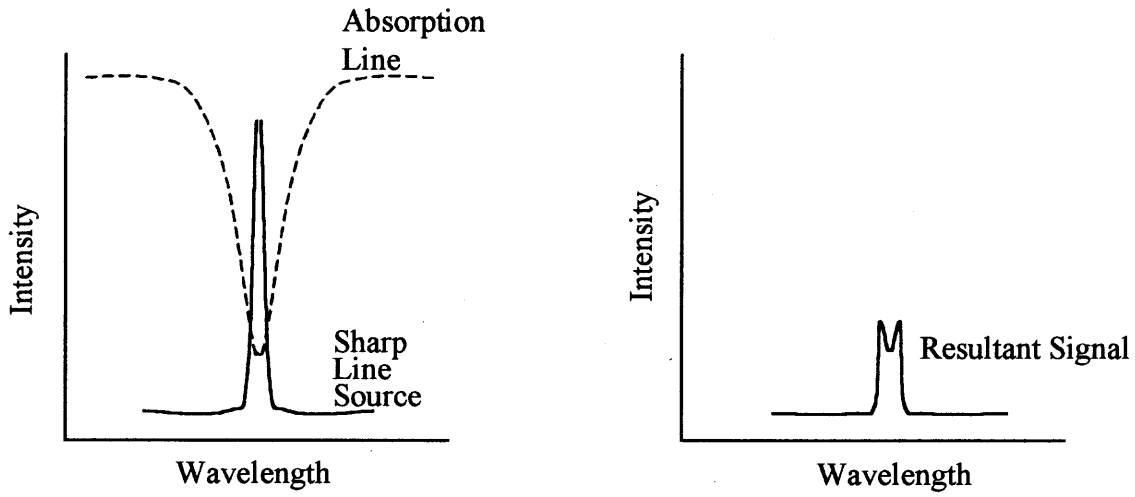

Figure 8.5(a) Atomic Absorption with a Sharp Line Source (76)

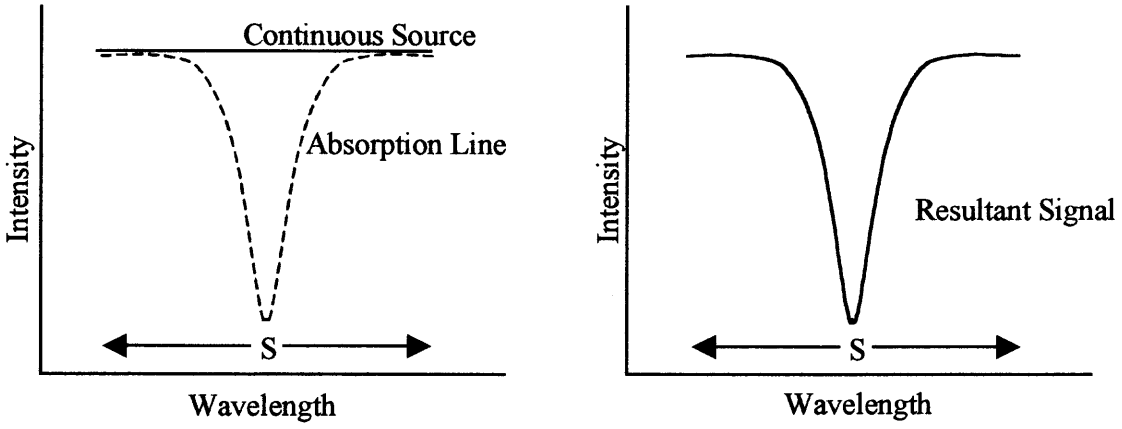

Figure 8.5(b) Atomic Absorption with a Continuous Source(76)

In figure (a), the source line and the absorption line are at the same wavelength, but the half-width of the source is narrower than that of the absorption line. Therefore, the entire center of the source line is absorbed, in accordance with Beer's Law. In the case of the continuous source, as

seen in figure (b), only a small fraction of the band of radiation passed by the monochromator is absorbed and a large portion of unabsorbed light falls on the detector. This results in a decreased sensitivity (absorbance) and a non-linear plot of absorbance versus concentration. The following figure illustrates the difference between calibration curves for the line and continuum source.

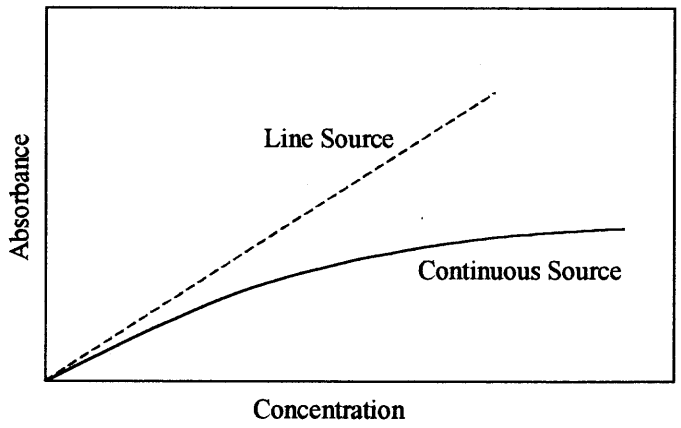

Figure 8.6 Comparison of Absorption from Continuum and Sharp-Line Sources (76)

Therefore, for all of the above reasons it would be more reasonable to expect the absorbance versus concentration profiles to behave in a non-linear fashion by asymptotically approaching an upper limit.

Applicability of Beer-Lambert Law

Light from the xenon arc lamp strikes the sample (hydrocarbon flame doped with atomic sodium) with incident radiant power, P_o, some of the light at 589

and 589.6 nm is absorbed by the sample. The radiant power of the beam emerging from the sample is P, such that $P \leq P_o$. The transmittance, T, is the fraction of the original light that passes through the sample and is calculated from the radiant power in the following manner:

$$T = \frac{P}{P_0} \tag{8.11}$$

The range of T is 0 to 1. The absorbance, A, (also referred to as the optical density) is defined as:

$$A = \ln \frac{P_0}{P} = \ln\left(\frac{1}{T}\right) \tag{8.12}$$

The incident power, P_o, can be calculated from the incident light intensity, I_o, where,

$$P_0 = \int_{-\infty}^{\infty} I_0(\lambda)\, d\lambda = I_0 \Delta\lambda_m \tag{8.13}$$

where $\Delta\lambda_m$ is the effective bandwidth of the monochromator. In a similar fashion, the emerging power, P, can be calculated as follows:

$$P_0 = \int_{-\infty}^{\infty} I_0(\lambda) \exp(-\delta(\lambda) c\, L)\, d\lambda \tag{8.14}$$

where c is the concentration of atoms in the sample and L is the path length. The absorbance cross section ,σ, is a function of wavelength as described in the previous section. Simplification of the above relationships results in the following expression which can be used to calculate the transmittance and consequently, the absorbance.

$$T = \frac{P}{P_0} = \frac{1}{\Delta\lambda_m} \int_{\lambda_0 - \frac{\Delta\lambda_m}{2}}^{\lambda_0 + \frac{\Delta\lambda_m}{2}} \exp(-\delta(\lambda) c\, L)\, d\lambda \tag{8.15}$$

At a constant temperature of 1949K, the following figure is an example of an absorbance versus concentration curve that was generated for a methane/air flame doped with sodium at $\phi = 1.86$.

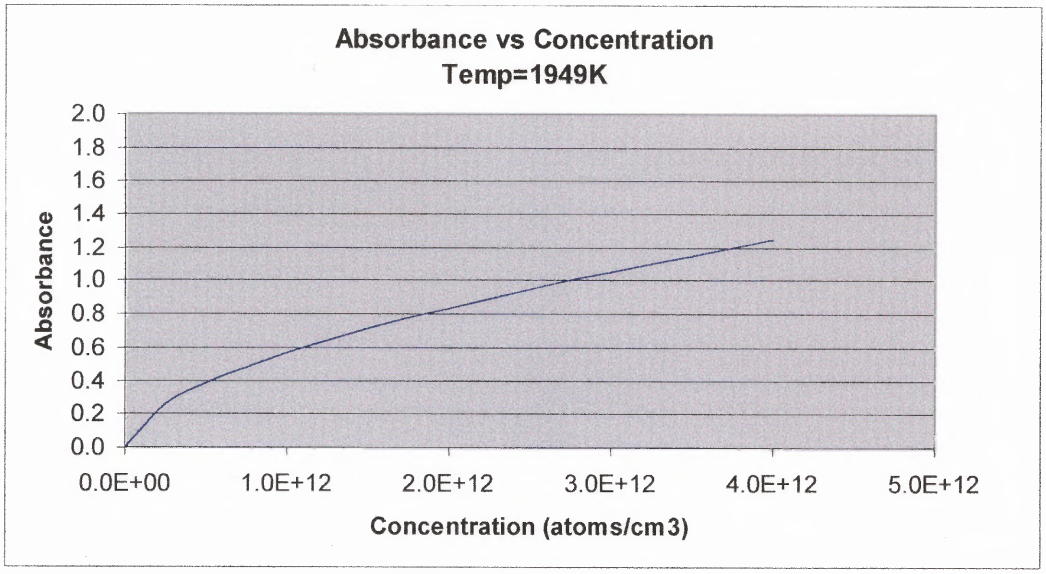

Figure 8.7 Non-Linear Absorbance versus Concentration Profile for a Methane/Air flame that has been doped with Sodium, $\phi = 1.86$

Note the non-linearity of the curve i.e., deviation from Beer's law. When a family of these curves was generated at various temperatures, a plot of absorbance versus HAB can be converted to absolute concentration of sodium atoms versus HAB. This conversion is illustrated in the following two graphs for a methane/air/sodium flame, $\phi = 1.86$.

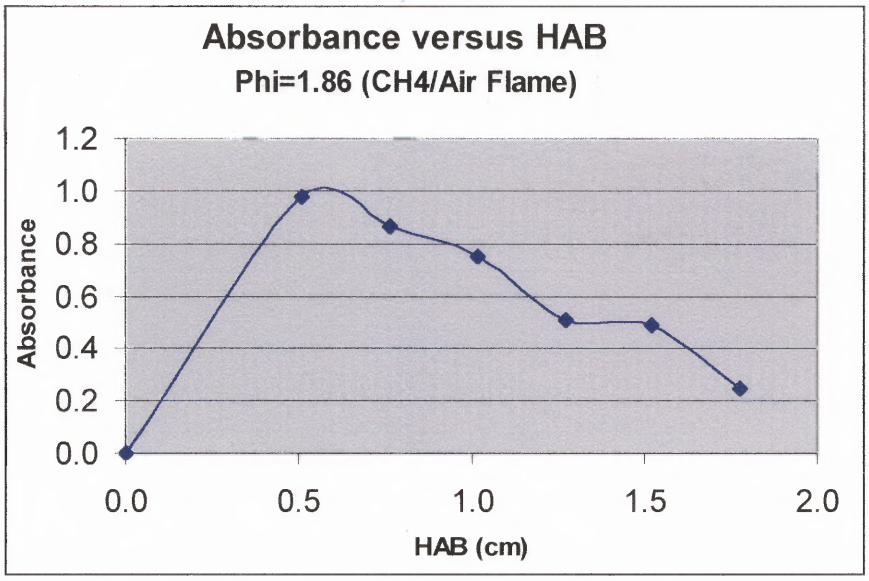

Figure 8.8 Absorbance vs. HAB for Sodium in a Methane/Air Flame, Phi=1.86

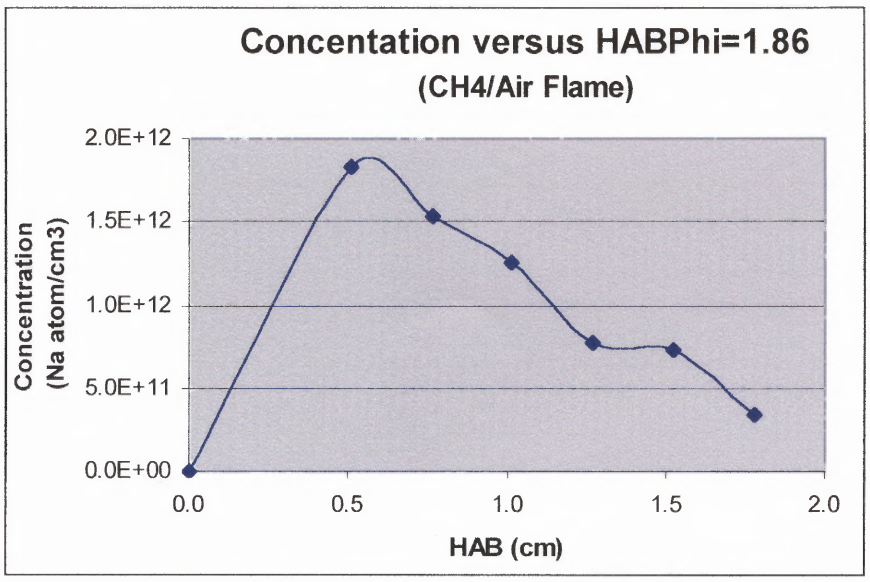

Figure 8.9 Concentration vs. HAB for Sodium in a Methane/Air Flame, Phi=1.86

As can be seen from the above figures, the profile of absorbance vs. HAB is similar in shape to that of concentration vs. HAB. In addition, the trends

observed in the absorbance versus HAB profiles in chapters 6 and 7 for methane/air and methane/methyl chloride/air flames were mimicked when converted to concentration versus HAB profiles. Sample conversions are represented by the following graphs.

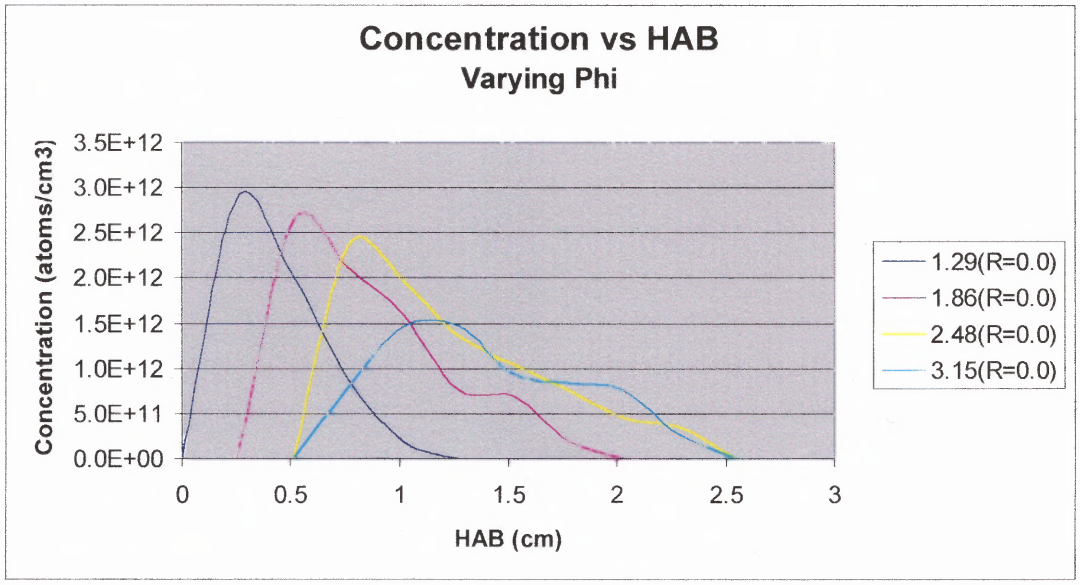

Figure 8.10 Concentration versus HAB Profiles for Methane/Air/Sodium Flames as Equivalence Ratio is Varied

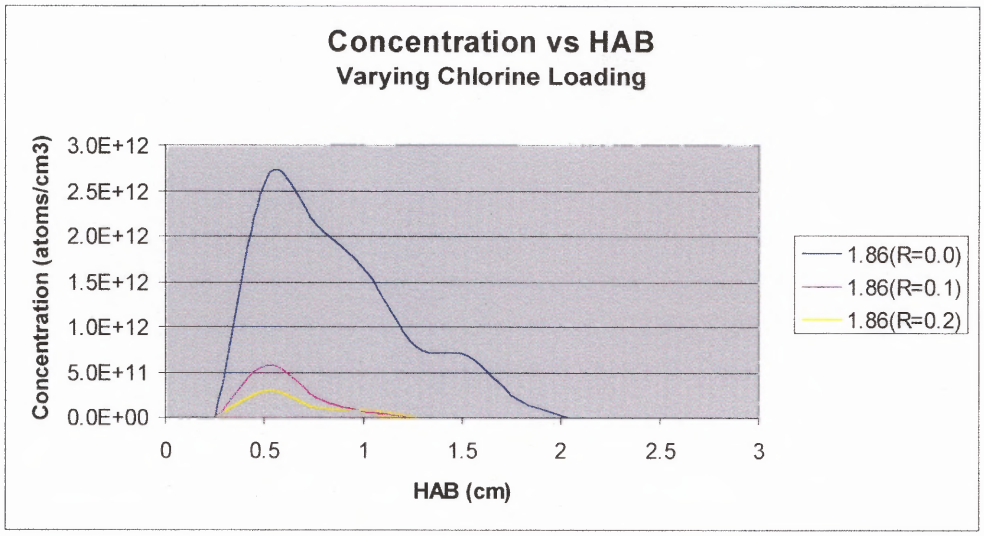

Figure 8.11 Concentration versus HAB Profiles for Methane/Methyl Chloride/Air/Sodium Flames as Chlorine Loading is Varied

As can be seen from the above figures, the maximum concentration of sodium atoms in the flame decreases with an increase in equivalence ratio as well as an increase in chlorine content. In addition, the location of maximum sodium atom concentration shifts to higher HAB with an increase in ϕ. Both of these trends were observed in the absorbance versus HAB profiles previously outlined in chapters 6 and 7.

8.1.2.2 Temperature Correction

The correction of flame temperature in this study work were flawed for the following reasons:

1. The flame temperature profiles collected during the course of this study were corrected for heat loss due to radiation. The correction due to the

conductive heat lost along/through the thermocouple wires (diameter=0.2 mm) was neglected. This was an incorrect assumption because the thickness of the thermocouple wires were such that the conductive term in the following expression for the gas temperature, T_G, was <u>not</u> insignificant. The following expression for the gas temperature, T_G, is a result of the manipulation of the heat balance around the thermocouple bead when the heat transfer due to conduction along the thermocouple wire is included.

$$T_G = T_B + \frac{\sigma\varepsilon}{h}\left(T_B^4 - T_s^4\right) - \frac{2k_w a_c}{ha}\frac{dT}{dw} \qquad (8.16)$$

The above parameters that were not outlined in chapter 5 of the thesis are as follows; k_w is the thermal conductivity of the wire, a_c is the wire cross sectional area; a is the bead surface area; dT/dw is the change in temperature along the thermocouple wire per unit length. The following graph shows the order of magnitude of a typical temperature correction (ϕ = 1.86, CH_4/Air/Na flame) that accounts for conductive heat loss along the thermocouple wire:

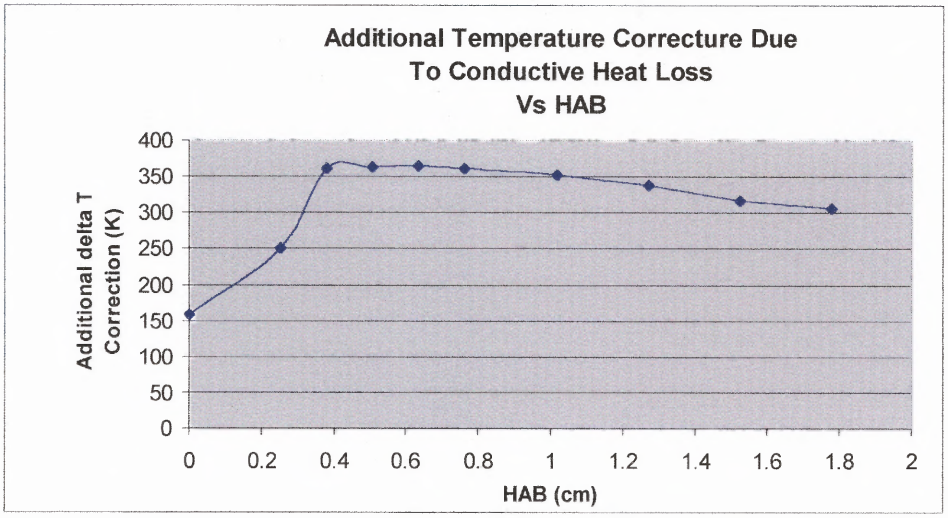

Figure 8.12 Additional Temperature Correction (K) Due to Conductive Heat Loss versus HAB

The relatively large thermocouple diameter was the most significant contribution to the size of the conductivity correction.

The following graph shows how the temperature correction due to conductive heat loss along the thermocouple wire varies as a function of thermocouple diameter.

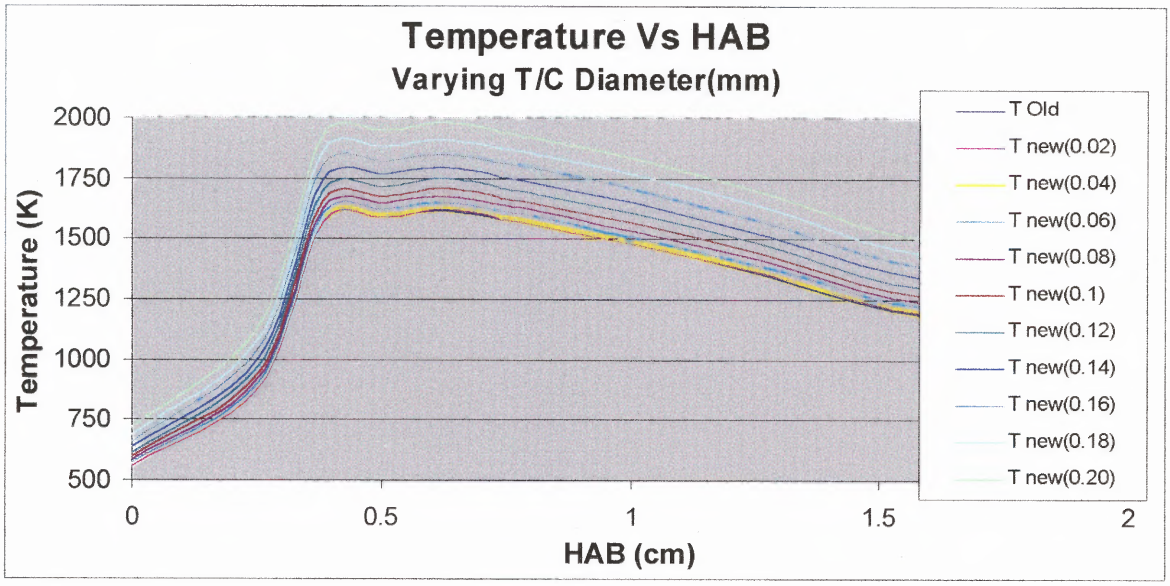

Figure 8.13 Temperature vs HAB as a function of Thermocouple Diameter for a Methane/Air Flame, ϕ=1.86

It can be seen that for any thermocouple wire with a diameter greater than 0.08 mm, the contribution to the temperature correction is 50K or larger. The following figure shows how the radiation correction affects the temperature profile of a methane/air/sodium flame (ϕ = 1.86) by comparing the temperature profile with and without the conductivity correction term.

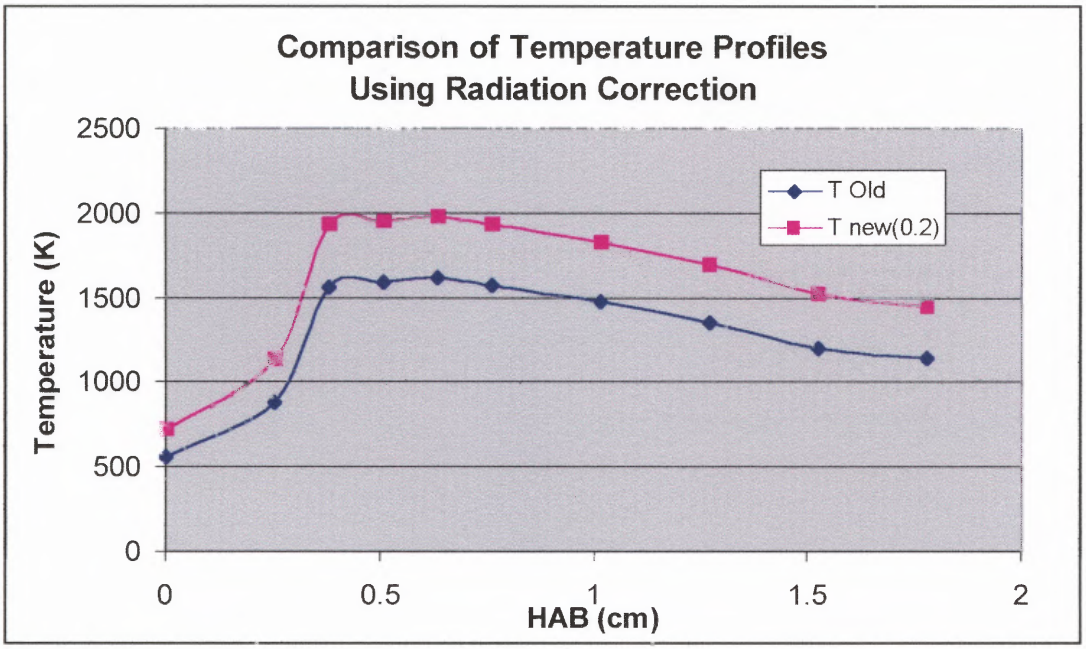

Figure 8.14 Comparison of Temperature Profile Correction With and Without Heat Loss due to Conduction Along the Thermocouple Wire

2. Ordinarily the two thermocouple wires are butt—welded so that there would be no detectable change in diameter, permitting the thermocouple to be modeled as a cylinder in a transverse flow field (34). In this study, the thermocouple wires were not butt—welded together but rather simply joined so as to form a bead. The resulting bead diameter was approximately 0.38mm, compared to a thermocouple wire diameter of 0.2mm.

8.1.2.3 Two Zone Flame

Examination of the CO_2 profiles of a CH_4/Air flame, with and without sodium (figure 6.19), showed that, at HAB greater than 1.5 cm, the CO_2 mole

fractions were reduced by as much as 75% in the flame without sodium. This was originally thought to be due to increased entrainment of air by the "faster", uninhibited CH_4/Air flame. However, this large amount of entrained air should have also manifested itself by significantly reducing the temperature profile of that flame—and it did not (see figure 6.6). Instead, the temperature profiles of the CH_4/Air flame and the CH_4/Air flame doped with sodium were remarkably similar. The effect of modified air entrainment is not evident in the CO_2 and temperature profiles equally. It is therefore necessary to develop an explanation of these results. The following hypotheses address discrepancies such as these and offer alternative ways of examining some of the data presented in this study.

The flames examined in this study have been simulated simply as *premixed* flat flames with air entrainment. However, it would be a more accurate description to describe them as flames consisting of two regions:

1. An inner premixed flame core—the primary combustion zone
2. An outer diffusion flame envelope

These two regions are illustrated in figure 8.15 Note should be taken that, for the slotted burner, the inner region of the flame has a rounded top as opposed to the pointed top typical of a round Bunsen flame.

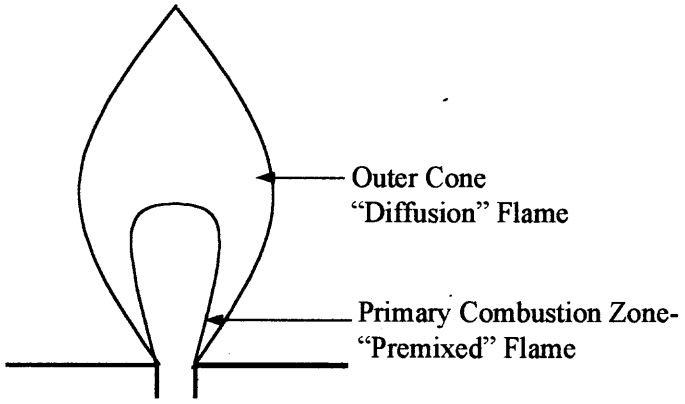

Figure 8.15 Illustration of Slotted Flame as Combination of Premixed Flame and Diffusion Flame (Side-View)

The primary combustion zone is similar to that of a shrouded, premixed flat flame. It consists mostly of a pre-heat zone where little reaction takes place. The edge of this primary combustion zone, i.e., the *interface* between the inner and outer zones (also known as the flame front or the reaction zone) is characterized by free-radical reactions that effect significant heat release. This thin reaction zone gives rise to a mixture of incomplete combustion products such as CH_4, CO, CO2 and H_2O—due to the premixed fuel-rich environment. It should be noted that, at this flame front, the oxygen used for the combustion of CH_4 is predominantly oxygen that was *fed* to the burner premixed with the fuel.

The outer region of the flame, also known as the outer cone, has the characteristic of a diffusion flame. In this region, additional oxygen used for combustion *diffuses* into the flame from the environment. This additional oxygen facilitates further conversion of the CH_4 and CO to CO_2 and H_2O.

8.1.2.4 Entrainment Expression

If the flame is re-examined as a two-zone flame, then by necessity, the expression that accounts for entrainment i.e., mass transfer, of species form the surroundings needs to be re-examined also. It has already been acknowledged that the expression for air entrainment presented in chapter 5 of this thesis was a coarse first approximation. It is postulated that no mass transfer of species occurs in the pre-mixed region of the flame. Instead mass transfer of species occurs in the diffusion section of the flame. The inclusion of mass transfer in the flame code would be effectively "turned off" until a HAB equal to the location of the interface between the outer and inner zone was reached. Then, the inclusion of mass transfer of species from the surroundings would be "turned on" in the code.

Experimentation of accounting for mass transfer of species from the surroundings, according to the above description, has already begun using a perfectly stirred reactor (PSR) code. Indeed, it has even been taken one step further from the above discussion in that mass transfer of species *from the flame to the surroundings* is also included e.g., the mass transfer driving force of CO_2 concentration is positive in the direction of the flame to the surroundings. The results show that the total mass flow rate in the flame changes only slightly from the initial mass flow rate. However, even though these results are preliminary, they clearly indicate the original expression used for entrainment needs to be critically re-examined and revised.

8.1.2.5 Sodium Ion Reactions

Re-examination of the sodium ion to atom conversion suggests that aqueous $NaNO_3$ solution aspirated into the flame does not produce Na^+ which then is directly converted to Na as suggested. Instead, elevated gas temperatures causes water evaporation which then produces a solid sodium ionic compound. Pyrolosis of this solid compound then produces sodium atoms. Therefore, the three sodium ion reactions presented in table 6.6 in chapter 6 should be removed the reaction mechanism.

8.1.2.6 Two-Dimensional Flame

In order to accept the initial hypothesis that these flames could be accurately simulated with a one-dimensional (1-D) model, one would also have to assume perfect transverse mixing across the flame. A 1-D flame such as this would produce profiles similar to those observed in a flat flame. This 1-D model ignored the two visible zones of the slotted flame.

However, for this study, the species produced at the flame front (e.g. CO), begin to diffuse *inwards* towards the interior of the premixed zone and *outwards* towards the diffusion zone. As a result, horizontal concentration profiles are created. Therefore, a 1-D simulation is unrealistic and a 2-D simulation (horizontal as well as vertical) is required. This lateral diffusion pathway of the stable species is described by figure 8.16.

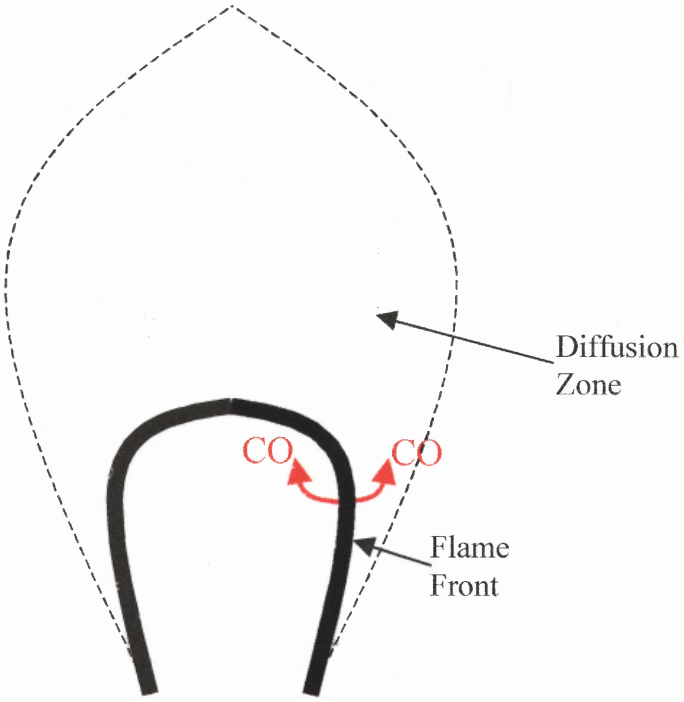

Figure 8.16 Schematic of Horizontal Diffusion Pathway for Stable Species

In accordance with Fick's law, the diffusion of a given species, such as CO, is dependent upon the following relationship:

$$J \approx -D\left(\frac{\Delta C}{\Delta x}\right) \tag{8.17}$$

and,

$$\Delta C = C_1 - C_0 \tag{8.18}$$

where J is the mass flux of the species; C_0 and C_1 are its concentrations at the flame front and just outside the flame front, as indicated in figure 8.17; D is the diffusion coefficient and Δx is the distance between the positions at which the concentrations C_0 and C_1 are measured.

Figure 8.17 depicts the hypothetical local concentrations of CO for a finite element of the reaction zone for flames with and without sodium. Note that $C_0 > \{C_1$ with Na$\} > \{C_1$ w/o Na$\}$.

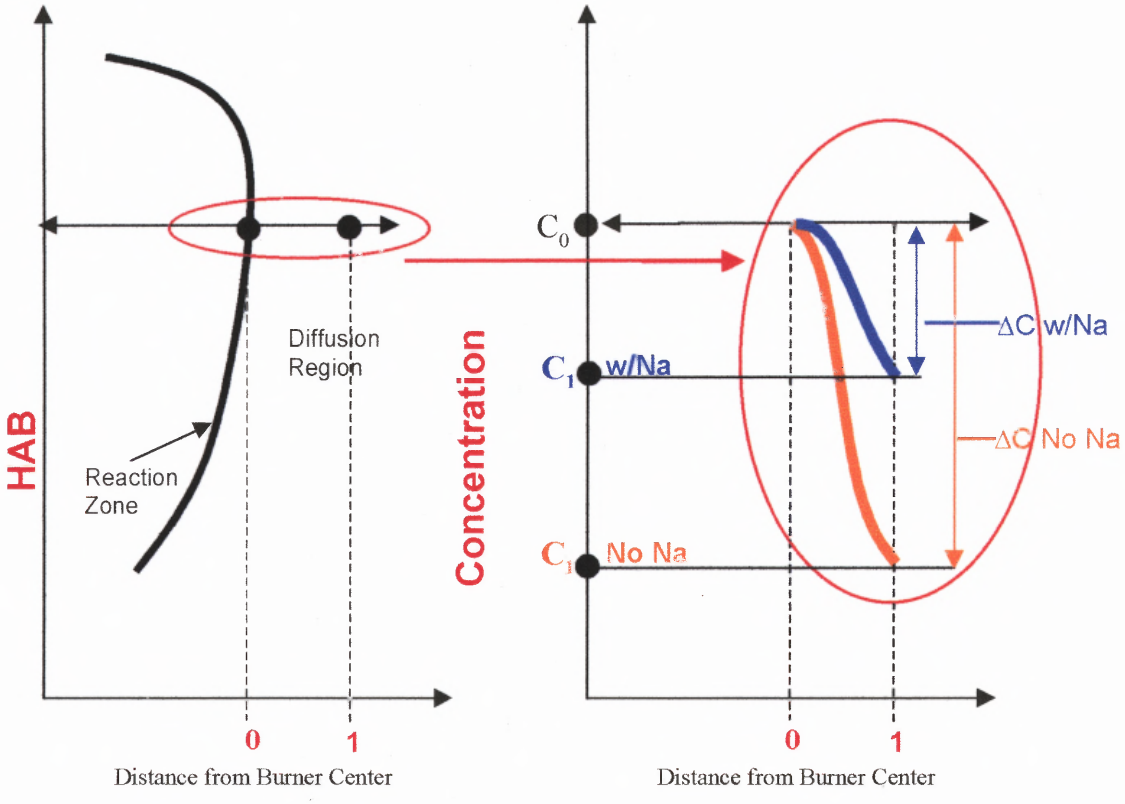

Figure 8.17 Local Concentration Gradients of CO for Finite Element of Reaction Zone for Flames With and Without Sodium

The presence or absence of sodium in the flame thus affects the local concentration gradient, which in turn affects the diffusion flux, which ultimately affects the concentration profiles.

The CO produced at the flame front has the potential to diffuse in two directions:

- inward towards the inner core
- outwards towards the diffusion region

According to Fick's law (eq. 8.17), the driving force that governs the rate and direction of diffusion of CO is the magnitude of the concentration gradient, which is proportional to $-\Delta C = C_0 - C_1$. Assuming that the concentration of CO produced at the flame front, C_0, is approximately equal for flames with and without sodium, the driving force is therefore dependent upon C_1, the amount of CO that remains in the diffusion region or the inner core after CO is converted to CO_2. The deviation in the value of C_1 is dependent upon whether or not sodium is present in the flame. Therefore, one of the following two concentration profiles may exist:

1. *Sodium Free Flame*

   Relative to the inner core, there is greater conversion of CO to CO_2 on the diffusion side of the reaction zone due to the greater availability of oxygen and free radicals in the diffusion region. This conversion of CO to CO_2 creates a CO sink just outside the reaction region. The difference between the CO concentration at the reaction zone and the CO concentration just

outside the reaction zone creates the driving force for mass transfer of CO, i.e. the flux. Since the CO sink created by the conversion of CO to CO_2 is different in the diffusion region compared to the inner core, the flux of CO into each region was is different. This difference in diffusion rates *away* from the reaction zone for a sodium free flame is illustrated in figure 8.18.

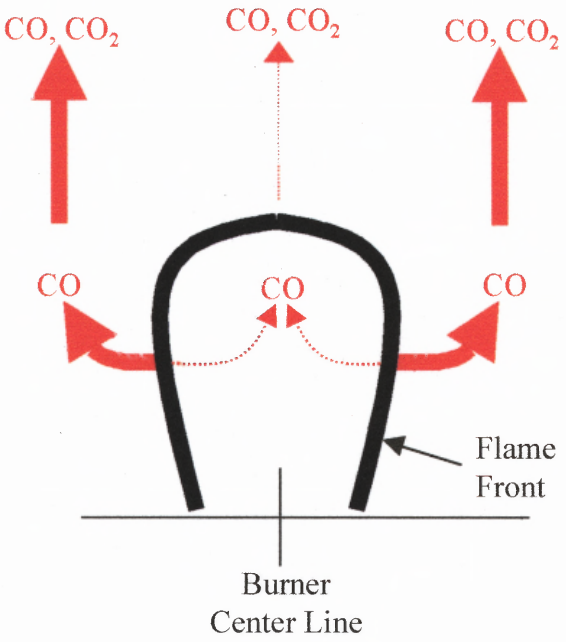

Figure 8.18 Relative Diffusion Rates of CO Away from the Flame Front—Sodium Free Flame

It is clear from the above figure that a considerable amount of the CO (and the resulting CO_2) diffuses outward from the flame front towards the outer region of the flame in a sodium free flame. Since stable species sampling occurred along the centerline of the flame, relatively lower

amounts of CO and CO_2 would be measured (figures 6.18 and 6.19—data only).

2. *Sodium is Present in the Flame*

In the diffusion region just outside the reaction zone, the sodium reactions inhibit oxygen utilization by competing with CO for available OH. As a result, the rate of the CO to CO_2 conversion is retarded in the presence of sodium and the driving force for the mass transfer of CO towards the diffusion region is decreased relative to the sodium free flame. The relative diffusion rate of CO away from the reaction zone in a flame that has been inhibited by sodium is illustrated in figure 8.19.

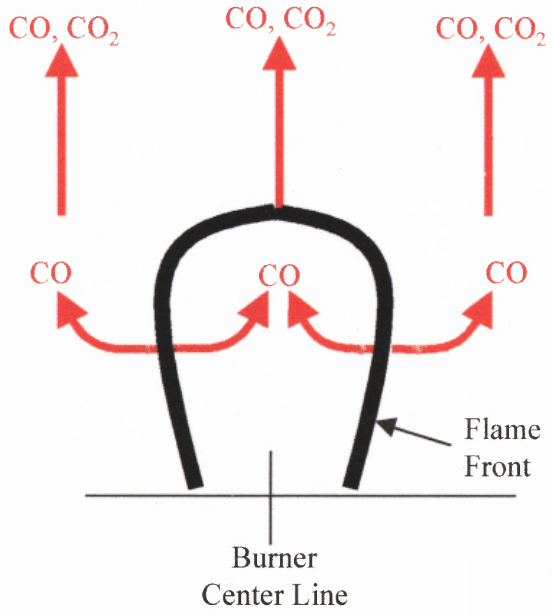

Figure 8.19 Relative Diffusion Rates of CO Away from Flame Front—Flame Inhibited by Sodium

In the case of the flame that has been inhibited by sodium, there is decreased driving force for the CO towards the diffusion region, relative to the sodium free flame. However, since stable species sampling occurred along the centerline of the flame, relatively larger amounts of CO and CO_2 would be measured (figures 6.18 and 6.19—data only).

As stated earlier, the effect of modified air entrainment did not manifest itself in the stable species and temperature profiles equally. This theory forms the working hypothesis that explains the significant difference between the CO and CO_2 profiles that was not evident in the temperature profiles.

8.1.2.7 Sodium—Chlorine Reaction Subset

A review of the reactions that accounted for the interactions between sodium and chlorine (Appendix D—Part I) showed that further examination of the rate constants of these reactions was necessary. The re-evaluated rate constants for the sodium—chlorine interactions can be found in Appendix D (Part II).

For all but two of the reactions, the pre-exponential factors, A, and the activation energies, E_a, used to calculate the rate constants were estimated from Evans-Polanyi relationships of ΔH_{rxn} versus E_a (energy of activation). Evans, Polanyi and Eyring are considered to be responsible for the present formulation of the equilibrium theory of reaction rates known as transition state theory (TST) (79). This method proposes that every molecule A that reacts does so by being excited to some state $A^{\#}$ at an energy $E^{\#}$, the critical

energy for the reaction. A# will then have the configuration that corresponds to a maximum in its potential energy. This configuration is referred to as the transition state. In addition to the Evans-Polanyi estimations, data from the literature (NIST Kinetics DataBase, Tabulations of Kerr and Moss, Benson) for generic systems (see Appendix D, Part II) were utilized to estimate the rate constants.

Somewhat more rigorous calculations were required to estimate the rate constants in the case of two of the sodium-chlorine reactions—specifically $NaO + HCl \rightarrow NaCl + OH$ and $NaO_2 + HCl \rightarrow NaCl + HO_2$. It should be noted that for this work, the rate constant, k, was expressed in the following manner:

$$k_f = A \cdot T^n \exp\left(\frac{-E_a}{RT}\right) \tag{8.19}$$

In these two cases, semi-empirical molecular orbital methods (MO) PM3 in the MOPAC 6.0 package were used to estimate thermodynamic parameters for the specific reaction systems (reactants, transition states and/or pre-encounter complexes and products). Systematic MO calculation studies have shown that these calculation methods provide correct fundamental vibrational frequencies and moments of inertia (from calculated molecular structures), leading to reliable results of entropies and heat capacities (77). The predicted entropies and heat capacities were therefore used directly with the packaged software, AFACT, to estimate a value for the

pre-exponential factors, A, and the temperature exponent, n, for each reaction.

Note: The results of these calculations for the parameters A and n along with sample output from AFACT are also presented in Appendix D (Part II and III).

The following table lists the thermodynamic properties for the transition states/pre-encounter complexes for these two reaction systems:

NaOHCl ≡ Pre-encounter Complex for $NaO + HCl \rightarrow NaCl + OH$

NaOOHCl ≡ Pre-encounter Complex for $NaO_2 + HCl \rightarrow NaCl + HO_2$

It should be noted that a transition state was sought for each of these reactions but none were found. Instead, pre-encounter complexes were located. Quite simply, the difference between pre-encounter complexes and transition states can be described in the following manner: pre-encounter complexes have minimum energy in all directions while transition states have minimum energy in all directions but one.

Table 8.1 Ideal Thermodynamic Gas Phase Properties; ΔH_{f298} (kcal,mol), S_{298} (cal/mol-K), and $C_p(T)$ (cal/mol-K), 300K < T < 1500K

Species	TNaOHCl	TNaOOHCl
HF(298)	-132	-151.96
S(298)	75.06	74.03
CP300	15.37	15.36
CP400	15.60	16.51
CP500	15.75	17.49
CP600	15.88	18.32
CP800	16.19	19.59
CP1000	16.49	20.51
CP1500	17.05	21.89

The PM3 semi-empirical molecular orbital calculations (MOPAC PM3) were not considered reliable for enthalpy calculations however. Instead, the total energy of the reactants, products and the pre-encounter complexes, were calculated using high level ab initio methods. Two model chemistries were employed using the Gaussian package (85). The G2 (Gaussian 2) method (82,83) uses combinations of large basis sets and various theoretical methods that account for increasing degrees of electron correlation to make an accurate estimate of the free energy of formation of a particular molecule. The errors associated with G2 estimates are typically 1-3 kcal/mol. The second method is based on density functional theory (DFT) (86). Electron correlation is evaluated using exchange and correlation functionals. For the calculations presented below, the B3LYP functional (Becke 3 parameter exchange functional and the Lee-Yang-Parr correlation functional) is used (81), together with a large basis set 6-311G(3df,2dp) to evaluate the energy.

The molecular geometry is found using the smaller 6-31G(d) basis set. The errors associated with this method are also typically 1-3 kcal/mol (80).

Gaussian 98 is capable of predicting many properties of molecules and reactions including: molecular energies and structures, energies and structures of transition states, and bond and reaction energies (80). B3LYP and Gaussian 2 (G2) are effective tools for computing the total energies of molecules at their equilibrium geometries. The total energy of the molecule, i.e. the Gibbs free energy of formation ΔG_f^0, is then used to determine ΔG_r^0, the free energy change of the reaction itself.

Tables 8.2(a) and 8.2(b) list the total energies (calculated and published) for all of the species in the previously described reactions.

TABLE 8.2(a): Calculated Total Energies[a,b] for Species in Reaction Schemes

Species	G2 at 298 K[a]	B3LYP/ 6-311 at 298 K[b]	B3LYP/ 6-311 at 1500 K[b]
NaO	-236.94	-237.45	-237.57
HCl	-460.36	-460.81	-460.91
NaCl	-621.70	-622.58	-622.70
OH	-75.66	-75.73	-75.83
NaO_2	-312.06	-312.64	-312.78
HO_2	-150.75	-150.91	-151.03
NaOHCl	n/a	-698.34	-698.51
NaClOHO	n/a	-773.47	-773.66
NaO_2HCl	n/a	-773.52	-773.71

[a] Total energy calculations based on G2 theory. Units in Hartrees.
[b] Total energy calculations based on the geometries optimized at B3LYP/6-311 level of theory. Units in Hartrees.

TABLE 8.2(b): Published Total Energies[a] for Species in Reaction Schemes

Species	Literature at 298 K[a]	Literature at 1500 K[a]
NaO	14.65	4.02
HCl	-22.78	-24.81
NaCl	-48.12	-55.80
OH	8.19	3.86
NaO_2	n/a	n/a
HO_2	3.45	16.98
NaOHCl	n/a	n/a
NaClOHO	n/a	n/a
NaO_2HCl	n/a	n/a

[a] "JANAF Thermochemical Tables, 3rd Edition." J. Phy. And Chem. Ref. Data vol 14 . Units in kcal/mol

The total energies were then used to compute the free energies of reaction for the *NaO+HCl* and *NaO_2+HCl* exchange reactions. Literature values provide the necessary information to check the theoretical G2 and B3LYP estimates. The results are presented in Table 8.3. The estimates of the ΔG_r using B3LYP at 298K and 1500K are –33.9 and –33.5 kcal/mol respectively. The estimates from the JANAF table thermochemistry are –31.8 and –31.1 kcal/mol, respectively (78). Thus the B3LYP calculations are within ~2 kcal/mol of the experimental results. The B3LYP results correctly predict a small temperature effect.

TABLE 8.3: Free Energies of Reaction at 298 and 1500 K (Units in kcal/mol)

Reaction Series	298 K[a]	298 K[b]	298 K[c]	1500 K[a]	1500 K[c]
NaO+HCl=NaOHCl	-51.57			-21.93	
NaO+HCl=NaCl+OH	-33.94	-39.23	-31.80	-33.55	-31.15
NaO_2+HCl=NaO_2HCl	-43.38			-13.52	
NaO_2+HCl=NaClOHO	-11.06			12.33	
NaO_2+HCl=NaCl+HO_2	-26.17	-23.28		-32.12	

[a] from B3LYP/6-311 theory
[b] from G2 theory
[c] "JANAF Thermochemical Tables, 3rd Edition." J. Phy. and Chem. Ref. Data, vol. 14

Table 8.4 outlines the estimated values of the bond lengths and bond angles for all of the reactants, pre-encounter complexes and products involved in the previously described reactions. It should be noted that literature values were available for comparison for the bond lengths of the reactants and products. In addition, the literature value of the HO_2 bond angle was also available. It is seen that the results compared quite favorably.

TABLE 8.4: Geometric Parameters[a]

Species		Bond Length[b]	Bond Length[c]		Bond Angle[b]
NaO		1.928			
HCl		1.276	1.2746		
NaCl		2.388	2.3606		
OH		0.976	0.9706		
NaO_2	Na-O	1.964			
	O-O	1.308		∠ Na-O-O	179.29
HO_2	H-O	0.984	0.977		
	O-O	1.324	1.335	∠ H-O-O	104.60[b]
					104.1[c]
NaOHCl	Na-O	2.134			
	O-H	0.969		∠ Na-O-H	122.71
	H-Cl	2.582		∠ O-H-Cl	78.88
	Cl-Na	2.484		∠ H-Cl-Na	66.54
				∠ Na-O-H-Cl[d]	-47.80
				∠ O-H-Cl-Na[d]	35.69
NaClOHO	Na-Cl	2.741			
	Cl-O	1.793		∠ Na-Cl-O	53.26
	O-H	1.427		∠Cl-O-H	100.54
	H-O	1.127		∠ O-H-O	151.72
	O-Na	2.265		∠ H-O-Na	70.76
				∠ Na-Cl-O-H[d]	68.63
				∠ Cl-O-H-O[d]	-90.00
				∠ O-H-O-Na[d]	7.95
				∠ H-O-Na-Cl[d]	36.90
NaO_2HCl	Na-O	2.312			
	O-O	1.322		∠ Na-O-O	108.00
	O-H	1.034		∠ O-O-H	105.48
	H-Cl	1.954		∠ O-H-Cl	165.52
	Cl-Na	2.465		∠ H-Cl-Na	71.23
				∠ Na-O-O-H[d]	0.00
				∠ O-O-H-Cl[d]	0.00
				∠ O-H-Cl-Na[d]	0.00
				∠ H-Cl-Na-O[d]	0.00

[a] Distances in angstroms and angles in degrees.
[b] from G2 theory.
[c] from "JANAF Thermochemical Tables, 3rd Edition." J. Phy. and Chem. Ref. Data, vol 14
[d] Dihedral angle

The free energies of reaction at 298 and 1500 K were used to construct potential energy diagrams for the $NaO + HCl$ and $NaO_2 + HCl$ reactions. These can be seen in figures 8.20 and 8.21, respectively. It should be noted

that extensive searches using B3LYP/6-31G(d) model chemistry produced no transition states for either reaction. However, pre-encounter optimums were found for both reactions. Therefore the reaction is assumed to proceed without passing through a transition state.

For the reaction, *NaO + HCl = NaCl + OH* at 298K, the pre-encounter complex, NaOHCl is 17.9 kcal/mol below the products (Fig. 8.20a), indicating a slow reaction rate. However, at 1500K the minimum disappears (Fig. 8.20b) and the reaction is favored throughout.

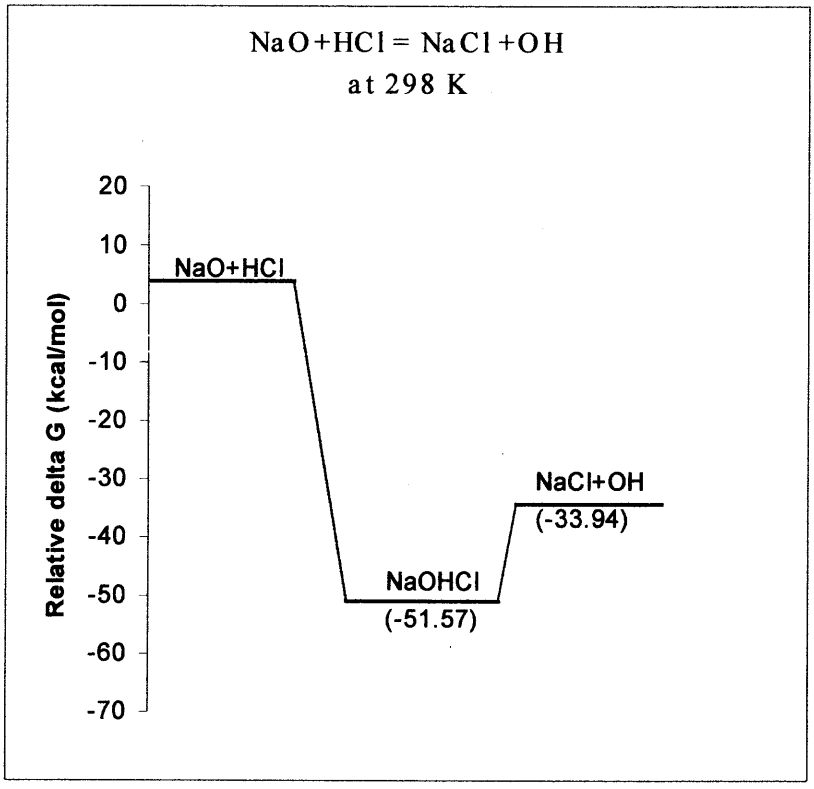

Figure 8.20(a) Potential Energy Diagram forNaO + HCl at 298 K

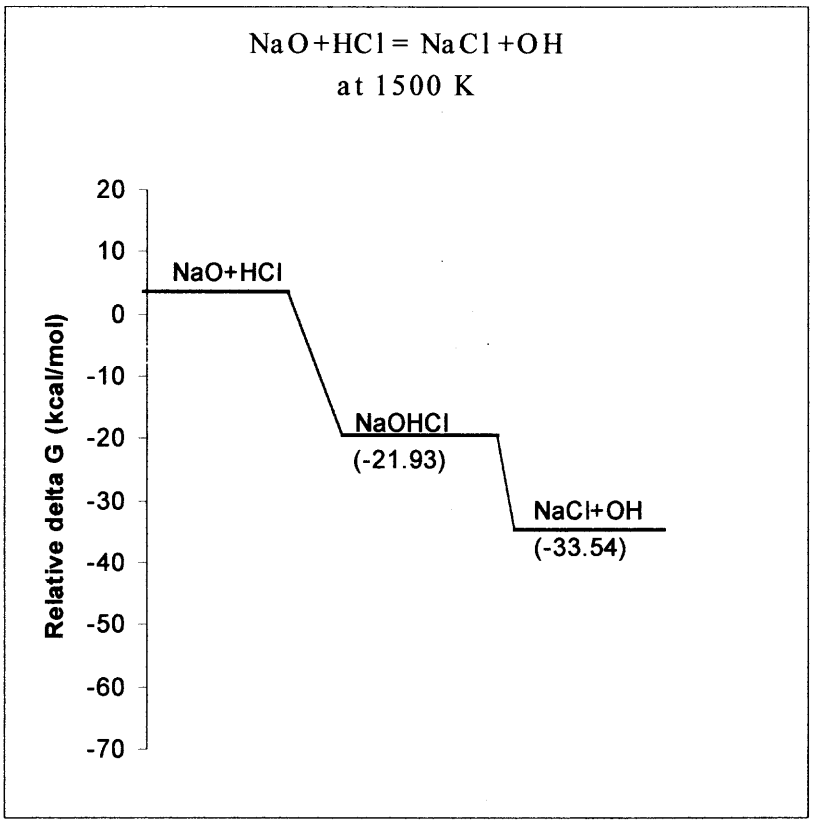

Figure 8.20(b) Potential Energy Diagram for NaO + HCl at 1500 K

The following observations were made from figures 8.20a and 8.20b:

- The reaction is exothermic.
- A stable pre-encounter complex exists. However, there is no evidence of the existence of a transition state i.e., one was not found
- Comparison of the reaction at 298 K and 1500 K indicates that the pre-encounter complex has strong temperature dependence (≈-51 kcal/mol vs. ≈-22kcal/mol, respectively). However, ΔG_r^0 does not (-33.9421 kcal/mol vs. –33.5462 kcal/mol, respectively).

- The pre-encounter complex for the *NaO + HCl* reaction lies *below* the reactants. Therefore, the activation energy, E_a, is assumed zero with respect to the estimation of the reaction rate constant.

For the reaction, $NaO_2 + HCl = NaCl + HO_2$ at 298K, there are two pre-encounter complexes, NaClOHO and NaO2HCl. The latter is 17.2 kcal/mol below the products, again suggesting that the reaction would be slow at room temperature, since this barrier must be crossed. However, at 1500K, NaO2HCl is above the products and the reaction is favored throughout.

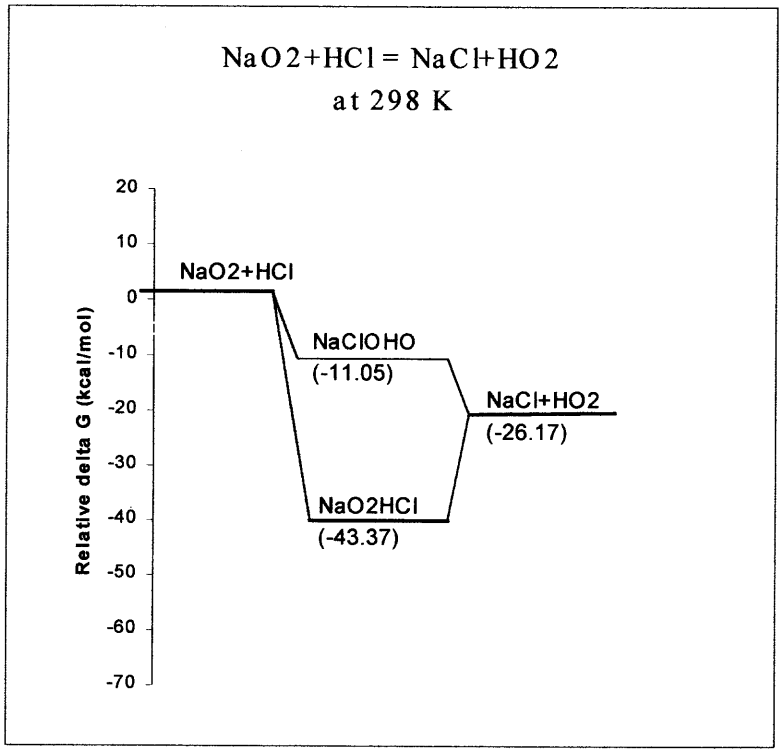

Figure 8.21(a) Potential Energy Diagram for NaO_2 + HCl at 298 K

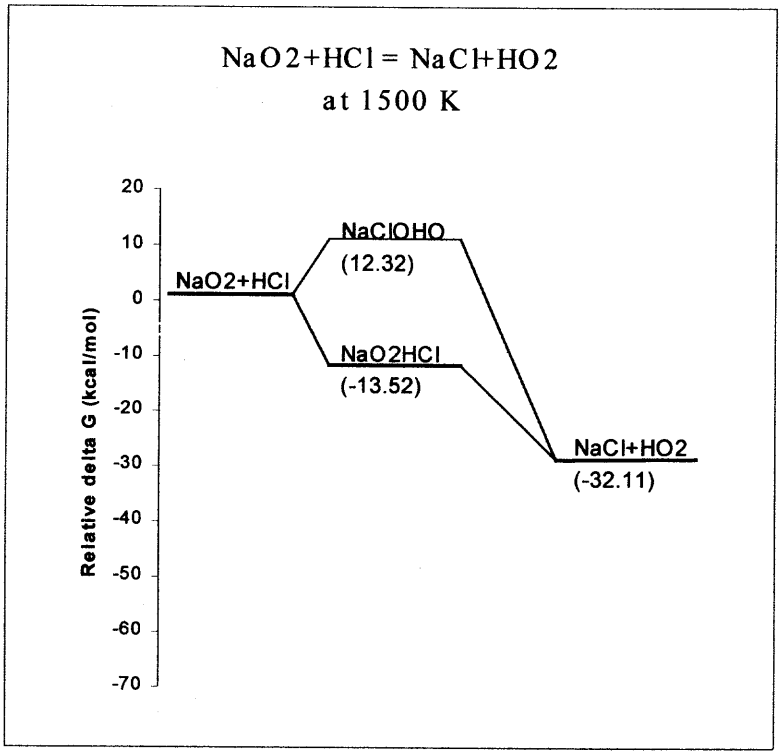

Figure 8.21(b) Potential Energy Diagram for NaO_2 + HCl at 1500 K

Examination of figures 8.21a and 8.21b resulted in the following observations:

- The reaction is exothermic.
- There is evidence of two different pre-encounter complexes, namely NaClOHO and NaO_2HCl. As with the previous reaction, there is no evidence of the existence of a transition state i.e., one was not found.
- NaO_2HCl is more energetically favored at 298 K relative to NaClOHO. Therefore, it is reasonable that the dominant pre-encounter complex at 298 K would be NaO_2HCl.

- From an energetically stable perspective, it is unlikely that the pre-encounter complex NaClOHO would form at 1500K.
- As with the $NaO + HCl$ reaction, all of the viable pre-encounter complexes lie *below* the reactants for the $NaO_2 + HCl$ reaction. Therefore, the activation energy, E_a, is assumed zero with respect to the estimation of the reaction rate constant.

Therefore the theoretical calculations support the importance of both reactions. Each are found to be thermodynamically favored at 1500K by ~30 kcal/mol.

A pictorial description of both reaction pathways outlined in the potential energy diagrams may be seen in figures 8.22-8.23.

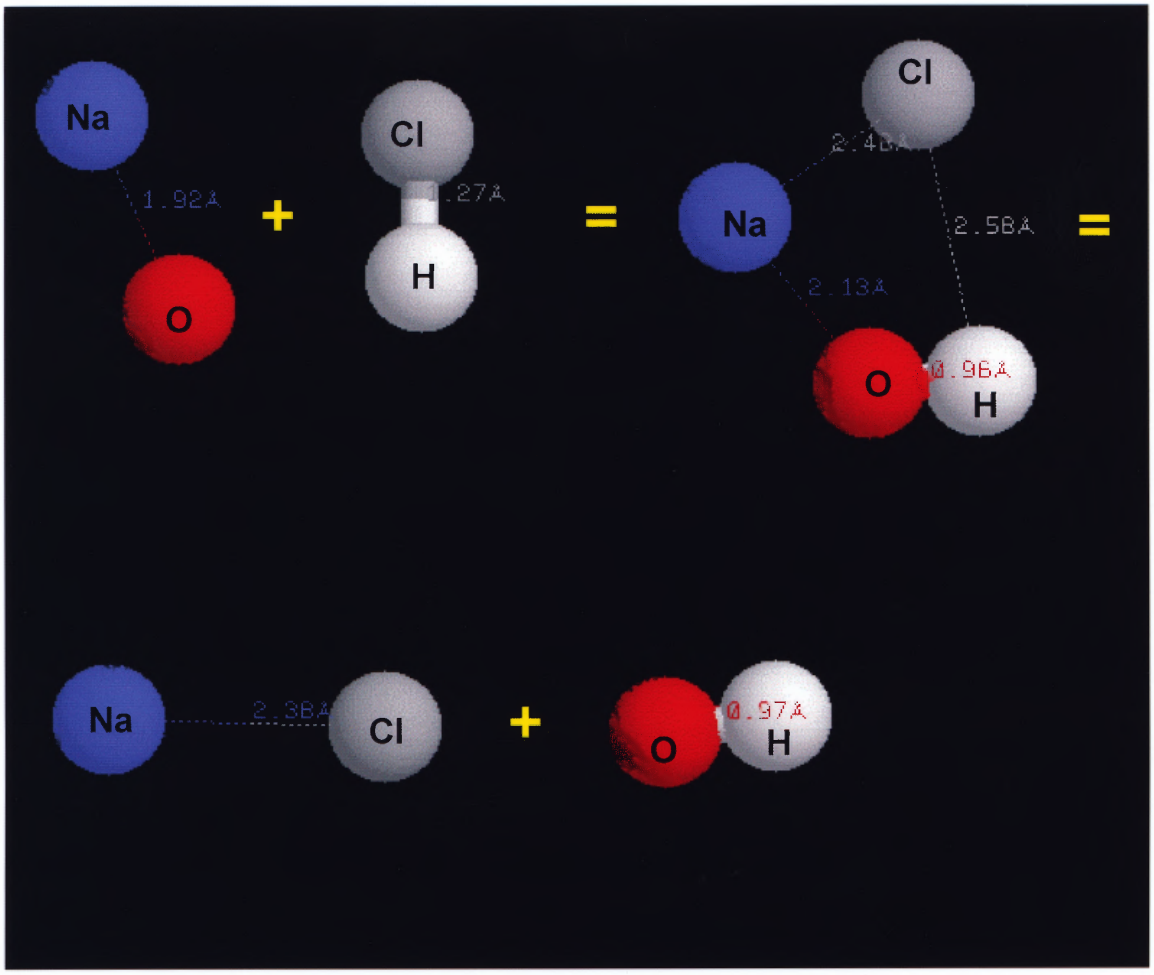

Figure 8.22 Pictorial Description of Reaction Pathway for $NaO + HCl \rightarrow NaOHCl \rightarrow NaCl + OH$

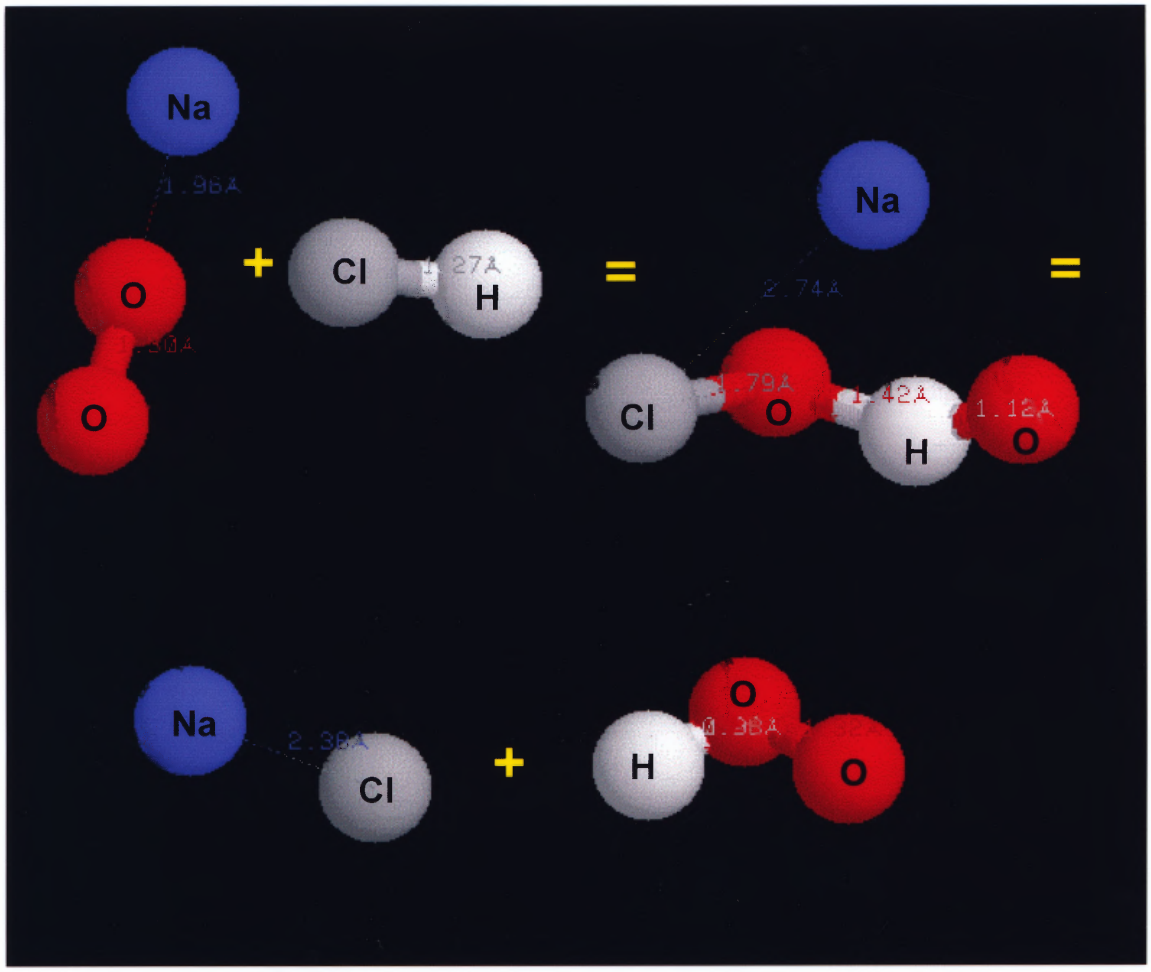

Figure 8.23(a) Pictorial Description of Reaction Pathway for
$NaO_2 + HCl \rightarrow NaClOHO \rightarrow NaCl + HO_2$

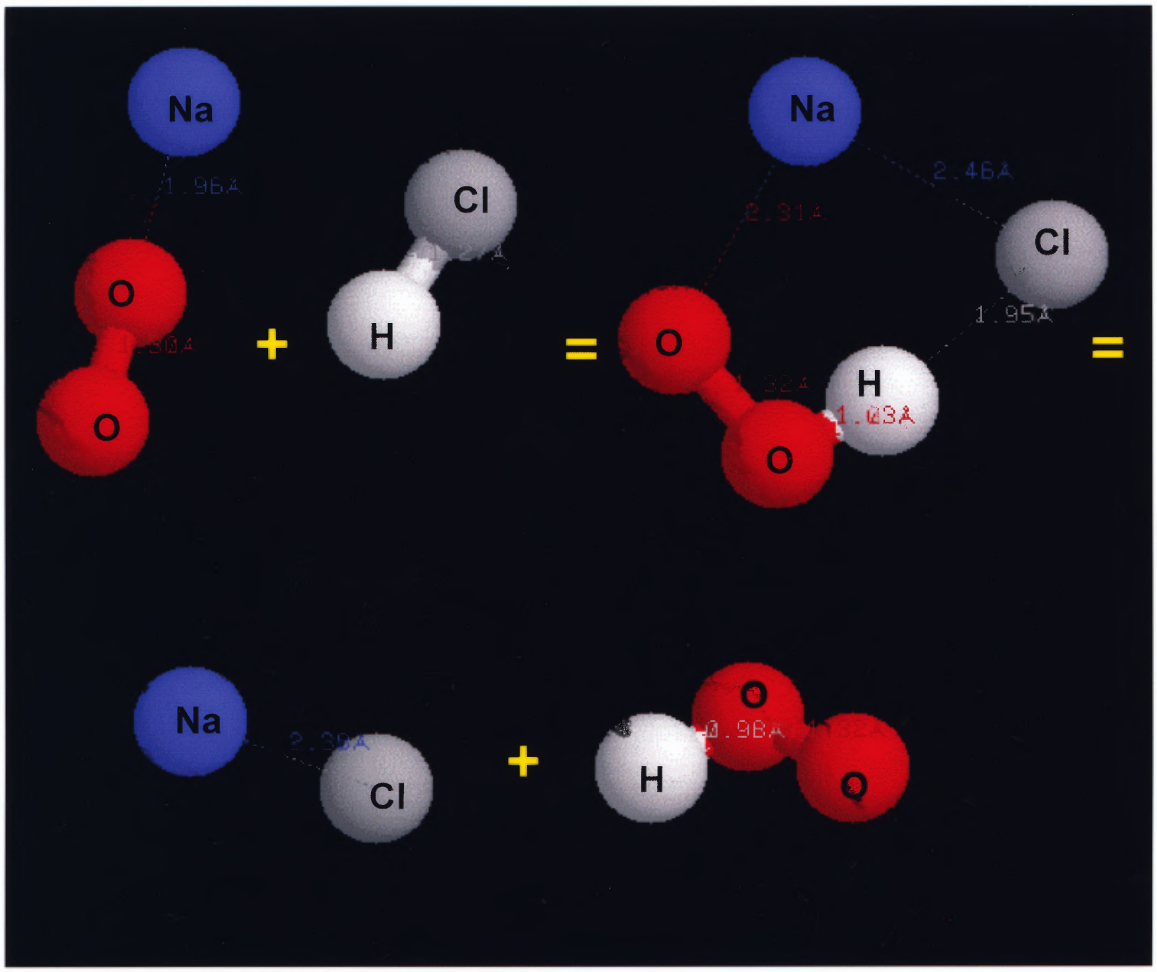

Figure 8.23(b) Pictorial Description of Reaction Pathway for
$NaO_2 + HCl \rightarrow NaOOHCl \rightarrow NaCl + HO_2$

8.2 Work in Progress and Recommendations for Future Work

While the 1-D model of these flames provided some utility and appeal, the data, upon even closer scrutiny, warrant a more sophisticated modeling approach. Such an effort, centering on development of a 2-D simulation, represents a next generation for this research. Work is in progress on both semi-quantitative (less complex) and 2-D (more complex) options to simulate these flames.

8.2.1 Horizontal Stable Species Profiles

It has been established in section 8.1.2 that the slotted flame used in this study would be better modeled as a two-dimensional (2-D) flame, i.e., horizontal as well as vertical. It is therefore desirable to re-assemble the experimental apparatus and collect horizontal stable species profiles, e.g., CH_4, CO, and CO_2, for the CH_4/Air and CH_4/CH_3Cl/Air flames with and without Na at ϕ=1.86.

8.2.2 Model the Slotted Flame as Two-Zone Flame

For the duration of this study, this flame has been described as a premixed flame that experienced entrainment of air. Upon further evaluation of the results of this study, an alternative description of this flame as a premixed inner core surrounded by a secondary diffusion region has been postulated. In other words, the inner core has access only to the oxygen that has been fed to

the burner and experiences little or no entrainment of outside air while the outer mantle has access to whatever oxygen remains from the original feed as well as oxygen that diffuses into the flame from the surroundings. The existing 1-D CHEMKIN code can be easily modified for semi-quantitative simulation. The entrainment constant is set to zero from zero HAB to a point roughly corresponding to the upper end of the inner core. Then the constant is set directly to its non-zero value for air entrainment. In this way, some semblance of the 2-zone nature of these flames is recognized.

8.2.3 Modeling Slotted Flame as Two-Dimensional

The Chemkin Premixed flame code used to model the slotted flame in this study had the capability to model one-dimensional (1-D) flames only. An alternative flame code known as KIVA has been identified and will be evaluated regarding the capability of modeling 2-D slotted flames. KIVA3V, the latest and most advanced version of KIVA, is a transient, three-dimensional, multiphase, multicomponent code for the analysis of chemically reacting flows with sprays and has been under development at the Los Alamos National Laboratory for the past several years. The range of validity of the code extends from low speeds to supersonic flows for both laminar and turbulent regimes. Arbitrary numbers of species and chemical reactions are allowed. Although specifically designed for performing internal combustion

engine calculations, the modularity of the code should allow modifications for simulating the 2-D slotted flames of this study.

8.2.4 Alternative Sodium Hydrocarbon Reaction Mechanisms

The sodium reaction mechanism that was used to model the sodium-methane interactions in this study was developed by Schoefield et al in 1984 (18). A more recent (1999) sodium-hydrocarbon reaction set has been developed by Zamansky et al. (36). This reaction set will be investigated in the re-modeling efforts. In addition, the entire sodium-chlorine reaction subset used to model the sodium-chlorinated hydrocarbon interactions will be re-evaluated.

APPENDIX A

SAMPLE OUTPUT FILE FOR FLAME MODEL

Sample Output File–Premix.out

The following output file is for the conditions outlined below:

1. CH_4/Air/Na Flame

2. ϕ=1.86

PREMIX: One-dimensional steady premixed laminar flame code
CHEMKIN-II Version 2.55d, January 1995
DOUBLE PRECISION

CKLIB: Chemical Kinetics Library
CHEMKIN-II Version 4.5, January 1995
DOUBLE PRECISION

TRANLIB: Multicomponent transport library,
CHEMKIN-II Version 3.8, January 1995
DOUBLE PRECISION

WORKING SPACE REQUIREMENTS

	PROVIDED	REQUIRED
LOGICAL	200	193
INTEGER	11000	10259
REAL	2300000	2050564
CHARACTER	100	89

KEYWORD INPUT

```
/ flame configuration, burner stabilized with specified temperature
BURN
/ENRG
TGIV
/ in the event of a Newton failure, take 100 timesteps of 1.E-6
TIME   100  5.00E-4
/ begin on a uniform mesh of 6 points
NPTS    6
/    definition of the computational interval
XEND    3.0
XSTR     0.0
/XCEN    0.16
/WMIX    0.10
/ pressure and inlet mass flow rate
PRES     1.0 (atmospheres)
/FLRT  (g/cm**2-sec)
FLRT     0.005
/ adaptive mesh criteria
GRAD  0.4
CURV  0.9
/ unreacted mole fractions
MOLE
REAC  CH4   1.5465E-01  0.0
REAC  O2    1.5688E-01  0.2
REAC  N2    6.2749E-01  0.8
REAC  NA+   2.1944E-05  0.0
REAC  H2O   6.0955E-02  0.0
/ estimated products
PROD  CO2    0.01
PROD  H2O    0.19
```

```
PROD  O2      0.1
PROD  N2      0.7
/  estimated intermediate mole fractions
INTM  CO      1.0E-2
INTM  H2      3.6E-3
INTM  CH2O    1.5E-3
INTM  C2H6    1.0E-3
INTM  C2H2    3.7E-4
INTM  C2H4    1.8E-3
INTM  CH3     7.2E-4
INTM  CH2     2.0E-7
INTM  CH2S    2.0E-8
INTM  C2H3    2.2E-6
INTM  C2H     2.9E-8
INTM  C2H5    8.9E-7
INTM  CH2CO   3.2E-5
INTM  HCCO    2.8E-5
INTM  OH      5.2E-4
INTM  H       1.0E-4
INTM  O       8.8E-5
INTM  HO2     2.1E-4
INTM  H2O2    1.8E-5
INTM  HCO     2.2E-6
INTM  CH3O    3.2E-5
INTM  NAO     3.0E-5
INTM  NAO2    3.0E-5
/  tolerances for the Newton iteration
ATOL  1.E-9
RTOL  1.E-4
/  tolerances for the time step Newton iteration
ATIM  1.E-9
RTIM  1.E-4
```

```
/  print control
PRNT   1
/     given temperature profile
TEMP    .0      560.
TEMP    .254    886.
TEMP    .381    1574.
TEMP    .508    1594.
TEMP    .635    1622.
TEMP    .762    1581.
TEMP    1.016   1481.
TEMP    1.27    1359.
TEMP    1.524   1211.
TEMP    1.778   1148.
TEMP    2.0     1000.
TEMP    3.0     800.
/TRANSPORT OPTION TAKING THERMAL DIFF USION
/TDIF
/read the solution from restart file
USTG
RSTR
/ASEN
END
```

TWOPNT: TWO-POINT BOUNDARY VALUE PROBLEM SOLVER,
VERSION 2.22D OF FEBRUARY 1994 BY DR. JOSEPH F. GRCAR.

DOUBLE PRECISION
PERMIT MESH REFINEMENT

TWOPNT: INITIAL GUESS:

	X	T	V	RHO	E	NA+	NA	NAOH	NAO2	NAO	HCO+
1	.0000	6.340E+02	9.878E+00	5.062E-04	4.882E-23	2.007E-05	7.359E-16	7.795E-09	7.617E-14	6.270E-17	1.120E-08
2	.1500	8.431E+02	9.956E+00	3.863E-04	-1.177E-36	1.620E-05	2.225E-15	3.189E-08	2.935E-13	2.248E-16	4.349E-08
3	.1875	8.953E+02	9.969E+00	3.648E-04	6.437E-34	1.531E-05	2.405E-14	5.113E-08	7.292E-13	1.108E-15	6.803E-08
4	.2250	9.476E+02	9.982E+00	3.455E-04	-1.053E-32	1.446E-05	9.012E-14	8.429E-08	7.532E-13	6.040E-15	1.091E-07
5	.2625	1.022E+03	1.021E+01	3.210E-04	-2.659E-31	1.361E-05	6.648E-13	1.398E-07	1.082E-12	3.896E-14	1.757E-07
6	.3000	1.171E+03	1.114E+01	2.806E-04	2.940E-27	1.278E-05	7.760E-12	2.277E-07	8.573E-13	3.698E-13	2.784E-07
7	.3187	1.245E+03	1.157E+01	2.639E-04	9.230E-26	1.237E-05	3.474E-11	2.892E-07	1.244E-12	9.431E-13	3.486E-07
8	.3375	1.319E+03	1.198E+01	2.492E-04	1.222E-22	1.195E-05	1.331E-10	3.659E-07	1.729E-12	2.061E-12	4.351E-07
9	.3563	1.394E+03	1.238E+01	2.359E-04	2.615E-20	1.153E-05	4.548E-10	4.609E-07	2.354E-12	4.095E-12	5.407E-07
10	.3656	1.431E+03	1.257E+01	2.298E-04	3.115E-19	1.132E-05	8.029E-10	5.166E-07	2.705E-12	5.778E-12	6.022E-07
11	.3750	1.468E+03	1.276E+01	2.240E-04	3.093E-18	1.110E-05	1.307E-09	5.784E-07	2.918E-12	8.184E-12	6.701E-07
12	.3797	1.487E+03	1.285E+01	2.212E-04	9.184E-18	1.099E-05	1.588E-09	6.120E-07	2.904E-12	9.717E-12	7.068E-07
13	.3844	1.493E+03	1.283E+01	2.203E-04	1.453E-17	1.088E-05	1.850E-09	6.475E-07	3.156E-12	1.105E-11	7.454E-07
14	.3937	1.495E+03	1.272E+01	2.199E-04	2.319E-17	1.066E-05	2.316E-09	7.253E-07	3.791E-12	1.386E-11	8.294E-07
15	.4031	1.498E+03	1.261E+01	2.196E-04	3.623E-17	1.043E-05	2.792E-09	8.130E-07	4.376E-12	1.734E-11	9.233E-07
16	.4125	1.500E+03	1.250E+01	2.192E-04	5.556E-17	1.019E-05	3.325E-09	9.117E-07	4.985E-12	2.161E-11	1.028E-06
17	.4219	1.503E+03	1.239E+01	2.188E-04	8.440E-17	9.939E-06	3.949E-09	1.022E-06	5.653E-12	2.689E-11	1.145E-06
18	.4312	1.505E+03	1.229E+01	2.184E-04	1.277E-16	9.682E-06	4.692E-09	1.147E-06	6.402E-12	3.346E-11	1.275E-06
19	.4500	1.510E+03	1.209E+01	2.177E-04	2.910E-16	9.137E-06	6.632E-09	1.440E-06	8.168E-12	5.203E-11	1.580E-06
20	.4594	1.513E+03	1.199E+01	2.173E-04	4.408E-16	8.847E-06	7.910E-09	1.612E-06	9.225E-12	6.523E-11	1.758E-06

21	.4687	1.515E+03	1.189E+01	2.170E-04	6.698E-16	8.545E-06	9.451E-09	1.804E-06	1.041E-11	8.222E-11	1.955E-06
22	.4781	1.518E+03	1.180E+01	2.166E-04	1.023E-15	8.229E-06	1.131E-08	2.017E-06	1.174E-11	1.043E-10	2.172E-06
23	.4875	1.521E+03	1.171E+01	2.162E-04	1.571E-15	7.898E-06	1.356E-08	2.254E-06	1.322E-11	1.334E-10	2.412E-06
24	.4969	1.523E+03	1.162E+01	2.159E-04	2.429E-15	7.553E-06	1.627E-08	2.515E-06	1.485E-11	1.722E-10	2.676E-06
25	.5062	1.526E+03	1.153E+01	2.155E-04	3.777E-15	7.193E-06	1.948E-08	2.801E-06	1.659E-11	2.244E-10	2.964E-06
26	.5156	1.526E+03	1.142E+01	2.155E-04	5.507E-15	6.818E-06	2.299E-08	3.114E-06	1.855E-11	2.940E-10	3.277E-06
27	.5250	1.526E+03	1.132E+01	2.155E-04	7.969E-15	6.430E-06	2.699E-08	3.454E-06	2.065E-11	3.892E-10	3.615E-06
28	.5437	1.527E+03	1.111E+01	2.155E-04	1.679E-14	5.616E-06	3.708E-08	4.207E-06	2.523E-11	7.045E-10	4.361E-06
29	.5625	1.527E+03	1.091E+01	2.157E-04	3.376E-14	4.787E-06	5.026E-08	5.021E-06	3.008E-11	1.304E-09	5.163E-06
30	.5813	1.527E+03	1.071E+01	2.160E-04	5.934E-14	4.000E-06	6.594E-08	5.819E-06	3.458E-11	2.365E-09	5.950E-06
31	.6000	1.527E+03	1.051E+01	2.163E-04	8.470E-14	3.327E-06	8.216E-08	6.503E-06	3.804E-11	4.015E-09	6.624E-06
32	.6187	1.528E+03	1.031E+01	2.168E-04	9.398E-14	2.824E-06	9.612E-08	6.990E-06	4.011E-11	6.180E-09	7.105E-06
33	.6375	1.528E+03	1.011E+01	2.173E-04	8.004E-14	2.497E-06	1.059E-07	7.263E-06	4.087E-11	8.538E-09	7.377E-06
34	.6563	1.530E+03	9.935E+00	2.176E-04	5.389E-14	2.311E-06	1.122E-07	7.363E-06	4.078E-11	1.073E-08	7.479E-06
35	.6750	1.531E+03	9.762E+00	2.180E-04	2.895E-14	2.210E-06	1.150E-07	7.355E-06	4.031E-11	1.244E-08	7.474E-06
36	.6938	1.533E+03	9.597E+00	2.182E-04	1.315E-14	2.154E-06	1.156E-07	7.295E-06	3.980E-11	1.362E-08	7.416E-06
37	.7125	1.534E+03	9.440E+00	2.184E-04	5.349E-15	2.116E-06	1.151E-07	7.213E-06	3.937E-11	1.432E-08	7.336E-06
38	.7312	1.536E+03	9.290E+00	2.186E-04	2.026E-15	2.086E-06	1.139E-07	7.124E-06	3.901E-11	1.466E-08	7.248E-06
39	.7500	1.537E+03	9.147E+00	2.186E-04	6.999E-16	2.059E-06	1.118E-07	7.034E-06	3.858E-11	1.465E-08	7.159E-06
40	.7875	1.527E+03	8.805E+00	2.205E-04	9.138E-17	2.009E-06	9.344E-08	6.879E-06	3.739E-11	1.317E-08	6.984E-06
41	.8250	1.511E+03	8.453E+00	2.232E-04	1.163E-17	1.961E-06	7.247E-08	6.736E-06	3.584E-11	1.111E-08	6.816E-06
42	.9000	1.479E+03	7.813E+00	2.286E-04	1.270E-18	1.874E-06	4.291E-08	6.461E-06	3.255E-11	7.620E-09	6.507E-06
43	1.0500	1.412E+03	6.714E+00	2.402E-04	8.102E-20	1.724E-06	1.402E-08	5.966E-06	2.600E-11	3.353E-09	5.977E-06
44	1.2000	1.331E+03	5.759E+00	2.553E-04	1.644E-21	1.597E-06	3.541E-09	5.531E-06	1.926E-11	1.096E-09	5.530E-06
45	1.5000	1.200E+03	4.395E+00	2.844E-04	8.581E-25	1.401E-06	2.846E-10	4.850E-06	1.116E-11	1.272E-10	4.847E-06
46	1.8000	1.100E+03	3.494E+00	3.111E-04	8.602E-28	1.247E-06	2.856E-11	4.313E-06	6.438E-12	2.003E-11	4.311E-06
47	1.9500	1.025E+03	3.053E+00	3.342E-04	2.411E-30	1.179E-06	4.611E-12	4.076E-06	4.513E-12	6.511E-12	4.074E-06
48	2.1000	9.800E+02	2.747E+00	3.500E-04	3.732E-32	1.118E-06	1.166E-12	3.862E-06	3.073E-12	2.927E-12	3.861E-06
49	2.1750	9.650E+02	2.628E+00	3.556E-04	7.995E-33	1.090E-06	6.748E-13	3.762E-06	2.532E-12	2.145E-12	3.761E-06
50	2.2500	9.500E+02	2.515E+00	3.614E-04	1.868E-33	1.063E-06	4.082E-13	3.666E-06	2.200E-12	1.625E-12	3.666E-06
51	2.3250	9.350E+02	2.409E+00	3.674E-04	4.154E-34	1.038E-06	2.505E-13	3.577E-06	1.956E-12	1.227E-12	3.577E-06
52	2.3438	9.313E+02	2.383E+00	3.689E-04	2.857E-34	1.032E-06	2.214E-13	3.555E-06	1.900E-12	1.140E-12	3.555E-06

53	2.3625	9.275E+02	2.358E+00	3.704E-04	1.986E-34	1.026E-06	1.958E-13	3.535E-06	1.847E-12	1.058E-12	3.535E-06
54	2.3812	9.238E+02	2.333E+00	3.719E-04	1.218E-34	1.021E-06	1.731E-13	3.515E-06	1.796E-12	9.812E-13	3.515E-06
55	2.4000	9.200E+02	2.308E+00	3.735E-04	8.916E-35	1.016E-06	1.530E-13	3.496E-06	1.748E-12	9.086E-13	3.496E-06
56	3.0000	8.000E+02	1.663E+00	4.295E-04	-8.974E-25	1.016E-06	1.530E-13	3.496E-06	1.748E-12	9.086E-13	3.496E-06

	X	OH	CH	O	CH3	C2H6	CH4	CH3O	CH2OH	C2H3	CH2
1	.0000	1.276E-10	2.634E-22	4.715E-14	2.572E-07	1.844E-05	1.414E-01	2.038E-09	1.462E-15	5.023E-14	2.802E-16
2	.1500	3.295E-10	6.454E-22	1.204E-13	8.226E-07	7.802E-05	1.131E-01	8.067E-09	5.742E-15	1.973E-13	8.822E-16
3	.1875	1.055E-09	3.054E-20	5.778E-13	1.608E-06	1.270E-04	1.062E-01	2.435E-08	3.363E-14	1.077E-12	5.525E-15
4	.2250	3.707E-09	1.295E-18	3.246E-12	3.304E-06	2.130E-04	9.911E-02	8.059E-08	2.017E-13	6.540E-12	3.628E-14
5	.2625	1.577E-08	1.113E-16	3.748E-11	7.894E-06	3.580E-04	9.167E-02	2.903E-07	1.567E-12	5.031E-11	3.578E-13
6	.3000	1.053E-07	5.837E-14	1.560E-09	2.405E-05	5.837E-04	8.369E-02	9.202E-07	2.317E-11	6.464E-10	8.188E-12
7	.3187	2.263E-07	7.401E-13	8.030E-09	4.176E-05	7.250E-04	7.945E-02	1.423E-06	7.698E-11	1.920E-09	3.780E-11
8	.3375	4.164E-07	6.404E-12	3.186E-08	7.139E-05	8.776E-04	7.501E-02	1.899E-06	2.216E-10	4.941E-09	1.610E-10
9	.3563	6.952E-07	3.940E-11	9.691E-08	1.231E-04	1.022E-03	7.036E-02	2.190E-06	5.816E-10	1.170E-08	6.274E-10
10	.3656	8.994E-07	8.826E-11	1.563E-07	1.623E-04	1.081E-03	6.797E-02	2.264E-06	9.517E-10	1.798E-08	1.203E-09
11	.3750	1.172E-06	1.842E-10	2.407E-07	2.101E-04	1.130E-03	6.552E-02	2.264E-06	1.563E-09	2.754E-08	2.208E-09
12	.3797	1.337E-06	2.619E-10	2.930E-07	2.331E-04	1.151E-03	6.429E-02	2.260E-06	1.972E-09	3.383E-08	2.877E-09
13	.3844	1.457E-06	3.100E-10	3.275E-07	2.513E-04	1.173E-03	6.305E-02	2.368E-06	2.319E-09	3.910E-08	3.431E-09
14	.3937	1.676E-06	3.874E-10	3.837E-07	2.744E-04	1.220E-03	6.051E-02	2.769E-06	2.951E-09	4.970E-08	4.356E-09
15	.4031	1.927E-06	4.766E-10	4.471E-07	2.913E-04	1.262E-03	5.792E-02	3.184E-06	3.664E-09	6.255E-08	5.357E-09
16	.4125	2.208E-06	5.784E-10	5.187E-07	3.058E-04	1.296E-03	5.525E-02	3.607E-06	4.495E-09	7.800E-08	6.521E-09
17	.4219	2.528E-06	6.971E-10	6.005E-07	3.193E-04	1.322E-03	5.253E-02	4.051E-06	5.486E-09	9.656E-08	7.922E-09
18	.4312	2.895E-06	8.373E-10	6.952E-07	3.321E-04	1.339E-03	4.975E-02	4.527E-06	6.685E-09	1.189E-07	9.638E-09
19	.4500	3.822E-06	1.203E-09	9.350E-07	3.563E-04	1.340E-03	4.402E-02	5.603E-06	9.945E-09	1.784E-07	1.440E-08
20	.4594	4.419E-06	1.444E-09	1.089E-06	3.679E-04	1.324E-03	4.109E-02	6.223E-06	1.219E-08	2.176E-07	1.772E-08
21	.4687	5.138E-06	1.737E-09	1.274E-06	3.791E-04	1.297E-03	3.813E-02	6.908E-06	1.502E-08	2.649E-07	2.192E-08
22	.4781	6.017E-06	2.094E-09	1.497E-06	3.898E-04	1.259E-03	3.514E-02	7.672E-06	1.864E-08	3.223E-07	2.727E-08
23	.4875	7.109E-06	2.534E-09	1.770E-06	4.000E-04	1.209E-03	3.214E-02	8.528E-06	2.332E-08	3.918E-07	3.416E-08
24	.4969	8.486E-06	3.078E-09	2.106E-06	4.094E-04	1.147E-03	2.915E-02	9.491E-06	2.947E-08	4.761E-07	4.305E-08
25	.5062	1.024E-05	3.753E-09	2.525E-06	4.173E-04	1.076E-03	2.619E-02	1.057E-05	3.760E-08	5.778E-07	5.452E-08

26	.5156	1.244E-05	4.490E-09	3.017E-06	4.210E-04	9.950E-04	2.327E-02	1.191E-05	4.789E-08	6.946E-07	6.849E-08
27	.5250	1.530E-05	5.355E-09	3.624E-06	4.218E-04	9.059E-04	2.043E-02	1.344E-05	6.150E-08	8.309E-07	8.607E-08
28	.5437	2.410E-05	7.565E-09	5.319E-06	4.161E-04	7.057E-04	1.506E-02	1.683E-05	1.046E-07	1.160E-06	1.359E-07
29	.5625	3.942E-05	1.021E-08	7.842E-06	3.959E-04	4.974E-04	1.035E-02	1.993E-05	1.802E-07	1.508E-06	2.063E-07
30	.5813	6.452E-05	1.237E-08	1.129E-05	3.547E-04	3.103E-04	6.556E-03	2.115E-05	2.946E-07	1.701E-06	2.818E-07
31	.6000	1.014E-04	1.275E-08	1.555E-05	2.916E-04	1.683E-04	3.797E-03	1.924E-05	4.231E-07	1.557E-06	3.242E-07
32	.6187	1.482E-04	1.076E-08	2.032E-05	2.153E-04	7.828E-05	2.012E-03	1.462E-05	5.002E-07	1.107E-06	2.992E-07
33	.6375	1.989E-04	7.340E-09	2.513E-05	1.410E-04	3.098E-05	9.847E-04	9.206E-06	4.708E-07	6.064E-07	2.174E-07
34	.6563	2.469E-04	4.145E-09	2.940E-05	8.240E-05	1.045E-05	4.521E-04	4.846E-06	3.569E-07	2.620E-07	1.266E-07
35	.6750	2.854E-04	1.988E-09	3.229E-05	4.357E-05	3.070E-06	1.986E-04	2.215E-06	2.233E-07	9.265E-08	6.079E-08
36	.6938	3.127E-04	8.500E-10	3.358E-05	2.141E-05	8.110E-07	8.502E-05	9.161E-07	1.211E-07	2.812E-08	2.536E-08
37	.7125	3.297E-04	3.386E-10	3.358E-05	1.003E-05	1.984E-07	3.592E-05	3.563E-07	5.950E-08	7.645E-09	9.666E-09
38	.7312	3.383E-04	1.290E-10	3.266E-05	4.540E-06	4.583E-08	1.504E-05	1.332E-07	2.729E-08	1.914E-09	3.482E-09
39	.7500	3.389E-04	4.583E-11	3.097E-05	1.938E-06	9.043E-09	6.016E-06	4.662E-08	1.145E-08	3.977E-10	1.151E-09
40	.7875	3.036E-04	7.535E-12	2.463E-05	4.943E-07	8.758E-10	1.463E-06	9.315E-09	2.469E-09	3.673E-11	1.851E-10
41	.8250	2.544E-04	1.182E-12	1.809E-05	1.260E-07	8.159E-11	3.676E-07	1.975E-09	4.922E-10	2.994E-12	3.053E-11
42	.9000	1.724E-04	8.042E-14	9.589E-06	1.998E-08	4.197E-12	5.999E-08	2.428E-10	4.618E-11	1.061E-13	2.709E-12
43	1.0500	7.398E-05	3.023E-15	2.708E-06	3.176E-09	2.605E-13	1.172E-08	3.542E-11	2.478E-12	2.662E-15	1.645E-13
44	1.2000	2.350E-05	1.587E-16	5.569E-07	8.544E-10	6.113E-14	5.290E-09	1.177E-11	1.701E-13	1.956E-16	1.477E-14
45	1.5000	2.592E-06	1.373E-18	4.055E-08	1.565E-10	2.559E-13	3.906E-09	3.254E-12	2.456E-15	2.766E-17	5.398E-16
46	1.8000	3.912E-07	1.276E-20	4.231E-09	3.531E-11	5.440E-13	3.383E-09	7.029E-13	6.593E-17	4.078E-18	3.766E-17
47	1.9500	1.228E-07	3.182E-22	7.503E-10	1.431E-11	5.817E-13	3.185E-09	2.714E-13	7.477E-18	1.079E-18	5.622E-18
48	2.1000	5.402E-08	1.980E-23	2.067E-10	6.754E-12	5.428E-13	3.013E-09	1.075E-13	1.518E-18	3.900E-19	1.342E-18
49	2.1750	3.930E-08	6.458E-24	1.226E-10	4.758E-12	5.098E-13	2.934E-09	6.767E-14	7.956E-19	2.565E-19	7.464E-19
50	2.2500	2.956E-08	2.187E-24	7.654E-11	3.519E-12	4.729E-13	2.859E-09	4.512E-14	4.530E-19	1.713E-19	4.383E-19
51	2.3250	2.218E-08	7.491E-25	4.814E-11	2.669E-12	4.377E-13	2.790E-09	3.105E-14	2.663E-19	1.149E-19	2.600E-19
52	2.3438	2.057E-08	5.704E-25	4.266E-11	2.488E-12	4.298E-13	2.774E-09	2.824E-14	2.330E-19	1.040E-19	2.272E-19
53	2.3625	1.906E-08	4.343E-25	3.782E-11	2.320E-12	4.223E-13	2.758E-09	2.572E-14	2.041E-19	9.422E-20	1.986E-19
54	2.3812	1.765E-08	3.304E-25	3.348E-11	2.164E-12	4.153E-13	2.743E-09	2.345E-14	1.790E-19	8.541E-20	1.734E-19
55	2.4000	1.632E-08	2.498E-25	2.953E-11	2.017E-12	4.087E-13	2.729E-09	2.137E-14	1.569E-19	7.750E-20	1.509E-19
56	3.0000	1.632E-08	2.510E-25	2.953E-11	2.017E-12	4.087E-13	2.729E-09	2.137E-14	1.569E-19	7.750E-20	1.509E-19
	X	CH2S	C2H4	C2H	CH2O	C2H5	C2H2	CH2CO	C	C4H2	C3H3	

1	.0000	8.130E-18	1.563E-05	1.909E-19	2.611E-05	2.223E-12	2.389E-06	8.194E-08	5.838E-24	6.130E-12	3.997E-18
2	.1500	2.560E-17	6.176E-05	7.389E-19	1.020E-04	9.351E-12	9.319E-06	3.606E-07	1.622E-23	3.439E-11	1.930E-17
3	.1875	1.762E-16	9.762E-05	6.215E-18	1.592E-04	4.473E-11	1.466E-05	5.996E-07	5.988E-29	6.500E-11	4.805E-16
4	.2250	1.251E-15	1.584E-04	5.574E-17	2.543E-04	2.332E-10	2.367E-05	1.030E-06	6.346E-28	1.293E-10	8.752E-15
5	.2625	1.349E-14	2.587E-04	7.041E-16	4.067E-04	1.415E-09	3.848E-05	1.780E-06	1.484E-24	2.597E-10	1.630E-13
6	.3000	3.447E-13	4.157E-04	2.113E-14	6.331E-04	8.360E-09	6.173E-05	3.020E-06	1.706E-20	5.101E-10	2.752E-12
7	.3187	1.607E-12	5.240E-04	9.074E-14	7.762E-04	1.556E-08	7.823E-05	3.907E-06	1.081E-18	7.161E-10	1.492E-11
8	.3375	7.052E-12	6.574E-04	3.268E-13	9.387E-04	2.655E-08	9.931E-05	5.027E-06	3.625E-17	1.007E-09	6.330E-11
9	.3563	3.019E-11	8.178E-04	1.054E-12	1.115E-03	4.438E-08	1.263E-04	6.417E-06	6.675E-16	1.414E-09	2.340E-10
10	.3656	6.183E-11	9.072E-04	1.883E-12	1.207E-03	5.752E-08	1.424E-04	7.222E-06	2.407E-15	1.676E-09	4.367E-10
11	.3750	1.211E-10	1.001E-03	3.353E-12	1.300E-03	7.376E-08	1.604E-04	8.105E-06	7.747E-15	1.988E-09	7.538E-10
12	.3797	1.619E-10	1.049E-03	4.443E-12	1.347E-03	8.260E-08	1.701E-04	8.573E-06	1.350E-14	2.165E-09	9.544E-10
13	.3844	1.937E-10	1.098E-03	5.309E-12	1.395E-03	9.091E-08	1.801E-04	9.061E-06	1.790E-14	2.357E-09	1.178E-09
14	.3937	2.395E-10	1.195E-03	6.980E-12	1.491E-03	1.074E-07	2.013E-04	1.010E-05	2.664E-14	2.797E-09	1.692E-09
15	.4031	2.831E-10	1.291E-03	9.119E-12	1.589E-03	1.247E-07	2.241E-04	1.121E-05	3.892E-14	3.318E-09	2.329E-09
16	.4125	3.294E-10	1.385E-03	1.184E-11	1.685E-03	1.432E-07	2.483E-04	1.240E-05	5.593E-14	3.934E-09	3.142E-09
17	.4219	3.812E-10	1.474E-03	1.531E-11	1.778E-03	1.630E-07	2.740E-04	1.367E-05	7.982E-14	4.660E-09	4.198E-09
18	.4312	4.408E-10	1.557E-03	1.976E-11	1.867E-03	1.845E-07	3.009E-04	1.500E-05	1.138E-13	5.510E-09	5.584E-09
19	.4500	5.929E-10	1.698E-03	3.286E-11	2.026E-03	2.329E-07	3.579E-04	1.783E-05	2.328E-13	7.632E-09	9.693E-09
20	.4594	6.919E-10	1.751E-03	4.240E-11	2.090E-03	2.604E-07	3.870E-04	1.928E-05	3.361E-13	8.928E-09	1.277E-08
21	.4687	8.123E-10	1.788E-03	5.484E-11	2.142E-03	2.901E-07	4.160E-04	2.074E-05	4.892E-13	1.040E-08	1.678E-08
22	.4781	9.605E-10	1.808E-03	7.116E-11	2.178E-03	3.224E-07	4.444E-04	2.217E-05	7.195E-13	1.206E-08	2.196E-08
23	.4875	1.145E-09	1.808E-03	9.273E-11	2.197E-03	3.573E-07	4.713E-04	2.355E-05	1.071E-12	1.390E-08	2.854E-08
24	.4969	1.378E-09	1.787E-03	1.214E-10	2.197E-03	3.950E-07	4.959E-04	2.484E-05	1.616E-12	1.590E-08	3.675E-08
25	.5062	1.672E-09	1.741E-03	1.598E-10	2.174E-03	4.349E-07	5.171E-04	2.598E-05	2.470E-12	1.801E-08	4.664E-08
26	.5156	2.009E-09	1.671E-03	2.081E-10	2.126E-03	4.758E-07	5.335E-04	2.694E-05	3.703E-12	2.017E-08	5.802E-08
27	.5250	2.422E-09	1.575E-03	2.715E-10	2.053E-03	5.171E-07	5.439E-04	2.764E-05	5.572E-12	2.227E-08	7.055E-08
28	.5437	3.578E-09	1.310E-03	4.650E-10	1.824E-03	5.879E-07	5.427E-04	2.811E-05	1.277E-11	2.586E-08	9.669E-08
29	.5625	5.194E-09	9.793E-04	7.754E-10	1.495E-03	6.117E-07	5.041E-04	2.691E-05	2.782E-11	2.719E-08	1.130E-07
30	.5813	6.893E-09	6.395E-04	1.174E-09	1.108E-03	5.485E-07	4.248E-04	2.365E-05	5.160E-11	2.466E-08	1.052E-07
31	.6000	7.779E-09	3.563E-04	1.492E-09	7.325E-04	4.035E-07	3.155E-04	1.850E-05	7.362E-11	1.817E-08	7.319E-08
32	.6187	7.073E-09	1.678E-04	1.501E-09	4.335E-04	2.365E-07	2.023E-04	1.253E-05	7.563E-11	1.038E-08	3.666E-08

33	.6375	5.078E-09	6.717E-05	1.169E-09	2.330E-04	1.098E-07	1.116E-04	7.276E-06	5.513E-11	4.560E-09	1.325E-08
34	.6563	2.935E-09	2.324E-05	7.245E-10	1.156E-04	4.088E-08	5.377E-05	3.665E-06	2.989E-11	1.591E-09	3.593E-09
35	.6750	1.404E-09	7.127E-06	3.706E-10	5.385E-05	1.265E-08	2.333E-05	1.648E-06	1.265E-11	4.660E-10	7.740E-10
36	.6938	5.850E-10	1.993E-06	1.652E-10	2.396E-05	3.403E-09	9.421E-06	6.847E-07	4.524E-12	1.216E-10	1.410E-10
37	.7125	2.233E-10	5.210E-07	6.732E-11	1.036E-05	8.291E-10	3.646E-06	2.711E-07	1.462E-12	2.980E-11	2.295E-11
38	.7312	8.073E-11	1.292E-07	2.592E-11	4.385E-06	1.878E-10	1.377E-06	1.045E-07	4.443E-13	7.247E-12	3.467E-12
39	.7500	2.685E-11	2.727E-08	9.126E-12	1.764E-06	3.580E-11	4.893E-07	3.804E-08	1.245E-13	1.767E-12	4.274E-13
40	.7875	4.171E-12	2.870E-09	1.644E-12	4.180E-07	3.104E-12	1.062E-07	8.532E-09	1.187E-14	4.265E-13	2.280E-14
41	.8250	6.490E-13	2.818E-10	3.027E-13	9.982E-08	2.528E-13	2.587E-08	2.185E-09	1.036E-15	2.216E-13	1.119E-15
42	.9000	5.037E-14	1.482E-11	3.262E-14	1.454E-08	9.935E-15	5.069E-09	4.603E-10	2.455E-17	1.391E-13	2.968E-17
43	1.0500	2.441E-15	8.026E-13	2.416E-15	2.213E-09	3.718E-16	1.337E-09	1.279E-10	1.710E-19	8.916E-14	1.112E-18
44	1.2000	1.725E-16	1.268E-13	2.385E-16	7.454E-10	4.535E-17	6.734E-10	6.667E-11	1.724E-21	6.682E-14	1.160E-19
45	1.5000	4.103E-18	2.450E-13	6.921E-18	4.728E-10	5.372E-17	4.177E-10	4.037E-11	9.569E-23	4.773E-14	3.318E-21
46	1.8000	1.972E-19	2.653E-13	3.940E-19	3.971E-10	3.346E-17	3.297E-10	2.984E-11	8.886E-28	3.802E-14	9.038E-23
47	1.9500	2.157E-20	2.229E-13	6.332E-20	3.717E-10	1.562E-17	3.035E-10	2.656E-11	1.664E-30	3.439E-14	6.524E-24
48	2.1000	4.171E-21	1.681E-13	1.748E-20	3.482E-10	7.041E-18	2.835E-10	2.432E-11	2.250E-32	3.175E-14	7.768E-24
49	2.1750	2.150E-21	1.416E-13	1.067E-20	3.370E-10	4.877E-18	2.745E-10	2.337E-11	4.098E-33	3.060E-14	6.616E-25
50	2.2500	1.168E-21	1.166E-13	6.734E-21	3.266E-10	3.436E-18	2.664E-10	2.253E-11	-6.628E-33	2.957E-14	2.292E-25
51	2.3250	6.399E-22	9.437E-14	4.236E-21	3.171E-10	2.402E-18	2.590E-10	2.178E-11	-5.570E-28	2.864E-14	1.143E-25
52	2.3438	5.478E-22	8.943E-14	3.759E-21	3.148E-10	2.190E-18	2.572E-10	2.160E-11	-3.400E-32	2.842E-14	7.640E-26
53	2.3625	4.692E-22	8.476E-14	3.334E-21	3.126E-10	1.997E-18	2.555E-10	2.143E-11	5.193E-35	2.821E-14	-3.815E-26
54	2.3812	4.015E-22	8.035E-14	2.954E-21	3.105E-10	1.821E-18	2.539E-10	2.127E-11	4.174E-35	2.800E-14	-5.976E-25
55	2.4000	3.423E-22	7.621E-14	2.615E-21	3.085E-10	1.659E-18	2.523E-10	2.112E-11	2.722E-35	2.780E-14	-3.634E-24
56	3.0000	3.423E-22	7.621E-14	2.615E-21	3.085E-10	1.659E-18	2.523E-10	2.112E-11	2.731E-35	2.780E-14	-4.840E-24

	X	C3H2	C4H3	O2	H	HO2	H2	H2O	CO2	CO	HCO
1	.0000	1.449E-20	7.308E-13	1.580E-01	1.070E-13	3.271E-07	1.592E-03	5.756E-02	4.826E-05	2.123E-04	9.328E-13
2	.1500	6.028E-20	4.110E-12	1.599E-01	1.493E-13	1.114E-06	2.637E-03	5.079E-02	1.942E-04	7.269E-04	3.622E-12
3	.1875	3.606E-19	7.781E-12	1.595E-01	1.163E-12	1.900E-06	3.003E-03	5.070E-02	3.097E-04	1.079E-03	1.450E-11
4	.2250	2.507E-18	1.550E-11	1.584E-01	9.436E-12	3.438E-06	3.417E-03	5.172E-02	5.079E-04	1.632E-03	6.409E-11
5	.2625	2.169E-17	3.117E-11	1.563E-01	1.247E-10	6.459E-06	3.880E-03	5.415E-02	8.384E-04	2.481E-03	3.337E-10
6	.3000	5.195E-16	6.125E-11	1.530E-01	5.896E-09	1.203E-05	4.383E-03	5.820E-02	1.361E-03	3.722E-03	2.187E-09

7	.3187	4.749E-15	8.577E-11	1.507E-01	2.909E-08	1.549E-05	4.649E-03	6.090E-02	1.725E-03	4.534E-03	4.684E-09
8	.3375	4.566E-14	1.199E-10	1.480E-01	1.112E-07	1.782E-05	4.927E-03	6.408E-02	2.177E-03	5.499E-03	8.796E-09
9	.3563	3.516E-13	1.666E-10	1.448E-01	3.271E-07	1.779E-05	5.217E-03	6.776E-02	2.733E-03	6.634E-03	1.534E-08
10	.3656	8.940E-13	1.958E-10	1.430E-01	5.203E-07	1.714E-05	5.367E-03	6.977E-02	3.057E-03	7.269E-03	2.026E-08
11	.3750	2.123E-12	2.295E-10	1.411E-01	7.926E-07	1.619E-05	5.517E-03	7.191E-02	3.414E-03	7.951E-03	2.674E-08
12	.3797	3.211E-12	2.480E-10	1.401E-01	9.681E-07	1.569E-05	5.592E-03	7.302E-02	3.607E-03	8.309E-03	3.058E-08
13	.3844	4.059E-12	2.678E-10	1.390E-01	1.076E-06	1.611E-05	5.667E-03	7.416E-02	3.810E-03	8.678E-03	3.408E-08
14	.3937	5.770E-12	3.113E-10	1.368E-01	1.261E-06	1.803E-05	5.817E-03	7.655E-02	4.252E-03	9.458E-03	4.150E-08
15	.4031	8.050E-12	3.602E-10	1.344E-01	1.472E-06	2.008E-05	5.966E-03	7.909E-02	4.744E-03	1.029E-02	5.019E-08
16	.4125	1.105E-11	4.145E-10	1.319E-01	1.710E-06	2.222E-05	6.113E-03	8.178E-02	5.293E-03	1.118E-02	6.025E-08
17	.4219	1.503E-11	4.741E-10	1.291E-01	1.984E-06	2.451E-05	6.256E-03	8.461E-02	5.903E-03	1.213E-02	7.191E-08
18	.4312	2.033E-11	5.388E-10	1.262E-01	2.302E-06	2.700E-05	6.394E-03	8.760E-02	6.581E-03	1.313E-02	8.545E-08
19	.4500	3.679E-11	6.811E-10	1.197E-01	3.113E-06	3.269E-05	6.647E-03	9.403E-02	8.155E-03	1.528E-02	1.195E-07
20	.4594	4.934E-11	7.547E-10	1.162E-01	3.637E-06	3.602E-05	6.755E-03	9.745E-02	9.065E-03	1.642E-02	1.408E-07
21	.4687	6.612E-11	8.283E-10	1.125E-01	4.264E-06	3.974E-05	6.847E-03	1.010E-01	1.007E-02	1.760E-02	1.657E-07
22	.4781	8.861E-11	8.993E-10	1.087E-01	5.025E-06	4.393E-05	6.920E-03	1.047E-01	1.117E-02	1.881E-02	1.947E-07
23	.4875	1.188E-10	9.648E-10	1.046E-01	5.955E-06	4.870E-05	6.969E-03	1.085E-01	1.238E-02	2.004E-02	2.286E-07
24	.4969	1.594E-10	1.022E-09	1.004E-01	7.101E-06	5.416E-05	6.990E-03	1.124E-01	1.371E-02	2.126E-02	2.684E-07
25	.5062	2.137E-10	1.066E-09	9.599E-02	8.521E-06	6.042E-05	6.977E-03	1.164E-01	1.515E-02	2.247E-02	3.147E-07
26	.5156	2.798E-10	1.094E-09	9.148E-02	1.018E-05	6.834E-05	6.926E-03	1.205E-01	1.672E-02	2.364E-02	3.679E-07
27	.5250	3.633E-10	1.103E-09	8.687E-02	1.221E-05	7.767E-05	6.831E-03	1.245E-01	1.842E-02	2.474E-02	4.289E-07
28	.5437	5.962E-10	1.059E-09	7.750E-02	1.769E-05	1.001E-04	6.494E-03	1.327E-01	2.220E-02	2.663E-02	5.724E-07
29	.5625	8.949E-10	9.386E-10	6.836E-02	2.526E-05	1.256E-04	5.935E-03	1.404E-01	2.645E-02	2.783E-02	7.223E-07
30	.5813	1.121E-09	7.626E-10	6.007E-02	3.403E-05	1.482E-04	5.163E-03	1.471E-01	3.103E-02	2.800E-02	8.153E-07
31	.6000	1.062E-09	5.686E-10	5.320E-02	4.176E-05	1.606E-04	4.246E-03	1.524E-01	3.577E-02	2.694E-02	7.858E-07
32	.6187	7.038E-10	3.943E-10	4.807E-02	4.597E-05	1.592E-04	3.305E-03	1.560E-01	4.041E-02	2.473E-02	6.330E-07
33	.6375	3.177E-10	2.618E-10	4.466E-02	4.561E-05	1.460E-04	2.456E-03	1.579E-01	4.471E-02	2.173E-02	4.283E-07
34	.6563	1.014E-10	1.725E-10	4.267E-02	4.182E-05	1.258E-04	1.767E-03	1.585E-01	4.848E-02	1.845E-02	2.492E-07
35	.6750	2.433E-11	1.160E-10	4.175E-02	3.608E-05	1.044E-04	1.252E-03	1.581E-01	5.161E-02	1.528E-02	1.282E-07
36	.6938	4.803E-12	8.074E-11	4.157E-02	3.002E-05	8.509E-05	8.845E-04	1.572E-01	5.408E-02	1.247E-02	6.032E-08
37	.7125	8.468E-13	5.828E-11	4.190E-02	2.453E-05	6.894E-05	6.305E-04	1.559E-01	5.595E-02	1.011E-02	2.678E-08
38	.7312	1.430E-13	4.356E-11	4.258E-02	1.988E-05	5.585E-05	4.562E-04	1.544E-01	5.728E-02	8.177E-03	1.144E-08

39	.7500	2.267E-14	3.362E-11	4.350E-02	1.601E-05	4.520E-05	3.358E-04	1.527E-01	5.817E-02	6.640E-03	4.577E-09
40	.7875	2.672E-15	2.290E-11	4.584E-02	9.743E-06	3.238E-05	1.995E-04	1.494E-01	5.886E-02	4.560E-03	1.018E-09
41	.8250	9.174E-16	1.701E-11	4.844E-02	5.708E-06	2.404E-05	1.246E-04	1.461E-01	5.876E-02	3.242E-03	2.275E-10
42	.9000	3.445E-16	1.187E-11	5.381E-02	2.199E-06	1.497E-05	5.971E-05	1.398E-01	5.732E-02	1.939E-03	2.920E-11
43	1.0500	8.030E-17	8.695E-12	6.368E-02	4.793E-07	9.020E-06	2.449E-05	1.288E-01	5.332E-02	1.137E-03	3.077E-12
44	1.2000	1.698E-17	7.447E-12	7.221E-02	1.044E-07	6.824E-06	1.413E-05	1.194E-01	4.951E-02	8.697E-04	5.712E-13
45	1.5000	1.149E-18	6.419E-12	8.540E-02	7.314E-09	4.861E-06	1.019E-05	1.049E-01	4.341E-02	7.241E-04	6.567E-14
46	1.8000	1.250E-19	5.693E-12	9.577E-02	5.558E-10	2.965E-06	8.827E-06	9.342E-02	3.861E-02	6.384E-04	9.696E-15
47	1.9500	3.431E-20	5.377E-12	1.003E-01	6.962E-11	2.185E-06	8.349E-06	8.838E-02	3.649E-02	6.026E-04	2.771E-15
48	2.1000	1.350E-20	5.093E-12	1.045E-01	1.582E-11	1.648E-06	7.950E-06	8.382E-02	3.457E-02	5.707E-04	1.110E-15
49	2.1750	9.327E-21	4.959E-12	1.064E-01	9.002E-12	1.439E-06	7.774E-06	8.169E-02	3.367E-02	5.558E-04	7.702E-16
50	2.2500	6.688E-21	4.832E-12	1.082E-01	5.112E-12	1.268E-06	7.616E-06	7.970E-02	3.282E-02	5.418E-04	5.496E-16
51	2.3250	4.800E-21	4.711E-12	1.099E-01	2.888E-12	1.125E-06	7.477E-06	7.785E-02	3.202E-02	5.287E-04	3.928E-16
52	2.3438	4.406E-21	4.682E-12	1.103E-01	2.499E-12	1.092E-06	7.445E-06	7.742E-02	3.183E-02	5.256E-04	3.604E-16
53	2.3625	4.042E-21	4.653E-12	1.107E-01	2.163E-12	1.061E-06	7.415E-06	7.700E-02	3.164E-02	5.226E-04	3.305E-16
54	2.3812	3.706E-21	4.626E-12	1.111E-01	1.871E-12	1.031E-06	7.387E-06	7.660E-02	3.146E-02	5.198E-04	3.031E-16
55	2.4000	3.395E-21	4.600E-12	1.114E-01	1.619E-12	1.002E-06	7.360E-06	7.622E-02	3.129E-02	5.170E-04	2.777E-16
56	3.0000	3.395E-21	4.600E-12	1.114E-01	1.619E-12	1.002E-06	7.360E-06	7.622E-02	3.129E-02	5.170E-04	2.777E-16

	X	HCCO	HCCOH	H2O2	N2
1	.0000	2.551E-13	3.383E-08	3.622E-06	6.411E-01
2	.1500	7.491E-13	9.964E-08	1.239E-05	6.724E-01
3	.1875	3.575E-12	1.386E-07	1.721E-05	6.788E-01
4	.2250	1.559E-11	1.953E-07	2.354E-05	6.845E-01
5	.2625	8.823E-11	2.757E-07	3.012E-05	6.895E-01
6	.3000	1.079E-09	3.849E-07	3.158E-05	6.939E-01
7	.3187	3.194E-09	4.523E-07	2.741E-05	6.958E-01
8	.3375	8.676E-09	5.297E-07	2.051E-05	6.976E-01
9	.3563	2.197E-08	6.181E-07	1.315E-05	6.992E-01
10	.3656	3.420E-08	6.671E-07	1.017E-05	7.000E-01

11	.3750	5.233E-08	7.196E-07	7.865E-06	7.007E-01
12	.3797	6.363E-08	7.472E-07	7.087E-06	7.011E-01
13	.3844	7.127E-08	7.759E-07	6.668E-06	7.014E-01
14	.3937	8.228E-08	8.369E-07	6.607E-06	7.022E-01
15	.4031	9.440E-08	9.030E-07	6.843E-06	7.029E-01
16	.4125	1.080E-07	9.742E-07	7.148E-06	7.035E-01
17	.4219	1.232E-07	1.051E-06	7.455E-06	7.042E-01
18	.4312	1.402E-07	1.133E-06	7.751E-06	7.049E-01
19	.4500	1.808E-07	1.313E-06	8.292E-06	7.063E-01
20	.4594	2.049E-07	1.410E-06	8.543E-06	7.070E-01
21	.4687	2.321E-07	1.512E-06	8.780E-06	7.077E-01
22	.4781	2.630E-07	1.618E-06	9.006E-06	7.084E-01
23	.4875	2.984E-07	1.727E-06	9.224E-06	7.092E-01
24	.4969	3.395E-07	1.838E-06	9.443E-06	7.099E-01
25	.5062	3.873E-07	1.950E-06	9.688E-06	7.107E-01
26	.5156	4.380E-07	2.062E-06	1.006E-05	7.116E-01
27	.5250	4.963E-07	2.171E-06	1.050E-05	7.125E-01
28	.5437	6.463E-07	2.373E-06	1.139E-05	7.144E-01
29	.5625	8.364E-07	2.528E-06	1.205E-05	7.165E-01
30	.5813	1.014E-06	2.587E-06	1.206E-05	7.189E-01
31	.6000	1.075E-06	2.483E-06	1.112E-05	7.214E-01
32	.6187	9.467E-07	2.182E-06	9.349E-06	7.239E-01
33	.6375	6.791E-07	1.734E-06	7.179E-06	7.265E-01
34	.6563	4.012E-07	1.257E-06	5.078E-06	7.289E-01
35	.6750	1.992E-07	8.497E-07	3.434E-06	7.312E-01
36	.6938	8.662E-08	5.507E-07	2.285E-06	7.332E-01
37	.7125	3.442E-08	3.512E-07	1.530E-06	7.350E-01
38	.7312	1.290E-08	2.247E-07	1.041E-06	7.367E-01
39	.7500	4.409E-09	1.458E-07	7.210E-07	7.382E-01
40	.7875	7.655E-10	7.631E-08	4.402E-07	7.408E-01
41	.8250	1.365E-10	4.586E-08	2.987E-07	7.430E-01
42	.9000	1.427E-11	2.652E-08	1.664E-07	7.469E-01

43	1.0500	1.155E-12	1.849E-08	9.611E-08	7.530E-01
44	1.2000	1.626E-13	1.588E-08	9.579E-08	7.579E-01
45	1.5000	1.459E-14	1.378E-08	2.067E-07	7.656E-01
46	1.8000	2.705E-15	1.226E-08	3.324E-07	7.715E-01
47	1.9500	8.152E-16	1.160E-08	4.974E-07	7.742E-01
48	2.1000	3.605E-16	1.100E-08	6.098E-07	7.766E-01
49	2.1750	2.676E-16	1.072E-08	6.488E-07	7.777E-01
50	2.2500	1.984E-16	1.045E-08	6.794E-07	7.787E-01
51	2.3250	1.463E-16	1.021E-08	7.047E-07	7.797E-01
52	2.3438	1.354E-16	1.015E-08	7.105E-07	7.799E-01
53	2.3625	1.253E-16	1.010E-08	7.160E-07	7.801E-01
54	2.3812	1.159E-16	1.004E-08	7.214E-07	7.803E-01
55	2.4000	1.072E-16	9.992E-09	7.265E-07	7.805E-01
56	3.0000	1.072E-16	9.992E-09	7.265E-07	7.805E-01

TWOPNT: LOG OF THE BOUNDARY VALUE PROBLEM SOLVER.

ACTIVITY	LOG10 MAX NORM RESIDUAL	LOG10 MAX CONDITION NUMBER	POINTS	STEPS	JACOBIANS	REMARK
START			56			
NEWTON	-8.65	39.51		54	8	
REFINE	-.28		57			NEW MESH
NEWTON	-4.65	39.81		18	1	
REFINE			57			

TWOPNT: FINAL SOLUTION:

	X	T	V	RHO	E	NA+	NA	NAOH	NAO2	NAO	HCO+
1	.0000	5.600E+02	8.715E+00	5.737E-04	1.481E-20	1.872E-05	1.485E-15	1.870E-07	2.686E-12	1.911E-15	2.236E-07
2	.1500	7.525E+02	1.156E+01	4.325E-04	-2.817E-42	1.426E-05	3.517E-15	5.832E-07	7.898E-12	5.259E-15	6.655E-07
3	.1875	8.006E+02	1.227E+01	4.074E-04	4.909E-39	1.310E-05	2.641E-14	8.264E-07	1.101E-11	1.912E-14	9.252E-07
4	.2250	8.488E+02	1.299E+01	3.850E-04	-1.195E-36	1.190E-05	1.728E-13	1.186E-06	1.567E-11	7.752E-14	1.300E-06
5	.2625	9.320E+02	1.424E+01	3.512E-04	1.144E-33	1.063E-05	2.458E-12	1.702E-06	2.258E-11	3.867E-13	1.826E-06
6	.3000	1.135E+03	1.731E+01	2.888E-04	1.573E-27	9.326E-06	6.708E-11	2.389E-06	9.299E-12	3.451E-12	2.509E-06
7	.3187	1.237E+03	1.885E+01	2.653E-04	1.932E-24	8.669E-06	4.877E-10	2.801E-06	1.306E-11	1.052E-11	2.913E-06
8	.3375	1.338E+03	2.038E+01	2.453E-04	4.661E-21	8.007E-06	2.732E-09	3.262E-06	1.741E-11	2.727E-11	3.364E-06
9	.3563	1.440E+03	2.191E+01	2.282E-04	4.947E-18	7.336E-06	1.269E-08	3.769E-06	2.259E-11	6.770E-11	3.864E-06
10	.3656	1.491E+03	2.267E+01	2.206E-04	9.822E-17	6.996E-06	2.538E-08	4.033E-06	2.504E-11	1.124E-10	4.134E-06
11	.3750	1.541E+03	2.343E+01	2.134E-04	1.100E-15	6.653E-06	4.488E-08	4.303E-06	2.521E-11	1.881E-10	4.417E-06
12	.3797	1.567E+03	2.381E+01	2.100E-04	2.852E-15	6.481E-06	5.580E-08	4.442E-06	2.387E-11	2.403E-10	4.564E-06
13	.3844	1.575E+03	2.392E+01	2.090E-04	4.596E-15	6.308E-06	6.569E-08	4.586E-06	2.529E-11	2.965E-10	4.714E-06
14	.3937	1.576E+03	2.393E+01	2.089E-04	9.231E-15	5.955E-06	8.228E-08	4.896E-06	2.899E-11	4.383E-10	5.029E-06
15	.4031	1.577E+03	2.394E+01	2.089E-04	1.880E-14	5.595E-06	9.904E-08	5.226E-06	3.170E-11	6.654E-10	5.363E-06
16	.4125	1.579E+03	2.395E+01	2.088E-04	3.851E-14	5.228E-06	1.184E-07	5.570E-06	3.414E-11	1.046E-09	5.713E-06
17	.4219	1.580E+03	2.395E+01	2.088E-04	7.660E-14	4.860E-06	1.416E-07	5.920E-06	3.652E-11	1.682E-09	6.074E-06
18	.4312	1.582E+03	2.395E+01	2.088E-04	1.410E-13	4.499E-06	1.693E-07	6.265E-06	3.881E-11	2.709E-09	6.434E-06
19	.4406	1.583E+03	2.395E+01	2.088E-04	2.308E-13	4.158E-06	2.010E-07	6.584E-06	4.086E-11	4.264E-09	6.776E-06
20	.4500	1.585E+03	2.394E+01	2.089E-04	3.280E-13	3.851E-06	2.353E-07	6.858E-06	4.254E-11	6.424E-09	7.079E-06
21	.4594	1.586E+03	2.393E+01	2.089E-04	4.012E-13	3.594E-06	2.697E-07	7.069E-06	4.374E-11	9.134E-09	7.324E-06
22	.4687	1.588E+03	2.392E+01	2.090E-04	4.203E-13	3.393E-06	3.011E-07	7.209E-06	4.445E-11	1.217E-08	7.498E-06
23	.4781	1.589E+03	2.390E+01	2.092E-04	3.759E-13	3.248E-06	3.269E-07	7.282E-06	4.471E-11	1.520E-08	7.602E-06
24	.4875	1.591E+03	2.389E+01	2.093E-04	2.869E-13	3.149E-06	3.460E-07	7.300E-06	4.465E-11	1.791E-08	7.646E-06
25	.4969	1.592E+03	2.388E+01	2.094E-04	1.889E-13	3.084E-06	3.586E-07	7.282E-06	4.442E-11	2.010E-08	7.646E-06
26	.5062	1.594E+03	2.387E+01	2.095E-04	1.098E-13	3.040E-06	3.660E-07	7.241E-06	4.417E-11	2.172E-08	7.619E-06

27	.5156	1.596E+03	2.387E+01	2.094E-04	5.790E-14	3.007E-06	3.706E-07	7.190E-06	4.390E-11	2.283E-08	7.577E-06
28	.5250	1.598E+03	2.388E+01	2.094E-04	2.771E-14	2.981E-06	3.728E-07	7.134E-06	4.369E-11	2.351E-08	7.528E-06
29	.5437	1.602E+03	2.390E+01	2.092E-04	6.783E-15	2.936E-06	3.711E-07	7.021E-06	4.340E-11	2.388E-08	7.421E-06
30	.5625	1.606E+03	2.392E+01	2.090E-04	1.598E-15	2.894E-06	3.652E-07	6.914E-06	4.319E-11	2.360E-08	7.312E-06
31	.5813	1.610E+03	2.396E+01	2.087E-04	3.878E-16	2.854E-06	3.574E-07	6.812E-06	4.299E-11	2.297E-08	7.206E-06
32	.6000	1.614E+03	2.400E+01	2.084E-04	1.068E-16	2.815E-06	3.488E-07	6.713E-06	4.276E-11	2.213E-08	7.103E-06
33	.6187	1.618E+03	2.404E+01	2.080E-04	4.000E-17	2.777E-06	3.388E-07	6.618E-06	4.230E-11	2.114E-08	7.002E-06
34	.6375	1.621E+03	2.406E+01	2.078E-04	2.306E-17	2.740E-06	3.230E-07	6.535E-06	4.147E-11	1.997E-08	6.904E-06
35	.6563	1.615E+03	2.395E+01	2.087E-04	1.726E-17	2.704E-06	2.938E-07	6.474E-06	4.183E-11	1.858E-08	6.809E-06
36	.6750	1.609E+03	2.385E+01	2.096E-04	1.454E-17	2.669E-06	2.644E-07	6.417E-06	4.162E-11	1.716E-08	6.717E-06
37	.6938	1.603E+03	2.375E+01	2.105E-04	1.273E-17	2.635E-06	2.374E-07	6.360E-06	4.125E-11	1.581E-08	6.627E-06
38	.7125	1.597E+03	2.365E+01	2.115E-04	1.129E-17	2.601E-06	2.134E-07	6.302E-06	4.082E-11	1.453E-08	6.540E-06
39	.7312	1.591E+03	2.354E+01	2.124E-04	1.007E-17	2.569E-06	1.920E-07	6.243E-06	4.036E-11	1.336E-08	6.456E-06
40	.7500	1.585E+03	2.344E+01	2.133E-04	8.983E-18	2.538E-06	1.730E-07	6.183E-06	3.986E-11	1.228E-08	6.374E-06
41	.7875	1.571E+03	2.322E+01	2.154E-04	7.076E-18	2.478E-06	1.400E-07	6.066E-06	3.924E-11	1.040E-08	6.217E-06
42	.8250	1.556E+03	2.298E+01	2.176E-04	5.485E-18	2.421E-06	1.132E-07	5.949E-06	3.870E-11	8.822E-09	6.069E-06
43	.9000	1.527E+03	2.251E+01	2.221E-04	3.136E-18	2.316E-06	7.530E-08	5.722E-06	3.784E-11	6.463E-09	5.798E-06
44	1.0500	1.465E+03	2.155E+01	2.321E-04	6.308E-19	2.136E-06	3.430E-08	5.305E-06	3.766E-11	3.706E-09	5.336E-06
45	1.2000	1.393E+03	2.044E+01	2.446E-04	4.114E-20	1.983E-06	1.429E-08	4.938E-06	3.881E-11	2.077E-09	4.947E-06
46	1.5000	1.225E+03	1.792E+01	2.790E-04	1.678E-23	1.745E-06	2.372E-09	4.348E-06	6.572E-11	7.115E-10	4.345E-06
47	1.8000	1.133E+03	1.654E+01	3.023E-04	7.628E-26	1.557E-06	5.995E-10	3.874E-06	7.746E-11	3.031E-10	3.871E-06
48	1.9500	1.033E+03	1.506E+01	3.319E-04	1.516E-28	1.475E-06	2.316E-10	3.666E-06	1.948E-10	1.888E-10	3.663E-06
49	2.1000	9.800E+02	1.427E+01	3.503E-04	2.425E-30	1.401E-06	9.294E-11	3.476E-06	2.482E-10	1.206E-10	3.475E-06
50	2.1750	9.650E+02	1.405E+01	3.559E-04	6.446E-31	1.367E-06	6.452E-11	3.388E-06	2.451E-10	9.629E-11	3.387E-06
51	2.2500	9.500E+02	1.382E+01	3.617E-04	1.647E-31	1.335E-06	4.445E-11	3.305E-06	2.421E-10	7.768E-11	3.304E-06
52	2.3250	9.350E+02	1.360E+01	3.676E-04	4.027E-32	1.306E-06	3.029E-11	3.228E-06	2.388E-10	6.304E-11	3.228E-06
53	2.3438	9.313E+02	1.354E+01	3.692E-04	2.809E-32	1.300E-06	2.745E-11	3.210E-06	2.377E-10	5.981E-11	3.210E-06
54	2.3625	9.275E+02	1.349E+01	3.707E-04	1.954E-32	1.293E-06	2.487E-11	3.192E-06	2.366E-10	5.677E-11	3.193E-06
55	2.3812	9.238E+02	1.343E+01	3.722E-04	1.355E-32	1.287E-06	2.251E-11	3.176E-06	2.355E-10	5.390E-11	3.176E-06
56	2.4000	9.200E+02	1.338E+01	3.738E-04	9.368E-33	1.281E-06	2.036E-11	3.160E-06	2.344E-10	5.119E-11	3.161E-06
57	3.0000	8.000E+02	9.638E+00	4.298E-04	4.957E-23	1.281E-06	2.036E-11	3.160E-06	2.344E-10	5.119E-11	3.161E-06

	X	OH	CH	O	CH3	C2H6	CH4	CH3O	CH2OH	C2H3	CH2
1	.0000	2.672E-10	2.006E-24	8.477E-15	1.791E-07	4.499E-05	1.310E-01	4.447E-09	2.124E-15	1.836E-13	9.070E-17
2	.1500	5.533E-10	3.974E-24	1.738E-14	4.463E-07	1.441E-04	9.666E-02	1.347E-08	6.387E-15	5.494E-13	2.230E-16
3	.1875	1.565E-09	2.704E-22	8.926E-14	9.233E-07	2.068E-04	8.702E-02	4.116E-08	3.566E-14	2.574E-12	1.352E-15
4	.2250	4.971E-09	1.774E-20	5.527E-13	1.998E-06	3.011E-04	7.650E-02	1.385E-07	1.987E-13	1.368E-11	1.014E-14
5	.2625	2.007E-08	6.314E-18	1.584E-11	5.483E-06	4.379E-04	6.482E-02	5.313E-07	1.782E-12	1.008E-10	1.892E-13
6	.3000	1.566E-07	4.904E-14	1.758E-09	2.107E-05	6.176E-04	5.225E-02	1.657E-06	4.753E-11	1.643E-09	1.628E-11
7	.3187	4.452E-07	1.593E-12	1.710E-08	4.351E-05	7.106E-04	4.570E-02	2.625E-06	2.242E-10	6.517E-09	1.656E-10
8	.3375	1.065E-06	2.726E-11	1.055E-07	8.871E-05	7.879E-04	3.898E-02	3.406E-06	9.559E-10	2.201E-08	1.263E-09
9	.3563	2.425E-06	2.675E-10	4.179E-07	1.824E-04	8.144E-04	3.211E-02	3.572E-06	4.313E-09	7.026E-08	7.124E-09
10	.3656	3.875E-06	7.302E-10	7.565E-07	2.600E-04	7.915E-04	2.866E-02	3.541E-06	1.023E-08	1.285E-07	1.603E-08
11	.3750	6.299E-06	1.798E-09	1.292E-06	3.562E-04	7.419E-04	2.523E-02	3.363E-06	2.449E-08	2.301E-07	3.407E-08
12	.3797	7.947E-06	2.756E-09	1.644E-06	4.017E-04	7.123E-04	2.354E-02	3.272E-06	3.642E-08	3.000E-07	4.762E-08
13	.3844	9.626E-06	3.514E-09	1.975E-06	4.357E-04	6.854E-04	2.187E-02	3.563E-06	4.966E-08	3.734E-07	6.152E-08
14	.3937	1.365E-05	5.204E-09	2.735E-06	4.740E-04	6.367E-04	1.855E-02	4.812E-06	8.231E-08	5.520E-07	9.413E-08
15	.4031	1.991E-05	7.706E-09	3.854E-06	4.986E-04	5.762E-04	1.533E-02	6.463E-06	1.368E-07	8.130E-07	1.444E-07
16	.4125	3.014E-05	1.134E-08	5.510E-06	5.150E-04	4.982E-04	1.226E-02	8.577E-06	2.332E-07	1.188E-06	2.241E-07
17	.4219	4.685E-05	1.622E-08	7.884E-06	5.201E-04	4.051E-04	9.426E-03	1.100E-05	4.014E-07	1.680E-06	3.450E-07
18	.4312	7.325E-05	2.184E-08	1.110E-05	5.075E-04	3.050E-04	6.927E-03	1.322E-05	6.740E-07	2.208E-06	5.094E-07
19	.4406	1.125E-04	2.682E-08	1.521E-05	4.717E-04	2.101E-04	4.838E-03	1.442E-05	1.059E-06	2.591E-06	6.961E-07
20	.4500	1.663E-04	2.935E-08	2.024E-05	4.119E-04	1.312E-04	3.202E-03	1.399E-05	1.498E-06	2.620E-06	8.538E-07
21	.4594	2.333E-04	2.820E-08	2.623E-05	3.342E-04	7.378E-05	2.008E-03	1.194E-05	1.854E-06	2.234E-06	9.186E-07
22	.4687	3.084E-04	2.362E-08	3.320E-05	2.502E-04	3.723E-05	1.197E-03	8.952E-06	1.970E-06	1.594E-06	8.550E-07
23	.4781	3.843E-04	1.726E-08	4.083E-05	1.725E-04	1.688E-05	6.834E-04	5.925E-06	1.793E-06	9.572E-07	6.854E-07
24	.4875	4.534E-04	1.111E-08	4.839E-05	1.101E-04	6.924E-06	3.765E-04	3.512E-06	1.411E-06	4.922E-07	4.758E-07
25	.4969	5.106E-04	6.414E-09	5.493E-05	6.596E-05	2.604E-06	2.020E-04	1.902E-06	9.806E-07	2.220E-07	2.905E-07
26	.5062	5.541E-04	3.398E-09	5.977E-05	3.756E-05	9.120E-07	1.062E-04	9.627E-07	6.169E-07	9.002E-08	1.594E-07
27	.5156	5.849E-04	1.689E-09	6.278E-05	2.053E-05	2.994E-07	5.484E-05	4.605E-07	3.588E-07	3.332E-08	8.026E-08
28	.5250	6.050E-04	7.820E-10	6.417E-05	1.068E-05	8.564E-08	2.724E-05	2.075E-07	1.931E-07	1.054E-08	3.681E-08
29	.5437	6.188E-04	1.900E-10	6.309E-05	3.285E-06	1.071E-08	7.972E-06	4.840E-08	5.941E-08	1.508E-09	8.702E-09
30	.5625	6.146E-04	4.588E-11	5.971E-05	1.015E-06	1.286E-09	2.372E-06	1.130E-08	1.758E-08	2.035E-10	2.018E-09
31	.5813	6.006E-04	1.136E-11	5.538E-05	3.191E-07	1.531E-10	7.241E-07	2.697E-09	5.171E-09	2.692E-11	4.837E-10

32	.6000	5.807E-04	2.951E-12	5.070E-05	1.030E-07	1.842E-11	2.278E-07	6.635E-10	1.540E-09	3.592E-12	1.246E-10
33	.6187	5.563E-04	8.333E-13	4.582E-05	3.434E-08	2.266E-12	7.430E-08	1.696E-10	4.692E-10	4.972E-13	3.578E-11
34	.6375	5.260E-04	2.751E-13	4.073E-05	1.190E-08	2.903E-13	2.531E-08	4.632E-11	1.466E-10	7.503E-14	1.177E-11
35	.6563	4.871E-04	1.152E-13	3.571E-05	4.290E-09	4.015E-14	9.078E-09	1.511E-11	4.645E-11	1.375E-14	4.488E-12
36	.6750	4.477E-04	6.586E-14	3.093E-05	1.622E-09	6.016E-15	3.434E-09	5.557E-12	1.534E-11	3.403E-15	1.972E-12
37	.6938	4.101E-04	4.718E-14	2.667E-05	6.444E-10	9.759E-16	1.368E-09	2.434E-12	5.314E-12	1.182E-15	9.747E-13
38	.7125	3.753E-04	3.792E-14	2.297E-05	2.682E-10	1.700E-16	5.726E-10	1.331E-12	1.932E-12	5.271E-16	5.273E-13
39	.7312	3.435E-04	3.201E-14	1.979E-05	1.158E-10	3.080E-17	2.491E-10	8.952E-13	7.306E-13	2.707E-16	3.048E-13
40	.7500	3.145E-04	2.754E-14	1.708E-05	4.954E-11	4.436E-18	1.075E-10	6.910E-13	2.742E-13	1.496E-16	1.844E-13
41	.7875	2.642E-04	2.057E-14	1.286E-05	1.332E-11	-3.939E-20	2.955E-11	5.116E-13	5.720E-14	5.573E-17	7.841E-14
42	.8250	2.223E-04	1.524E-14	9.753E-06	3.622E-12	-1.876E-19	8.253E-12	4.004E-13	1.215E-14	2.281E-17	3.609E-14
43	.9000	1.606E-04	8.031E-15	5.869E-06	5.662E-13	-6.875E-20	1.365E-12	2.440E-13	1.204E-15	5.239E-18	9.913E-15
44	1.0500	8.992E-05	1.410E-15	2.495E-06	7.344E-14	-2.664E-20	2.027E-13	5.836E-14	7.029E-17	6.090E-19	1.352E-15
45	1.2000	4.910E-05	8.245E-17	1.067E-06	1.441E-14	-1.407E-20	4.765E-14	4.979E-15	6.203E-18	8.540E-20	2.048E-16
46	1.5000	1.579E-05	2.893E-20	2.777E-07	3.503E-15	1.604E-19	1.551E-14	1.562E-17	3.365E-19	2.983E-21	1.012E-17
47	1.8000	6.482E-06	1.165E-22	9.122E-08	1.416E-15	3.280E-18	7.975E-15	1.617E-18	4.409E-20	5.646E-22	9.873E-19
48	1.9500	3.859E-06	1.219E-24	6.791E-08	8.325E-16	2.902E-18	4.598E-15	1.025E-18	1.292E-20	-1.835E-22	3.901E-19
49	2.1000	2.404E-06	2.029E-25	4.321E-08	6.316E-16	-9.281E-17	1.026E-15	5.670E-19	6.210E-21	-4.670E-21	1.521E-19
50	2.1750	1.907E-06	9.048E-26	3.227E-08	9.315E-16	-3.688E-16	5.651E-17	6.570E-19	7.666E-21	-1.211E-20	9.179E-20
51	2.2500	1.529E-06	4.254E-26	2.446E-08	9.861E-16	-8.302E-16	4.207E-16	3.197E-19	8.095E-21	-2.372E-20	5.768E-20
52	2.3250	1.234E-06	2.074E-26	1.880E-08	-3.269E-16	-1.240E-15	1.922E-15	-1.283E-18	4.682E-21	-3.551E-20	3.735E-20
53	2.3438	1.169E-06	1.731E-26	1.760E-08	-1.106E-15	-1.249E-15	2.342E-15	-1.610E-18	2.820E-21	-3.758E-20	3.349E-20
54	2.3625	1.108E-06	1.445E-26	1.649E-08	-2.091E-15	-1.169E-15	2.729E-15	-2.210E-18	6.645E-22	-3.902E-20	3.004E-20
55	2.3812	1.050E-06	1.206E-26	1.545E-08	-3.201E-15	-1.017E-15	3.076E-15	-2.894E-18	-1.478E-21	-3.988E-20	2.697E-20
56	2.4000	9.963E-07	1.006E-26	1.449E-08	-4.329E-15	-8.300E-16	3.388E-15	-3.728E-18	-3.320E-21	-4.026E-20	2.423E-20
57	3.0000	9.963E-07	1.006E-26	1.449E-08	-4.329E-15	-8.300E-16	3.388E-15	-3.728E-18	-3.320E-21	-4.026E-20	2.423E-20

	X	CH2S	C2H4	C2H	CH2O	C2H5	C2H2	CH2CO	C	C4H2	C3H3
1	.0000	9.986E-19	4.588E-05	8.245E-19	7.407E-05	6.698E-12	1.911E-05	7.466E-07	1.355E-25	3.289E-10	1.939E-16
2	.1500	2.455E-18	1.382E-04	2.436E-18	2.216E-04	2.133E-11	5.684E-05	2.486E-06	2.986E-25	1.366E-09	6.998E-16
3	.1875	2.126E-17	1.935E-04	1.819E-17	3.076E-04	8.679E-11	7.920E-05	3.623E-06	1.727E-29	2.204E-09	3.590E-14
4	.2250	1.879E-16	2.742E-04	1.475E-16	4.309E-04	4.063E-10	1.117E-04	5.364E-06	4.492E-29	3.660E-09	7.819E-13

5	.2625	3.626E-15	3.885E-04	2.071E-15	6.002E-04	2.457E-09	1.575E-04	7.946E-06	1.273E-24	6.099E-09	1.523E-11
6	.3000	3.055E-13	5.394E-04	1.186E-13	8.087E-04	1.585E-08	2.180E-04	1.149E-05	2.539E-20	9.896E-09	2.432E-10
7	.3187	2.922E-12	6.298E-04	7.815E-13	9.171E-04	3.003E-08	2.551E-04	1.365E-05	7.987E-18	1.252E-08	1.274E-09
8	.3375	2.513E-11	7.308E-04	4.116E-12	1.019E-03	5.361E-08	2.983E-04	1.606E-05	8.723E-16	1.582E-08	4.976E-09
9	.3563	1.839E-10	8.381E-04	1.988E-11	1.098E-03	9.726E-08	3.500E-04	1.868E-05	3.646E-14	2.001E-08	1.665E-08
10	.3656	4.750E-10	8.866E-04	4.537E-11	1.124E-03	1.323E-07	3.795E-04	2.003E-05	1.920E-13	2.254E-08	2.939E-08
11	.3750	1.141E-09	9.259E-04	1.035E-10	1.141E-03	1.751E-07	4.108E-04	2.138E-05	8.681E-13	2.539E-08	4.835E-08
12	.3797	1.673E-09	9.389E-04	1.534E-10	1.145E-03	1.975E-07	4.262E-04	2.203E-05	1.764E-12	2.692E-08	6.018E-08
13	.3844	2.169E-09	9.463E-04	2.031E-10	1.147E-03	2.233E-07	4.412E-04	2.265E-05	2.821E-12	2.852E-08	7.338E-08
14	.3937	3.186E-09	9.421E-04	3.243E-10	1.144E-03	2.847E-07	4.683E-04	2.379E-05	6.376E-12	3.185E-08	1.037E-07
15	.4031	4.675E-09	9.074E-04	5.270E-10	1.123E-03	3.604E-07	4.894E-04	2.471E-05	1.478E-11	3.523E-08	1.381E-07
16	.4125	6.982E-09	8.378E-04	8.734E-10	1.076E-03	4.476E-07	5.006E-04	2.528E-05	3.477E-11	3.832E-08	1.734E-07
17	.4219	1.043E-08	7.317E-04	1.448E-09	9.975E-04	5.296E-07	4.973E-04	2.533E-05	7.971E-11	4.052E-08	2.023E-07
18	.4312	1.504E-08	5.948E-04	2.318E-09	8.832E-04	5.746E-07	4.741E-04	2.461E-05	1.678E-10	4.090E-08	2.145E-07
19	.4406	2.014E-08	4.423E-04	3.443E-09	7.380E-04	5.520E-07	4.272E-04	2.286E-05	3.064E-10	3.840E-08	2.012E-07
20	.4500	2.423E-08	2.965E-04	4.558E-09	5.773E-04	4.579E-07	3.579E-04	1.993E-05	4.646E-10	3.247E-08	1.622E-07
21	.4594	2.558E-08	1.777E-04	5.214E-09	4.217E-04	3.232E-07	2.747E-04	1.602E-05	5.696E-10	2.399E-08	1.098E-07
22	.4687	2.338E-08	9.505E-05	5.061E-09	2.887E-04	1.934E-07	1.916E-04	1.174E-05	5.585E-10	1.519E-08	6.165E-08
23	.4781	1.844E-08	4.565E-05	4.165E-09	1.862E-04	9.865E-08	1.216E-04	7.813E-06	4.396E-10	8.223E-09	2.872E-08
24	.4875	1.262E-08	1.991E-05	2.946E-09	1.138E-04	4.357E-08	7.076E-05	4.752E-06	2.835E-10	3.862E-09	1.126E-08
25	.4969	7.628E-09	8.008E-06	1.834E-09	6.622E-05	1.704E-08	3.835E-05	2.677E-06	1.547E-10	1.614E-09	3.802E-09
26	.5062	4.158E-09	3.015E-06	1.032E-09	3.697E-05	6.051E-09	1.967E-05	1.418E-06	7.424E-11	6.169E-10	1.137E-09
27	.5156	2.087E-09	1.069E-06	5.370E-10	1.987E-05	1.976E-09	9.628E-06	7.136E-07	3.248E-11	2.196E-10	3.066E-10
28	.5250	9.583E-10	3.308E-07	2.552E-10	1.016E-05	5.559E-10	4.416E-06	3.358E-07	1.298E-11	6.852E-11	6.774E-11
29	.5437	2.266E-10	4.773E-08	6.639E-11	3.020E-06	6.546E-11	1.131E-06	8.886E-08	2.293E-12	1.039E-11	5.858E-12
30	.5625	5.262E-11	6.692E-09	1.704E-11	9.004E-07	7.322E-12	2.969E-07	2.404E-08	3.954E-13	1.741E-12	4.765E-13
31	.5813	1.260E-11	9.321E-10	4.544E-12	2.739E-07	8.089E-13	8.260E-08	6.913E-09	6.964E-14	4.202E-13	3.853E-14
32	.6000	3.227E-12	1.309E-10	1.311E-12	8.586E-08	9.004E-14	2.517E-08	2.195E-09	1.289E-14	1.850E-13	3.228E-15
33	.6187	9.136E-13	1.877E-11	4.251E-13	2.794E-08	1.022E-14	8.706E-09	7.967E-10	2.604E-15	1.225E-13	2.995E-16
34	.6375	2.934E-13	2.787E-12	1.583E-13	9.521E-09	1.204E-15	3.516E-09	3.379E-10	6.143E-16	9.319E-14	3.797E-17
35	.6563	1.072E-13	4.367E-13	6.581E-14	3.425E-09	1.555E-16	1.665E-09	1.667E-10	1.823E-16	7.058E-14	9.624E-18
36	.6750	4.529E-14	7.357E-14	3.126E-14	1.314E-09	2.165E-17	9.067E-10	9.342E-11	7.405E-17	5.464E-14	4.754E-18

37	.6938	2.167E-14	1.382E-14	1.653E-14	5.436E-10	3.263E-18	5.509E-10	5.772E-11	3.795E-17	4.322E-14	3.083E-18
38	.7125	1.142E-14	3.117E-15	9.472E-15	2.457E-10	5.303E-19	3.627E-10	3.832E-11	2.202E-17	3.481E-14	2.175E-18
39	.7312	6.454E-15	9.337E-16	5.756E-15	1.220E-10	9.053E-20	2.530E-10	2.681E-11	1.354E-17	2.846E-14	1.589E-18
40	.7500	3.830E-15	3.706E-16	3.644E-15	6.572E-11	1.279E-20	1.835E-10	1.948E-11	8.563E-18	2.356E-14	1.182E-18
41	.7875	1.569E-15	1.319E-16	1.656E-15	2.940E-11	1.532E-22	1.097E-10	1.159E-11	3.587E-18	1.672E-14	6.798E-19
42	.8250	6.964E-16	5.765E-17	8.042E-16	1.637E-11	-3.158E-22	6.996E-11	7.364E-12	1.530E-18	1.215E-14	3.982E-19
43	.9000	1.781E-16	1.636E-17	2.384E-16	7.998E-12	-1.060E-22	3.475E-11	3.629E-12	3.023E-19	7.252E-15	1.556E-19
44	1.0500	2.092E-17	2.794E-18	3.432E-17	2.767E-12	-3.331E-23	1.299E-11	1.346E-12	1.089E-20	3.444E-15	3.084E-20
45	1.2000	2.649E-18	5.595E-19	5.017E-18	9.166E-13	-1.448E-23	5.248E-12	5.406E-13	1.360E-22	1.691E-15	5.274E-21
46	1.5000	8.166E-20	2.356E-19	1.372E-19	1.826E-13	1.639E-22	1.203E-12	1.050E-13	1.358E-24	2.969E-16	9.099E-23
47	1.8000	5.789E-21	3.168E-18	9.986E-21	5.777E-14	2.232E-21	4.110E-13	3.166E-14	-3.489E-25	8.674E-17	2.558E-24
48	1.9500	1.544E-21	2.249E-18	1.666E-21	3.146E-14	-3.156E-21	2.419E-13	1.591E-14	-6.432E-30	2.783E-17	1.159E-25
49	2.1000	4.709E-22	-9.400E-17	4.362E-22	2.019E-14	-8.188E-20	1.608E-13	9.891E-15	-6.742E-35	1.066E-17	8.743E-27
50	2.1750	2.636E-22	-3.574E-16	2.498E-22	1.711E-14	-2.305E-19	1.339E-13	8.079E-15	4.395E-36	6.663E-18	2.764E-27
51	2.2500	1.534E-22	-9.428E-16	1.478E-22	1.513E-14	-4.283E-19	1.142E-13	6.796E-15	-9.595E-33	4.447E-18	1.050E-27
52	2.3250	9.176E-23	-1.824E-15	8.945E-23	1.263E-14	-5.863E-19	9.917E-14	5.834E-15	-7.312E-28	3.096E-18	4.229E-28
53	2.3438	8.063E-23	-2.050E-15	7.895E-23	1.144E-14	-5.967E-19	9.587E-14	5.624E-15	-2.568E-31	2.821E-18	3.341E-28
54	2.3625	7.089E-23	-2.254E-15	6.977E-23	9.800E-15	-5.846E-19	9.277E-14	5.427E-15	-7.424E-35	2.573E-18	2.665E-28
55	2.3812	6.235E-23	-2.432E-15	6.174E-23	7.813E-15	-5.577E-19	8.986E-14	5.243E-15	1.161E-37	2.347E-18	2.137E-28
56	2.4000	5.487E-23	-2.589E-15	5.469E-23	5.698E-15	-5.259E-19	8.711E-14	5.070E-15	9.963E-38	2.138E-18	1.708E-28
57	3.0000	5.487E-23	-2.589E-15	5.469E-23	5.698E-15	-5.259E-19	8.711E-14	5.070E-15	9.963E-38	2.138E-18	1.708E-28

	X	C3H2	C4H3	O2	H	HO2	H2	H2O	CO2	CO	HCO
1	.0000	1.454E-18	1.338E-11	1.524E-01	1.921E-14	9.697E-07	2.067E-03	6.564E-02	1.335E-03	1.216E-03	3.738E-12
2	.1500	4.582E-18	5.569E-11	1.445E-01	2.436E-14	2.550E-06	2.983E-03	7.164E-02	4.087E-03	3.213E-03	1.112E-11
3	.1875	2.136E-17	8.995E-11	1.392E-01	1.490E-13	4.036E-06	3.265E-03	7.703E-02	5.762E-03	4.278E-03	3.999E-11
4	.2250	1.175E-16	1.495E-10	1.316E-01	1.147E-12	6.682E-06	3.569E-03	8.471E-02	8.233E-03	5.744E-03	1.596E-10
5	.2625	8.459E-16	2.492E-10	1.211E-01	2.623E-11	1.142E-05	3.891E-03	9.493E-02	1.177E-02	7.704E-03	7.981E-10
6	.3000	1.320E-14	4.038E-10	1.079E-01	6.894E-09	1.981E-05	4.216E-03	1.073E-01	1.648E-02	1.016E-02	5.093E-09
7	.3187	9.625E-14	5.079E-10	1.004E-01	6.372E-08	2.595E-05	4.378E-03	1.142E-01	1.932E-02	1.157E-02	1.185E-08
8	.3375	1.150E-12	6.330E-10	9.214E-02	3.840E-07	2.893E-05	4.544E-03	1.214E-01	2.251E-02	1.310E-02	2.390E-08

9	.3563	1.272E-11	7.772E-10	8.329E-02	1.510E-06	2.585E-05	4.710E-03	1.290E-01	2.607E-02	1.475E-02	4.644E-08
10	.3656	3.920E-11	8.507E-10	7.865E-02	2.753E-06	2.391E-05	4.787E-03	1.329E-01	2.800E-02	1.559E-02	6.706E-08
11	.3750	1.104E-10	9.201E-10	7.389E-02	4.781E-06	2.183E-05	4.854E-03	1.368E-01	3.003E-02	1.644E-02	9.642E-08
12	.3797	1.800E-10	9.499E-10	7.148E-02	6.185E-06	2.072E-05	4.880E-03	1.388E-01	3.108E-02	1.686E-02	1.138E-07
13	.3844	2.484E-10	9.747E-10	6.904E-02	7.494E-06	2.235E-05	4.900E-03	1.408E-01	3.216E-02	1.727E-02	1.344E-07
14	.3937	4.306E-10	1.007E-09	6.406E-02	1.063E-05	2.897E-05	4.918E-03	1.448E-01	3.444E-02	1.806E-02	1.865E-07
15	.4031	7.432E-10	1.010E-09	5.898E-02	1.536E-05	3.793E-05	4.896E-03	1.488E-01	3.686E-02	1.879E-02	2.603E-07
16	.4125	1.266E-09	9.818E-10	5.387E-02	2.251E-05	4.997E-05	4.822E-03	1.527E-01	3.942E-02	1.940E-02	3.645E-07
17	.4219	2.072E-09	9.203E-10	4.883E-02	3.284E-05	6.506E-05	4.679E-03	1.566E-01	4.211E-02	1.984E-02	5.011E-07
18	.4312	3.119E-09	8.284E-10	4.400E-02	4.653E-05	8.177E-05	4.452E-03	1.602E-01	4.491E-02	2.003E-02	6.550E-07
19	.4406	4.119E-09	7.131E-10	3.955E-02	6.254E-05	9.726E-05	4.137E-03	1.634E-01	4.777E-02	1.987E-02	7.885E-07
20	.4500	4.565E-09	5.847E-10	3.565E-02	7.852E-05	1.084E-04	3.742E-03	1.661E-01	5.063E-02	1.929E-02	8.540E-07
21	.4594	4.094E-09	4.561E-10	3.242E-02	9.149E-05	1.131E-04	3.292E-03	1.682E-01	5.344E-02	1.829E-02	8.225E-07
22	.4687	2.906E-09	3.399E-10	2.990E-02	9.904E-05	1.112E-04	2.823E-03	1.697E-01	5.609E-02	1.692E-02	7.042E-07
23	.4781	1.627E-09	2.448E-10	2.807E-02	1.003E-04	1.041E-04	2.370E-03	1.706E-01	5.853E-02	1.529E-02	5.395E-07
24	.4875	7.309E-10	1.732E-10	2.685E-02	9.612E-05	9.394E-05	1.959E-03	1.709E-01	6.070E-02	1.356E-02	3.738E-07
25	.4969	2.720E-10	1.224E-10	2.612E-02	8.834E-05	8.272E-05	1.603E-03	1.709E-01	6.257E-02	1.183E-02	2.373E-07
26	.5062	8.715E-11	8.738E-11	2.579E-02	7.889E-05	7.183E-05	1.307E-03	1.706E-01	6.413E-02	1.021E-02	1.401E-07
27	.5156	2.485E-11	6.332E-11	2.576E-02	6.928E-05	6.173E-05	1.066E-03	1.701E-01	6.540E-02	8.755E-03	7.772E-08
28	.5250	5.915E-12	4.663E-11	2.596E-02	6.022E-05	5.294E-05	8.726E-04	1.694E-01	6.641E-02	7.476E-03	4.034E-08
29	.5437	5.559E-13	2.777E-11	2.688E-02	4.515E-05	3.939E-05	6.019E-04	1.677E-01	6.771E-02	5.450E-03	1.200E-08
30	.5625	5.674E-14	1.754E-11	2.820E-02	3.371E-05	2.958E-05	4.280E-04	1.657E-01	6.835E-02	3.984E-03	3.528E-09
31	.5813	8.559E-15	1.161E-11	2.976E-02	2.523E-05	2.240E-05	3.131E-04	1.637E-01	6.851E-02	2.932E-03	1.063E-09
32	.6000	2.782E-15	7.971E-12	3.145E-02	1.896E-05	1.705E-05	2.348E-04	1.617E-01	6.835E-02	2.179E-03	3.367E-10
33	.6187	1.588E-15	5.635E-12	3.321E-02	1.428E-05	1.302E-05	1.796E-04	1.596E-01	6.797E-02	1.637E-03	1.147E-10
34	.6375	1.074E-15	4.091E-12	3.500E-02	1.073E-05	1.003E-05	1.394E-04	1.576E-01	6.745E-02	1.245E-03	4.291E-11
35	.6563	7.159E-16	3.053E-12	3.680E-02	7.983E-06	8.332E-06	1.091E-04	1.557E-01	6.682E-02	9.598E-04	1.814E-11
36	.6750	4.855E-16	2.332E-12	3.858E-02	5.937E-06	6.908E-06	8.607E-05	1.537E-01	6.614E-02	7.489E-04	8.531E-12
37	.6938	3.364E-16	1.816E-12	4.035E-02	4.431E-06	5.736E-06	6.841E-05	1.518E-01	6.542E-02	5.915E-04	4.411E-12
38	.7125	2.377E-16	1.439E-12	4.208E-02	3.328E-06	4.782E-06	5.476E-05	1.500E-01	6.469E-02	4.725E-04	2.462E-12
39	.7312	1.710E-16	1.158E-12	4.378E-02	2.516E-06	4.005E-06	4.413E-05	1.482E-01	6.394E-02	3.814E-04	1.455E-12
40	.7500	1.248E-16	9.443E-13	4.544E-02	1.915E-06	3.370E-06	3.577E-05	1.464E-01	6.320E-02	3.108E-04	8.964E-13

41	.7875	6.954E-17	6.652E-13	4.863E-02	1.145E-06	2.500E-06	2.417E-05	1.431E-01	6.173E-02	2.153E-04	3.936E-13
42	.8250	4.002E-17	4.872E-13	5.167E-02	6.990E-07	1.900E-06	1.656E-05	1.398E-01	6.032E-02	1.532E-04	1.880E-13
43	.9000	1.560E-17	3.056E-13	5.728E-02	2.894E-07	1.209E-06	8.472E-06	1.339E-01	5.767E-02	8.764E-05	5.744E-14
44	1.0500	3.566E-18	1.867E-13	6.689E-02	6.906E-08	6.981E-07	3.016E-06	1.236E-01	5.308E-02	4.232E-05	1.036E-14
45	1.2000	8.582E-19	1.435E-13	7.501E-02	1.662E-08	4.757E-07	1.147E-06	1.150E-01	4.920E-02	2.465E-05	2.035E-15
46	1.5000	4.229E-20	1.224E-13	8.763E-02	7.732E-10	3.373E-07	3.302E-07	1.013E-01	4.320E-02	1.485E-05	1.706E-16
47	1.8000	4.613E-21	1.084E-13	9.758E-02	7.195E-11	1.950E-07	1.567E-07	9.051E-02	3.847E-02	1.096E-05	2.595E-17
48	1.9500	8.589E-22	1.024E-13	1.019E-01	6.090E-12	1.573E-07	1.200E-07	8.580E-02	3.639E-02	9.709E-06	8.763E-18
49	2.1000	1.995E-22	9.703E-14	1.059E-01	1.221E-12	1.270E-07	9.929E-08	8.153E-02	3.451E-02	8.802E-06	3.646E-18
50	2.1750	9.755E-23	9.451E-14	1.077E-01	7.199E-13	1.145E-07	9.189E-08	7.957E-02	3.363E-02	8.425E-06	2.442E-18
51	2.2500	5.156E-23	9.212E-14	1.094E-01	4.241E-13	1.042E-07	8.608E-08	7.775E-02	3.281E-02	8.098E-06	1.709E-18
52	2.3250	2.864E-23	8.988E-14	1.110E-01	2.496E-13	9.570E-08	8.147E-08	7.610E-02	3.204E-02	7.813E-06	1.202E-18
53	2.3438	2.466E-23	8.934E-14	1.114E-01	2.184E-13	9.379E-08	8.047E-08	7.572E-02	3.186E-02	7.748E-06	1.082E-18
54	2.3625	2.127E-23	8.882E-14	1.117E-01	1.912E-13	9.198E-08	7.952E-08	7.535E-02	3.169E-02	7.685E-06	9.579E-19
55	2.3812	1.836E-23	8.832E-14	1.120E-01	1.674E-13	9.026E-08	7.863E-08	7.500E-02	3.153E-02	7.626E-06	8.350E-19
56	2.4000	1.583E-23	8.785E-14	1.124E-01	1.465E-13	8.864E-08	7.780E-08	7.467E-02	3.137E-02	7.570E-06	7.211E-19
57	3.0000	1.583E-23	8.785E-14	1.124E-01	1.465E-13	8.864E-08	7.780E-08	7.467E-02	3.137E-02	7.570E-06	7.211E-19

	X	HCCO	HCCOH	H2O2	N2
1	.0000	2.124E-13	2.387E-07	7.284E-06	6.461E-01
2	.1500	4.914E-13	5.537E-07	1.923E-05	6.763E-01
3	.1875	2.426E-12	7.024E-07	2.468E-05	6.826E-01
4	.2250	1.069E-11	8.947E-07	3.116E-05	6.885E-01
5	.2625	8.305E-11	1.137E-06	3.722E-05	6.941E-01
6	.3000	2.511E-09	1.424E-06	3.712E-05	6.994E-01
7	.3187	9.856E-09	1.581E-06	2.914E-05	7.019E-01
8	.3375	3.350E-08	1.748E-06	1.763E-05	7.043E-01
9	.3563	1.033E-07	1.928E-06	7.990E-06	7.067E-01
10	.3656	1.778E-07	2.027E-06	5.071E-06	7.079E-01
11	.3750	2.989E-07	2.136E-06	3.246E-06	7.091E-01
12	.3797	3.762E-07	2.193E-06	2.702E-06	7.097E-01
13	.3844	4.375E-07	2.252E-06	2.468E-06	7.102E-01

14	.3937	5.476E-07	2.373E-06	2.562E-06	7.114E-01
15	.4031	7.022E-07	2.497E-06	2.846E-06	7.127E-01
16	.4125	9.269E-07	2.622E-06	3.199E-06	7.139E-01
17	.4219	1.236E-06	2.741E-06	3.557E-06	7.152E-01
18	.4312	1.610E-06	2.838E-06	3.841E-06	7.165E-01
19	.4406	1.976E-06	2.883E-06	3.962E-06	7.178E-01
20	.4500	2.218E-06	2.834E-06	3.858E-06	7.192E-01
21	.4594	2.241E-06	2.654E-06	3.530E-06	7.206E-01
22	.4687	2.017E-06	2.338E-06	3.045E-06	7.219E-01
23	.4781	1.614E-06	1.930E-06	2.500E-06	7.233E-01
24	.4875	1.149E-06	1.498E-06	1.982E-06	7.246E-01
25	.4969	7.342E-07	1.105E-06	1.544E-06	7.258E-01
26	.5062	4.271E-07	7.837E-07	1.199E-06	7.269E-01
27	.5156	2.290E-07	5.406E-07	9.333E-07	7.280E-01
28	.5250	1.119E-07	3.657E-07	7.362E-07	7.290E-01
29	.5437	2.968E-08	1.783E-07	4.902E-07	7.309E-01
30	.5625	7.625E-09	9.145E-08	3.491E-07	7.325E-01
31	.5813	1.998E-09	5.015E-08	2.627E-07	7.340E-01
32	.6000	5.595E-10	2.959E-08	2.058E-07	7.354E-01
33	.6187	1.746E-10	1.879E-08	1.652E-07	7.367E-01
34	.6375	6.250E-11	1.281E-08	1.356E-07	7.379E-01
35	.6563	2.553E-11	9.303E-09	1.192E-07	7.391E-01
36	.6750	1.188E-11	7.142E-09	1.046E-07	7.402E-01
37	.6938	6.151E-12	5.743E-09	9.167E-08	7.413E-01
38	.7125	3.455E-12	4.799E-09	8.051E-08	7.423E-01
39	.7312	2.061E-12	4.138E-09	7.093E-08	7.433E-01
40	.7500	1.283E-12	3.658E-09	6.272E-08	7.442E-01
41	.7875	5.722E-13	3.061E-09	5.051E-08	7.460E-01
42	.8250	2.759E-13	2.691E-09	4.146E-08	7.478E-01
43	.9000	8.337E-14	2.309E-09	2.960E-08	7.509E-01
44	1.0500	1.374E-14	2.005E-09	1.892E-08	7.562E-01
45	1.2000	2.509E-15	1.832E-09	1.408E-08	7.607E-01

46	1.5000	1.118E-16	1.610E-09	1.816E-08	7.678E-01
47	1.8000	1.170E-17	1.437E-09	1.751E-08	7.734E-01
48	1.9500	2.621E-18	1.362E-09	3.397E-08	7.758E-01
49	2.1000	8.790E-19	1.294E-09	4.114E-08	7.780E-01
50	2.1750	5.498E-19	1.262E-09	4.199E-08	7.791E-01
51	2.2500	3.569E-19	1.233E-09	4.190E-08	7.800E-01
52	2.3250	2.376E-19	1.207E-09	4.142E-08	7.808E-01
53	2.3438	2.148E-19	1.200E-09	4.129E-08	7.810E-01
54	2.3625	1.946E-19	1.195E-09	4.115E-08	7.812E-01
55	2.3812	1.764E-19	1.189E-09	4.101E-08	7.814E-01
56	2.4000	1.602E-19	1.184E-09	4.088E-08	7.816E-01
57	3.0000	1.602E-19	1.184E-09	4.088E-08	7.816E-01

TWOPNT: SUCCESS. BOUNDARY VALUE PROBLEM SOLVED.

APPENDIX B

PROCEDURE FOR EXECUTING THE CHEMKIN PREMIXED FLAT FLAME CODE ON A PERSONAL COMPUTER

When the necessary modifications were incorporated into the Sandia Premixed Flat Flame code, new executable files were created to simulate all variations of flame types seen in this study. The two files that vary from case to case are Chem.inp and Premix.inp. The input file, Chem.inp, varies according to each flame type, e.g. CH_4/Air, CH_4/CH_3Cl/Air etc., since this file contains the reaction mechanism. The input file, Premix.inp, varies not only as a function of flame type, but also from case to case within each flame type, e.g. CH_4/Air ($\phi = 1.29$), CH_4/Air ($\phi = 2.48$) etc. This input file contains the reactant mole fractions as well as the corrected temperature profile for that case. Each of these items is unique to each case. This study simulated 25 different cases.

Once the required input files were in place, the following procedure was followed to run the model:

- the CHEMKIN Interpreter, Chem. exe, is executed (this is done by double-clicking the filename when in Windows™). Chem.exe requires Chem.inp and Tran.dat
- the binary file, Chem.bin is created
- the transport property fitting program, Tran.exe, is executed. Tran.exe requires the newly created Chem.bin and Tran.dat.
- the binary file, Tran.bin, is created. Note that an *empty* Tran.bin needs to be in place. Tran.exe does not create a new Tran.bin but rather rewrites an old Tran.bin.
- the main Fortran program, Premix.exe, is executed using the recently created Chem.bin, Tran.bin and Premix.inp as inputs. The user is prompted to supply the entrainment constant used in the mass flow rate expression (real number format is required)

- two new files are created
- Premix.out contains the results that are used for analysis against the experimental data
- Save.bin is used as a restart file to run the same program again, if better convergence is required.
- Save.bin is renamed Rest.bin if it is to be used as a restart file.

APPENDIX C

SODIUM REACTION MECHANISM

REACTION	A	n	E_a	Source
$CH + O = HCO^+ + E$	5.75E15	0.	0.	a
!SAME AS CH+O=CO+H				
$HCO^+ + E = H + CO$	1.0E13	0.	0.	a
$NA + M = NA^+ + E + M$	4.7E5	0.	120.	a
NA + H2O = NAOH + H	1.8E13	0.5	44400.	b
NA + O2 + M = NAO2 + M	7.3E19	-1.	0.	b
NA + OH + M = NAOH + M	2.5E19	-1.	0.	b
NAO2 + H = NA + HO2	1.2E12	0.5	0.	b
NA + OH = NAO + H	1.2E13	0.5	43800.	b
NAO + OH = NA + HO2	1.8E11	0.5	0.	b
NA + O2 = NAO + O	1.2E13	0.5	59300.	b
NAOH + O = NA + HO2	2.4E9	0.5	8400.	b
NAO2 + H = NAO + OH	4.2E12	0.5	0.	b
NAO2 + O = NAO + O2	6.0E10	0.5	0.	b
NAO2 + OH = NAO + HO2	1.2E11	0.5	28750.	b
NAO2 + H = NAOH + O	1.2E11	0.5	0.	b
NAO2 + OH = NAOH + O2	1.8E10	0.5	0.	b
NAOH + OH = NAO + H2O	6.0E12	0.5	0.	b
NAOH + H = NAO + H2	4.2E13	0.5	14000.	b
NAOH + O = NAO + OH	1.2E13	0.5	16000.	b
NAOH + O2 = NAO + HO2	1.2E13	0.5	67800	b

a. Developed in this work (section 6.4.1).

b. Taken from Hynes, Steinberg and Schoefield (18)

Reaction Rate Constant: $k = A T^n \exp(-E_a / R / T)$; Units: K, second, cm^3, cal/mol.

APPENDIX D

SODIUM—CHLORINE REACTIONS AND CALCULATIONS

PART I (Original Sodium—Chlorine Reactions)

$$NaCl + H \xrightarrow{k_f} Na + HCl$$

Parameter	Value	Source
ΔH_R	-30.8 kcal/mole	Calculated from H_f (35,71,72)
E_a	3.5 kcal/mole	Assumed to be half E_a of analogous reaction: $CH_3Cl + H \rightarrow HCl + CH_3$
k_f	3.01E10 cm^3/mole-s	NIST Database (69)
A	1.1E13 cm^3/mole/s	Calculated from $k_f = A\exp(-E_a / RT)$; where R=1.987 cal/mole·K, T=298K

$$NaO + HCl \xrightarrow{k_f} NaCl + OH$$

Parameter	Value	Source
ΔH_R	-31.98 kcal/mole	Calculated from H_f (35,71,72)
E_a	+2.0 kcal/mole	Small barrier assumed
A	1.69E14 cm^3/mole/s	NIST Database (69)
k_f		Calculated from $k_f = A\exp(-E_a / RT)$; where R=1.987 cal/mole·K, T=298K

$$Cl + NaOH \xrightarrow{k_f} HCl + NaO$$

Parameter	Value	Source
ΔH_R	+16.1 kcal/mole	Calculated from H_f (35,71,72)
E_a	+16.1 kcal/mole	Assumed $E_a = \Delta H_R$
A	1.0E14 cm^3/mole/s	Assume equal to A from analogous reaction: $Cl + C_3H_8 \rightarrow HCl + n\text{-}C_3H_7$
k_f		Calculated from $k_f = A\exp(-E_a / RT)$; where R=1.987 cal/mole·K, T=298K

$$NaO_2 + HCl \xrightarrow{k_f} NaCl + HO_2$$

Parameter	Value	Source
ΔH_R	-5.79 kcal/mole	Calculated from H_f (35,71,72)
E_a	+2.0 kcal/mole	Small barrier assumed
A	1.39E14 cm^3/mole/s	NIST Database (69)
k_f		Calculated from $k_f = A\exp(-E_a / RT)$; where R=1.987 cal/mole·K, T=298K

$$Na + Cl_2 \xrightarrow{k_f} NaCl + Cl$$

Parameter	Value	Source
ΔH_R	-40.85 kcal/mole	Calculated from H_f (35,71,72)
E_a	+2.0 kcal/mole	Small barrier assumed
A	4.4E14 cm^3/mole/s	NIST Database (69)
k_f		Calculated from $k_f = A\exp(-E_a/RT)$; where R=1.987 cal/mole·K, T=298K

$$Na + CH_3Cl \xrightarrow{k_f} NaCl + CH_3$$

Parameter	Value	Source
ΔH_R	+12.10 kcal/mole	Calculated from H_f (35,71,72)
E_a	+12.10 kcal/mole	Assumed $E_a=\Delta H_R$
A	5.0E14 cm^3/mole/s	NIST Database (69)
k_f		Calculated from $k_f = A\exp(-E_a/RT)$; where R=1.987 cal/mole·K, T=298K

$$Na + Cl + M \xrightarrow{k_f} NaCl + M$$

Input Parameter for QRRK Calculation	Value	Source (73)	Calculated Parameter from QRRK
ν	1668 cm^{-1}	From CH_3Cl	
δ	4.18 Å	From CH_3Cl	
ε/κ	350.0 K	From CH_3Cl	
ΔH_R	+98.2 kcal/mole	From analogous reaction: $CH_3Cl=Cl+CH_3$ (high pressure limit)	
E_a	+98.2 kcal/mole	Assumed $E_a=\Delta H_R$	100.87 kcal/mole
A	1.0E15 cm^3/mole/s	From analogous reaction: $CH_3Cl=Cl+CH_3$ (high pressure limit)	1.261E15 cm^3/mole/s
n			-2.02
k_f			$k_f = AT^n \exp(-E_a/RT)$ where R=1.987 cal/mole·K, T=298K

Part II (Re-evaluated Sodium—Chlorine Reactions)

$$NaCl + H \xrightarrow{k_f} Na + HCl$$

Parameter	Value	Source
ΔH_{Rxn}	6 kcal/mole	Calculated from ΔH_f°(298K) (35,71,72)
E_a	10.5 kcal/mole	Estimated from Evans Polanyi: $E_A = E_A(TN) - \frac{\Delta H_{Rxn}}{3}$; $E_A(TN)$=12.5 kcal/mole
A	1.0E14 $cm^3mol^{-1}s^{-1}$	Estimated from: H + CH_4 and H + C_2H_6 (Allara, D.L and Shaw, R., *J. Phys. Chem. Ref. Data*, vol. 9 (1980))
k	$1.0E14 \cdot T^{0.0} e^{\frac{-10500}{RT}}$	$k_f = AT^n \exp(-E_a/RT)$; where R=1.987 cal/mole·K, T=298K

$$NaO + HCl \xrightarrow{k_f} NaCl + OH$$

Parameter	Value	Source
n	1.6534	Estimated from MOPAC6/PM3
E_a	0.0 kcal/mole	B3LYP indicates pre-encounter complex lies below reactants
A	2.48343E7 $cm^3mol^{-1}s^{-1}$	Estimated from MOPAC6/PM3
k	$2.4834E7 \cdot T^{1.6534} \cdot e^{\frac{-0}{RT}}$	$k_f = AT^n \exp(-E_a/RT)$; where R=1.987 cal/mole·K, T=298K

$$NaO + HCl \xrightarrow{k_f} NaOH + Cl$$

Parameter	Value	Source
ΔH_{Rxn}	-16.3 kcal/mole	Calculated from $\Delta H_f^o(298K)$ (35,71,72)
E_a	7.1 kcal/mole	Estimated from Evans Polanyi: $E_A = E_A(TN) - \frac{\Delta H_{Rxn}}{3}$; $E_A(TN)$=12.5 kcal/mole
A	2.0E11 $cm^3mol^{-1}s^{-1}$	From HO_2 and CH_3 (Allara, D.L., and Shaw, R., *J. Phys. Chem. Ref. Data,* vol. 9 (1980))
k	$2.0E11 \cdot T^{0.0} \cdot e^{\frac{-7100}{RT}}$	$k_f = AT^n \exp(-E_a/RT)$; where R=1.987 cal/mole·K, T=298K

$$NaO_2 + HCl \xrightarrow{k_f} NaCl + HO_2$$

Parameter	Value	Source
n	-0.50032	Estimated from MOPAC6/PM3
E_a	0.0 kcal/mole	B3LYP indicates pre-encounter complex lies below reactants
A	6.6079E12 $cm^3mol^{-1}s^{-1}$	Estimated MOPAC6/PM3
k	$6.6079E12 \cdot T^{-0.50032} \cdot e^{\frac{-0}{RT}}$	$k_f = AT^n \exp(-E_a/RT)$; where R=1.987 cal/mole·K, T=298K

$$Na + Cl_2 \xrightarrow{k_f} NaCl + Cl$$

Parameter	Value	Source
ΔH_{Rxn}	-40.85 kcal/mole	Calculated from $\Delta H_f^o(298K)$ (35,71,72)
E_a	+2.0 kcal/mole	Small barrier assumed
A	4.4E14 $cm^3mol^{-1}s^{-1}$	NIST Database (69)
k_f	$4.4E14 \cdot T^{0.0} \cdot e^{\frac{-2000}{RT}}$	Calculated from $k_f = AT^n \exp(-E_a/RT)$; where R=1.987 cal/mole·K, T=298K

$$Na + CH_3Cl \xrightarrow{k_f} NaCl + CH_3$$

Parameter	Value	Source
ΔH_{Rxn}	-12.10 kcal/mole	Calculated from $\Delta H_f^o(298K)$ (35,71,72)
E_a	8.5 kcal/mole	Estimated from $E_A = E_A(TN) - \frac{\Delta H_{Rxn}}{3}$ $E_A(TN)$ = 12.5 kcal/mol from H atom rxn
A	≈1.5E14 $cm^3mol^{-1}s^{-1}$	Estimated from analogous H+HC rxns (Allara, D.L and Shaw, R., *J. Phys. Chem. Ref. Data*, vol. 9 (1980))
k	$1.5E14 \cdot T^{0.0} \cdot e^{\frac{-8500}{RT}}$	$k_f = AT^n \exp(-E_a/RT)$; where R=1.987 cal/mole·K, T=298K

$$Na + Cl + M \xrightarrow{k_f} NaCl + M$$

Parameter	Value	Source
E_a	0.0 kcal/mole	From analogous reaction H + Cl + M→ HCl + M (Ho, W.P., and Bozzelli, J.W., 24th International Symp. Combustion, p. 743-745 (1990)
A	7.2E-21 $cm^3mol^{-1}s^{-1}$	
n	-2.0	
k	$7.2E-21 \cdot T^{-2.0} \cdot e^{\frac{-0}{RT}}$	$k_f = AT^n \exp(-E_a/RT)$; where R=1.987 cal/mole·K, T=298K

Part III (AFACT Output)

```
      THERMODYNAMIC ANALYSIS for REACTION
 Rx          NAOOHCL     = TNAQCL
 Hf {Kcal/mol} -151.980    -151.960
 S {cal/mol K}   79.630      74.030


dHr {kcal/mol}   (298K) =         .02     dHr avg (298., 1500. K) =       -1.74
dU (dE) {kcal/mol} (")  =         .02     dUr avg (298., 1500. K) =       -1.74
dSr {cal/mol K}  ( " )  =       -5.60     dSr avg (298., 1500. K) =       -8.00
dGr  {kcal/mol}  ( " )  =        1.69     dGr avg (298., 1500. K) =        5.45
          Kc     ( " )  =   5.772E-02     Kc avg (298., 1500. K ) =   4.727E-02
Fit Af/Ar      : A = 2.664E+03 n = -1.88 alpha =-4.427E-04 avg error    6.16 %
Fit Af/Ar w/ddU: A = 2.308E+07 n = -3.53 alpha =-1.618E-03 avg error    7.93 %

     T (K)  dH(Kcal/mol)  dU(Kcal/mol) dS(cal/mol K)      Kc       dG(Kcal/mol)
     300.00    1.707E-02    1.707E-02   -5.610E+00    5.774E-02    1.700E+00
     400.00   -2.059E-01   -2.059E-01   -6.243E+00    5.597E-02    2.291E+00
     500.00   -5.189E-01   -5.189E-01   -6.939E+00    5.131E-02    2.951E+00
     600.00   -8.776E-01   -8.776E-01   -7.592E+00    4.574E-02    3.678E+00
     800.00   -1.613E+00   -1.613E+00   -8.651E+00    3.547E-02    5.308E+00
    1000.00   -2.270E+00   -2.270E+00   -9.386E+00    2.783E-02    7.116E+00
    1200.00   -2.818E+00   -2.818E+00   -9.887E+00    2.250E-02    9.047E+00
    1500.00   -3.494E+00   -3.494E+00   -1.039E+01    1.729E-02    1.209E+01
    2000.00   -4.345E+00   -4.345E+00   -1.089E+01    1.246E-02    1.743E+01

  The model fitted is for uni-molecular reaction.

 The equation to the 2 parameter model of A(T)
 for A(T) = Aprime * T^n
     Aprime = 6.6079E+12        n =   -.50032

 Temp(K)          AF(T)        AF-fit(T)        LnAF(T)       LnAF_fit(T)
 300.00       3.714E+11        3.808E+11      2.664E+01        2.667E+01
 400.00       3.600E+11        3.298E+11      2.661E+01        2.652E+01
 500.00       3.171E+11        2.949E+11      2.648E+01        2.641E+01
 600.00       2.739E+11        2.692E+11      2.634E+01        2.632E+01
 800.00       2.143E+11        2.331E+11      2.609E+01        2.617E+01
1000.00       1.850E+11        2.085E+11      2.594E+01        2.606E+01
1200.00       1.726E+11        1.903E+11      2.587E+01        2.597E+01
1500.00       1.673E+11        1.702E+11      2.584E+01        2.586E+01
2000.00       1.740E+11        1.474E+11      2.588E+01        2.572E+01


      THERMODYNAMIC ANALYSIS for REACTION  use only for entropy
 Rx          NAO2       + HCL        = NAOOHCL    energies = not correct
 Hf {Kcal/mol}  -13.000    -22.000   -151.980
 S {cal/mol K}   54.800     44.600     79.630

dHr {kcal/mol}   (298K) =     -116.98     dHr avg (298., 1500. K) =     -112.63
dU (dE) {kcal/mol} (")  =     -116.39     dUr avg (298., 1500. K) =     -110.84
dSr {cal/mol K}  ( " )  =      -19.77     dSr avg (298., 1500. K) =      -14.46
dGr  {kcal/mol}  ( " )  =     -111.09     dGr avg (298., 1500. K) =      -99.63
          Kc     ( " )  =   6.660E+82     Kc avg (298., 1500. K ) =   1.224E+26
Fit Af/Ar      : A = 8.072E-09 n =  3.36 alpha =-1.383E-03 avg error   13.19 %
Fit Af/Ar w/ddU: A = 9.398E-17 n =  6.62 alpha =-1.756E-04 avg error   17.74 %
```

T (K)	dH(Kcal/mol)	dU(Kcal/mol)	dS(cal/mol K)	Kc	dG(Kcal/mol)
300.00	-1.170E+02	-1.164E+02	-1.976E+01	1.983E+82	-1.110E+02
400.00	-1.166E+02	-1.158E+02	-1.878E+01	1.385E+61	-1.091E+02
500.00	-1.161E+02	-1.151E+02	-1.759E+01	3.297E+48	-1.073E+02
600.00	-1.154E+02	-1.142E+02	-1.640E+01	1.448E+40	-1.056E+02
800.00	-1.139E+02	-1.123E+02	-1.422E+01	6.823E+29	-1.025E+02
1000.00	-1.123E+02	-1.103E+02	-1.242E+01	5.580E+23	-9.989E+01
1200.00	-1.107E+02	-1.083E+02	-1.095E+01	5.784E+19	-9.756E+01
1500.00	-1.083E+02	-1.053E+02	-9.151E+00	7.372E+15	-9.455E+01
2000.00	-1.043E+02	-1.004E+02	-6.876E+00	1.299E+12	-9.057E+01

use only for entropy

THERMODYNAMIC ANALYSIS for REACTION

Rx	NAO2	+ HCL	= NACL	+ HO2
Hf {Kcal/mol}	-13.000	-22.000	-43.359	2.500
S {cal/mol K}	54.800	44.600	54.901	54.730

dHr {kcal/mol}	(298K) =	-5.86	dHr avg (298., 1500. K) =	-3.11
dU (dE) {kcal/mol}	(") =	-5.86	dUr avg (298., 1500. K) =	-3.11
dSr {cal/mol K}	(") =	10.23	dSr avg (298., 1500. K) =	13.56
dGr {kcal/mol}	(") =	-8.91	dGr avg (298., 1500. K) =	-15.30
Kc	(") =	3.399E+06	Kc avg (298., 1500. K) =	5.242E+03

Fit Af/Ar : A = 1.235E-01 n = 1.20 alpha =-1.189E-03 avg error 4.01 %

Fit Af/Ar w/ddU: A = 1.141E-04 n = 2.43 alpha =-1.069E-03 avg error 4.75 %

T (K)	dH(Kcal/mol)	dU(Kcal/mol)	dS(cal/mol K)	Kc	dG(Kcal/mol)
300.00	-5.855E+00	-5.855E+00	1.024E+01	3.198E+06	-8.928E+00
400.00	-5.590E+00	-5.590E+00	1.100E+01	2.880E+05	-9.991E+00
500.00	-5.269E+00	-5.269E+00	1.172E+01	7.315E+04	-1.113E+01
600.00	-4.900E+00	-4.900E+00	1.239E+01	3.110E+04	-1.233E+01
800.00	-4.046E+00	-4.046E+00	1.361E+01	1.204E+04	-1.494E+01
1000.00	-3.080E+00	-3.080E+00	1.469E+01	7.648E+03	-1.777E+01
1200.00	-2.034E+00	-2.034E+00	1.564E+01	6.152E+03	-2.080E+01
1500.00	-3.662E-01	-3.662E-01	1.688E+01	5.531E+03	-2.569E+01
2000.00	2.558E+00	2.558E+00	1.856E+01	5.987E+03	-3.456E+01

REFERENCES

1. Zander, A.T., T.C. O'Haver and P.N. Keliher, *Anal. Chem.*, 48,1166 (1976)

2. Cochran, R.L. and G.M. Hieftje, *Anal. Chem.*, 49, 98 (1977)

3. Fernando, R., C. Calloway and B.T. Jones, *Anal. Chem.*, 64, 1556-1560 (1992)

4. Furutta, N., H.Harguchi and K. Fuwa, *Anal. Chem.*, 49, 1263-1265 (1977)

5. Johnson, D.J., F.W. Plankey and J.D. Winefordner, *Anal. Chem.*, 46, 1898-1902 (1974)

6. Davis, L.A., R.J. Krupa and J.D. Winefordner, *Anal. Chim. Acta*, 173, 51-62 (1985)

7. Fowler, W.K., D.O.Knapp and J.D. Winefordner, *Anal. Chem.*, 46, 601-602 (1974)

8. Kindevater, J. and T. C. O' Haver, *J. Anal. Chem. Spec.*, 1, 89-91 (1986)

9. Jones, B.T., B.W. Smith and J.D. Winefordner, *Anal. Chem.*, 61, 1670-1674 (1989)

10. Tittarelli, P.T., R. Lancia and T. Zerlia, *Anal. Chem.*, 57, 2002-2005 (1985)

11. Harris, D.C., Quantitative Chemical Analysis, W.H. Freeman and Company, New York (1995)

12. Rann, C.S. and A.N. Hambley, *Anal. Chem.*, 37, 879-884 (1965)

13. Moore, J.H., C.C. Davis, M.A. Coplan, Building Scientific Apparatus, Addison Wesley Publishing Company (1983)

14. Van Loon, J.C., Analytical Atomic Absorption Spectroscopy, Academic Press, New York (1980)

15. Robinson, J.W., Atomic Spectroscopy, Marcel Dekker, New York (1990)

16. Skoog, D.A., Principles of Instrumental Analysis, Saunders College Publishing (1985)

17. Fontijn, A., Gas Phase Metal Reactions. " Metal Ion Chemistry In Flames" by John M. Goodings, Elsevier Science Publishers (1992)

18. Hynes, A.J., M. Steinberg and K. Schofield, *J. Chem. Phys.*, 80, 2585-2597 (1984)

REFERENCES
(Continued)

19. Fontijn, A., Gas Phase Metal Reactions, " The Flame Chemistry of Alkali and Alkaline Earth Metals" by Keith Schofield, Elsevier Science Publishers (1992)

20. Oppelt, E.T., JAPCA, 37, 558-586 (1987)

21. Oppelt, E.T., Environ. Sci. Technol., 20 (1986)

22. Cross, F.L., H.E. Hesketh, Controlled Air Incineration, Technomic Publishing Company (1985)

23. Waterland, L.R., D.J. Fournier, W.E. Whitworth and G. J. Carroll, *Ninth AAAR Annual Meeting, Philadelphia*, p 221 (1990)

24. Wu, C.Y. and P. Biswas, *Combustion and Flame*, 93, 31-40 (1993)

25. Barton, R.G., W. D. Clark, and W. R. Seeker, *Combust. Sci. Technol.*, 74, 327-342 (1990)

26. Kee, R.J., J.F. Grcar, M.D. Smooke, J.A. Miller, " A Fortran Program for Modeling Steady Laminar One-Dimensional Premixed Flames," Sandia National Laboratories Report SAND85-8240 (1985)

27. Mao, F., *Combustion of Methyl Chloride, Monomethyl Amine and Their Mixtures in a Two Stage Turbulent Flow Reactor*, Ph.D. Dissertation, New Jersey Institute of Technology (1995)

28. Kee, R.J., J. A. Miller, and T.H. Jefferson, "CHEMKIN: A General Purpose Problem-Independent, Transportable, Fortran, Chemical Kinetic Program Package," Sandia National Laboratories Report SAND80-8003 (1980)

29. Kee, R.J., J. Warnatz, and J.A. Miller, "A Fortran Computer Program for the Evaluation of Gas-Phase Viscosities, Conductivities, and Diffusion Coefficients," Sandia National Laboratories Report SAND83-8209 (1983)

30. Spalding, D.B., Combustion and Mass Transfer, Pergamon Press, New York (1979)

31. Perry, R.H., Perry's Chemical Engineers' Handbook, Seventh Edition, McGraw-Hill, New York (1997)

REFERENCES
(Continued)

32. Curtis, C.F., and J.O. Hirschfelder, "Transport Properties of Multicomponent Gas Mixtures", *J. Chem. Phys.*, 17, p.550 (1949)

33. Coffee, T.P., and J.M. Heimerl, "A Transport Algorithm for Premixed, Laminar, Steady-state Flames", *Comb. and Flame*, 43, p.273 (1981)

34. Westmoreland, P., *Experimental and Theoretical Analysis of Oxidation and Growth Chemistry in a Fuel-Rich Acetylene Flame*, Ph.D. Dissertation, Department of Chemical Engineering, MIT, Cambridge, MA (1986)

35. Handbook of Chemistry and Physics, 55th ed., CRC Press, Boca Raton, Fla. (1974)

36. Zamansky, V.M., V.V. Lissianski, P.M. Maly, L. Ho, D. Rusli, and W.C. Gardiner, *Combustion and Flame,* vol. 117, p. 821-831 (1999)

37. Fristrom, R.M., and A.A. Westenberg, Flame Structure, McGraw-Hill, New York (1965)

38. Finley, B.L., Proctor, D.M., Paustenbach, D.J., *Regul Toxicol Pharmacol*, 16(2), 161-176 (1992)

39. Folinsbee, L.J., *Environ. Health Perspect.*, 100, 45-46 (1993)

40. Lee, S.D., *Toxicol. Ind. Health*, 6(5), 245-255 (1990)

41. Gurjar, B.R., Mohan, M., Sidhu, K.S., *Regul Toxicol Pharmacol*, 24(2 Pt 1), 141-148 (1996)

42. Kleinman, M.T., Baily, R.M., Whynot, J.D., Anderson, K.R., Linn, W.S., Hackney, J.D., *Arch. Environ. Health*, 40(4), 197-201 (1985)

43. Kaskan, W.: "The Dependence Flame Temperature on Mass Burning Velocity", *Sixth Symposium (International) on Combustion*, Reinhold, N.Y., 134 (1957)

44. Kim, H.T., *Temperature and Particle Size Dependence of Sodium Bicarbonate Inhibition of Methane/Air Flames*, M.S. Dissertion, The Pennsylvania State University, PA, USA (1983)

45. Wang, L. and Barat, R.B., *Hazardous Waste and Hazardous Substances*, vol. 12, p51+ (1995)

REFERENCES
(Continued)

46. Wang, L., Jalvy, P., and Barat, R.B., *Combustion Science and Technology*, vol. 97, p 13-36 (1994)

47. Iya, K., Wollowitz, S. and Kashan, W., *Symp (International) Combust.*, [Proc], 15, 329-336 (1975)

48. Iya, K., Wollowitz, S. and Kashan, W., *Combust. Flame*, 22, 415-417 (1974)

49. Vanpee, M. and Sherodkar, P., *Seventeenth Symposium (Int) on Combustion*, 787-795 (1978)

50. Skoog, D.A., Principles of Instrumental Analysis, 3rd Edition, Saunders College Publishing (1985)

51. Wang, L., Jalvy, P., and Barat, R.B., *Combust. Sci. and Tech.*, vol. 97, p. 13-36 (1994)

52. Valeiras, H., Gupta, A.K. and Senkan, S. M., *Combust. Sci. and Tech.*, vol. 36, p.123-133 (1984)

53. Strehlow, R.A., Fundamentals of Combustion, International Textbook Company, Scranton, PA

54. Kim, H.T., *Korean J. of Chem. Eng.*, 9(1), 1-7 (1992)

55. Barat, R.B., A.F. Sarofim, J.P. Longwell, and J.W. Bozzelli, *Combustion Science and Technology,* vol. 74, p.361 (1990)

56. Brouwer, J., J.P. Longwell, A.F. Sarofim, R. B. Barat, and J.W. Bozzelli, *Combustion Science and Technology,* vol. 85, no. 1-6, p. 87, (1992)

57. Ho, W.P., Q.R. Yu, and J.W. Bozzelli, *Combustion and Flame,* vol. 88, p. 265, (1992a)

58. Lee, K.Y. and I.K. Puri, *Combustion and Flame*, 94, p. 191-204 (1993)

59. Beer, J., N. Chigier, Combustion Aeromodynamics, Krieger Publishing, Malabar, Fla. (1983)

60. Gaydon, A.G., The Spectroscopy of Flames, 2nd ed., Chapman and Hall, London (1974)

REFERENCES
(Continued)

61. Gupta, A.K., and H.A. Valeiras, *Combustion and Flame,* 55, p. 245 (1984)

62. Ho, W., *Pyrolysis and Oxidation of Chloromethanes, Experiments and Modeling,* PH.D. Dissertation, New Jersey Institute of Technology (1993)

63. Jensen, D.E., G.A. Jones, *J. Chem. Soc., Faraday Trans. I,* 78, p. 2843-2850, (1982)

64. McNesby, K.L., R.G. Daniel, A.W. Miziolek, and S.H. Modiano, *Applied Spectroscopy,* vol. 51, p. 678-683 (1997)

65. Glazkova, A.P., V.P. Karpov, and P.V., Phil, *Archivum Combustionis,* vol. 11, p. 273-282, (1991)

66. Lewis, B., and G. von Elbe, Combustion, Flames and Explosions of Gases, 3rd Edition, Academic Press, Inc. (1987)

67. Barat, R.B., "Modeling Laminar Burning Velocities", Submitted to *Combustion Theory and Modeling* (1999)

68. Kerr, J.A., and S.J. Moss, eds., Handbook of Bimolecular and Termolecular Reactions, vols. I and II, CRC Press, Boca Raton, Fla. (1981)

69. National Institute of Standards and Technology (NIST), Standard Reference Database 17, Version 4.0 (1992)

70. Ritter, E.R. and J.W. Bozzelli, *International Journal of Chemical Kinetics*, vol. 23, p.767 (1991)

71. Kee, R.J., F.M. Rupley, J.A. Miller, "The CHEMKIN Thermodynamic Data Base", Sandia National Laboratories Report SAND87-8215B (1993)

72. Wagman, D.D., The National Bureau of Standards Tables of Chemical Thermodynamic Properties: Selected Values for Inorganic and C1 and C2 Organic Substances in S.I. Units, American Chemical Society and American Institute of Physics Publishers (1982)

73. Barat, R.B., *Characterization of the Mixing/Chemistry Interaction in the Toroidal Jet Stirred Combustor*, Ph.D. Dissertation, Department of Chemical Engineering, MIT, Cambridge, MA (1990)

REFERENCES
(Continued)

74. Fairbank, W.M., T.W. Hansch, and A.L. Schawlow, *Journal of the Optical Society of America*, vol. 65, p.199 (1975)

75. Nefedov, A.P., V.A. Sinel'shchikov and A.D. Usachev, *J. Quant. Spectrosc. Radiat. Transfer*, vol. 61, p. 73 (1999)

76. Bauer, H.H., G.D. Christian, J.E. O'Reilly, Instrumental Analysis, Allyn and Bacon Inc. (1978)

77. Lay, T.H., J.W. Bozzelli, and J.H. Seinfeld, *J. Phys. Chem., (in Press)*

78. "JANAF Thermochemical Tables, 3rd Edition." *J. Phys. Chem. Ref. Data*, vol.14

79. Benson, S.W., The Foundations of Chemical Kinetics, McGraw-Hill Book Company, Inc., New York (1960)

80. Foresman, J.B., A. Frisch, Exploring Chemistry with Electronic Structure Methods: A Guide to Using Gaussian, Gaussian Inc., Pittsburgh, Pennsylvania (1993)

81. Becke, A. D. (1993). "Density-functional thermochemistry. III. The role of exact exchange." J. Chem. Phys. 98(7): 5648-5652.

82. Curtiss, L. A., K. Raghavachari, et al. (1997). "Assessment of Gaussian-2 and density functional theories for the computation of enthalpies of formation." J. Chem. Phys. 106(15): 1063-1079.

83. Curtiss, L. A., K. Raghavachari, et al. (1991). "Gaussian-2 theory for molecular energies of first- and second-row compounds." J. Chem. Phys. 94(11): 7221-7230.

84. Foresman, J. B. and A. Frisch (1996). Exploring Chemistry with Electronic Structure Methods. 2nd Ed. Pittsburgh, PA, Gaussian, Inc.

85. Frisch, M. J., G. W. Trucks, et al. (1998). Gaussian 98 (Revision A.1). Pittsburgh PA, Gaussian Inc.

86. Parr, R. G. and W. Yang (1989). Density-Functional Theory of Atoms and Molecules. New York, Oxford.